Improving Fine Grid Meteorological Simulations for Air Quality Applications

Phase 1 Final Report

For

CRC Project Number A-46

Submitted to:
Mr. Brent K. Bailey
Coordinating Research Council
3650 Mansell Road, Suite 140
Alpharetta, GA 30022

by
David R. Stauffer and Aijun Deng

Department of Meteorology
The Pennsylvania State University
University Park, Pennsylvania 16802

Technical Contact: David R. Stauffer, (814)863-3932, stauffer@mail.meteo.psu.edu, FAX (814)865-3663

October 8, 2004

ABSTRACT

In a previous study funded by the Coordinating Research Council (CRC), it was shown that use of four dimensional data assimilation (FDDA) and improved physics in the Penn State University (PSU)/National Center for Atmospheric Research (NCAR) MM5 produced the best overall performance on the 12-km domain. However, further reduction of the grid length from 12 km to 4 km in the simulation of the 18-19 September 1983 CAPTEX case had detrimental effects on the meteorological solutions. The primary cause of the poor mesoscale model performance was traced to the explicit representation of convection accompanying a cold front advancing across the lower Great Lakes and into New England. Because no convective parameterization was used on the 4-km grid, the convective updrafts were forced on coarser-than-realistic scales (normal updraft diameter for most storms in the eastern United States is ~ 2 km), and the rainfall and the atmospheric response to the convection were too strong. The evaporative cooling and the associated downdrafts were too vigorous, causing widespread disruption of the low-level winds and spurious advection of the simulated tracer.

Penn State has completed the first year of this new follow-on project to improve the MM5 model simulations on the 4-km grid with special attention given to quantitative precipitation forecasts (QPF) and meteorological accuracy. A series of experiments was designed to address model sensitivities on the 4-km domain to mixed-phase microphysics, planetary boundary layer (PBL) physics, convective parameterization, enhanced horizontal diffusion, and use of analysis nudging versus observation nudging.

Some of the conclusions from this study include 1) modification of the vertical mixing length scales to enhance the vertical mixing in Penn State's Gayno-Seaman Turbulent Kinetic Energy (TKE) PBL scheme has shown marked improvements in the simulated fields, 2) use of

the new Kain-Fritsch convection scheme on the 4-km domain, with its simple treatment of shallow convection, tended to reduce the tendency for the 4-km explicit convection to produce grid point storms with excessive precipitation, which caused anomalous low-level winds and evaporative cold pools, 3) use of the National Centers for Environmental Prediction (NCEP) Medium Range Forecast (MRF) PBL scheme, originally written for the MRF model and now used in Global Forecast System (GFS) model, generally showed larger model errors within the PBL and a clear tendency to overestimate the PBL height, 4) use of weak analysis nudging FDDA on the 4-km domain as used on the 12-km domain improved the results, and 5) use of observation nudging is more appropriate for the fine-scale 4-km domain and produced much better results than analysis nudging. The best results were obtained by applying observation nudging and the new Kain Fritsch convective scheme on the 4-km domain along with the modifications to the TKE PBL scheme. In year 2 of the project, we will test some of the conclusions from this MM5 study in the Weather Research and Forecast (WRF) model to further investigate this problem of 4-km quantitative precipitation forecasts (QPF) and compare the WRF results with the MM5 results.

EXECUTIVE SUMMARY

An inter-regional transport (IRT) study (CRC Project No. A-28) was conducted by Seaman et al. (2002) using the Penn State University (PSU)/National Center for Atmospheric Research (NCAR) mesoscale model, MM5, based on the 18-19 September 1983 Cross Appalachian Tracer Experiment (CAPTEX) case. It was found that a baseline model configuration reflecting typical capabilities of the late 1980s [70-km horizontal grid resolution, 15 vertical layers below the model top at 100 hPa, older sub-grid physics, and no four dimensional data assimilation (FDDA)] produced large meteorological errors that severely degraded the accuracy of the surface tracer concentrations predicted by the Second-Order Closure Integrated Puff (SCIPUFF) dispersion model. Improving the horizontal and vertical resolution of the MM5 to 12 km (typical for current operational models) and 32 layers (12 layers in the lowest kilometer) led to some improvements in the statistical skill, but the addition of more advanced physics produced much greater reductions of simulation errors. Use of FDDA, the incorporation of observational information into the model as it is running, along with 12-km resolution and improved physics, produced the overall best performance.

However, further reduction of the grid length from 12 km to 4 km in the simulation had detrimental effects on the meteorological and plume dispersion solutions. The primary cause of the poor mesoscale model performance was traced to the explicit (grid-resolved) representation of convection accompanying a cold front advancing across the lower Great Lakes and into New England. Clouds and precipitation occur in the atmosphere due to upward motions and the availability of moisture. A convective parameterization accounts for the effects of sub-grid scale

updrafts and convection by using a set of rules based on the grid-resolved fields. The grid-resolved vertical motion need not be upward for parameterized sub-grid convection to occur.

When a convective parameterization is not used, as is common for a 4-km grid, then the grid-resolved fields must reflect both upward motion and a local moisture source to produce model precipitation. These conditions are more difficult for the model to simulate given the limited observations available to define the model initial state, and the convective updrafts must be forced explicitly on the 4-km grid. A 4-km updraft is too large since normal updraft diameters for most storms in the eastern United States is ~ 2 km, and therefore the rainfall and the atmospheric response to the explicit convection are too strong. The evaporative cooling and the associated downdrafts are too vigorous, causing widespread disruption of the low-level winds and spurious advection of the simulated tracer. This result should not be interpreted to mean that 4-km grids are unsuitable for air-quality studies in general. However, model simulations on a grid of 4 km or less cannot be automatically assumed to be superior to coarser resolution simulations in all situations.

The objectives of this study are to investigate the role of 1) model physics, 2) FDDA and 3) numerics (e.g., numerical diffusion) on the accuracy of cloud and precipitation fields simulated at Δx =4 km during CAPTEX'83. There are thirteen MM5 experiments at 4-km resolution conducted in this research. The detailed experimental design is summarized in Table 3.

This study has resulted in a number of important specific conclusions about improving the MM5 model simulations on the 4-km grid:

(1) The baseline experiment (Exp. MB1) used the current most up-to-date version of the MM5 modeling system without any convective parameterization or FDDA. During a night time period ending at the 21-h model time, Exp. MB1 produced a wide-spread pattern of precipitation over a large area ahead of the model-simulated cold front, with a maximum 3-hourly precipitation value of 108 mm over Lake Erie. At 30 h, Exp. MB1 reproduced the spurious convective system reported in the original study during this day time period (Figure 27). It was associated with divergent outflow boundaries and a cold pool in northwestern Pennsylvania (PA) near Lake Erie. Statistical analysis showed that Exp. MB1 had relatively large mean absolute error (*MAE)* in simulated wind speed and wind direction which would adversely affect transport and dispersion calculations using these model-simulated fields.

(2) Use of FDDA in Exps. MS1 (analysis nudging, relaxation of the model fields towards the gridded observational analyses with the corrections interpolated in time and applied to every grid cell) and MS1.1 (observation nudging, relaxation of the model fields towards the individual observations with the corrections spread appropriately in space and time) on the 4-km domain without any convective parameterization reduced the erroneous maximum value of precipitation at 21 h over Lake Erie by about 25 percent and made the rain band associated with the cold front narrower and more organized although the convective precipitation was still overpredicted. At the 30-h time, both precipitation amount and areal coverage were reduced compared to the baseline experiment, Exp. MB1, but FDDA alone could not completely eliminate the

spurious convective system. Statistical results indicated that use of FDDA made a significant contribution to reducing the model errors. It was shown that using analysis nudging of surface wind in the planetary boundary layer (PBL) based on conventional data had some detrimental effects while the strategy of withholding assimilation of coarse resolution mass field data in the PBL was re-affirmed. The use of obs nudging produced much better results as expected on these finer scales.

(3) Enhanced vertical mixing in Penn State's Gayno-Seaman PBL (GSPBL) scheme without any convective parameterization or FDDA showed marked improvements in the simulated wind and mass fields compared to the Exp. MB1. Thus, Exp. MS2 was considered to be a new baseline experiment (Exp. MB2) for all other experiments, and the Exp. MS2 mixing length modifications were adopted in all other sensitivity experiments. However, it was apparent that using the enhanced vertical mixing alone did not alleviate the problem with excessive grid-point convection on the 4-km domain because a 111-mm maximum still existed in southern Lake Erie at the 21-h time and a clear surface wind divergent pattern accompanying a spurious convective system cold pool appeared at the 30-h time.

(4) When NCAR's MRF PBL scheme was applied in lieu of the GSPBL scheme in Exp. MS3 without any convective parameterization or FDDA, MM5 produced worse precipitation patterns at both the 21-h and 30-h times. At 21 h, the lack of precipitation in this southern Lake Erie region by Exp. MS3 was not consistent with the surface and satellite observations. The larger vertical mixing and deeper PBL heights, even during the night, were apparently eliminating the precipitation in the Lake Erie region. At 30 h, Exp. MS3 produced a significantly worse

simulation than Exp. MB2 in the model-simulated precipitation field because the spurious convection had spread to a much larger area, associated with an even larger area of disturbed flow with outflow boundaries and cold pools (Figure31). Statistical evaluation indicated that Exp. MS3 produced degraded model simulations in all fields including wind speed, wind direction, temperature and sea-level pressure. The only improvement (mainly during the night time) was in the water vapor mixing ratio field and this was likely caused by the overestimation of the PBL depth. Based on the findings in this research and other studies at Penn State, the MRF PBL scheme should not be considered an attractive scheme for representing boundary layer structure in the MM5.

(5) Use of mixed-phase microphysics (accounting for both liquid and frozen water species at the same time), along with no convective parameterization or FDDA, in Exp. MS4 produced a precipitation pattern that showed enhanced and more localized precipitation at both times. At 30 h, accompanying the more intense precipitation in northwestern PA was a divergent pattern evident in the simulated surface wind field, and associated with a cold pool in the surface temperature field. The *MAE* error analysis indicated that use of mixed-phase microphysics had some improvements over Exp. MB2 for model-simulated wind speed, temperature, water vapor mixing ratio and sea-level pressure.

(6) When the new Kain-Fritsch convective parameterization scheme (KF2) was applied directly to the 4-km grid in Exp. MS5 with no FDDA, the model-simulated non-convective (grid-resolved) rain produced by the explicit microphysics was significantly reduced and therefore improved. The convective

scheme as hypothesized appeared to release some of the atmospheric convective instability so that the explicit scheme response was now much weaker. Use of the convective scheme produced light or no precipitation in northwestern PA at 30 h (Figure 34) where none was observed and grid-point type storms had developed in all of the other experiments. Thus, the total precipitation was also generally much lighter than that of the other experiments in this region. Adding mixed phase to the Kain-Fritsch sub-grid physics on the 4-km domain with no FDDA in Exp. MS5.1 produced somewhat larger local maxima and a more concentrated explicit pattern. Statistical score comparisons with the baseline experiment, MB2, indicated that use of KF2 on the 4-km domain had produced some improvements for the model-simulated fields of wind speed, temperature, water vapor mixing ratio and sea-level pressure.

(7) Several experiments (e.g., Exps. MS6) using enhanced horizontal diffusion (numerical smoothing) and no convective parameterization or FDDA suggested that use of larger horizontal diffusion alone as a solution to this grid-point storm problem was largely ineffective because it had very little effect on the model-simulated precipitation at 21 h. In fact, two of the enhanced diffusion experiments produced even stronger grid-point storms at this time. The statistical results showed a relatively small impact from the use of the different enhanced diffusion strategies overall, and although increased horizontal diffusion may show some advantage at certain times such as at 30 h with the spurious precipitation, it can adversely affect the model's ability to produce important mesoscale structures and cannot be considered a general solution.

(8) Combining KF2 and observation nudging, FDDA on the 4-km domain in Exp. MS7 produced the best overall results in both the subjective (e.g., Figure 37) and statistical (e.g., Figure 38) evaluations. It produced the largest reduction (50 percent) in the total maximum precipitation for the Lake Erie region grid-point storm at 21 h, and it did not produce the spurious mesoscale convective system at 30 h which allowed the simulated low-level flow at this time to be consistent with the observations. Thus, use of the combination of observation nudging and the new Kain-Fritsch cumulus convection parameterization on the 4-km domain seemed to have the most significant positive impact on the model solutions on the 4-km grid in this CAPTEX '83 case.

(9) It must be pointed out that use of a convective sub-grid physics scheme such as KF2 at 4-km resolution for deep (precipitating) convection violates the underlying assumption that the size of the updraft being parameterized is much smaller than the grid size. However, its shallow convective parameterization should still be valid (Deng et al. 2003). It is also clear that in general, explicit microphysics alone cannot completely represent deep convection on these 4-km grid scales and some type of parameterization is needed. Since there is no readily identifiable approach to do this, this presents a serious dilemma when using 4-km grids to simulate deep convective environments. The results presented here show that use of KF2 on the 4-km grid may still be helpful in these situations where 4-km resolution is desired and explicit microphysics alone produces grossly unrealistic quantitative precipitation forecasts (QPF).

Note that this is only one case study, but this case is representative of mid-latitude frontal rain and deep convection cases, so these results should be generally representative of other cases. Additional cases are still needed to determine the general added value of this approach. Also, additional sensitivity experiments should be performed to assess the respective roles of alternate turbulence and convective parameterizations. For example, additional experiments to be performed before publication of these results should include Grell convective parameterization with the GSPBL, and Grell convection coupled to the MRF PBL (a common MM5 physics combination). Furthermore, these findings should be investigated using a different mesoscale model, such as the new Weather Research and Forecast (WRF) model.

TABLE OF CONTENTS

LIST OF ACRONYMS

AGL	Above ground level
C	Celsius
CAPE	Convective available potential energy
CAPTEX	Cross Appalachian Tracer Experiment
CAPTEX'83	Cross Appalachian Tracer Experiment of 1983
CONUS	Continental United States
CPS	Convective parameterization scheme
CRC	Coordinating Research Council, Inc.
DEG	Degree
ºF	Degree Fahrenheit
FDDA	Four dimensional data assimilation
g/kg or g kg^{-1}	Gram per kilogram
GSPBL	Penn State Gayno-Seaman PBL scheme
hPa	Hectopascal
I	Index of agreement
IRT	Inter-regional transport
kg	Kilogram
km	Kilometer
KF2	The new Kain-Fritsch convective parameterization scheme
LLJ	Low-level jet
MB1DRY	MM5 Baseline experiment 1 without latent heating
MBn	MM5 Baseline experiment n
MAE	Mean absolute error
m/s or m s^{-1}	Meter per second
ME	Mean error
mm	Millimeter
MM5	Fifth-generation Penn State/NCAR mesoscale model
MM5V3	Version 3 of MM5
MRF	Medium range forecast
MRF PBL	NCEP Hong and Pan MRF PBL scheme
MSn	MM5 sensitivity experiment n
NCAR	National Center for Atmospheric Research
NCEP	National Centers for Environmental Prediction
PBL	Planetary Boundary Layer
PSU	Pennsylvania State University
QPF	Quantitative precipitation forecast
RMSE	Root mean square error
RRTM	Rapid radiative transfer model
SCIPUFF	Second-order Closure Integrated Puff model
SFC	Surface
States:	
CO, IA, MD, ME	Colorado, Iowa, Maryland, Maine
MI, NJ, NY, OH	Michigan, New Jersey, New York, Ohio
PA, WI	Pennsylvania, Wisconsin

Titan	Titan Cooperation
TKE	Turbulent Kinetic Energy
TR_{α}	Critical threshold for variable α
TRP	Threshold percentage
UTC	Universal time or Greenwich mean time (GMT)
WRF	Weather Research and Forecast model
WRF-CHEM	Chemistry version of WRF

LIST OF TABLES

LIST OF FIGURES

1. INTRODUCTION

1.1 Background

An inter-regional transport (IRT) study was conducted by Seaman et al. (2002) and published by Deng et al. (2004) using the Penn State/NCAR MM5 and the Titan SCIPUFF dispersion model. The goals of that study were to: 1) evaluate the current state of the science for simulating IRT and diffusion of a tracer when using MM5 to represent the meteorology (wind, turbulence, convective processes, etc.) and SCIPUFF to represent dispersion, 2) identify which of the meteorological model's attributes introduced or improved over the past decade (finer resolution, better physics, FDDA), are most effective for improving the accuracy of IRT, and 3) explore whether there are issues related to very fine grid resolution that may at present limit its effectiveness for use in IRT applications.

In the previous study, the MM5 was applied to the 18-19 September 1983 CAPTEX case with horizontal mesh sizes of 70, 12, and 4 km, and with physics parameterizations similar to the late 1980s and today. FDDA via analysis nudging was used in some of the experiments. The SCIPUFF plume dispersion model was used to simulate tracer concentrations, using six different MM5 simulations for the meteorological inputs. Model evaluations were based on verifications against surface and upper-air meteorological data and against the surface tracer observations.

It was found in the previous research that a baseline model configuration reflecting typical capabilities of the late 1980s (70-km horizontal grid, 15 vertical layers, older sub-grid physics, and no FDDA) produced large meteorological errors that severely degraded the accuracy of the surface tracer concentrations predicted by SCIPUFF. Improving the horizontal and vertical resolution of the MM5 to 12 km (typical for current operational models) and 32 layers led to some improvements in the statistical skill, but the further addition of more advanced physics produced much greater reductions of simulation errors. Use of FDDA, along with 12-km resolution and improved physics, produced the overall best performance.

However, further reduction of the grid length from 12 km to 4 km in the simulation of the 18-19 September 1983 CAPTEX case had detrimental effects on the meteorological and plume dispersion solutions. The primary cause of the poor mesoscale model performance was traced to the explicit (grid-resolved) representation of convection accompanying a cold front advancing across the lower Great Lakes and into New England. Because no convective parameterization was used on the 4-km grid, the convective updrafts were forced on coarser-than-realistic scales (normal updraft diameter for most storms in the eastern United States is ~ 2 km), and the rainfall and the atmospheric response to the convection were too strong. The evaporative cooling and the associated downdrafts were too vigorous causing widespread disruption of the low-level winds and spurious advection of the simulated tracer. This result should not be interpreted to mean that 4-km grids are unsuitable for air-quality studies in general. However, model simulations on a grid of 4 km or less cannot be automatically assumed to be superior to coarser resolution simulations in all situations, as was also found in the NARSTO-Northeast study (ENVIRON 2002).

Fully explicit approaches cannot provide a general solution for models with grid spacing exceeding 5~10 km because atmospheric convection has to be parameterized on these scales (Molinari and Dudek 1992, Tao et al. 2002). Although cumulus parameterizations have been successful, they fail on the smaller scales because the scale-separation assumption is no longer valid on these scales (e.g., Molinari and Dudek 1992). Another study on the resolution dependence of explicitly modeled convective systems (Weisman et al. 1997) has shown that although degradation was found in the model response as the resolution is decreased, resolution of 4 km was sufficient to reproduce much of the mesoscale structure and evolution of a squall-line-type convective system. It is important to note, however, that environmental conditions (e.g., lifting condensation level, mid-level moisture) in the northeast U.S., for example, cannot be assumed to be the same as those typical in the Midwest where squall lines have often been studied. These differences in environmental conditions can lead to differences in convective organization and updraft width. Furthermore, the Weisman et al. 1997 study used a 1-km resolution simulation as the ground truth. The recent Ph.D. work of George Bryan (Bryan 2002) at Penn State suggests that much finer model resolutions are needed (~125 m) to accurately represent the details of squall-line convection. Bryan's results show that the 125-m simulations contain sub-cloud-scale turbulent eddies that stretch and distort plumes of high equivalent potential temperature (θ_e) that rise from the pre-squall-line boundary layer. In contrast, with 1-km grid spacing the high θ_e plumes rise in a laminar manner, and require parameterized sub-grid terms to diffuse the high θ_e air. There are different ways to model these sub-grid terms, and Bryan found his solutions to be sensitive to the particular formulation that was used. Therefore, accurate representation of modeled convection on the 1-5 km scales requires proper attention to the details in the sub-grid turbulence parameterization in both the vertical and horizontal dimensions.

Reduction of the model grid size to 4 km or less has been shown to produce more realistic mesoscale structures and evolutions, especially for simulation of circulations forced by topography and surface contrasts (see the review of the literature cited in Mass et al. 2002). Use of fine model resolution during predominantly dry cases appears to pose less risk that the 4-km results will be inferior to the 12-km results. However, when moist convective instability exists, mesoscale model performance at fine resolutions is likely to be even more sensitive to the treatment of land-surface processes, atmospheric turbulence and its vertical and horizontal mixing characteristics, the choice of microphysics, and the convective parameterization on the coarser grid. Some studies have shown that use of a convective parameterization in the "no-man's land" ($\Delta x \sim 6 - 10$ km) where current convective parameterizations are not truly applicable can nonetheless yield more accurate simulations. Better results can sometimes be obtained at ~4-km resolution by using a convective parameterization to *gradually* release the convective energy, thereby reducing the intensity and atmospheric response to the grid-resolved convection (Drs. Georg Grell and John Kain, 2002, personal communications). Naturally, model numerics (e.g., advection and diffusion) may also influence the cloud and precipitation fields, and the associated flow fields, on these scales.

1.2 *Objectives*

The objectives of this study are to investigate the role of 1) model physics, 2) data assimilation and 3) numerics on the accuracy of cloud and precipitation fields simulated at Δx =4 km during CAPTEX'83. As a result, we will gain better understanding as to how these fields may be improved in the Penn State University / National Center for Atmospheric Research fifth generation mesoscale model MM5 (Grell et al. 1994). In the second phase of the project, we will continue our model simulations using the new Weather Research and Forecasting model (WRF) (Wicker and Skamarock 2002, Klemp et al. 2003) for the same CAPTEX'83 case. The WRF model (the mass coordinate core) uses a terrain-following dry hydrostatic pressure vertical coordinate and conserves mass and dry entropy. Mass conservation is very important for air-quality modeling applications; and the mass-coordinate WRF is the dynamical core used in

WRF-CHEM, which contains fully coupled meteorology and chemistry and represents the future in state-of-the-science air-quality modeling (Dr. Georg Grell, 2002, personal communication).

Since producing SCIPUFF results from the 4-km MM5 experiments requires more time than allotted for this phase of the study, our focus for this report will be placed on describing the meteorological results. Section 2 of this report describes the meteorology of the CAPTEX ’83 case used in this study. In Section 3 the numerical model and those options applied to this study are described. The design of the numerical experiments is given in Section 4, and the model results are presented in Section 5. Finally, a summary of the most relevant findings is given in Section 6.

2. OVERVIEW OF THE 18-19 SEPTEMBER 1983 CAPTEX CASE

The case chosen for experimentation in this study is the 18-19 September episode from the Cross Appalachian Tracer Experiment of 1983 (CAPTEX ‘83). This is the same case used previously in CRC project A-28 (Seaman et al. 2002). This case was selected because it was shown by Seaman et al (2002) in their inter-regional transport study that further reduction of the MM5 horizontal grid size to 4 km had detrimental effects on meteorological and plume dispersion solutions in this case due to misrepresentation of convection associated with a cold front by the MM5's explicit moist physics.

The meteorological conditions for the CAPTEX ’83 case used in the previous study (18-19 September 1983) were characterized by a large anticyclone centered over the Mid-Atlantic Coast, with broad southwesterly wind flow over the Midwest and Northeast U.S. Figure 1 shows this anticyclone at 1200 UTC, 18 September. To the northwest of the high, warm and cold fronts (associated with a deep 982-mb occluded storm located in central Canada) were approaching the Northeast, but still lay well to the west. The Canadian storm and the pressure gradient in the Midwest ahead of the cold front were rather strong for this early in the autumn. Consistent with the strength of the deep baroclinic storm, the frontal system was propagating rapidly through the western Great Lakes at nearly 15 m s^{-1}. Meanwhile, ahead of the cold front in southern Michigan (MI), a warm-sector low-level jet (LLJ) at 850 hPa contained wind speeds of 30 m s^{-1} at 1200 UTC, 18 September (not shown).

As the cold front approached the Northeast from the Great Lakes, the strongest surface pressure gradient had shifted eastward by 0000 UTC on 19 September to the vicinity of Buffalo, New York (NY) (Figure 2). At this time the center of the 850-mb LLJ was analyzed just west of Niagara Falls with maximum winds of ~26 m s^{-1} (Figure 3). This LLJ led to rapid transport of air from the Midwest to northern New England between 0000-1200 UTC, 19 September. By 1200 UTC, 19 September, the occlusion point of the frontal system was north of Maine (ME) in the province of Quebec, while the trailing cold front had decelerated and was just beginning to push into northern NY from Lake Ontario (Figure 4). Notice that even in this synoptic-scale analysis, a modest surface trough can be detected at this time over New England in the warm sector ahead of the front. Also, the pressure gradient ahead of the cold front had relaxed by 1200 UTC, September 19, so that winds in the 850-mb LLJ had weakened to ~20 m s^{-1} from the west (not shown).

The synoptic-scale objective analysis at 0000 UTC, 20 September (Figure 5) indicates that the original Canadian storm had become quasi-stationary over Hudson Bay, while a secondary 999-mb cyclone had formed along the occluded front in Labrador. Since upper-level dynamic support for the Labrador storm was by this time far to the northeast of New England, the cold front had been able to push southward into central ME, but had made only slow progress into NY. Farther to the west, from Iowa (IA) to MI, the frontal boundary had reversed direction toward the north as a warm front. In Colorado (CO), another new baroclinic storm was gathering strength as a strong high-pressure system pushed southward from western Canada into the central Rocky Mountains.

To further understand the mesoscale structure of the weather systems for this case including fronts and precipitation that are not resolved easily in the synoptic-scale objective analyses, we have analyzed the surface observations over the Midwest and Northeast U.S. at 6-h intervals from 1200 UTC, 18 September through 0000 UTC, 20 September 1983. In Figure 6, at 1200 UTC on 18 September, there are many thunderstorms close to the warm front from southeastern Wisconsin (WI) to southern MI, with widespread showers throughout the rest of

MI. The rain then shifts eastward with the advancing warm front, so that by 1800 UTC, the rain showers are mostly around Lake Ontario (Figure 7) before weakening at 0000 UTC, 19 September (Figure 8). Later during the evening, by 0600 UTC, thunderstorm activity and showers again become more widespread along the cold frontal boundary and ahead of the warm front (Figure 9). Satellite imagery (Figure 10) at 0830 UTC confirms that convective clouds associated with the precipitation existed over the Great Lakes area. These reinvigorated storms were likely triggered by the ageostrophic wind circulations associated with the acceleration of the nocturnal LLJ just ahead of the cold front. Figure 11 shows that the convective storms persisted through the night, mostly along the cold front, but weakened toward morning, especially from Lake Erie to Montreal. As on the previous day, Figure 12 indicates that the frontal showers in the Northeast were weakest around early afternoon (1800 UTC). Even though the surface reports at this time failed to show frontal rain at the observing stations from Detroit to Maine, renewed thunderstorms and showers were evident once more by 0000 UTC, 20 September (not shown).

During many mid-summer episodes with poor air quality, convective outbreaks occur in synoptic environments that have relatively weak baroclinicity (i.e., weak dynamic forcing). In that type of situation, it is not unusual for an outbreak of thunderstorms to grow and consolidate into a mesoscale convective system. These fairly well organized thunderstorm clusters often generate mesoscale high- and low-pressure centers and outflow boundaries, accompanied by strong gusty winds. They can distort the synoptic wind pattern over hundreds of kilometers and can last for 6-18 h (sometimes longer). Thus, the mesoscale patterns analyzed in mid-summer cases can be quite distinct.

In the CAPTEX ‘83 study, however, Episode 1 differed from a mid-summer case in that it took place in the middle of September, when a relatively strong baroclinic frontal system was in the area. At this time of year, large high-pressure systems along the Mid-Atlantic coast (westward extensions of the quasi-permanent Bermuda High) can cause enhanced advection of warm moist air from the Gulf of Mexico to the northern states. A quick review of the pressure gradient and 850-mb winds in Figure 3 indicates that this scenario was the primary source of moisture for the convective rainfall that accompanied the fronts shown in Figures 6-12. Also, afternoon temperatures just south of the fronts reached 28-30 C (mid-80s ºF) during Episode 1, so that conditions were ideal for thunderstorm development when the warm moist air was lifted over the frontal surfaces. At the same time, strong subsidence in the broad interior of the Bermuda High suppressed rain through most of the area covered by the anticyclone.

3. MODEL DESCRIPTION

3.1 Basic Model Structure

The meteorological model used in this study is the non-hydrostatic Pennsylvania State University/National Center for Atmospheric Research (PSU/NCAR) mesoscale model, known as MM5. The MM5 is a nonhydrostatic, fully compressible three dimensional primitive equation model with a terrain following sigma (non-dimensional pressure) vertical coordinate (Dudhia 1993, Grell et al. 1994), given by

$$\sigma = \frac{p - p_t}{p_s - p_t} \qquad (1)$$

where, p is the pressure, p_s is the surface pressure, and p_t is the pressure at the top of the model. All the sigma layers are defined using a time-invariant "background" pressure field, based on a standard atmospheric lapse rate, while a much smaller prognostic pressure perturbation field ($p' = p'(x, y, \sigma, t)$) represents the time-varying 3-D departure from the background. The MM5 also contains prognostic equations for the three wind components (u,v,w), temperature (T) and water-vapor mixing ratio (q_v), each of which are written in flux form. The model uses a split semi-implicit temporal integration scheme to increase computational efficiency. The MM5 is flexible enough to be applied to a wide range of synoptic and mesoscale phenomena, including baroclinic storm development, tropical cyclones, and the role of physical processes, such as convection and planetary boundary layer (PBL) influences. For a more complete description of the MM5 formalism, see Dudhia (1993) and Grell et al. (1994).

The MM5 is a nested grid model with the horizontal grid system of the MM5 domains based on the staggered Arakawa-B grid described by Arakawa and Lamb (1977). In this grid configuration, the wind components, u and v, are defined on the so-called "dot points" at the corners of a grid box, while all the other variables are defined on the "cross points" at the center of the boxes. The vertical structure of the model's grid is such that vertical motion, w, and the *TKE* are defined on the full sigma-layer boundaries, while the other variables (e.g., u, v, T, and q_v) are defined on the half levels (middle of the layers) (also see Grell et al. 1994).

3.2 Model Physics

For this study the nested domains of 108 km, 36 km, 12 km and 4 km are used, as in the original study by Seaman et al. 2002. On all of these domains, resolved-scale moist processes are represented using explicit prognostic equations for cloud water or ice (q_c) and rain water or snow (q_r) according to a formulation described by Dudhia (1989). One experiment includes mixed phase processes as well (Reisner et al. 1998).

The Kain-Fritsch convective parameterization (Kain and Fritsch 1990, Kain and Fritsch 1993) is used on the various domains as described in the experimental design. The Kain-Fritsch scheme has a fully entraining/detraining cloud model and uses an energy-equilibrium closure. First, the potential for convective clouds is diagnosed by lifting low-level parcels to their saturation levels. Then, a convection-forming parcel is initiated from the saturated parcel below 700 hPa having the highest θ_e (equivalent potential temperature). Rain is triggered when the cloud exceeds a critical depth (3-4 km). Once convection is initiated in a grid column, it continues until all convective available potential energy (CAPE) has been eliminated.

The new version of the Kain Fritsch scheme (KF2) that has been tested in the National Centers for Environmental Prediction's (NCEP) Eta model (Kain 2004) and used in this study contains a number of modifications to the original scheme. The updraft formulation was changed in several ways: (1) a minimum entrainment rate (50% of the maximum possible entrainment rate used in the original scheme) is imposed, primarily to suppress convective initiation in marginally buoyant, relatively dry environments, (2) the cloud radius is now specified to vary as a function of subcloud-layer convergence so that it promotes activation in strongly convergent regimes and suppresses deep convection activation in weakly convergent or divergent environments, (3) a minimum cloud depth, required for activation of deep convection (4 km in the original scheme), is allowed to vary as a function of cloud-base temperature so that relatively shallow clouds are allowed, (4) non-precipitating shallow convective clouds are allowed when buoyant updrafts can form but cannot reach the imposed minimum cloud depth for deep convection, with cloud-base mass flux being defined as a function of the turbulent kinetic energy (TKE) in the subcloud layer (Deng et al. 2003), rather than CAPE. The downdraft formulation was also changed. Downdrafts are formed from air in the layer at 150–200 hPa above cloud base, and they detrain over a fairly deep layer below cloud base. Downdraft mass flux is estimated as a function of the relative humidity and stability just above cloud base but is no longer related to vertical wind shear. Modifications to the closure assumption were made. For the closure assumption, although the scheme is still programmed to eliminate CAPE, the calculation of CAPE is based on the path of an entraining (diluted) parcel rather than one that ascends without dilution. Although the details of the impact of the new Kain-Fritsch scheme on this study are not clear, our hypothesis is that the shallow convection module may have the most significant effect on the model results in this research because it would help to gradually remove the CAPE on the grid. The hypothesis that application of this scheme on the 4-km domain can reduce the tendency of the explicit moisture scheme to overestimate precipitation and produce grid point storms is put to the test. These spurious rain areas cause serious disruption of the larger scale wind patterns which largely affect transport and dispersion.

Two different types of planetary boundary layer (PBL: vertical mixing only) turbulence parameterizations are used in this study: a widely used first-order closure scheme known as the NCEP MRF PBL (Hong and Pan 1996), and the Penn State Gayno-Seaman PBL (GSPBL) (Shafran et al. 2000, Stauffer et al. 1999), a 1.5-order closure turbulent kinetic energy (TKE) predicting scheme developed at Penn State and based on the Mellor-Yamada scheme. The MRF PBL scheme is known for overestimating the PBL mixing and producing PBL depths that are too high. It may be more suitable for use in large scale models but widely used in the MM5 because if its simplicity and speed. The effectiveness of the MRF PBL scheme for use in the MM5 is evaluated in this study.

The GSPBL is a 1.5-order closure approach developed by Gayno et al. (1994) and described by Shafran et al. (2000), with additional improvements described by Stauffer et al. (1999). It has a second-order predictive equation for TKE, while the eddy viscosity is a function of the predicted TKE and several stability-dependent mixing lengths. Turbulent fluxes of momentum, moisture and heat are parameterized using K-theory in which the turbulent transfer occurs down gradient. However, since basic K-theory fails under certain convective situations (Moeng and Wyngaard, 1989), countergradient flux terms are included to correct the turbulent transport terms near the surface and near the top of the convective mixed layer (Gayno et al. 1994). The TKE-predicting scheme is representative of newer higher-order PBL physics and has been shown to generate both shear-driven turbulence and in-cloud mixing associated with cloud-top radiative flux divergence (Stauffer et al. 1999). It has also been shown to predict more accurate boundary-layer structure for convectively unstable conditions, compared to the Blackadar scheme (Shafran et al. 2000). In addition, Stauffer et al. (1999) added the capability to account for the effects of saturation on the buoyancy production of TKE, which makes this 1.5-order scheme more accurate in cloudy or foggy conditions than the other turbulence parameterizations available in MM5.

For atmospheric radiation, the Rapid Radiative Transfer Model (RRTM) (Mlawer et al. 1997) is used for longwave, and the simple Dudhia scheme (Grell et al. 1994) is used for shortwave. The Dudhia radiation scheme is based on a two-stream, single-band approach. It is fully interactive with dry air, water vapor and cloud liquid/ice.

3.3 Four Dimensional Data Assimilation (FDDA)

Four-dimensional data assimilation (FDDA) is a process in which observations are used to correct for numerical forecast errors in a model simulation, instead of using data only at the initial time. It has been shown to reduce error accumulation during the assimilation period (e.g., Seaman et al. 1995, Michelson and Seaman 2000). The FDDA approach, which was also developed at Penn State by Stauffer and Seaman (1990, 1994) and Stauffer et al. (1991), uses "nudging" to relax the model solutions toward the observations. In this method, the model state is relaxed continuously at each time step toward the observed state by adding to the prognostic equations an artificial tendency term, which is based on the difference between the two states. The assimilation can be accomplished by nudging the model solutions towards gridded analyses based on observations (analysis nudging) or directly toward the individual observations (observational nudging). In the present study, both analysis nudging and observational nudging are used.

3.3.1 Analysis Nudging

In analysis nudging, the model fields are nudged at every grid point toward an analysis of the observations on the model grid in a manner such that the nudging term is proportional to the difference between the model and the analysis at each grid point. This process is depicted in the MM5 by:

$$\frac{\partial p^{*}\alpha}{\partial t} = F(\alpha, \vec{x}, t) + G_{\alpha} \cdot W(\vec{x}, t) \cdot \varepsilon(\vec{x}) \cdot p^{*}(\hat{\alpha}_{o} - \alpha) \tag{2}$$

which is the tendency equation for any variable α, coupled with p^{*} $(= p_s - p_t)$ defined in the model by p_s, the reference state surface pressure and p_t, the model top pressure. The term F represents all natural processes that affect the change in the forecast variable, such as the pressure gradient force, gravity, friction and the Coriolis effect. The second term is the nudging term. The nudging factor G_{α} determines the relative magnitude of the nudging term to the other terms in the equation. The nudging term should be smaller in magnitude than any of the other terms in the equation so that the nudging term does not control the tendency. If the nudging is too strong, the model may lose important mesoscale features created by the model, but if it is too weak, the observations will have a minimal effect on the evolution of the model state, allowing phase and amplitude errors to grow. For this reason, the value of the nudging factor should be rather small (on the order of 10^{-4} s^{-1}) (Stauffer and Seaman 1990). The spatial and temporal variation of the nudging term is determined by the four-dimensional weighting function, W. The estimate of the observation analyzed to the grid point is $\hat{\alpha}_{o}$. If each model grid point is matched with a temporally interpolated value of $\hat{\alpha}_o$ at every observation time, the weighting function in analysis nudging cases is typically set equal to 1 (Stauffer and Seaman 1990). The analysis quality factor, ε, which ranges from 0 to 1, is a representation of the quality and data distribution of the data that went into the analysis. This factor is often assumed to be unity if the system includes quality control (e.g., gross error checks, "buddy checks", vertical consistency checks) in the data pre-processing. In the surface analysis nudging option (Stauffer et al. 1991), where surface analyses are used to define the FDDA corrections throughout the model-diagnosed PBL, this factor is defined based on the minimum distance between the grid cell and closest surface observation. This way a gridded surface analysis which largely reflects the background because surface observations are not available or too far away is weighted less in the FDDA.

As summarized in Table 1, the analysis nudging coefficients for the 12-hourly three-dimensional (3D) wind and temperature fields based on rawinsonde data are set to G = 2.5 X 10^{-4} s^{-1} on the 108-km and 36-km grids, and G = 1 x 10^{-4} s^{-1} on the 12-km domain. In this study 3-hourly surface analyses of wind are assimilated throughout the model-diagnosed PBL with the aforementioned nudging coefficient values for each grid. No mass fields are used in the surface analysis nudging. Although analysis nudging is not recommended for a 4-km domain as discussed by Stauffer and Seaman (1994), and especially when only conventional data are available, one experiment (see Section 4) does include analysis nudging FDDA on the 4-km domain as it was applied on the 12-km domain with G = 1 x 10^{-4} s^{-1}. Because rawinsonde moisture fields are too smooth due to the coarse rawinsonde spacing, which can cause damage to the model QPF, analysis nudging of 3D moisture uses a relatively small nudging coefficient G = 1 X 10^{-5} s^{-1}. Lastly, because we had only conventional rawinsonde data in this study, we also withheld the use of 3D analysis nudging in the lowest 2 km above ground level (AGL) to allow the model to produce fine-scale structures not resolved by the rawinsonde network.

3.3.2 Observation Nudging

For asynoptic observations, sparse data, or mesobeta-scale model simulations, especially in complex terrain, a realistic analysis of observations cannot be performed and obs nudging is the preferred technique. Obs nudging computes the difference between the model and the observation at the observation site and applies this innovation or correction to a neighborhood of grid points that surround the observation location in space and time. The obs nudging tendency equation in MM5 is depicted by:

$$\frac{\partial p^* \alpha}{\partial t} = F(\alpha, \vec{x}, t) + G_\alpha \cdot p^* \frac{[\sum_{i=1}^{N} W_i^2(\vec{x}, t) \cdot \gamma_i \cdot (\alpha_0 - \alpha)_i]}{\sum_{i=1}^{N} W_i(\vec{x}, t)} \tag{3}$$

In this case, the symbols are the same as in equation 2, except γ_i is the observational quality factor, the subscript *i* denotes the *i*th observation of a total of *N* which are located within a preset radius of a given grid point, α_o is the locally observed value of α, and $\hat{\alpha}$ is the model prognostic variable interpolated to the observation location in three dimensions. As can be observed from the sums in the nudging term, each observation that is within a predefined distance from a particular grid point will have an influence on that particular grid point (Stauffer and Seaman 1990).

The weight that is given to a nudging correction at a particular grid point depends on a horizontal weighting function, w_{xy}, a vertical weighting function, w_σ, and a temporal weighting function, w_t, where

$$W(\vec{x},t) = w_{xy} w_\sigma w_t \tag{4}$$

Due to the fact that nudging to a single observation at a single grid point may cause an unreasonable imbalance in the model fields, the corrective weight of each observation is applied to the grid in a region surrounding each observation. For this reason, the standard horizontal weighting function is a Cressman-type function, as defined in:

$$\begin{aligned} w_{xy} &= (R^2 - D^2)/(R^2 + D^2), && 0 \le D \le R \\ w_{xy} &= 0, && D > R \end{aligned} \tag{5}$$

where, R is the radius of influence of the observations (see Figure 13) and D is the actual distance from the observation location to the grid point to which the correction is being applied. Assimilation of single-level data has been shown to be an ineffective means of modifying the solution of a three-dimensional model (e.g., Barwell and Lorenc 1985). For this reason, corrections can be spread vertically over several sigma levels using:

$$\begin{aligned} w_\sigma &= 1 - \left|\sigma_{obs} - \sigma\right| / R_\sigma, && \left|\sigma_{obs} - \sigma\right| \le R_\sigma \\ w_\sigma &= 0, && \left|\sigma_{obs} - \sigma\right| > R_\sigma \end{aligned} \tag{6}$$

Here, R_σ is the vertical radius of influence, σ_{obs} is the vertical position (in sigma coordinates) of the observation that the correction is based on, and σ is the model sigma level (Stauffer and Seaman 1990). For computational efficiency, vertical sounding data are interpolated to the model surfaces as part of the data pre-processing step, so that each observation above the model surface layer affects only one sigma layer at a given horizontal point as depicted in the top panel of Figure 13 (Stauffer and Seaman 1994). Corrections computed at a given observation site are spread horizontally along a constant base state pressure surface (height surface) and thus across several sigma surfaces in regions of sloping terrain.

As can also be seen in the top panel of Figure 13, the horizontal radius of influence increases linearly in the vertical with decreasing pressure. This linear increase in radius of influence continues up to some predetermined pressure level, usually 500 hPa, where the radius of influence is twice that of the near-surface value. So in this study the radius of influence increases from 100 km near the surface to 200 km at 500 hPa and then is held constant at 200 km to the model top. The radius of influence is made larger above the surface layer because meteorological fields and their error correlation length scales have larger scales above the surface. This means that the model errors at a given observation location are more strongly correlated with errors say 100 km from the observation location above the surface than at the surface.

Stauffer and Seaman (1994) determined that the simple circles that are used as the horizontal weighting functions in the Cressman scheme are not the most realistic way to spread the influence of observations in complex terrain and that the influence of observations should be treated differently at the surface and for upper air observations. Above the surface, corrections are spread laterally along constant reference pressure surfaces and R_σ is small so that each observation above the model surface layer influences only one sigma layer at a given horizontal grid point. In the surface layer, observations are spread along constant sigma surfaces, but with a modified Cressman function using,

$$D_m = D + R_s C_m^{-1} \left| p_{so} - p_s \right| \tag{7}$$

where D_m replaces D in equation 5. This reduces the influence of an observation as a function of the difference in surface pressure between the observation location and that at the grid point that is being influenced. In equation 7, D is defined as in equation 5, C_m is a constant, p_{so} is the reference surface pressure at the observation location, p_s is the reference surface pressure at the model grid point, and R_s is the surface-layer value for the horizontal radius of influence defined here as 67 km. The fact that the influence is spread on a sigma surface means that the influence is spread continuously in the surface layer (i.e. there are no areas where there is no influence because a constant pressure surface would go below ground level). The dependence of the weighting function on the difference in pressure between the observation location and the grid point location helps to prevent observations that are taken in a valley from strongly influencing grid points that lie on mountain peaks and vice versa in regions of complex terrain. The surface data corrections are also spread in the vertical near the surface with a linearly decreasing weight through those model sigma layers that fall within the lowest 250 m AGL.

There is also a temporal contribution to the weighting function used in the standard obs nudging scheme. In a similar manner to the way that assimilating an observation at one point would be a shock to the model system, assimilating an observation at a single time step would also shock the system and cause ripples (gravity waves) to propagate through the model domain. For this reason, the temporal weighting function, w_t, is given by:

$$\begin{aligned} w_t &= 1, && |t - t_0| < \tau/2 \\ w_t &= \frac{\left(\tau - |t - t_0|\right)}{\tau/2}, && \tau/2 \le |t - t_0| \le \tau \\ w_t &= 0, && |t - t_0| > \tau \end{aligned} \tag{8}$$

where t is the model-relative time, t_o is the model-relative time of the observation, and τ is the half-period of a predetermined time window over which the observation will influence a grid point (Stauffer and Seaman 1990). The temporal weight of the observation in the obs nudging term in the model is spread out over a period of time. For example, if τ were to equal 2 hours, as it is in this study, then within 1 hour of the observation time, the nudging correction will carry full temporal weight of 1.0. From 1 to 2 hours before or after the observation time, the weight of the nudging correction is ramped down linearly from 1.0 to 0.0, and it remains 0.0 outside of the 2-hour time window. (See bottom panel in Figure 13) As with the radius of influence, surface data are treated as a special case due to their greater data density and shorter error correlation scales by using a 50 percent smaller time window at the surface (1 hour).

Observation nudging is applied to the 4-km domain in this study for two experiments (see Section 4) for wind, temperature and mixing ratio. By default the mass fields are not assimilated in the model-diagnosed PBL due to the poor 12-hourly temporal resolution of the standard rawinsonde network data. The nudging coefficients are set to $G = 4 \times 10^{-4}\ s^{-1}$.

4. EXPERIMENTAL DESIGN

4.1 MM5 Model Domains

For this study the grid configuration used 108, 36, 12 and 4-km domains (Figure 14). The coarsest domain has a resolution of 108 km and covers most of North America with a mesh of 55 X 69 points. The second domain covers the continental United States (CONUS), southern Canada and northern Mexico at 36-km resolution with a mesh of 103 X 151 points. The third domain in Figure 14 has a resolution of 12 km and covers the eastern U.S. and parts of southeastern Canada with a mesh of 190 X 208 points. The fourth domain has a resolution of 4 km and is embedded over the Northeast U.S. Inspection of Figure 14 indicates that the area of this 4-km domain covers the entire monitoring network of CAPTEX '83. The 4-km grid has 289 X 316 points, covering an area of 1152 X 1220 km.

The terrain field for the 4-km domain is shown in Figure 15, which shows very detailed mountainous terrain over northeastern U.S. The Adirondack, Green and White Mountains have maximum elevations of 898, 717, and 916 m in Figure 15, respectively. While still not capturing the full height of the actual peaks, it appears that 4-km resolution can adequately represent the height of the main ridges. Thus, the blocking effects of the terrain should be represented well.

Model configuration in the vertical is summarized in Table 2. All four of the domains have 32 layers in the vertical direction. The lowest layer is located at ~29 m AGL. The thickness of the layers increases gradually with height, with 16 layers below 850 m (~1560 m AGL). The top of the model was set at 100 hPa (~ 14 km AGL).

4.2 Initialization and Lateral Boundary Conditions

The same initial and lateral boundary conditions that were used in the previous study (Seaman et al. 2002 and Deng et al. 2004) are used here in this study. Generation of initial and lateral boundary began with the NCEP 2.5-degree global spectral analyses. The 1^{O} X 1^{O} global model fields of temperature, horizontal wind components and relative humidity were accessed at mandatory and supplemental pressure levels (1000, 975, 950, 925, 900, 875, 850, 800, 750, 700, 650, 600, 550, 500, 400, 300, 250, 200, 150, 100 hPa), plus sea-level pressure and ground temperature, and were projected onto the outermost MM5 domains to be used as background (first-guess) fields prior to an objective analysis. Next, in the objective-analysis step, the analyses are enhanced by incorporating standard radiosonde and surface data through use of an anisotropic successive-correction objective analysis (Benjamin and Seaman 1985). The completed pressure-level analyses then are interpolated to the model's sigma levels to be used as initial conditions. For the nested grids, the 108-km analyses also are interpolated to provide initial conditions for the successive nested domains (i.e., 36-km fields are interpolated from the 108-km domain, 12-km fields from the 36-km domain, and 4-km fields from the 12-km domain).

The lateral boundary conditions of the 108-km domains are defined at 12-h intervals from analyses generated in a way similar to that used for the initial conditions. The pressure-level analyses were created at 12-h intervals, while surface fields were generated at 3-h intervals. For the nested grids, the 36-km domain received its lateral boundary conditions directly from the 108-km domain at every time step, since these two domains are run at the same time two-way interactively. However, the one-way lateral boundary conditions of the 12 and 4-km domain are created by interpolation from the next coarser grid at one-hour intervals.

4.3 Model Experiments

There are thirteen experiments conducted in this research involving MM5 simulations at 4-km resolution. The detailed experimental design is summarized in Table 3 and briefly described below:

4.3.1 Experiment MB1

A new MM5 baseline experiment for CAPTEX '83 is designed to be very similar to Exp. 2D/3A in the original study (Seaman et al. 2002 and Deng et al. 2004), except use the most recent version of the MM5 and any of its improvements, including the newer versions of its model physics and its model initialization software. We performed several baseline sensitivity experiments, not in the original work plan, to determine if any one of these new changes significantly affects the 4-km domain flow and precipitation results as compared to those reported in Seaman et al. (2002). These baseline sensitivity experiments included (1) Exp. MBS1 which is the same as Exp. MB1 except it uses the original initialization (initial conditions, lateral boundary conditions, 13-category landuse) from Exp. 3A (Seaman et al. 2002), and (2) Exp. MBS2 which is the same as Exp. MB1 except that it uses the original radiation physics from Exp. 3A (Seaman et al 2002) (Dudhia longwave instead of RRTM), and (3) Exp. MBS3 which is the same as Exp. MB1 except it uses the original initialization and radiation physics from Exp. 3A (Seaman et al. 2002), and (4) Exp. MB1DRY which is the same as Exp. MB1 except that latent heating and evaporative cooling effects were turned off although precipitation was still allowed. The last experiment was conducted to test our hypothesis that the excessive precipitation in Exp. 3A of the original study was likely causing the anomalous low-level flow and thermal patterns.

Exp. MB1DRY produced much weaker precipitation amounts and smaller areal coverages compared to Exp. MB1. Therefore, there was much less disruption of the larger scale flow by the convection which was hypothesized to causes the spurious winds in Exp. MB1. The subjective analysis indicated that Exps. MBS1, MBS2 and MBS3 all produced flow and precipitation fields similar to Exp. MB1 (not shown). The statistical results for the wind and mass fields (not shown) also suggested that all of the baseline experiments produced comparable meteorology to Exp. 3A (Seaman et al. 2002). We found that the 4-km precipitation amounts and patterns associated with the advancing cold front in the original study Exp. 3A were generally reproduced by all of the new baseline runs despite a new initialization, a newer version of the MM5 and its model physics. Therefore, we adopted Exp. MB1 as our new baseline experiment and confirmed that the poor results in the previous study were reproducable and not sensitive to the specifics of the previous 4-km model configuration.

For Exp. MB1, the same four grids used in Seaman et al. (2002) with resolutions of 108 km, 36 km, 12 km and 4 km are used with the same 32 vertical layers. No FDDA is used on the 4-km grid, but analysis nudging FDDA is used on the outer three grids as described in Section 3.3.1. No convective parameterization scheme (CPS) is used on the 4-km grids, but a newer version of Kain-Fritsch convection scheme (KF2) described in Section 3.2 is used on the outer three grids. The Penn State 1.5-order closure GSPBL scheme and simple ice microphysics (either ice-only or liquid-only dependent on temperature) are included in the baseline on all four domains, along with the Slab Force-Restore energy budget at the surface which includes the radiative effects of the Rapid Radiative Transfer Model (RRTM) longwave radiation and Dudhia shortwave radiation schemes in the atmosphere. See Table 3 for a comparison and summary of all the experiments described in this section.

4.3.2 Experiment MS1

The first MM5 sensitivity experiment is configured identical to the baseline Exp. MB1 except that it applies analysis nudging as used on the 12-km domain to the 4-km domain. This experiment is designed to reveal if the lack of FDDA on the 4-km domain and the potential for greater phase errors in the frontal location contributed to the poorer 4-km results. The 12-km 3D and surface analyses were interpolated to the 4-km domain and applied the same way as on the 12-km domain.

4.3.3 Experiment MS1.1

The next MM5 sensitivity experiment is configured identical to the baseline Exp. MB1 except that it uses observation nudging (Obs nudging) FDDA on the 4-km domain. This experiment is to evaluate the effectiveness of Obs nudging in this CAPTEX '83 case and to compare this technique with the analysis nudging, especially in the PBL. This approach is more appropriate for use on finer resolution domains than analysis nudging.

4.3.4 Experiment MS2 (MB2)

This sensitivity experiment is identical to the baseline except that it included some changes to the vertical mixing length scales in the 1.5-order TKE scheme (GSPBL) to increase the parameterized mixing. Recent experimentation at Penn State has shown improvements in PBL structure when increasing the parameterized mixing lengths in the GSPBL. A tendency for the MM5 to produce horizontal convective rolls (HCRs) with unrealistically large wavelengths on the 4-km grid is greatly reduced (Schroeder 2002). Furthermore, the intensity of the low-level mixing and the ability of the model to simulate surface superadiabatic layers will also influence the convective available potential energy (CAPE) and thus will affect the triggering and the intensity of the 4-km grid-resolved convection. This experiment uses 50 percent larger mixing lengths and K in the first layer above the surface layer, and double the default values above this layer. This enhanced vertical mixing (double K) in the GSPBL scheme produced improved model simulations on the 4-km grid (see details in the next section). These improvements were adopted for all GSPBL sensitivity experiments from this point forward and therefore, Exp. MS2 may be considered a new baseline experiment (MB2). No FDDA is used on the 4-km grid.

4.3.5 Experiment MS3

This sensitivity experiment is identical to the baseline MB1 except the Hong and Pan MRF first-order closure planetary boundary layer (PBL) scheme is used. This experiment is to evaluate the effect of the different turbulence (PBL) scheme and its potential for greater vertical mixing, and its ability to simulate a surface superadiabatic layer and its impact on the grid-resolved convection at 4-km resolution. No FDDA is used on the 4-km grid.

4.3.6 Experiment MS4

This sensitivity experiment is identical to Exp. MB2 which uses simple ice microphysics, except that it is to investigate the impact of mixed-phase microphysics on the 4-km cloud, precipitation and flow fields. In this experiment both ice and liquid can co-exist in a given grid cell. The hydrometeor type and its fall velocity can influence the intensity of the downdraft and the cold pool, and thus the low-level wind patterns. No FDDA is used on the 4-km grid.

4.3.7 Experiment MS5

This sensitivity experiment is designed to investigate the use of the new Kain-Fritsch convective parameterization (KF2) on the 4-km domain to gradually release the CAPE thereby reducing the intensity of the grid-resolved convection. No FDDA was used on the 4-km grid.

4.3.8 Experiment MS5.1

This sensitivity experiment is identical to Exp. MS5 except that mixed-phase microphysics is introduced. The purpose of this experiment is to investigate the impact of combining mixed-phase microphysics on the 4-km grid with the new Kain-Fritsch scheme. No FDDA is used in this experiment.

4.3.9 Experiment MS6

This sensitivity experiment is to investigate the MM5 model sensitivity to horizontal diffusion. Note that the simulated updrafts and downdrafts on a 4-km grid are occurring on scales that are generally larger than those found in nature in the northeast U.S. The Smagorinsky horizontal diffusion in MM5 (based on the sum of a constant background term and a term based on the horizontal deformation field) can be adjusted to further increase the numerical smoothing and thus the entrainment and detrainment of a moist updraft. The horizontal diffusion coefficient can be given by:

$$K_H = K_{H0} + K \cdot Def \qquad (4)$$

where K_{H0} is a background value of diffusion coefficient, with a default value of $4 \cdot 10^3 m^2 s^{-1}$ for the 4-km grid, K is a dimensional constant, with a default value of 160 m for the 4-km grid and

Def is the deformation term given by Smagorinsky et al. (1965). Note that there are no physically realistic lateral (horizontal) mixing processes in MM5 to dilute the 4-km updraft. The turbulence schemes used in mesoscale models were originally developed for scales where the horizontal mixing effects are much smaller than the vertical mixing effects and therefore can be ignored. However, as resolutions approach 1 – 5 km or so, the lateral mixing across, say, a cloud boundary may be important and should be included. We investigate this in an approximate way by increasing the horizontal smoothing. Additional terms are actually needed, such as those involving the horizontal gradients of vertical motion. These terms are found in the three-dimensional sub-grid turbulence schemes within a large eddy simulation (LES) or cloud-scale model, and they are also included in WRF. This capability can be tested in year 2 of the project using WRF.

Exp. MS6 uses exactly the same configuration as Exp. MB2, except that it uses a doubled background horizontal diffusion coefficient (K_{H0}) in equation (4). Again, No FDDA is used on the 4-km grid.

4.3.10 Experiment MS6.1

This sensitivity experiment is identical to Exp. MS6 except that it uses a background horizontal diffusion coefficient that is five times larger than the default value used for Exp. MB2. No FDDA is used on the 4-km grid.

4.3.11 Experiment MS6.2

This sensitivity experiment is the same as MS6 except that it increases the deformation term in equation (4) by five times while keeping the original default background term

(Exp.MB2) to investigate how enhanced diffusion determined by the deformation field impacts the MM5 simulations on the 4-km grid. No FDDA is used on the 4-km grid.

4.3.12 Experiment MS6.3

This sensitivity experiment is identical to Exp. MS6.2 except that it only applies the enhanced diffusion via the deformation term on the grid cells where precipitation occurred in the previous times step, with a threshold precipitation value of $1 \cdot 10^{-6} cm$. No FDDA is used on the 4-km grid.

4.3.13 Experiment MS7

This sensitivity experiment is identical to MB2 except that it uses the new Kain-Fritsch cumulus convection scheme (KF2) on the 4-km grid. It uses default values for horizontal diffusion coefficient, and the enhanced vertical mixing in the GSPBL scheme as used in MB2. In addition, observation nudging is applied on the 4-km domain to investigate how results using Obs nudging combined with KF2 on the 4-km domain compare with those of the other experiments and MS1.1 (analysis nudging on the 4-km domain) in particular. Does the use of KF2 on the 4-km domain further improve on the results using observation nudging? The obs nudging coefficients are summarized in Section 3.3.2.

4.4 Evaluation Procedures

Evaluation of a complex set of output fields generated by a numerical model is always a challenging task. There are several ways to verify the model's accuracy, but no single method is adequate by itself. For example, a statistical analysis of model performance, calculated from the errors between observed and simulated values of key variables, can give very useful insights that help to quantify the level of skill. However, because the statistics are generally calculated over all the observing sites on an entire domain, they also may mask problems regarding how the model treats important mesoscale features, which cover only a portion of the domain. Therefore, subjective comparison of individual mesoscale features is a useful complement to a statistical analysis.

In this research we perform both subjective and objective evaluations of the model results. Evaluation of simulated meteorological features is accomplished by subjectively comparing the model's 4-km surface fields including precipitation and wind to the observed surface data and satellite images. The most effective objective approach to statistical evaluation of meteorological model fields is to use a variety of measures, instead of relying on one particular statistical score. Here, we use root mean square errors (*RMSE*), mean absolute errors (*MAE*), mean errors (*ME*), an index of agreement (*I*), and a threshold percentage (*TRP*). The definition of each statistical measure was discussed in detail in Seaman et al. (2002) and is summarized here in the Appendix. Generally, these quantities are calculated as domain-wide averages for one or more layers. *MAE* gives a measure of the most "typical" error, in the sense that it is the average size of the absolute value of individual errors. Thus positive and negative errors cannot cancel one another (in contrast to *ME*, which reflects biases). The *RMSE* is somewhat similar to the *MAE*, but it magnifies the impact of "outliers". An experiment with comparatively few outliers will have similar scores for the *RMSE* and *MAE*. The value of *I* ranges from 0 to 1, with a score of 1 representing perfect agreement to the data. It measures how well the variability in the model simulations matches the variability in the data, in a spatially paired manner. In mesoscale model applications, a value of *I* on the order of 0.5-0.6 is considered to be typical for a successful simulation of the wind field (e.g., Seaman et al. 1995, Lyons et al. 1995, Shafran et al. 2000). *TRP* measures how often the model-predicted values fall within some specified threshold of accuracy. The value of TR_{α} (see Appendix) is chosen to represent a tolerable standard level of error for any variable α. For example, if it is necessary that surface air temperature be simulated within 2 C in order for an emissions model to calculate sufficiently accurate biogenic emissions, then one might specify TR_{α} =2.0. In this study, we arbitrarily set TR_{α} according to the values given in Table 4.

We have also developed a new plotting capability for our statistical analysis. We include vertical profile and time series plots of various statistics for the set of experiments. These allow an easier interpretation of results than using only tables since direct comparisons between various experiments are available on a single chart. The tables also show only case-mean statistics while the new time series plots will allow us to investigate how the errors vary in time, from day time to night time, etc.

5. MODEL RESULTS

To evaluate the model performance, both subjective and objective approaches are used in this research. Evaluation of simulated meteorological features is accomplished by subjectively comparing the model's 4-km surface fields including precipitation, surface wind and surface temperature to the observed surface data and satellite images. Objective evaluation is performed by comparing the statistical scores of the model-simulated fields including wind speed, wind direction, temperature, water vapor mixing ratio and sea-level pressure.

5.1 Subjective Evaluation of the MM5-Simulated Mesoscale Features

To compare the structure of mesoscale features for the experiments listed in Table 3, we will mainly focus our discussion on the precipitation fields and the surface wind and temperature fields at two model times: 0900 UTC, 19 September 1983 (21 h) and 1800 UTC, 19 September 1983 (30 h). The 21-h time represents a night time condition and the 30-h time represents a day time condition. The 21-h model time is chosen because an infrared (IR) satellite image (Figure 10) is available near this time (0830 UTC, 19 September 1983). It shows the cloud band associated with the frontal system and can be used to subjectively evaluate the model skill for precipitation. The current weather is plotted 3 hours earlier at 18 h (Figure 9), and the position and movement of the frontal system can be deduced from the observed locations at 18 h (Figure 9) and 24 h (Figure 11) times. The 30-h time is chosen because this is the time at which poor MM5 simulations on the 4-k grids were reported in the previous study by Seaman et al. (2002) and Deng et al. (2004).

5.1.1 21-h model time

Figures 16 through 26 show the MM5-simulated 3-h precipitation fields ending at 0900 UTC, 19 September 1983 (21 h). Although the mesoscale features of the precipitation fields are somewhat different from one experiment to another, all experiments produce a banded structure of heavy precipitation associated with the frontal system. Based on the observed front location for 0600 UTC, 19 September 1983 and 1200 UTC, 19 September 1983, we can deduce the observed front location at 0900 UTC, 19 September 1983, which is shown as a dashed curve in Figure 16. The model-simulated frontal positions are determined using the low-level wind and mass fields. Examination of the wind field at the lowest model layer indicates that the simulated frontal positions for each experiment are quite similar, and they are generally slower than the observed front at this time. As indicated by Seaman et al. (2002), slower-than-observed phase speeds are known to be a characteristic of models having second-order finite-difference numerics, like MM5.

Figure 16 shows that the model-simulated 3-h precipitation field ending at 21 h for Exp. MB1 has a wide-spread pattern over a large area ahead of the model-simulated cold front, with a maximum value of 108 mm over Lake Erie. The satellite photo does show enhanced cloudiness in the region, but the 108-mm maximum due to a grid-point storm is surely much larger than observed for this 3-h period. Note that in this baseline experiment and in all but two of the other experiments, no convective scheme is applied to the 4-km domain and all precipitation is produced by the explicit moisture physics.

Since analysis nudging FDDA was shown in the previous study by Seaman et al. (2002) to have produced the best overall model results on the 12-km grids, analysis nudging FDDA as applied on the 12-km domain is also applied here on the 4-km grid (Exp. MS1). However, observation nudging is generally more appropriate for a 4-km domain, so a new experiment using obs nudging is also performed (Exp. MS1.1). Figures 17 and 18 show the model-simulated 3-h precipitation field ending at 21 h for Exp. MS1 (analysis nudging) and Exp. MS1.1 (observation nudging), respectively. It is clear that both experiments reduce the erroneous maximum value of precipitation over Lake Erie by about 25 percent and the rain band associated with the cold front has narrowed somewhat and has become more organized. However, the convective precipitation area still appears to be overpredicted from Lake Erie extending to the northeast along the front based on the satellite imagery (Figure 10). The surface weather maps bracketing this time also do not support the heavier precipitation amounts.

Since enhanced vertical mixing in the GSPBL scheme has been shown to produce better model results based on other related research at Penn State, in the next experiment (MS2) the turbulence length scales in the GSPBL are increased one layer above the surface by 50 percent, and above this layer, the K values are effectively doubled compared to those in the default scheme. Exp. MS2 uses exactly same model configuration as in Exp. MB1 except that enhanced vertical mixing (referred to as "double K") is applied. No FDDA is applied in this experiment. Figure 19a shows the model-simulated 3-h precipitation field ending at 21 h. Although significant improvements in the precipitation field in Exp.MS2 may not be readily apparent with the 111-mm maximum still located in southern Lake Erie, more realistic mixed-layer profiles of mixing ratio (not shown) and improvements in the statistical scores (Section 5) suggest that this double K modification to the GSPBL be adopted for all other GSPBL sensitivity experiments.

Figure 19b shows the model-simulated surface wind field. It is shown that the precipitation over Lake Erie is located in the warm sector of the cold front which is clearly defined by the surface wind convergent zone. Maximum southwesterly wind speed (21.8 m/s) is found near the precipitation region.

To investigate how the model results change if a completely different type of boundary layer scheme is used, the MRF PBL scheme is applied in lieu of the GSPBL scheme in Exp. MS3. The simulated 3-h precipitation field ending at 21 h is shown in Figure 20. Note that the precipitation patterns over Lake Erie that existed in other experiments have completely disappeared. This lack of precipitation in this southern Lake Erie region by Exp. MS3 is not consistent with the surface observations or satellite imagery (see Figures 9, 10 and 11). The larger vertical mixing, even during the night, when using the MRF PBL in Exp. MS3 (Figure 21b) compared to the GSPBL in Exp. MS2 (MB2) (Figure 21a) and all other experiments (Figure 21c), is apparently eliminating the precipitation in the Lake Erie region where the other experiments overproduced the rain associated with the lower enhanced cloudiness in this region (Figure 10).

Figure 22 shows the simulated 3-h precipitation field ending at 21 h for Exp. MS4 which is identical to Exp. MB2 except that mixed-phase microphysics is used. A large maximum of 92.7 mm is still located over Lake Erie, but compared with Exp. MB2, Exp. MS4 has a precipitation pattern that shows enhanced and more localized precipitation. There appears to be smaller areal coverage of lighter precipitation amounts and more concentrated coverage of the higher precipitation amounts. This may be explained by the fact that mixed-phase microphysics allows more ice particles, and they do not advect as far from the updraft as liquid drops because of their higher fall speeds, so that the precipitation becomes more localized.

Next, both Exp. MS5 and MS5.1 have identical model configurations and physics to Exp. MB2 except that they use the new Kain-Fritsch scheme (KF2) on the 4-km domain, with mixed-phase microphysics also applied in Exp. MS5.1. No FDDA is used in these two experiments. Model-simulated precipitation fields ending at 21 h for Exp. MS5 (Figure 23a, 23b and 23c) and for Exp. MS5.1 (Figure 24a, 24b and 24c) show similar patterns with Lake Erie total precipitation (explicit plus convectively parameterized) maxima of 62.0 mm and 62.9 mm, respectively, with a narrower explicit precipitation band distributed along the cold front. Along the precipitation band the maximum values are generally smaller than those in Exp. MS2 (MB2). The narrow precipitation bands in Figure 23c and 24c are quite consistent with the cloud band that was observed at 0830 UTC, 19 September 1983 (see Figure 10). The convective scheme appears to release some of the CAPE so that the explicit scheme response is now much weaker. The Exp. MS5 explicit maximum over Lake Erie is about 50 percent smaller than that in MS2 (52.5 mm versus 111 mm) and the total MS5 rain maximum is slightly higher than the explicit value at 62.0 mm. Adding mixed phase to Kain Fritsch (KF2) on the 4-km domain in Exp. MS5.1 again produces somewhat larger local maxima and a more concentrated explicit pattern (compare Figures 23a and 24a)

Although several experiments involving an enhanced horizontal diffusion coefficient are conducted in this research, the statistical scores for the model-simulated results are quite similar with MS6.1 producing the overall best statistical results of the enhanced diffusion experiments. Thus only Exp. MS6.1 is presented here for subjective evaluation. Figure 25 shows the 3-hourly model-simulated precipitation field ending at 21 h for Exp. MS6.1 which uses a five times larger background value of the horizontal diffusion coefficient (Table 3). Notice that the precipitation pattern including the Lake Erie maximum value is quite similar to that in Exp. MB2. Enhanced artificial smoothing appears to have very little effect on the grid-point storm problem, and may at the same time smooth out important mesoscale details in regions where it is not raining. Exp.

MS6.2 applies the additional smoothing through the deformation term while Exp. MS6.3 does so only where it was raining the previous time step, but the results of these other diffusion experiments are similar to those presented here in seriously overestimating localized precipitation. Use of an even larger value for diffusion, that is increasing it by more than a factor of five, cannot be justified since it would adversely affect the ability of the model to produce mesoscale structures. The value of enhanced background horizontal diffusion used in MS6.1 is five times larger than the default value but still only 50% percent of the maximum value allowed for numerical stability. Use of larger horizontal diffusion as a solution to this grid-point storm problem appears to be ineffective since again it is the model physics that requires some modification at 4-km resolutions.

Since applying FDDA and KF2 to the 4-km domain had the most significant positive impact on the model results presented so far, including the statistics presented in Section 5.2, one last experiment (Exp. MS7) that uses both KF2 and observational nudging on the 4-km domain is conducted. Figure 25 shows the model-simulated precipitation field ending at 21 h for Exp. MS7. Comparison of Figures 23c, 24c and 26c reveals that Exp. MS7 produces very similar total precipitation patterns to the others except that the maximum value of precipitation over Lake Erie is further reduced to 55.0 mm. The maximum surface wind speed near the precipitation region over Lake Erie is reduced from 21.8 ms^{-1} in Exp. MB2 to 14.2 m/s (Figure 26d).

Table 5 summarizes the model-simulated maximum precipitation and surface winds for this night time period ending at 0900 UTC, 19 September (21 h) over the Lake Erie region. It is shown that the baseline experiments (both Exp. MB1 and MB2) produce quite significant precipitation amounts associated with grid point storm over Lake Erie. Enhanced diffusion (Exp.

6.1) has little impact on reducing the precipitation amounts. In fact two of the enhanced diffusion experiments produce even larger precipitation amounts than the baseline MB2. A moderate reduction in the precipitation is achieved when FDDA or KF2 is applied. When the MRF PBL scheme is used, the precipitation pattern in this region is dry and not consistent with the observations. Combining KF2 and observation nudging FDDA on the 4-km domain in Exp. MS7 produces the largest reduction (50 percent) in the total maximum precipitation for the Lake Erie region compared to the baseline MB2, although the maximum is still seriously overestimated over the lake at this time.

5.1.2 30 h model time

Observed surface conditions at 1800 UTC 19 September 1983 over the 4–km domain show no reported precipitation (Figure 12). Note the general southwesterly flow through most of Pennsylvania (PA). There are some surface stations having obstructions to visibility (e.g., fog, haze, etc.) mainly along the front from west to east through northern Lake Erie and central NY and also along a trough extending northeast-southwest through New England into New Jersey (NJ) and Maryland (MD). Cloudy skies are found further to the north of the cold front. The satellite photo at this time (not shown) confirmed the absence of significant clouds over PA and southern NY where the 4-km domain Exp. 3A in the previous study by Seaman et al. (2002) and Exp. MB1 in this study produced a mesoscale convective system (Figure 27a) ahead of the front in northwestern PA with divergent low-level flow seriously disrupting the southwesterly flow at the surface (Figure 27b) and a cold pool in the surface temperature field (Figure 27c). This convective system is not observed.

The maximum amount of model-simulated 3-h precipitation for Exp. MB1 at 30 h is 66.5 mm located in northwestern PA, associated with outflow boundaries and a cold pool temperature of 17.0 ºC and a mesohigh of 1022 hPa (see Table 5). As discussed in Seaman et al. (2002), the primary cause of the poor mesoscale model performance was likely due to the explicit (grid-resolved) representation of convection. Because no convective parameterization is used on the 4-km grid in Exp. MB1, the convective updrafts are forced on coarser-than-realistic scales (normal updraft diameter for most storms in the eastern United States is ~ 2 km), and the rainfall and the atmospheric response to the convection are too strong. The evaporative cooling and the associated downdrafts are too vigorous, causing widespread disruption of the low-level winds.

When FDDA is applied on the 4-km grid, both precipitation amount and the area coverage at 30 h are reduced compared to Exp. MB1. In Exp. MS1 where analysis nudging is used, precipitation appears in southern NY with a maximum amount of 53.3 mm and another area with maximum of 11.5 mm in eastern NY (Figure 28a). Surface wind fields (Figure 28b) do not show a divergent pattern in northwestern PA, but there is a disturbed pattern over southern NY near Lake Erie. The surface temperature field (Figure 28c) shows a cold pool (18.0 ºC) and sea-level pressure field shows a weaker mesohigh (1019 hPa) associated with the precipitation in southern NY near Lake Erie 9 (see Table 5). In Exp. MS1.1 where observation nudging is used, the simulated 3-h precipitation ending at 30 h (Figure 29a) is reduced in magnitude and expanded in area compared to Exp. MS1 in northwestern PA near Lake Erie, with a maximum value of 21.9 mm compared to Exp. MS1 at 53.3 mm (Figure 28a). Similarly the surface wind field for Exp. MS1.1 at this time (Figure 29b) does not show any strong divergence although the winds are more southerly or even southeasterly in northwestern PA where the temperature field (Figure 29c) is locally cooler (18.5 ºC).

Exp. MS2 (also refers to MB2) is identical to Exp. MB1 except that the turbulence mixing length scales and coefficients are doubled in the GSPBL scheme. Although the simulated precipitation patterns at 30 h (Figure 30a) are similar to Exp. MB1, the maximum values of precipitation in Exp. MB2 are reduced from 66.5 mm to 56.7 mm in northwestern PA. Associated with the precipitation field at this time, there is a clear divergent pattern (outflow boundaries) in the simulated surface wind field (Figure 30b) and a cold pool (17.5 ºC) in the simulated surface temperature field (Figure 30c) and a mesohigh (1020 hPa) in the simulated sea-level pressure field. Apparently, enhancing the vertical mixing does not help to resolve the problem with excessive grid-point convection on the 4-km domain when no convection scheme is applied.

Exp. MS3 is identical to Exp. MB1 except that the MRF PBL scheme is used in lieu of the GSPBL scheme. Figure 31a shows that Exp. MS3 has produced a significantly worse simulation in the model-simulated precipitation field at 30 h than that in Exp. MB1 because the spurious convection has spread to a much larger area, covering a portion of Lake Erie and the entire northern third of PA. The simulated surface wind field at 30 h (Figure 31b) also shows an even larger area of disturbed flow with outflow boundaries. The simulated surface temperature field at 30 h (Figure 31c) indicates a much broader area of cold pools across northern PA, with colder minimum temperatures of 16.1 ºC and 16.6 ºC and mesohigh of 1022 hPa embedded within the evaporatively cooled air across northern PA. Therefore, Exp. MS3 greatly increased the magnitude and coverage of the erroneous rain and anomalous surface meteorology at this time.

The cross sections of PBL height for MS2 (MB2) versus MS3 at this time are shown in Figures 32a and 32 b. The AGL PBL heights for all experiments are shown in Figure 32c. Note again the much deeper simulated PBL heights when using the MRF PBL scheme, this time during the day time. The stronger vertical mixing associated with the MRF scheme is producing much different and worse QPF. The MRF scheme appears to introduce significant error in this case.

Exp. MS4 is identical to Exp. MB2 except that mixed-phase microphysics (i.e., both ice and liquid can exist in a given grid cell, and supercooled water can exist at below-freezing temperatures) is used rather than simple ice microphysics (only liquid or ice can exist at a given grid cell based on the temperature being above or below freezing). The model-simulated precipitation field at 30 h for Exp. MS4 is shown in Figure 33a. Compared with Exp. MB2 (Figure 30a), the MS4 simulated precipitation (Figure 33a) tends to cover a smaller area, with even more intense precipitation (88.6 mm) in northeast Ohio (OH) and northwest PA. The precipitating area in central PA in Exp. MB2 has disappeared. Accompanying the precipitation in northwestern PA is a divergent pattern evident in the simulated surface wind field (Figure 33b), and associated with a cold pool (18.0 ºC) in the surface temperature field (Figure 33c) and a mesohigh (1020 hPa) in the sea-level pressure field, although the areal coverage of the precipitation is smaller than that in Exp. MS2 (Figure 30a).

In Exp. MS5, the new Kain-Fritsch scheme (KF2) is applied on the 4-km domain. Figure 34 shows the model-simulated explicit (Figure 34a), convective (Figure 34b) and total precipitation (Figure 34c) fields at the 30-h time, respectively. From the precipitation fields, it is clear that Exp. MS5 greatly reduces the non-convective rain produced by the explicit microphysics (compare Figure 34a with Figure 30a). The explicit precipitation pattern showing a 32.7 mm maximum over the southern portion of Lake Huron seems to be related to the MM5 front that moved slower than the observed front. The position of the simulated cold front is confirmed by the surface wind field (Figure 34d) in which a zone of wind shear is clearly seen to the north of Lake Erie. The convective scheme produces light or no precipitation in northwestern PA (Figure 34b) where grid-point type storms had developed in all of the other experiments (Exp. MB1, MS1, MS2/MB2, MS3, MS4). Thus the Exp. MS5 total precipitation shown in Figure 34c is also generally much lighter than that of the other experiments in this region. One of our hypotheses is that use of a convective scheme at 4-km resolution may diffuse the grid-resolved convective instability as it develops and thus reduce the model's tendency to produce strong grid-point storms, and this appears to be the case here. However, the use of a convective scheme on a 4-km domain is generally not recommended due to the fact that the parameterized convection would not be less than the assumed 10 percent of the area of the 4-km grid cell. Nevertheless, these results show that its use may still be helpful in these situations where the explicit microphysics alone is producing grossly unrealistic grid-point storms.

Examination of the model-simulated surface wind field at 30 h (Figure 34d) verifies that the MM5 surface wind fields at this time in Exp. MS5 are much improved by the model not producing the significant precipitation and low-level divergent response to the evaporative cooling caused by the excessive grid-resolved precipitation in this region in the other experiments. The surface temperature pattern and minimum temperature of 21.2 C in Figure 34e in northcentral PA appear to reflect the higher terrain in this area (see Figure 15). Therefore, Exp. MS5 produced some very interesting and also positive results on the 4-km domain by not producing the spurious grid-point precipitation and its effects on the surface wind and mass fields.

Since use of mixed-phase microphysics seems to have had some positive impact on the model performance, as revealed in the statistics to be presented in Section 5.2, a new experiment, Exp. MS5.1, is performed with both KF2 and mixed-phase microphysics on the 4-km domain. Figures 35a, 35b and 35c show the model-simulated explicit, convective and total precipitation field at 30 h for Exp. MS5.1, respectively. Similar to Exp. MS4 where mixed-phase microphysics is also used, the precipitation in Exp. MS5.1 tends to cover smaller areas and become more concentrated locally. Compared with Exp. MS5, the amount and patterns of the MS5.1 precipitation seems to be very similar, with light or no rain in northwestern PA but with more intense rain in northern PA and southern NY. Similar to Exp. MS5, the simulated surface wind field in Exp. MS5.1 at this time (Figure 35d) is southwesterly across PA and does not show the divergent flow patterns in northwestern PA. Again the surface temperature minimum (Figure 35e) is collocated with the terrain maximum in northcentral PA (see Figure 15).

The purpose of the MS6.n series of experiments (Table 3) is to investigate the impact of enhanced horizontal diffusion on the 4-km simulation and its grid-point storms. Figure 36a shows the simulated MS6.1 precipitation field at 30 h in this experiment. It is shown that the maximum amount of precipitation over northwestern PA has been reduced to 11.1 mm and the entire area of the precipitation has also been reduced, although the simulated surface wind field (Figure 36b) at 30 h is southerly in northwestern PA rather than southwesterly and still shows a divergent pattern located in southwestern NY. A cold pool of 18.7 ºC (Figure 36c) is seen over the region of southwestern NY.

Figures 37a, 37b and 37c show the model-simulated explicit, convective and total 3-h precipitation field at 30 h for Exp. MS7, respectively, in which both FDDA (observation nudging) and KF2 are used on the 4-km domain. Compared with the non-convective precipitation in Exp. MS5 (Figure 34a), which also used KF2 on the 4-km domain, Exp. MS7 produces little precipitation (7.45 mm) in northeastern MI and scattered light precipitation in

NY. The convective precipitation is also similar, with slightly larger values found in Exp. MS7 (Figure 37b). There is also light convective precipitation in NY in both experiments. The total precipitation in Exp. MS7 (Figure 37c) covers a slightly larger area than that in MS5 although the precipitation amounts are still generally small.

Figure 37d shows the model-simulated surface wind field. It is shown that southwesterly wind over northwestern PA and Lake Erie are well simulated, with a maximum wind speed of 10.4 ms^{-1}over Lake Erie. No divergent outflow boundaries are found in this experiment. The simulated temperature field does not show any cold pool associated with the precipitation. The minimum temperature of 22.1 ºC found in northcentral PA is likely related to the topography (Figure 37e).

To further compare the model performance for each experiment at 1800 UTC, September 1983 (30 h), Table 5 summarizes the maximum values of the precipitation pattern in northwestern PA/southwestern NY near Lake Erie and the associated cold pool temperatures and mesohigh pressures for all experiments. The Table indicates that at 30 h in Exp. MB1, MS1, MS2, MS3, and MS4, the simulated precipitation maxima are quite large; and each of these experiments shows an evaporatively induced cold pool in the simulated surface temperature field and locally higher sea-level pressures. It is worth mentioning that Exp. MS3 which used the MRF PBL scheme has the coldest and broadest surface cold pool with it minimum (16.1 C) in the higher terrain of northcentral PA associated with a 27.8 mm precipitation maximum. Exp. MS1.1 using observation nudging shows light precipitation and a cold pool (18.5 C). Experiments MS5, MS5.1 and MS7 show very little precipitation and no cold pool or mesohigh associated with the precipitation. Exp. MS7 appears to produce the best low-level flow pattern at this time with consistent southwesterly flow across PA into southern NY (compare with observations in Figure 12). Thus, use of the combination of observation nudging and the new Kain-Fritsch cumulus convection parameterization on the 4-km domain seems to have the most significant positive impact on the model solutions on the 4-km grid in this CAPTEX '83 case. This conclusion will be further investigated using the statistic evaluation in next section.

5.2 Objective Evaluation of the MM5 Solutions Using a Statistical Approach

The subjective examination of the mesoscale and synoptic-scale structures simulated by the MM5 model in the previous section led to some preliminary conclusions; this section objectively examines the model's statistical performance for Episode 1 of the CAPTEX '83 study to further test these findings. The statistical measures of accuracy selected for this evaluation were described in Section 4.4 and are summarized in Appendix A. The statistics are calculated over the entire 4-km domain.

The statistical results for all experiments (from Exp. MB1 to MS7) conducted in this research are summarized in Table 6. Tables 6a through 6m show statistical scores of *RMSE*, *MAE*, *ME*, *I* and *TRP* for wind speed, wind direction, temperature, water vapor mixing ratio and sea level pressure, averaged over the entire 30-h modeling period for each experiment and grouped into 4 different vertical zones. Use of these tables alone makes it difficult to compare statistical measures when there are so many experiments involved. Thus the MM5 statistical performances are also evaluated using graphics of time series and vertical profiles of the statistical measures. Although the statistical tables contain more statistical measures and have information stratified in a condensed and easy-to-understand format, the new graphics designed for this project make it easier to compare experimental results and analyze the time variation and vertical distribution of the statistical measures for all model variables including wind speed, wind direction, temperature water vapor mixing ratio and sea level pressure.

5.2.1. Wind Speed

Figure 38a shows the *MAE* of the MM5-simulated surface-layer wind speed versus time over the entire 4-km domain for all experiments (Exp. MS5.1 is omitted because its results are very similar to Exp. MS5). It is shown that *MAE* for surface wind speed for Exp. MB1, MS2, MS3, MS4, MS5, and MS6 (refer to Table 3) are very similar, and errors are generally larger during the night time hours (12 – 24 h) than the day time hours. When analysis nudging is added to the 4-km domain in Exp. MS1 (Curve 1, Figure 38a), the MAE for surface wind speed has been reduced significantly. When obs nudging is used on the 4-km domain, a further reduction is seen in the surface wind speed error in both Exp. MS1.1 (curve 7, Figure 38a) and MS7 (curve 8, Figure 38a) which also includes KF2 on the 4-km domain. The 30-h mean statistics may also be found in Table 6, and they are plotted on the right end of each time series chart (or top of each vertical profile chart) with the digital values also included above the experiment key at the bottom of the figure.

Figure 38b shows the all-layer averaged *MAE* of the MM5-simulated wind speed versus time over the entire 4-km domain. Note that because upper air data are available only at 0 h, 12 h and 24 h times, the differences between Figures 38b and 38a are expected to occur at these three times. (The 30-h mean statistics in the tables and throughout the figures exclude the initial condition time.) Comparison of Figures 38a and 38b indicates that the spread in the experimental results is even larger in Figure 38b than Figure 38a and that the FDDA experiments further increase their advantage over the other experiments when levels above the surface are included.

It appears that including KF2 with the observation nudging on the 4-km domain in Exp. MS7 produces a slightly smaller error than in Exp. MS1.1 in the atmosphere above the surface. Figure 38c shows vertical profiles of 30-h averaged *MAE* of the MM5-simulated wind speed at all model layers over the entire 4-km domain. It is shown at the top of Figure 38c and in the values in the experiment key at the bottom, and Table 6, that on average Exp. MS7 (curve 8) produces the best results with MS1.1 (curve 7) close behind and MS1 further behind but still much ahead of the other experiments. Exp. MS1.1 has a small advantage over MS7 in the lowest few layers in the PBL. Therefore, FDDA and obs nudging in particular seem to have the most significant contribution to reducing model errors in wind speed on the 4-km domain. Note that analysis nudging using conventional surface wind analyses in the PBL(MS1, curve 1) does not perform as well in the PBL (lowest 1 km) as obs nudging or the non-FDDA model experiments on this 4-km grid scale. The model error in wind speed for Exp. MS1 in Figure 38c is significantly reduced in the atmosphere above the PBL and the first two model layers near the surface. However in the PBL, the *MAE* for Exp. MS1 is even larger than that in the baseline experiment, Exp. MB1. This is likely because the analyses are too coarse to represent the structure within the PBL and have a detrimental effect because their use tends to destroy the mesoscale structures that are naturally produced by the MM5 at 4-km grid resolution. This result confirms why analysis nudging is not recommended for fine-resolution domains, especially in the PBL or lower troposphere (e.g., Stauffer and Seaman 1994, Shafran et al. 2000).

Inspection of the results in Figure 38c from Exps. MB1, MS2, MS3, MS4, MS5 and MS6.1 indicates that a large spread among these six experiments is found in the PBL below 1 km

AGL, with Exp. MB1 (curve 9) having the largest error in wind speed, and Exp. MS5 (curve 5) having the smallest error in the upper PBL and Exp. MS4 (curve 4) having the smallest error in the lower PBL. Exp. MS3 (curve 3), using the MRF PBL scheme, is one of the worst experiments in the PBL. Exp. MS2 (using enhanced vertical mixing in GSPBL scheme) shows a distinct improvement over Exp. MB1 (compare curves 2 and 9), and further improvement is evident when using Exp. MS4 (mixed phase) and MS5 (KF2 on 4-km domain).

All experiments show positive wind biases (wind speed being too fast) in simulated surface wind speed during the night time between 12 h and 24 h times (Figure 39a) and most have slightly negative biases during the day time, with the smallest biases seen in experiments involving obs FDDA (Exps. MS1.1 and MS7). For the upper air, simulated wind speeds show negative biases above 300 m AGL (Figure 39b) in the vertical profiles of the 30-h averaged *ME* of wind speed for all model layers for all experiments. Figure 39b also indicates that wind speed tends to be too fast in the lower PBL and too slow above, with Exp. MS3 (using MRF PBL scheme) producing the largest *ME* in wind speed above 300 m AGL. It is clear that use of obs nudging (curves 7 and 8) tends to produce the best simulations for wind speed.

Figure 40a shows the index agreement (*I*) versus time for the simulated surface wind speed. Recall that the perfect score for *I* is 1.0. This figure indicates that by using FDDA, analysis nudging and especially obs nudging, the 4-km model produces the best wind anomaly structure at the surface. The same conclusion can be drawn for the upper air wind speed structure shown in Figure 40b. The average *I* values are increased by including layers above the surface. This is confirmed by Figure 40c which shows the vertical profiles of 30-h averaged *I* at all model layers for all experiments. Again, it is seen that obs nudging experiments (Exp. MS1.1 and MS7) produce the best model results, with Exp. MS7 better than Exp. MS1.1. That is, including Kain-Fritsch (KF2) on the 4-km domain along with the obs nudging further improves the results. In the PBL, Exp. MB1 and MS1 show the worst results for wind speed structure.

5.2.2. Wind Direction

Figure 41a shows the *MAE* versus time for the model-simulated surface wind direction for all experiments over the entire 4-km domain. It is shown that using analysis nudging and observation nudging FDDA consistently improves the model simulation of surface wind direction, with the best simulation achieved in Exp. MS7 where both obs nudging and KF2 are used. Inspection of the 30-h averaged values of *MAE* for each experiment indicates that Exps. MB1 and MS3 have the largest model error and Exp. MS7 has the smallest error.

For the upper air, the *MAE* of wind direction at 12h and 24 h times can be seen in Figure 41b. Again, using FDDA (both analysis nudging and obs nudging) has the most significant contribution in improving the simulated wind direction. This conclusion can be verified by Figure 41c which shows the vertical profiles of the 30-h averaged *MAE* of wind direction for all model layers for all the experiments conducted in this study. It is shown that using obs nudging tends to produce the smallest model error in simulated wind direction, with obs nudging combined with KF2 being more effective than the obs nudging alone. Notice that using analysis nudging only shows much greater improvement above the PBL, with some detrimental effects within the PBL compared to all experiments except the baseline Exp. MB1 and Exp. MS3 (MRF PBL). In fact use of the MRF PBL produces the worst result for wind direction in the PBL (lowest 1 km AGL) and also the average value over all layers (see Table 6 and curve 3 at the top and bottom of the figure).

The baseline experiment, Exp. MB1, also has a relatively large wind direction error in the PBL, and enhancing the vertical mixing in the GSPBL in Exp. MS2 produces marked improvements in the PBL (compare curve 2 with curve 9). All of these other experiments (Exp. MS1, MS2, MS4, MS5 and MS6.1) have similar statistical scores and are better than the baseline Exp. MB1 and Exp. MS3. In summary, it appears that Exp. MS7 (obs nudging and KF2) produces the best overall wind results while Exp. MS3 (MRF PBL) results are generally worse than the other experiments.

5.2.3. Temperature

Figure 42a shows the *MAE* versus time for the model-simulated surface (lowest model layer) temperature for all experiments over the entire 4-km domain. Although all the experiments seem to have quite similar *MAE* scores for surface temperature, there is a general increase in surface temperature error towards the end of the simulation when the model-simulated rain was overestimated (see Section 4). Comparison of the 30-h averaged *MAE* score for each experiment indicates that Exp. MS3 has the largest error and that Exp. MS7 has the smallest error. Note that in Exp. MS7 only the wind fields are assimilated in the PBL and surface layer (see Section 3.3.2), so the small improvement in the surface temperature is indirectly caused by assimilation of winds in the PBL and/or temperature and winds above the PBL. This is a positive sign that the FDDA is effective when an improvement is seen in a field not directly assimilated by the model.

Figure 42b shows the all-layer averaged *MAE* of the MM5-simulated temperature field versus time over the entire 4-km domain. Since upper-air observations are available at 12 h and 24 h (0 h is the initial condition) and both analysis and obs nudging for the mass fields are applied in the free atmosphere above the PBL, the direct FDDA effects are clearly seen at these two times. As a result, the all-layer average errors are smaller than the surface errors for the FDDA experiments at these times. Exp. MS7 produces the best 30-h averaged *MAE* score for the temperature fields, and Exp. MS3 which uses the MRF PBL scheme stays the worst.

Figure 42c shows the vertical profiles of the 30-h averaged *MAE* of temperature for all model layers for all experiments conducted in this study. It is evident that the obs nudging plays the most significant role in reducing the model error in temperature, with Exp. MS7 (which involves both obs nudging and KF2) having the smallest *MAE* error. It is again encouraging that use of KF2 along with the obs nudging is producing smaller errors than using obs nudging alone. Exp. MS1 that uses analysis nudging shows most of its reduction of *MAE* in the layers above the PBL (1 km AGL). However, within the PBL, where the thermal and moisture nudging are completely turned off (Section 3.3), the MS1 results are quite good compared to the other experiments. So the potential degradation of these fields by assimilating coarse temporal and/or spatial resolution data is minimized by not assimilating these fields in the PBL. As discussed earlier for the wind field, some degradation in the model simulation is possible when using coarse resolution analyses in the PBL. Special attention must be given to data assimilation in the PBL so that the mesoscale structure developed by the MM5 is not destroyed by the FDDA.

Comparisons among the other experiments (Exp. MB1, MS2, MS3, MS4, MS5 and MS6.1) indicate that *MAE* scores are very similar. However, Exp. MS5 (KF2 on the 4-km domain) is slightly better for MAE temperature than the others while Exp. MS3 which uses MRF PBL scheme is slightly worse than the other experiments.

Figure 43a shows the all-layer averaged *ME* of the MM5-simulated temperature for all experiments over the entire 4-km domain. The figure shows that all experiments have developed a 2.0-3.0 ºC cold bias after 24 h into the model simulation. This cold bias at 27 h and 30 h is likely related to excessive evaporative cooling associated with the overestimation of rainfall by the model. The surface analysis at 1800 UTC 19 September 1983 (Figure 12) and satellite imagery at 1731 UTC 19 September 1983 (not shown) confirm that there was no significant precipitation over the entire 4-km domain by 30 h. Although the cold bias at 27 h and 30 h exists in all experiments, a closer inspection of the 30-h averaged *ME* score for each experiment indicates that the baseline experiment, Exp MB1, shows the largest cold bias and Exp. MS7 (which involve both obs nudging and KF2) has the smallest cold bias. Therefore, combination of obs nudging and use of the new Kain-Fritsch scheme (KF2) again shows the most significant improvement in the model-simulated temperature field. The vertical profile of temperature *ME* based on the sondes at 12 h and 24 h (Figure 43b) shows that the *ME* is quite small though the entire atmosphere (see cluster of experiments at top of figure around the zero line), with a slight cold bias (-0.5 ºC) near the top of the boundary layer.

5.2.4. Water Vapor Mixing Ratio

Figure 44a shows the all-layer averaged *ME* error of the MM5-simulated water vapor mixing ratio versus time for all experiments over the entire 4-km domain. For all experiments, MM5 produces negative moisture biases (too dry) during the day between 0 h and 12 h times, and positive moisture biases (too moist) at night between 12 h and 24 h times. It appears that Exp. MS3 which uses MRF PBL scheme tends to produce the strongest dry bias. This could be related to the fact that MRF PBL scheme tends to mix too vigorously and the PBL is much deeper than the other experiments (see Figures 21c and 32c). However during the night time between 12 h and 24 h, the MRF PBL scheme tends to have the smallest moist bias, possibly due to compensating errors.

Figure 44b shows the *MAE* versus time for the model-simulated surface (lowest model layer) water vapor mixing ratio for all experiments over the entire 4-km domain. All experiments produce similar *MAE* scores except that Exp. MS3 (MRF PBL scheme) tends to have larger *MAE* during the day time and smaller errors during night time. Closer inspection of the 30-h mean values of *MAE* score for each experiment indicates that Exp. MS3 has the largest *MAE* error, and both Exp. MS1.1 and MS7 have the smallest errors. This means that FDDA helps to improve the simulated surface moisture field indirectly because no surface mass field data are directly used in the FDDA.

Figure 44c shows the all-layer averaged *MAE* versus time for the model-simulated water vapor mixing ratio for all experiments over the entire 4-km domain. The noticeable differences between this figure and Figure 44b take place at 12 h and 24 h times where upper air *MAE* scores are involved in computing the all-layer average. It is shown in Figure 44c that the most significant reduction in *MAE* errors at these two times is due to use of FDDA. This fact is confirmed again by Figure 44d that shows the vertical profiles of the 30-h averaged *MAE* of model-simulated water vapor mixing ratio for all model layers for all experiments conducted in this study. It is shown that obs nudging experiments (Exp. MS1.1 and MS7) produce the best model results for the moisture field, with Exp. MS7 (combination of obs nudging and KF2) again being better than Exp. MS1.1 (obs nudging alone). Comparisons among all other experiments in the PBL indicates that the baseline experiment, Exp. MB1, has the largest *MAE* error for simulated water vapor mixing ratio. Although the experiments including Exp. MS1, MS2, MS4, MS5 and MS6.1 show some positive effect in reducing *MAE* error, Exp. MS3 indicates an even larger reduction in *MAE* error. As discussed earlier, the MRF PBL scheme tends to dry the boundary layer due to its unrealistically strong mixing that causes a deeper boundary layer (even at night times). Notice that Exp. MS1 in which analysis nudging of moisture is not used in the PBL is among the best non-FDDA experiments for reasons discussed earlier for the temperature field.

5.2.5. Sea-Level Pressure

Figure 45 shows the *MAE* versus time for model-simulated sea-level pressure for all experiments over the entire 4-km domain. It is shown that all experiments produce quite small *MAE* error for sea-level pressure (less than 1.4 hPa at all times and averaging less than 1 hPa), although noticeable spread is found after 15 h model time when precipitation effects become larger in the real world (Section 2) and in the model simulations (Section 5). Although all the *MAE* values are relatively small, inspection of the 30-h mean values of *MAE* indicates that Exp. MS3 (MRF PBL) has the largest error of all the experiments and Exp. MS1.1 (obs nudging) has the smallest *MAE* for simulated sea-level pressure. Again, the pressure field is not directly assimilated via analysis nudging or obs nudging, but reflects the combined data assimilation effects in the mass, wind and precipitation fields. The mean errors (*ME*) for sea-level pressure are also generally small for all experiments (< 1.0 hPa, not shown).

6. CONCLUSIONS

6.1. Summary

To improve the MM5 model simulations on the 4-km grid where the previous study by Seaman et al. (2002) indicated that simulation of the 18-19 September 1983 CAPTEX case had detrimental effects on the meteorological solutions, a series of experiments was designed to address model sensitivities to mixed-phase microphysics, planetary boundary layer (PBL) physics, convective parameterization, enhanced horizontal diffusion, and use of analysis nudging versus observation nudging FDDA on the 4-km domain. Both subjective and objective analysis of 4-km model results was performed with special attention given to quantitative precipitation forecasts (QPF) and overall meteorological accuracy. The subjective analysis of this case involving frontal rain and convective precipitation focused on two times: a night time period and a day time period. The former period was associated with a strong grid point storm in all of the experiments ahead of the front over Lake Erie while the latter period spawned a spurious mesoscale convective system that seriously disrupted the low-level wind and mass fields. A detailed statistical analysis of the meteorology was then used to study the temporal variability and vertical structures of the model errors. Over all, using obs nudging and the new Kain-Fritsch cumulus convective scheme on the 4-km domain has shown the best performance. Use of MRF PBL scheme generally produced the worst model simulations.

The baseline experiment (Exp. MB1) used the current most up-to-date version of the MM5 modeling system without FDDA. During a night time period ending at the 21-h model time, Exp. MB1 produced a wide-spread pattern of precipitation over a large area ahead of the model-simulated cold front, with a maximum 3-hourly precipitation value of 108 mm over Lake Erie. At 30 h, Exp. MB1 reproduced the spurious convective system reported in the original study during this day time period. It was associated with divergent outflow boundaries and a cold pool in northwestern PA near Lake Erie.   Statistical analysis showed that Exp. MB1 had relatively large *MAE* in simulated wind speed and wind direction which would adversely affect transport and dispersion calculations using these model-simulated fields.

Use of FDDA in Exps. MS1 (analysis nudging) and MS1.1 (obs nudging) on the 4-km domain reduced the erroneous maximum value of precipitation at 21 h over Lake Erie by about 25 percent and made the rain band associated with the cold front narrower and more organized although the convective precipitation was still overpredicted. At the 30-h time, both precipitation amount and areal coverage were reduced compared to the baseline experiment, Exp. MB1, but FDDA alone could not completely eliminate the spurious convective system. Statistic results indicated that use of FDDA made a significant contribution to reducing the model errors. It was shown that using analysis nudging of surface wind in the boundary layer based on conventional data had some detrimental effects while the strategy of withholding assimilation of coarse resolution mass field data in the PBL was re-affirmed. The use of obs nudging produced much better results as expected on these finer scales.

Enhanced vertical mixing in the GSPBL scheme showed marked improvements in the simulated wind and mass fields compared to the Exp. MB1. Thus Exp. MS2 was considered to be a new baseline experiment (Exp. MB2) for all other experiments, since the Exp. MS2 mixing length modifications were adopted in all other sensitivity experiments. However, it was apparent that using the enhanced vertical mixing alone did not alleviate the problem with excessive grid-point convection on the 4-km domain because a 111-mm maximum still existed in southern Lake Erie at the 21-h time and a clear surface wind divergent pattern accompanying a spurious convective system cold pool appeared at the 30-h time.

When the MRF PBL scheme was applied in lieu of the GSPBL scheme in Exp. MS3, MM5 produced worse precipitation patterns at both the 21-h and 30-h times. At 21 h the lack of precipitation in this southern Lake Erie region by Exp. MS3 was not consistent with the surface and satellite observations. The larger vertical mixing, even during the night, was apparently eliminating the precipitation in the Lake Erie region. At 30 h, Exp. MS3 produced a significantly worse simulation than Exp. MB2 in the model-simulated precipitation field because the spurious convection had spread to a much larger area, associated with an even larger area of disturbed flow with outflow boundaries and cold pools. Statistical evaluation indicated that Exp. MS3 produced degraded model simulations in all fields including wind speed, wind direction, temperature and sea-level pressure. The only improvement (mainly during night time) was in the water vapor mixing ratio field and was likely caused by the overestimation of the PBL depth. Based on the findings in this research, the MRF PBL scheme should not be considered an attractive scheme for representing boundary layer structure in the MM5.

Use of mixed-phase microphysics (Exp. MS4) produced a precipitation pattern that showed enhanced and more localized precipitation at both times. At 30 h, accompanying the more intense precipitation in northwestern PA was a divergent pattern evident in the simulated surface wind field, and associated with a cold pool in the surface temperature field. The *MAE* error analysis indicated that use of mixed-phase microphysics had some improvements over Exp. MB2 for model-simulated wind speed, temperature, water vapor mixing ratio and sea-level pressure.

When the new Kain-Fritsch scheme was applied to the 4-km grid in Exp. MS5, the model-simulated non-convective rain produced by the explicit microphysics was significantly reduced and therefore improved. The convective scheme as hypothesized appeared to release some of the CAPE so that the explicit scheme response was now much weaker. The convective scheme produced light or no precipitation in northwestern PA (at 30 h) where none was observed and grid-point type storms had developed in all of the other experiments. Thus the total precipitation was also generally much lighter than that of the other experiments in this region. Adding mixed phase to Kain Fritsch (KF2) on the 4-km domain in Exp. MS5.1 produced somewhat larger local maxima and a more concentrated explicit pattern. Statistical score comparisons with the baseline experiment, MB2, indicated that use of KF2 on the 4-km domain had produced some improvements for the model-simulated fields of wind speed, temperature, water vapor mixing ratio and sea-level pressure.

Several experiments (e.g., Exps. MS6) using enhanced horizontal diffusion suggested that use of larger horizontal diffusion alone as a solution to this grid-point storm problem was largely ineffective because it had very little effect on the model-simulated precipitation at 21 h. In fact, two of the enhanced diffusion experiments produced even stronger grid-point storms at this time. The statistical results showed a relatively small impact from the use of the different enhanced diffusion strategies overall, and although increased horizontal diffusion may show some advantage at certain times such as at 30 h with the spurious precipitation, it can adversely affect the model's ability to produce important mesoscale structures and cannot be considered a general solution.

Combining KF2 and observation nudging FDDA on the 4-km domain in Exp. MS7 produced the best overall results in both the subjective and statistical evaluations. It produced the largest reduction (50 percent) in the total maximum precipitation for the Lake Erie region grid-point storm at 21 h, and it did not produce the spurious mesoscale convective system at 30 h which allowed the simulated low-level flow at this time to be consistent with the observations.

Thus, use of the combination of observation nudging and the new Kain-Fritsch cumulus convection parameterization on the 4-km domain seemed to have the most significant positive impact on the model solutions on the 4-km grid in this CAPTEX '83 case.

6.2 Limitations of the Study and Future Work

However, it must be pointed out that use of a convective sub-grid physics scheme such as Kain Fritsch (KF2) at 4-km resolution for deep (precipitating) convection violates the underlying assumption that the size of the updraft being parameterized is much smaller than the grid size. However, its shallow convective parameterization should still be valid (Deng et al. 2003). It is also clear that in general, explicit microphysics alone cannot completely represent deep convection on these 4-km grid scales and some type of parameterization is needed. Since there is no readily identifiable approach to do this, this presents a serious dilemma when using 4-km grids to simulate deep convective environments. The results presented here show that use of KF2 on the 4-km grid may still be helpful in these situations where 4-km resolution is desired and explicit microphysics alone produces grossly unrealistic QPF.

Note that this is only one case study, but this case is representative of mid-latitude frontal rain and deep convection cases, so these results should be generally representative of other cases. Additional cases are still needed to determine the general added value of this approach. Also, additional sensitivity experiments should be performed to assess the respective roles of alternate turbulence and convective parameterizations. For example, additional experiments to be performed before publication of these results should include Grell convective parameterization with the GSPBL, and Grell convection coupled to the MRF PBL (a common MM5 physics combination). Furthermore, these findings should be investigated using a different mesoscale model, such as the new Weather Research and Forecast (WRF) model.

For Phase 2 of this study in year 2 of the project, some of the conclusions reported here regarding 4-km resolution model simulations, QPF and its potentially adverse effects on the wind and mass fields will be re-tested for this CAPTEX ’83 case using the new mass vertical coordinate core of the Weather Research and Forecast (WRF) model which offers improved numerics and mass conservation.

Appendix: A List of Statistical Measures Used in This Study

1). Mean Error (*ME*)

$$ME = \left[\sum_{n=1}^{N} (\alpha_n - \alpha_n^{\ O}) \right] \Big/ N \tag{1}$$

2). Mean Absolute Error (*MAE*)

$$MAE = \left[\sum_{n=1}^{N} \left| \alpha_n - \alpha_n^{\ O} \right| \right] \Big/ N \tag{2}$$

3). Root Mean Square Error (*RMSE*)

$$RMSE = \left[\frac{1}{N} \sum_{n=1}^{N} (\alpha_n - \alpha_n^{\ O})^2 \right]^{1/2} \tag{3}$$

4). Index of agreement (*I*) (Willmott 1982, Willmott et al. 1985).

$$I = 1 - \left[\sum_{n=1}^{N} (\alpha_n - \alpha_n^{\ O})^2 \Big/ \sum_{n=1}^{N} (|\alpha_n^{'}| + |\alpha_n^{'\ O}|)^2 \right], \qquad 0 \le I \le 1 \tag{4}$$

5). Threshold Percentage (*TRP*)

$$TRP = [N_T / N] X100 \tag{5}$$

Note, for (1), (2) and (3) $\alpha_n^{\ O}$ is the n^{th} observation of some scalar variable α, N is the total number of observations on the verification domain, and α_n is the model field for variable α interpolated to the observation site. For (4), $\alpha_n^{'} = (\alpha_n - \overline{\alpha})$, $\alpha_n^{'\ O} = (\alpha_n^{\ O} - \overline{\alpha})$, and $\overline{\alpha}$ is the mean of the observations on the verification domain. For (5), N_T is the total number of points on the domain for which $(\alpha_n - \alpha_n^{\ O}) \le TR_\alpha$ and where TR_α is a specified critical threshold for the variable α.

REFERENCES

Arakawa, A., and V.R. Lamb, 1977: Computational design of the basic dynamical process of the UCLA general circulation model. *Methods in Comp. Physics*, **17**, 173-265.

Barwell, B. R., and A. C. Lorenc, 1985: A study of the impact of aircraft wind observations on a large-scale analysis and numerical weather prediction system. *Quarterly Journal of the Royal Meteorological Society*, **111**, 103-129.

Benjamin, S.G. and N.L. Seaman, 1985: A Simple Scheme for Objective Analysis in Curved Flow. *Mon. Wea. Rev*., **113**, 1184-1198.

Bryan, G., 2002: An investigation of the convective region of numerically simulated squall lines. Ph.D. dissertation, The Pennsylvania State University, 181 pp.

Deng, A, N.L. Seaman and J.S. Kain, 2003: A shallow-convection parameterization for mesoscale models Part I: Sub-model description and preliminary applications. *J. Atmos. Sci*., **60**, 34-56.

Deng, A, N.L. Seaman, G.K. Hunter and D.R. Stauffer, 2004: Evaluation of inter-regional transport using the MM5/SCIPUFF system. Submitted to *J. Appl. Meteor*., 29 pp.

Dudhia, J., 1989: Numerical study of convection observed during the Winter Monsoon Experiment using a mesoscale two-dimensional model. *J. Atmos. Sci*., **46**, 3077-3107.

Dudhia, J., 1993: A nonhydrostatic version of the Penn State/NCAR mesoscale model: Validation tests and simulation of an Atlantic cyclone and cold front. *Mon. Wea. Rev.,* **121,** 1493-1513.

ENVIRON, 2002: Photochemical Modeling Study of the July 1995 NARSTO-Northeast Episode. *Final report for CRC Projects A-24 and A-35A*. 35 pp.

Gayno, G.A., N.L. Seaman, A.M. Lario, and D.R. Stauffer, 1994: Forecasting visibility using a 1.5-order closure boundary layer scheme in a 12-km non-hydrostatic model. 10th AMS Conf. on Num. Wea. Pred., Portland, OR, 18-22 July, 18-20.

Grell, G. A., J. Dudhia and D. R. Stauffer, 1994: A description of the fifth generation Penn State/NCAR mesoscale model (MM5). NCAR Tech. Note NCAR/TN-398+STR, 138 pp. [Available from NCAR Information Support Services, P.O. Box 3000, Boulder, CO 80397]

Hong, S.-Y., H.-L. Pan, 1996: Nonlocal boundary vertical diffusion in a medium-range forecast model. *Mon. Wea. Rev*., **124**, 2322-2339

Kain, J. S. and J. M. Fritsch, 1990: A one-dimensional entraining/detraining plume model and its application in convective parameterization. *J. Atmos. Sci*., **47**, 2784–2802.

Kain, J.S. and J.M. Fritsch, 1993: Convective parameterization for mesoscale models: The Kain-Fritsch scheme. The Representation of cumulus in numerical models. K. A. Emanuel and D. J. Raymond, eds, Meteorological Monographs. Amer. Meteor. Soc., 165-170.

Kain, J. S., 2004: The Kain-Fritsch convective parameterization: An update. *J. Appl. Meteor.*, **43**, 170–181.

Klemp, J.B., W.C. Skamarock and O. Fuhrer, 2003: Numerical consistency of metric terms in terrain-following coordinates. *Mon. Wea. Rev*. **131**, 1229–1239.

Lyons, W. A., C. J. Tremback, and R. A. Pielke, 1995: Applications of the Regional Atmospheric Modeling System (RAMS) to provide input to photochemical grid models for the Lake Michigan Ozone Study (LMOS). *J. Appl. Meteor*., **34**, 1762-1784.

Mass, C. F., D. Owens, K. Westrick and B. A. Colle, 2002: Does increasing the horizontal resolution produce more skillful forecasts? Bull. Amer. Meteor. Soc., March 2002, 407-430.

Michelson, S.A. and N.L. Seaman, 2000: Assimilation of NEXRAD-VAD Winds in Meteorological Simulations over the Northeast U.S. *J. Appl. Meteor*., **39**, 367-383.

Mlawer, E. J., S. J. Taubman, P. D. Brown, M. J. Iacono, and S. A. Clough, 1997: Radiative transfer for inhomogeneous atmosphere: RRTM, a validated correlated-k model for the longwave. *J. of Geophys. Res*., **102** (D14), 16663-16682.

Moeng, C.-H., and J.C. Wyngaard, 1989: Evaluation of turbulent transport and dissipation closures in second-order modeling. *J. Atmos. Sci*., **46**, 2311-2330.

Molinari, J. and M. Dudek, 1992: Parameterization of convective precipitation in mesoscale numerical models: A critical review. *Mon. Wea. Rev*., **120**, 326-344.

Reisner, J., R. M. Rasmussen, and R. T. Bruintjes, 1998: Explicit forecasting of supercooled liquid water in winter storms using the MM5 mesoscale model. *Quart. J. Roy. Metero. Soc.*, **124** B, 1071-1107.

Schroeder, A. J., 2002: Evaluation and testing of a high-resolution, rapidly relocatable meteorological nowcasting and prediction system. M.S. thesis, The Pennsylvania State University, 187 pp.

Seaman, N.L., D.R. Stauffer and A.M. Lario-Gibbs, 1995: A multi-scale four-dimensional data assimilation system applied in the San Joaquin valley during SARMAP: Part I: Modeling design and basic performance characteristics. *J. Appl. Meteor*., **34**, 1739-1761.

Seaman, N. L., A. Deng, G. K. Hunter and D. R. Stauffer, 2002: Evaluation of a regional model for interregional transport. Final report for CRC Contract No. A-28. 216 pp.

Shafran, P.C., N.L. Seaman and G.A. Gayno, 2000: Evaluation of Numerical Predictions of Boundary-Layer Structure during the Lake Michigan Ozone Study (LMOS). *J. Appl. Meteor*., **39**, 412-426.

Smagorinsky, J., S. Manabe and J.L. Holloway, Jr., 1965: Numerical results from a nine-level general circulation model of the atmosphere. *Mon. Wea. Rev*., **93**, 727-768.

Stauffer, D.R. and N.L. Seaman, 1990: Use of Four-Dimensional Data Assimilation in a Limited-Area Mesoscale Model. Part I: Experiments with Synoptic-Scale Data. *Mon. Wea. Rev*., **118**, 1250-1277.

Stauffer, D.R., N.L. Seaman and F.S. Binkowski, 1991: Use of four-dimensional data assimilation in a limited-area mesoscale model. Part II: Effects of data assimilation within the planetary boundary layer. *Mon. Wea. Rev*., 119, 734-754.

Stauffer, D.R. and N.L. Seaman, 1994: On Multi-Scale Four-Dimensional Data Assimilation. *J. Appl. Meteor*., **33**, 416-434.

Stauffer, D.R., R.C. Munoz, and N.L. Seaman, 1999: In-cloud turbulence and explicit microphysics in the MM5. 9th PSU/NCAR Mesoscale Model Users' Workshop. Boulder, CO, 23-25 June, 177-180.

Tao, W., D. Starr, A, Hou, P. Newman, and Y. Sud, 2002: Summary of cumulus parameterization workshop. Submitted to Bull. *Amer. Meteor. Soc.* 30pp.

Weisman, M. L., W. C. Skamarock and J. B. Klemp, 1997: The resolution dependence of explicitly modeled convective systems. *Mon. Wea. Rev*., **125**, 527-548.

Wicker, L.J. and W.C. Skamarock, 2002: Time-splitting methods for elastic models using forward time schemes. *Mon. Wea. Rev.,* **130**, 2088–2097.

Willmott, C.J., 1982: Some comments on the evaluation of model performance. *Bull. Amer. Meteor. Soc*., **63**, 1309-1313.

Willmott, C.J., S.G. Ackleson, R.E. Davis, J.J. Feddema, K.M. Klink, D.R. Legates, J. O'Donnell, and C.M. Rowe, 1985: Statistics for the evaluation and comparison of models. *J. of Geophys. Res*., **90**, 8995-9005.

Table 1. Summary of analysis-nudging coefficients (s^{-1}). Note that 12-hourly 3D analysis nudging of all variables is set to zero in the lowest 2 km AGL and that 3-hourly surface analysis nudging using surface-layer wind corrections is applied within the model-diagnosed PBL. See Section 3.3.1 for details.

MM5 Domain	108 km	36 km	12 km	4km
Wind	$2.5 \cdot 10^{-4}$	$2.5 \cdot 10^{-4}$	$1.0 \cdot 10^{-4}$	$1.0 \cdot 10^{-4}$
Temperature	$2.5 \cdot 10^{-4}$	$2.5 \cdot 10^{-4}$	$1.0 \cdot 10^{-4}$	$1.0 \cdot 10^{-4}$
Moisture	$1.0 \cdot 10^{-5}$	$1.0 \cdot 10^{-5}$	$1.0 \cdot 10^{-5}$	$1.0 \cdot 10^{-5}$

Table 2. Vertical distribution of σ levels (half layers) and model-layer heights (m AGL) for all four domains.

Layer	σ	**Height (m)**
32	0.996	28.9
31	0.988	85.9
30	0.980	143.3
29	0.972	201.0
28	0.964	259.0
27	0.955	324.7
26	0.945	398.3
25	0.935	472.4
24	0.925	547.0
23	0.915	622.3
22	0.900	736.3
21	0.880	890.4
20	0.860	1047.1
19	0.840	1206.4
18	0.820	1368.3
17	0.800	1533.1
16	0.780	1700.8
15	0.760	1871.6
14	0.730	2133.7
13	0.690	2494.9
12	0.650	2870.8
11	0.610	3262.7
10	0.570	3672.1
9	0.525	4156.0
8	0.475	4726.1
7	0.425	5335.4
6	0.375	5990.3
5	0.325	6699.2
4	0.275	7472.8
3	0.225	8325.9
2	0.150	9802.3
1	0.050	12347.4

Table 3. Summary of 4-km domain experimental design. CPS refers to the cumulus parameterization scheme with KF2 referring to the new Kain-Fritsch cumulus parameterization scheme. TKE PBL refers to the Gayno-Seaman PBL (GSPBL) scheme and MRF PBL is the version of the Hong-Pan PBL within the MM5. FDDA refers to four-dimensional data assimilation via analysis nudging or observation nudging. K_{H0} refers to the background horizontal diffusion coefficient; Def refers to the deformation term in the diffusion calculation. See text in Sections 3 and 4 for further details and references.

Exp. Name	**MM5 Physics on 4-km Domain**	**Enhanced Vertical Mixing on 4-km domain**	**Enhanced Horizontal Diffusion on 4-km domain**	**MM5 FDDA on 4-km domain Note: All experiments use FDDA Analysis Nudging on coarser domains**
MB1	TKE PBL, No CPS, RRTM radiation	None	None	No FDDA
MS1	Same as MB1	None	None	FDDA Analysis Nudging
MS1.1	Same as MB1	None	None	FDDA Observation Nudging
MS2 (MB2)	Same as MB1	Modified length scales in GS PBL	None	No FDDA
MS3	Same as MB2 except for MRF PBL	None	None	No FDDA
MS4	Same as MB2 except for Mixed phase	Same as MB2	None	No FDDA
MS5	Same as MB2 except for KF2 CPS	Same as MB2	None	No FDDA
MS5.1	Same as MS5 except for Mixed phase	Same as MB2	None	No FDDA
MS6	Same as MB2	Same as MB2	Double K_{H0}	No FDDA
MS6.1	Same as MB2	Same as MB2	Five times K_{H0}	No FDDA
MS6.2	Same as MB2	Same as MB2	Five times Def	No FDDA
MS6.3	Same as MB2	Same as MB2	Five times Def where it is raining	No FDDA
MS7	Same as MB2 except for KF2 CPS	Same as MB2	None	FDDA Observation Nudging

Table 4. Critical thresholds chosen for desired accuracy of meteorological variables.

Variable	**Critical Threshold,** TR_α
Wind Speed (ms^{-1})	2.0 ms^{-1} (surface & PBL) 2.5 ms^{-1} (1000-5000 m) 3.0 ms^{-1} (5000-10,000 m)
Wind Direction (deg.)	30 deg. (surface) 15 deg. (PBL) 10 deg. (layers above PBL)
Temperature (C)	2.0 C (all levels)
Water Vap. Mix. Ratio (g kg^{-1})	1.0 g kg^{-1} (below 5 km) 0.5 g kg^{-1} (above 5 km)
Sea-Level Pressure (hPa)	2.0 hPa

Table 5. Model-simulated maximum 3-h precipitation (mm) and maximum surface wind speed (m/s) over the precipitation region for 21 h (0900 UTC 19 September 1983) and model-simulated maximum 3-h precipitation (mm), minimum cold pool temperature and mesohigh pressure value associated with the precipitation pattern at 30 h (1800 UTC 19 September 1983) over the 4-km domain for each experiment.

Exp. No.	**3-h precip. (mm) at 21 h**	**Maximum surface wind speed (m/s) at 21 h**	**3-h precip. (mm) at 30 h**	**Cold pool temperature (ºC) at 30 h**	**Cold pool pressure (hPa) at 30 h**
MB1	108.0	23.0	66.5	17.0	1022
MS1	74.4	15.1	53.3	18.0	1019
MS1.1	78.5	20.0	21.9	18.5	1018
MS2 (MB2)	111.0	21.8	56.7	17.5	1020
MS3	0.0	17.3	51.7	16.1	1022
MS4	92.7	18.2	88.6	18.0	1020
MS5	62.0	16.9	3.9	N/A	N/A
MS5.1	69.2	19.2	4.6	N/A	N/A
MS6	123.0	19.6	23.6	19.3	1016
MS6.1	111.0	22.0	11.1	18.7	1018
MS6.2	94.0	22.0	22.3	17.9	1016
MS6.3	118.0	21.2	37.9	18.0	1016
MS7	55.0	14.2	11.7	N/A	N/A

Table 6. Statistical summary of MM5 performance for wind speed, wind direction, temperature, water vapor mixing ratio and sea-level pressure in CAPTEX-83 Episode 1 (1200 UTC, 18 September - 1800 UTC, 19 September 1983) on the 4-km domain of (a) EXP. MB1, (b) Exp. MS1, (c) Exp. MS1.1, (d) Exp. MS2 (MB2), (e) Exp. MS3, (f) Exp. MS4, (g) Exp. MS5, (h) Exp. MS5.1 (i) Exp. MS6, (j) Exp. MS6.1, (k) Exp. MS6.2, (l) Exp. MS6.3, (m) Exp. MS7.

(a) Exp. MB1

Wind Speed (ms^{-1})	RMSE (ms^{-1})	MAE (ms^{-1})	ME (ms^{-1})	I	TRP (%)
5000 - 10000 m AGL	3.75	3.12	-0.90	0.96	58.7
1000 - 5000 m AGL	3.96	3.11	-1.45	0.88	49.7
58 - 1000 m AGL	3.55	2.73	-0.28	0.74	51.3
Sfc. Layer (29 m AGL)	2.74	2.23	+0.97	0.63	49.1
Wind Direction (deg.)	RMSE (deg.)	MAE (deg.)	ME (deg.)		TRP (%)
5000 - 10000 m AGL	31.6	20.7	+4.4		42.0
1000 - 5000 m AGL	15.3	12.0	-1.4		52.9
58 - 1000 m AGL	21.1	14.9	-3.9		63.9
Sfc. Layer (29 m AGL)	49.3	34.3	-2.6		60.7
Temperature (C)	RMSE (C)	MAE (C)	ME (C)		TRP (%)
5000 - 10000 m AGL	1.00	0.80	+0.35		96.0
1000 - 5000 m AGL	1.04	0.85	-0.38		90.2
58 - 1000 m AGL	1.35	1.14	-0.29		86.2
Sfc. Layer (29 m AGL)	2.48	1.92	-0.38		62.5
Mixing Ratio ($g\ kg^{-1}$)	RMSE ($g\ kg^{-1}$)	MAE ($g\ kg^{-1}$)	ME ($g\ kg^{-1}$)		TRP (%)
5000 - 10000 m AGL	0.44	0.32	+0.18		77.3
1000 - 5000 m AGL	1.64	1.28	+0.35		48.3
58 - 1000 m AGL	2.25	1.79	+0.73		38.2
Sfc. Layer (29 m AGL)	1.75	1.35	+0.43		48.1
Pressure (hPa)	RMSE (hPa)	MAE (hPa)	ME (hPa)		TRP (%)
Sfc. Layer (29 m AGL)	1.20	0.94	-0.19		91.3

Table 6 (Continued)

(b) Exp. MS1

Wind Speed (ms^{-1})	RMSE (ms^{-1})	MAE (ms^{-1})	ME (ms^{-1})	I	TRP (%)
5000 - 10000 m AGL	2.36	1.94	-1.25	0.99	85.3
1000 - 5000 m AGL	2.39	1.88	-1.27	0.95	72.8
58 - 1000 m AGL	3.45	2.76	-0.31	0.75	51.0
Sfc. Layer (29 m AGL)	2.26	1.85	+0.70	0.69	60.6
Wind Direction (deg.)	**RMSE (deg.)**	**MAE (deg.)**	**ME (deg.)**		**TRP (%)**
5000 - 10000 m AGL	14.5	10.6	+4.3		67.1
1000 - 5000 m AGL	11.1	8.8	+0.4		65.1
58 - 1000 m AGL	16.7	12.7	-3.1		68.8
Sfc. Layer (29 m AGL)	40.1	28.0	-2.5		66.2
Temperature (C)	**RMSE (C)**	**MAE (C)**	**ME (C)**		**TRP (%)**
5000 - 10000 m AGL	0.69	0.56	+0.22		100.0
1000 - 5000 m AGL	0.81	0.64	-0.21		94.8
58 - 1000 m AGL	1.43	1.17	-0.43		84.0
Sfc. Layer (29 m AGL)	2.43	1.86	-0.24		63.6
Mixing Ratio ($g\ kg^{-1}$)	**RMSE ($g\ kg^{-1}$)**	**MAE ($g\ kg^{-1}$)**	**ME ($g\ kg^{-1}$)**		**TRP (%)**
5000 - 10000 m AGL	0.42	0.31	+0.22		77.3
1000 - 5000 m AGL	1.56	1.27	+0.41		43.1
58 - 1000 m AGL	2.05	1.55	+0.75		45.8
Sfc. Layer (29 m AGL)	1.72	1.30	+0.37		51.0
Pressure (hPa)	**RMSE (hPa)**	**MAE (hPa)**	**ME (hPa)**		**TRP (%)**
Sfc. Layer (29 m AGL)	1.15	0.92	-0.31		93.7

Table 6 (Continued)

(c) MS1.1

Wind Speed (ms^{-1})	RMSE (ms^{-1})	MAE (ms^{-1})	ME (ms^{-1})	I	TRP (%)
5000 - 10000 m AGL	1.82	1.44	-0.71	0.99	90.9
1000 - 5000 m AGL	2.03	1.48	-0.71	0.97	80.4
58 - 1000 m AGL	1.77	1.35	-0.01	0.92	78.7
Sfc. Layer (29 m AGL)	2.08	1.65	+0.52	0.75	66.0
Wind Direction (deg.)	**RMSE (deg.)**	**MAE (deg.)**	**ME (deg.)**		**TRP (%)**
5000 - 10000 m AGL	15.1	8.8	-0.5		80.4
1000 - 5000 m AGL	6.6	5.4	-1.0		91.0
58 - 1000 m AGL	10.9	8.0	-1.9		81.7
Sfc. Layer (29 m AGL)	36.3	25.1	-1.9		70.9
Temperature (C)	**RMSE (C)**	**MAE (C)**	**ME (C)**		**TRP (%)**
5000 - 10000 m AGL	0.62	0.50	+0.29		98.7
1000 - 5000 m AGL	0.64	0.50	-0.24		97.8
58 - 1000 m AGL	0.88	0.67	-0.38		96.0
Sfc. Layer (29 m AGL)	2.44	1.88	-0.25		64.0
Mixing Ratio ($g\ kg^{-1}$)	**RMSE ($g\ kg^{-1}$)**	**MAE ($g\ kg^{-1}$)**	**ME ($g\ kg^{-1}$)**		**TRP (%)**
5000 - 10000 m AGL	0.20	0.13	+0.08		92.7
1000 - 5000 m AGL	0.64	0.48	+0.13		85.2
58 - 1000 m AGL	1.11	0.83	+0.48		70.5
Sfc. Layer (29 m AGL)	1.68	1.29	+0.33		50.5
Pressure (hPa)	**RMSE (hPa)**	**MAE (hPa)**	**ME (hPa)**		**TRP (%)**
Sfc. Layer (29 m AGL)	1.16	0.91	-0.23		92.8

Table 6 (Continued)

(d) Exp. MB2

Wind Speed (ms^{-1})	RMSE (ms^{-1})	MAE (ms^{-1})	ME (ms^{-1})	I	TRP (%)
5000 - 10000 m AGL	3.42	2.85	-1.25	0.97	59.4
1000 - 5000 m AGL	4.07	3.13	-1.70	0.87	53.2
58 - 1000 m AGL	3.03	2.44	-0.52	0.79	49.4
Sfc. Layer (29 m AGL)	2.86	2.31	+1.18	0.62	49.4
Wind Direction (deg.)	**RMSE (deg.)**	**MAE (deg.)**	**ME (deg.)**		**TRP (%)**
5000 - 10000 m AGL	33.8	22.2	+4.3		42.7
1000 - 5000 m AGL	14.7	11.9	-1.8		48.1
58 - 1000 m AGL	14.4	11.3	-1.5		73.8
Sfc. Layer (29 m AGL)	45.3	32.3	+1.6		62.0
Temperature (C)	**RMSE (C)**	**MAE (C)**	**ME (C)**		**TRP (%)**
5000 - 10000 m AGL	1.02	0.82	+0.35		94.7
1000 - 5000 m AGL	1.14	0.93	-0.39		88.9
58 - 1000 m AGL	1.48	1.19	-0.36		85.1
Sfc. Layer (29 m AGL)	2.44	1.91	-0.29		61.8
Mixing Ratio ($g\ kg^{-1}$)	**RMSE ($g\ kg^{-1}$)**	**MAE ($g\ kg^{-1}$)**	**ME ($g\ kg^{-1}$)**		**TRP (%)**
5000 - 10000 m AGL	0.41	0.31	+0.17		77.3
1000 - 5000 m AGL	1.74	1.35	+0.37		46.5
58 - 1000 m AGL	2.07	1.56	+0.78		44.7
Sfc. Layer (29 m AGL)	1.73	1.34	+0.29		48.0
Pressure (hPa)	**RMSE (hPa)**	**MAE (hPa)**	**ME (hPa)**		**TRP (%)**
Sfc. Layer (29 m AGL)	1.21	0.97	-0.28		92.2

Table 6 (Continued)

(e) Exp. MS3

Wind Speed (ms^{-1})	RMSE (ms^{-1})	MAE (ms^{-1})	ME (ms^{-1})	I	TRP (%)
5000 - 10000 m AGL	3.89	3.24	-1.71	0.96	56.6
1000 - 5000 m AGL	4.13	3.17	-1.89	0.87	52.2
58 - 1000 m AGL	3.11	2.58	-0.78	0.80	49.8
Sfc. Layer (29 m AGL)	2.64	2.19	+1.18	0.65	51.2
Wind Direction (deg.)	**RMSE (deg.)**	**MAE (deg.)**	**ME (deg.)**		**TRP (%)**
5000 - 10000 m AGL	28.7	19.4	+2.2		46.2
1000 - 5000 m AGL	14.9	11.8	-0.5		52.2
58 - 1000 m AGL	21.4	17.2	-1.2		50.2
Sfc. Layer (29 m AGL)	48.5	34.4	+3.8		58.9
Temperature (C)	**RMSE (C)**	**MAE (C)**	**ME (C)**		**TRP (%)**
5000 - 10000 m AGL	0.96	0.75	+0.36		95.3
1000 - 5000 m AGL	1.21	0.95	-0.40		87.4
58 - 1000 m AGL	1.44	1.19	-0.16		86.2
Sfc. Layer (29 m AGL)	2.56	2.02	-0.10		59.4
Mixing Ratio ($g\ kg^{-1}$)	**RMSE ($g\ kg^{-1}$)**	**MAE ($g\ kg^{-1}$)**	**ME ($g\ kg^{-1}$)**		**TRP (%)**
5000 - 10000 m AGL	0.43	0.33	+0.18		76.0
1000 - 5000 m AGL	1.64	1.23	+0.40		54.5
58 - 1000 m AGL	1.85	1.24	+0.29		62.9
Sfc. Layer (29 m AGL)	1.75	1.38	-0.20		46.5
Pressure (hPa)	**RMSE (hPa)**	**MAE (hPa)**	**ME (hPa)**		**TRP (%)**
Sfc. Layer (29 m AGL)	1.34	1.10	-0.42		86.6

Table 6 (Continued)

(f) Exp. MS4

Wind Speed (ms^{-1})	RMSE (ms^{-1})	MAE (ms^{-1})	ME (ms^{-1})	I	TRP (%)
5000 - 10000 m AGL	3.66	2.91	-1.62	0.96	62.2
1000 - 5000 m AGL	4.00	3.05	-1.60	0.88	52.6
58 - 1000 m AGL	2.86	2.36	-0.38	0.81	48.7
Sfc. Layer (29 m AGL)	2.72	2.23	+1.16	0.63	50.5
Wind Direction (deg.)	**RMSE (deg.)**	**MAE (deg.)**	**ME (deg.)**		**TRP (%)**
5000 - 10000 m AGL	30.1	19.6	+7.9		41.3
1000 - 5000 m AGL	14.9	11.8	-3.3		49.7
58 - 1000 m AGL	15.2	11.7	-2.4		68.4
Sfc. Layer (29 m AGL)	43.8	31.1	+1.5		63.1
Temperature (C)	**RMSE (C)**	**MAE (C)**	**ME (C)**		**TRP (%)**
5000 - 10000 m AGL	0.95	0.75	+0.30		96.7
1000 - 5000 m AGL	1.09	0.88	-0.29		88.9
58 - 1000 m AGL	1.41	1.17	-0.33		84.7
Sfc. Layer (29 m AGL)	2.37	1.84	-0.20		63.0
Mixing Ratio ($g\ kg^{-1}$)	**RMSE ($g\ kg^{-1}$)**	**MAE ($g\ kg^{-1}$)**	**ME ($g\ kg^{-1}$)**		**TRP (%)**
5000 - 10000 m AGL	0.44	0.32	+0.15		78.7
1000 - 5000 m AGL	1.72	1.31	+0.37		51.7
58 - 1000 m AGL	1.99	1.44	+0.84		50.2
Sfc. Layer (29 m AGL)	1.72	1.33	+0.36		49.1
Pressure (hPa)	**RMSE (hPa)**	**MAE (hPa)**	**ME (hPa)**		**TRP (%)**
Sfc. Layer (29 m AGL)	1.22	1.00	-0.40		91.1

Table 6 (Continued)

(g) Exp. MS5

Wind Speed (ms^{-1})	RMSE (ms^{-1})	MAE (ms^{-1})	ME (ms^{-1})	I	TRP (%)
5000 - 10000 m AGL	3.39	2.81	-1.54	0.97	63.6
1000 - 5000 m AGL	4.18	3.20	-1.59	0.86	49.4
58 - 1000 m AGL	3.02	2.38	-0.24	0.78	54.0
Sfc. Layer (29 m AGL)	2.83	2.30	+1.23	0.63	50.0
Wind Direction (deg.)	**RMSE (deg.)**	**MAE (deg.)**	**ME (deg.)**		**TRP (%)**
5000 - 10000 m AGL	32.4	21.5	+8.6		43.4
1000 - 5000 m AGL	14.4	11.7	-2.2		49.0
58 - 1000 m AGL	14.7	12.2	-3.8		65.4
Sfc. Layer (29 m AGL)	44.1	30.9	+1.3		64.7
Temperature (C)	**RMSE (C)**	**MAE (C)**	**ME (C)**		**TRP (%)**
5000 - 10000 m AGL	1.07	0.83	+0.41		94.7
1000 - 5000 m AGL	1.02	0.81	-0.21		90.2
58 - 1000 m AGL	1.37	1.15	-0.32		85.8
Sfc. Layer (29 m AGL)	2.39	1.87	-0.25		63.0
Mixing Ratio ($g\ kg^{-1}$)	**RMSE ($g\ kg^{-1}$)**	**MAE ($g\ kg^{-1}$)**	**ME ($g\ kg^{-1}$)**		**TRP (%)**
5000 - 10000 m AGL	0.45	0.33	+0.19		75.3
1000 - 5000 m AGL	1.67	1.28	+0.32		50.5
58 - 1000 m AGL	2.04	1.54	+0.80		44.0
Sfc. Layer (29 m AGL)	1.70	1.32	+0.32		48.5
Pressure (hPa)	**RMSE (hPa)**	**MAE (hPa)**	**ME (hPa)**		**TRP (%)**
Sfc. Layer (29 m AGL)	1.23	1.00	-0.47		91.0

Table 6 (Continued)

(h) Exp. MS5.1

Wind Speed (ms^{-1})	RMSE (ms^{-1})	MAE (ms^{-1})	ME (ms^{-1})	I	TRP (%)
5000 - 10000 m AGL	3.47	2.82	-1.75	0.97	63.6
1000 - 5000 m AGL	4.15	3.18	-1.38	0.87	50.6
58 - 1000 m AGL	3.07	2.40	-0.17	0.77	55.5
Sfc. Layer (29 m AGL)	2.72	2.23	+1.22	0.64	50.9
Wind Direction (deg.)	RMSE (deg.)	MAE (deg.)	ME (deg.)		TRP (%)
5000 - 10000 m AGL	31.4	21.1	+8.5		43.4
1000 - 5000 m AGL	14.1	11.4	-2.5		50.3
58 - 1000 m AGL	16.2	12.4	-1.8		66.9
Sfc. Layer (29 m AGL)	43.9	31.1	+1.5		64.3
Temperature (C)	RMSE (C)	MAE (C)	ME (C)		TRP (%)
5000 - 10000 m AGL	0.97	0.76	+0.32		97.3
1000 - 5000 m AGL	1.03	0.82	-0.18		88.3
58 - 1000 m AGL	1.34	1.11	-0.21		88.7
Sfc. Layer (29 m AGL)	2.35	1.82	-0.18		64.2
Mixing Ratio ($g\ kg^{-1}$)	RMSE ($g\ kg^{-1}$)	MAE ($g\ kg^{-1}$)	ME ($g\ kg^{-1}$)		TRP (%)
5000 - 10000 m AGL	0.42	0.30	+0.16		78.0
1000 - 5000 m AGL	1.67	1.26	+0.34		51.1
58 - 1000 m AGL	2.05	1.53	+0.73		45.8
Sfc. Layer (29 m AGL)	1.70	1.32	+0.36		48.4
Pressure (hPa)	RMSE (hPa)	MAE (hPa)	ME (hPa)		TRP (%)
Sfc. Layer (29 m AGL)	1.23	1.00	-0.53		90.6

Table 6 (Continued)

(i) Exp. MS6

Wind Speed (ms^{-1})	RMSE (ms^{-1})	MAE (ms^{-1})	ME (ms^{-1})	I	TRP (%)
5000 - 10000 m AGL	3.48	2.87	-1.50	0.96	63.6
1000 - 5000 m AGL	4.16	3.12	-1.67	0.87	54.5
58 - 1000 m AGL	3.09	2.45	-0.34	0.78	52.9
Sfc. Layer (29 m AGL)	2.75	2.25	+1.15	0.64	50.7
Wind Direction (deg.)	**RMSE (deg.)**	**MAE (deg.)**	**ME (deg.)**		**TRP (%)**
5000 - 10000 m AGL	32.9	21.7	+8.4		41.3
1000 - 5000 m AGL	14.6	11.6	-1.8		53.2
58 - 1000 m AGL	14.8	11.6	-0.5		70.7
Sfc. Layer (29 m AGL)	45.0	31.8	+0.8		62.3
Temperature (C)	**RMSE (C)**	**MAE (C)**	**ME (C)**		**TRP (%)**
5000 - 10000 m AGL	1.02	0.81	+0.33		96.0
1000 - 5000 m AGL	1.07	0.86	-0.35		88.9
58 - 1000 m AGL	1.47	1.20	-0.32		84.4
Sfc. Layer (29 m AGL)	2.45	1.91	-0.27		61.8
Mixing Ratio ($g\ kg^{-1}$)	**RMSE ($g\ kg^{-1}$)**	**MAE ($g\ kg^{-1}$)**	**ME ($g\ kg^{-1}$)**		**TRP (%)**
5000 - 10000 m AGL	0.42	0.32	+0.17		76.7
1000 - 5000 m AGL	1.75	1.34	+0.41		50.2
58 - 1000 m AGL	2.10	1.55	+0.78		46.9
Sfc. Layer (29 m AGL)	1.72	1.34	+0.32		49.7
Pressure (hPa)	**RMSE (hPa)**	**MAE (hPa)**	**ME (hPa)**		**TRP (%)**
Sfc. Layer (29 m AGL)	1.22	0.98	-0.29		92.3

Table 6 (Continued)

(j) Exp. MS6.1

Wind Speed (ms^{-1})	RMSE (ms^{-1})	MAE (ms^{-1})	ME (ms^{-1})	I	TRP (%)
5000 - 10000 m AGL	3.37	2.71	-1.58	0.97	63.6
1000 - 5000 m AGL	4.06	3.02	-1.75	0.87	53.2
58 - 1000 m AGL	2.94	2.32	-0.28	0.79	52.9
Sfc. Layer (29 m AGL)	2.80	2.27	+1.17	0.63	50.5
Wind Direction (deg.)	**RMSE (deg.)**	**MAE (deg.)**	**ME (deg.)**		**TRP (%)**
5000 - 10000 m AGL	32.9	22.2	+9.1		41.3
1000 - 5000 m AGL	14.2	11.5	-2.6		49.0
58 - 1000 m AGL	14.0	11.7	-1.8		68.8
Sfc. Layer (29 m AGL)	45.6	32.3	+0.4		62.7
Temperature (C)	**RMSE (C)**	**MAE (C)**	**ME (C)**		**TRP (%)**
5000 - 10000 m AGL	1.04	0.83	+0.36		94.7
1000 - 5000 m AGL	1.07	0.86	-0.36		88.6
58 - 1000 m AGL	1.44	1.19	-0.31		86.5
Sfc. Layer (29 m AGL)	2.44	1.90	-0.24		62.1
Mixing Ratio ($g\ kg^{-1}$)	**RMSE ($g\ kg^{-1}$)**	**MAE ($g\ kg^{-1}$)**	**ME ($g\ kg^{-1}$)**		**TRP (%)**
5000 - 10000 m AGL	0.43	0.32	+0.17		77.3
1000 - 5000 m AGL	1.69	1.31	+0.33		49.8
58 - 1000 m AGL	2.04	1.51	+0.83		46.5
Sfc. Layer (29 m AGL)	1.71	1.33	+0.32		48.3
Pressure (hPa)	**RMSE (hPa)**	**MAE (hPa)**	**ME (hPa)**		**TRP (%)**
Sfc. Layer (29 m AGL)	1.19	0.95	-0.27		92.4

Table 6 (Continued)

(k) Exp. MS6.2

Wind Speed (ms^{-1})	RMSE (ms^{-1})	MAE (ms^{-1})	ME (ms^{-1})	I	TRP (%)
5000 - 10000 m AGL	3.52	2.90	-1.15	0.97	63.6
1000 - 5000 m AGL	4.14	3.16	-1.80	0.87	52.2
58 - 1000 m AGL	3.03	2.46	-0.42	0.78	51.7
Sfc. Layer (29 m AGL)	2.78	2.26	+1.14	0.63	48.5
Wind Direction (deg.)	**RMSE (deg.)**	**MAE (deg.)**	**ME (deg.)**		**TRP (%)**
5000 - 10000 m AGL	33.1	21.7	+8.9		43.4
1000 - 5000 m AGL	14.8	11.7	-2.7		51.3
58 - 1000 m AGL	14.4	11.0	-1.4		74.1
Sfc. Layer (29 m AGL)	44.3	31.7	+1.1		61.1
Temperature (C)	**RMSE (C)**	**MAE (C)**	**ME (C)**		**TRP (%)**
5000 - 10000 m AGL	0.98	0.79	+0.34		95.3
1000 - 5000 m AGL	1.11	0.89	-0.37		88.0
58 - 1000 m AGL	1.48	1.19	-0.38		86.2
Sfc. Layer (29 m AGL)	2.44	1.90	-0.27		62.7
Mixing Ratio ($g\ kg^{-1}$)	**RMSE ($g\ kg^{-1}$)**	**MAE ($g\ kg^{-1}$)**	**ME ($g\ kg^{-1}$)**		**TRP (%)**
5000 - 10000 m AGL	0.42	0.31	+0.16		76.7
1000 - 5000 m AGL	1.70	1.30	+0.37		49.5
58 - 1000 m AGL	2.06	1.53	+0.81		45.5
Sfc. Layer (29 m AGL)	1.72	1.33	+0.32		48.4
Pressure (hPa)	**RMSE (hPa)**	**MAE (hPa)**	**ME (hPa)**		**TRP (%)**
Sfc. Layer (29 m AGL)	1.20	0.97	-0.29		92.3

Table 6 (Continued)

(l) Exp. MS6.3

Wind Speed (ms^{-1})	RMSE (ms^{-1})	MAE (ms^{-1})	ME (ms^{-1})	I	TRP (%)
5000 - 10000 m AGL	3.54	2.93	-1.41	0.96	59.4
1000 - 5000 m AGL	4.36	3.29	-1.73	0.86	53.2
58 - 1000 m AGL	3.22	2.54	-0.43	0.77	49.8
Sfc. Layer (29 m AGL)	2.78	2.26	+1.15	0.63	49.3
Wind Direction (deg.)	**RMSE (deg.)**	**MAE (deg.)**	**ME (deg.)**		**TRP (%)**
5000 - 10000 m AGL	33.3	21.7	+4.4		42.7
1000 - 5000 m AGL	15.1	11.9	-2.6		51.9
58 - 1000 m AGL	15.6	11.9	-0.8		70.7
Sfc. Layer (29 m AGL)	44.8	31.7	+1.9		61.7
Temperature (C)	**RMSE (C)**	**MAE (C)**	**ME (C)**		**TRP (%)**
5000 - 10000 m AGL	0.99	0.79	+0.34		96.0
1000 - 5000 m AGL	1.09	0.88	-0.35		88.9
58 - 1000 m AGL	1.44	1.17	-0.38		84.7
Sfc. Layer (29 m AGL)	2.45	1.91	-0.28		62.1
Mixing Ratio ($g\ kg^{-1}$)	**RMSE ($g\ kg^{-1}$)**	**MAE ($g\ kg^{-1}$)**	**ME ($g\ kg^{-1}$)**		**TRP (%)**
5000 - 10000 m AGL	0.43	0.32	+0.17		77.3
1000 - 5000 m AGL	1.69	1.31	+0.37		49.5
58 - 1000 m AGL	2.06	1.55	+0.82		45.8
Sfc. Layer (29 m AGL)	1.72	1.34	+0.32		48.5
Pressure (hPa)	**RMSE (hPa)**	**MAE (hPa)**	**ME (hPa)**		**TRP (%)**
Sfc. Layer (29 m AGL)	1.20	0.97	-0.29		92.3

Table 6 (Continued)

(m) Exp. MS7

Wind Speed (ms^{-1})	RMSE (ms^{-1})	MAE (ms^{-1})	ME (ms^{-1})	I	TRP (%)
5000 - 10000 m AGL	1.71	1.34	-0.97	0.99	93.7
1000 - 5000 m AGL	1.84	1.36	-0.77	0.98	82.1
58 - 1000 m AGL	1.74	1.33	-0.07	0.92	73.4
Sfc. Layer (29 m AGL)	2.15	1.69	+0.74	0.76	66.7
Wind Direction (deg.)	**RMSE (deg.)**	**MAE (deg.)**	**ME (deg.)**		**TRP (%)**
5000 - 10000 m AGL	14.3	8.5	-1.4		83.0
1000 - 5000 m AGL	5.7	4.7	-1.5		92.0
58 - 1000 m AGL	7.7	6.0	-1.7		92.8
Sfc. Layer (29 m AGL)	33.6	23.4	+0.1		73.4
Temperature (C)	**RMSE (C)**	**MAE (C)**	**ME (C)**		**TRP (%)**
5000 - 10000 m AGL	0.60	0.48	+0.25		99.3
1000 - 5000 m AGL	0.52	0.42	-0.11		99.7
58 - 1000 m AGL	0.79	0.61	-0.18		98.2
Sfc. Layer (29 m AGL)	2.34	1.82	-0.10		63.5
Mixing Ratio ($g\ kg^{-1}$)	**RMSE ($g\ kg^{-1}$)**	**MAE ($g\ kg^{-1}$)**	**ME ($g\ kg^{-1}$)**		**TRP (%)**
5000 - 10000 m AGL	0.21	0.14	+0.08		92.0
1000 - 5000 m AGL	0.62	0.47	+0.10		86.2
58 - 1000 m AGL	0.92	0.64	+0.41		82.2
Sfc. Layer (29 m AGL)	1.64	1.27	+0.20		50.5
Pressure (hPa)	**RMSE (hPa)**	**MAE (hPa)**	**ME (hPa)**		**TRP (%)**
Sfc. Layer (29 m AGL)	1.21	0.98	-0.46		91.6

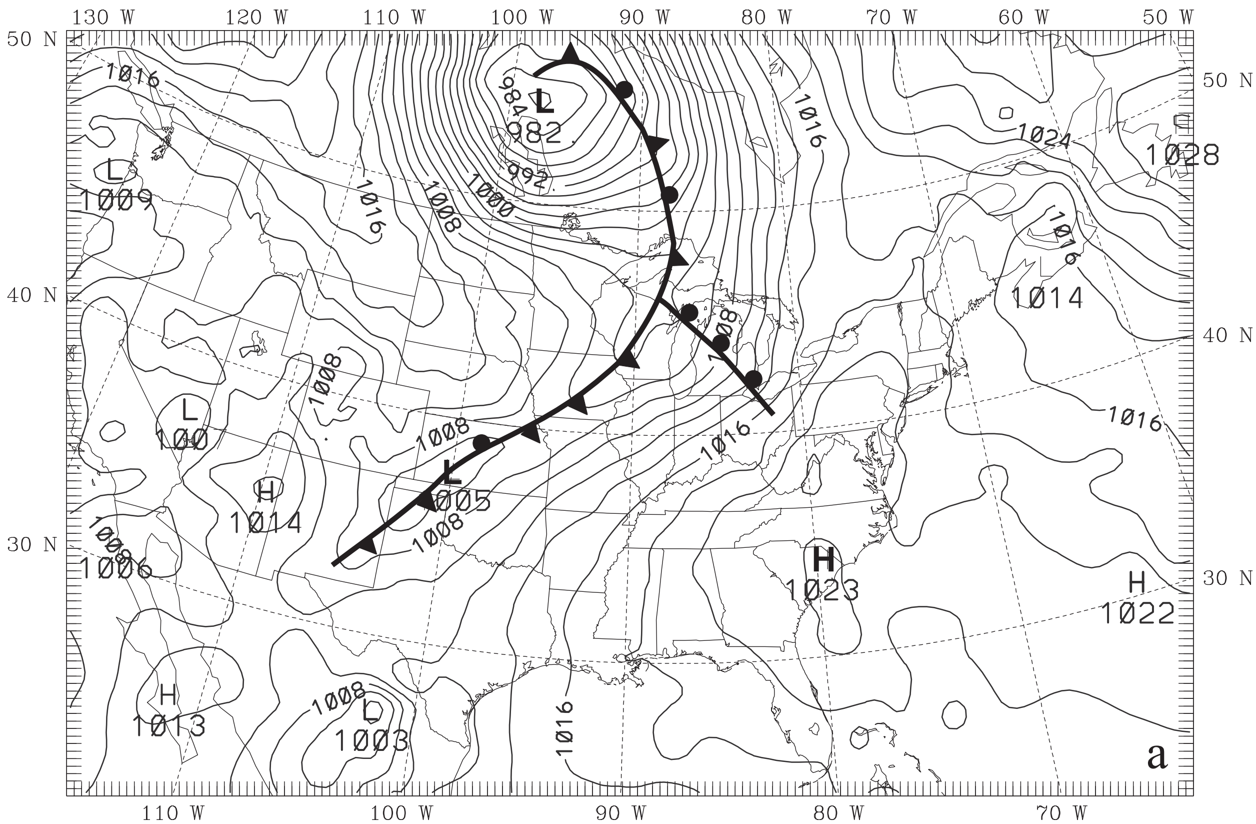

Figure 1. Objective analysis of sea-level pressure (hPa) for 1200 UTC, 18 September 1983. Isobar interval is 2 hPa. Grid resolution is 36 km.

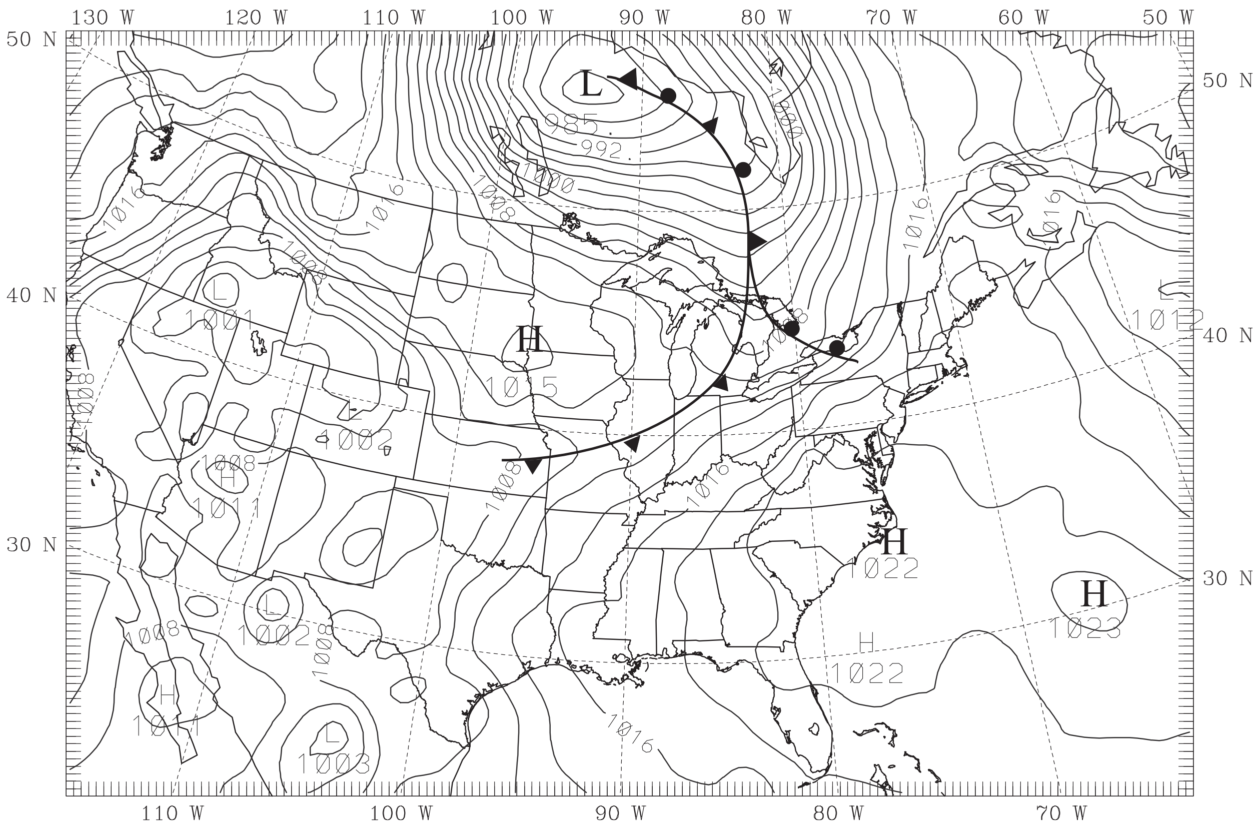

Figure 2. Objective analysis of sea-level pressure (hPa) for 0000 UTC, 19 September 1983. Isobar interval is 2 hPa. Grid resolution is 36 km.

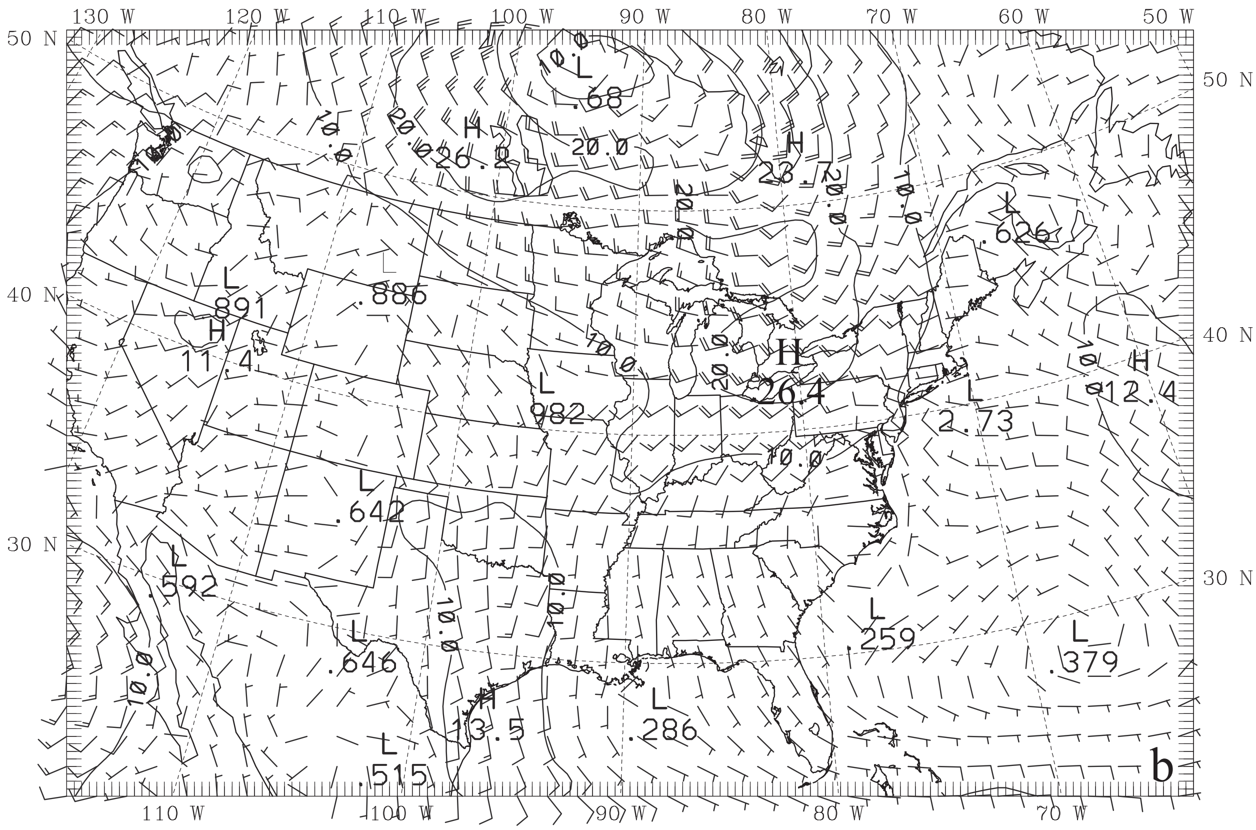

Figure 3. Objective analysis of 850-mb winds (m s^{-1}) for 0000 UTC, 19 September 1983. Isotach interval is 10 m s^{-1}. Grid resolution is 36 km.

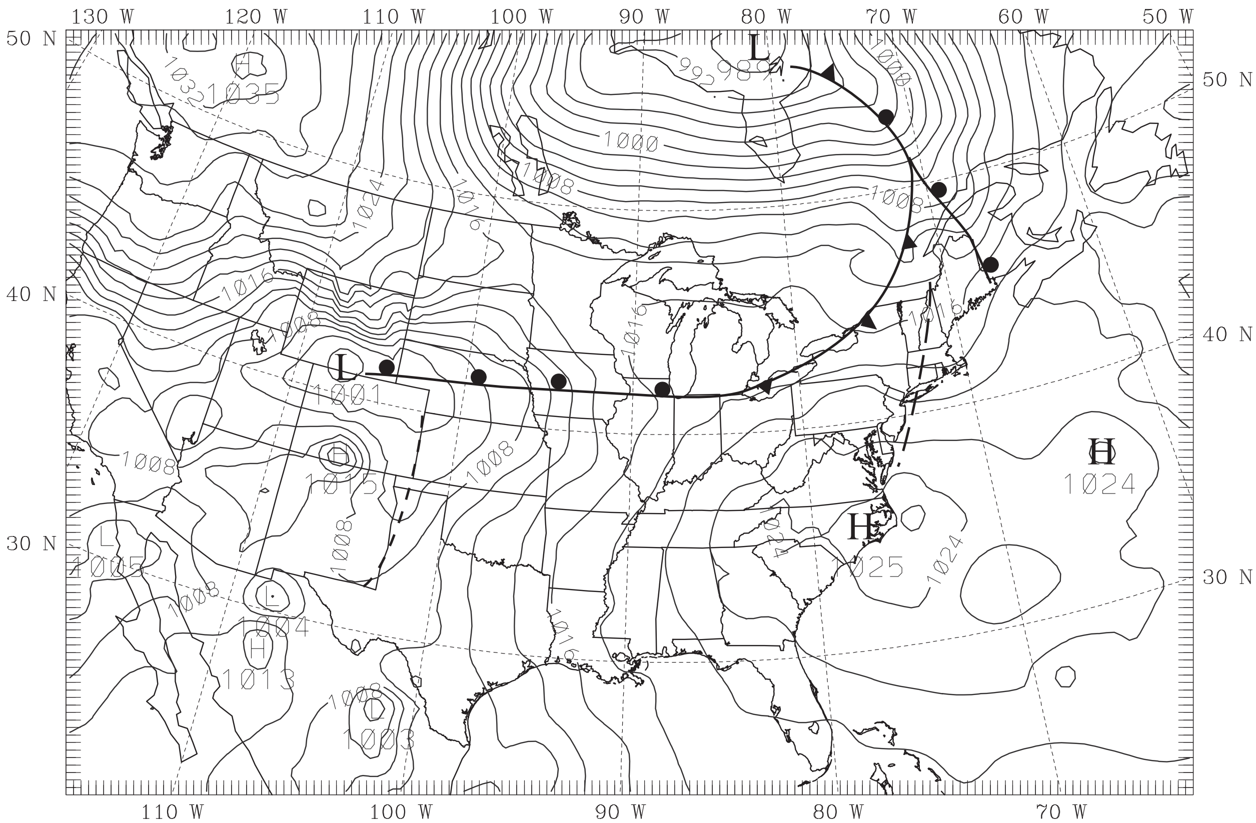

Figure 4. Objective analysis of sea-level pressure (hPa) for 1200 UTC, 19 September 1983. Isobar interval is 2 hPa. Grid resolution is 36 km.

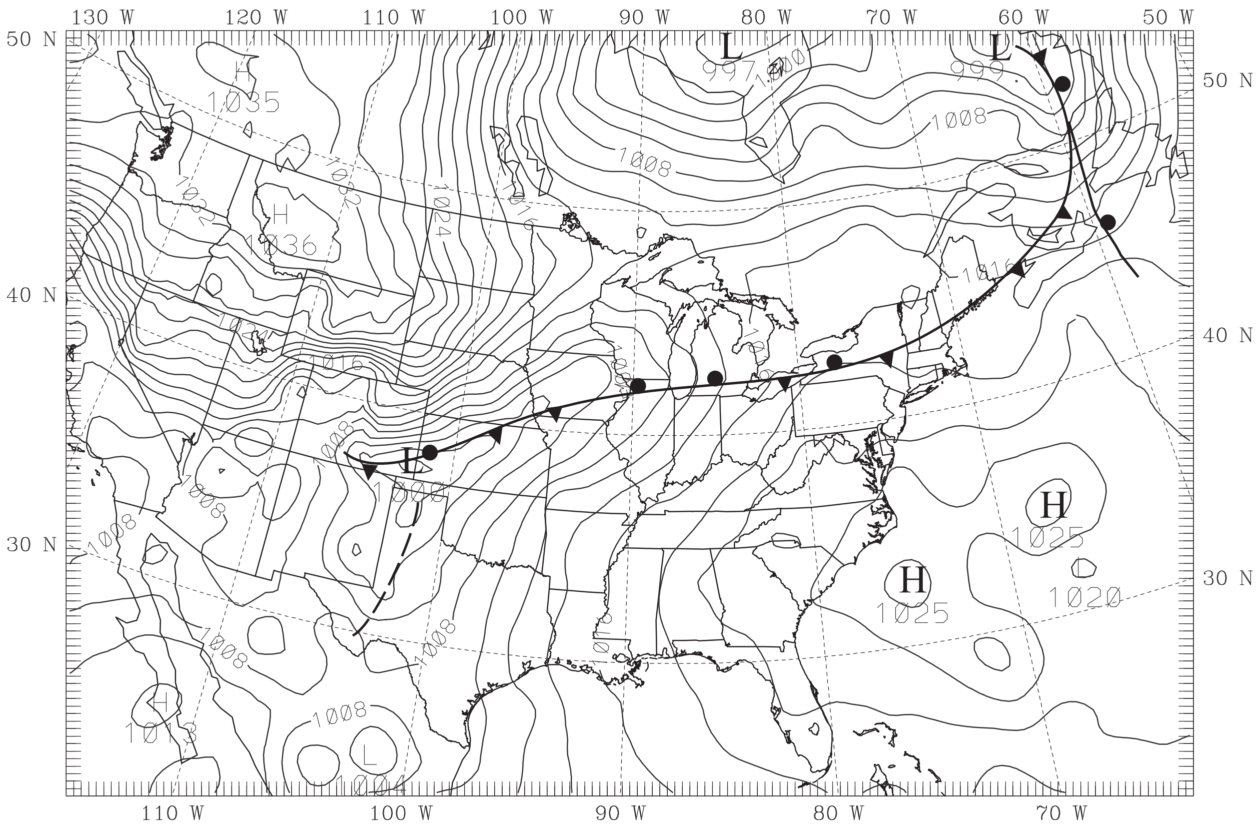

Figure 5. Objective analysis of sea-level pressure (hPa) for 0000 UTC, 20 September 1983. Isobar interval is 2 hPa. Grid resolution is 36 km.

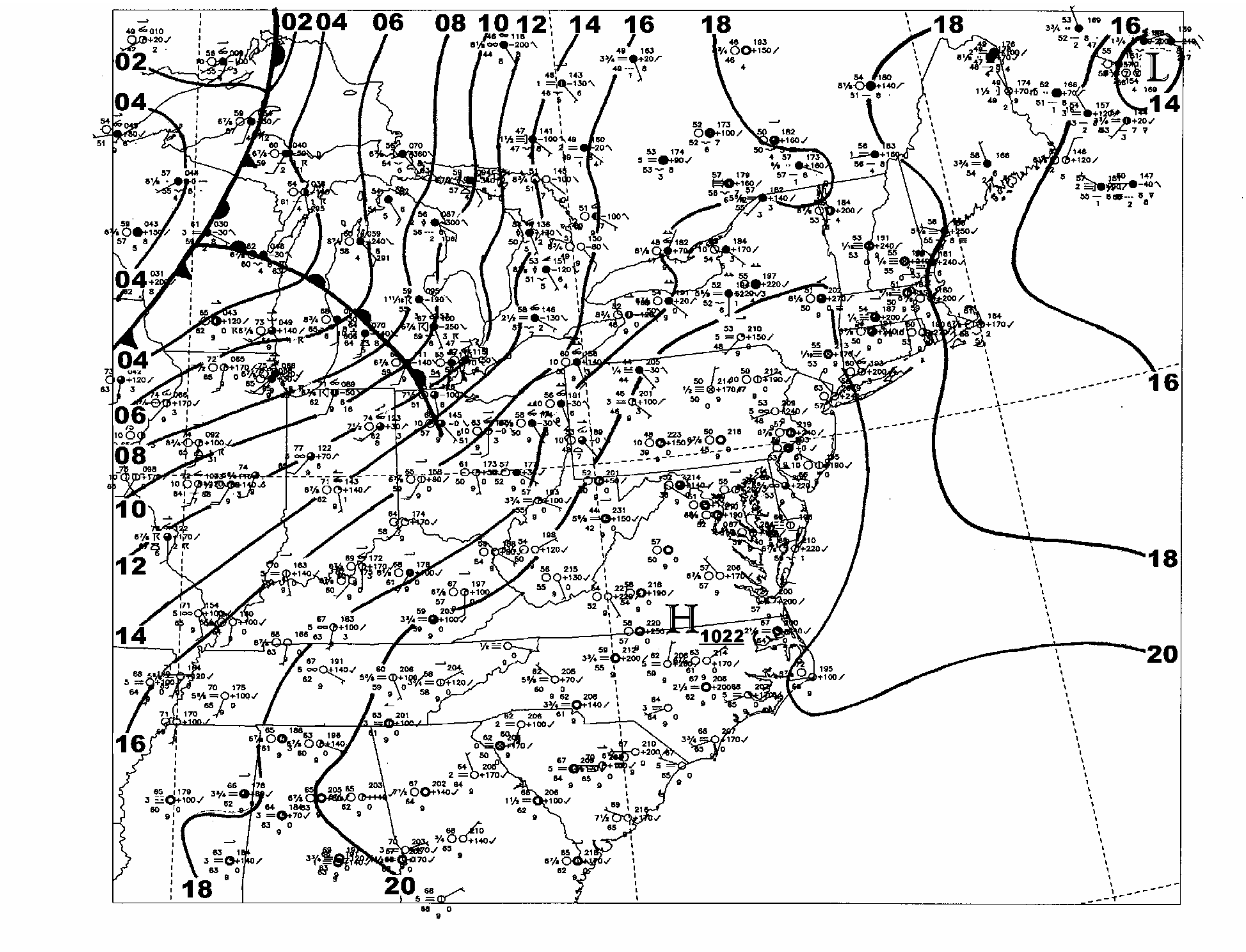

Figure 6. Manual analysis of sea-level pressure (hPa) for 1200 UTC, 18 September 1983 over the approximate area of the 12-km domain. Isobar interval is 2 hPa. Winds are plotted in kts.

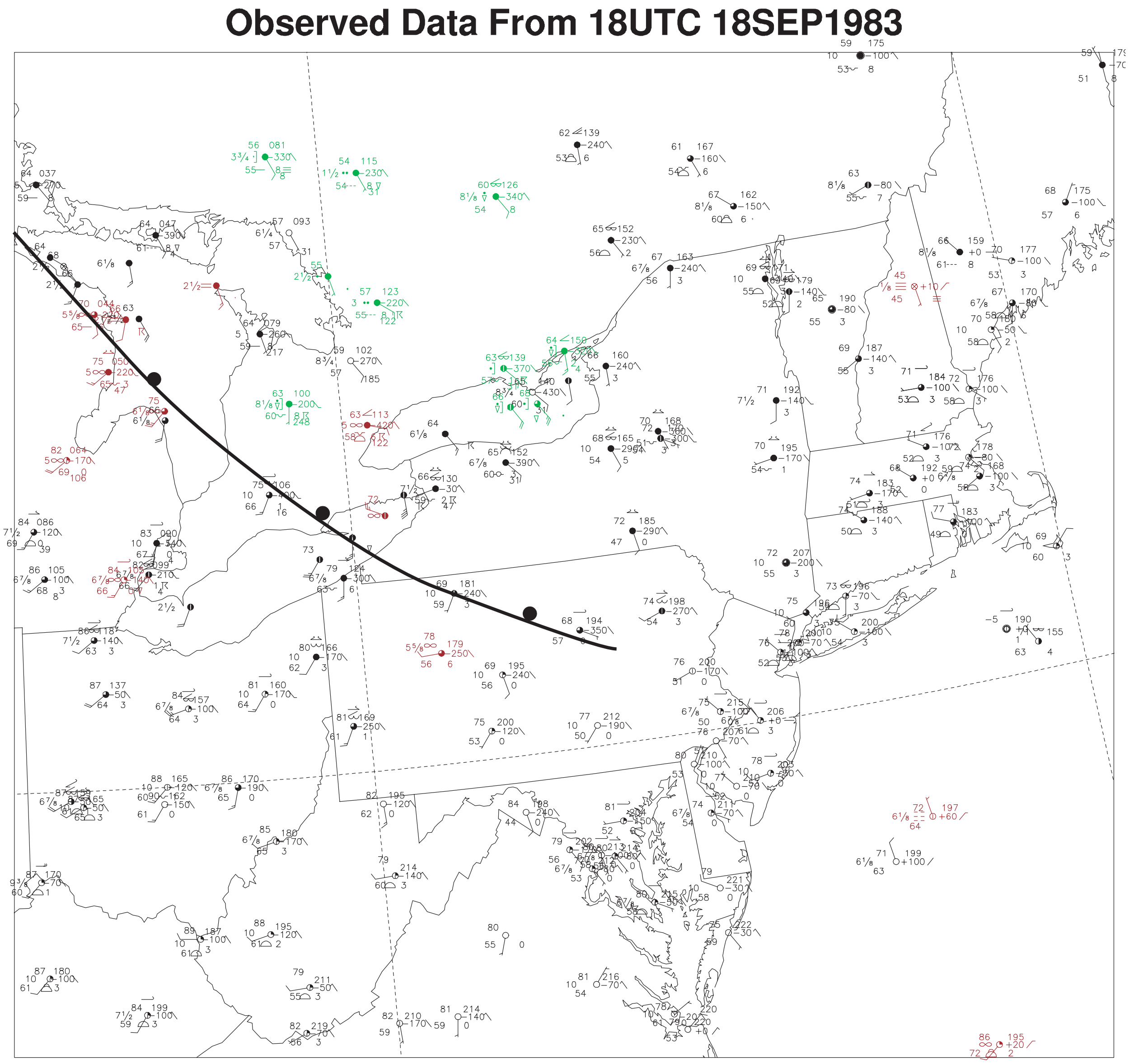

Figure 7. Standard surface weather reports at 1800 UTC 18 September 1983. A color coded station model is used for quick identification of current weather categories: Green symbols indicate reports of rain or showers, blue symbols represent frozen precipitation, red symbols denote thunderstorms, pink symbols indicate a thunderstorm nearby but not overhead, brown symbols represent obstructions to visibility (fog, haze) and black symbols indicate no significant weather.

Observed Data From 00UTC 19SEP1983

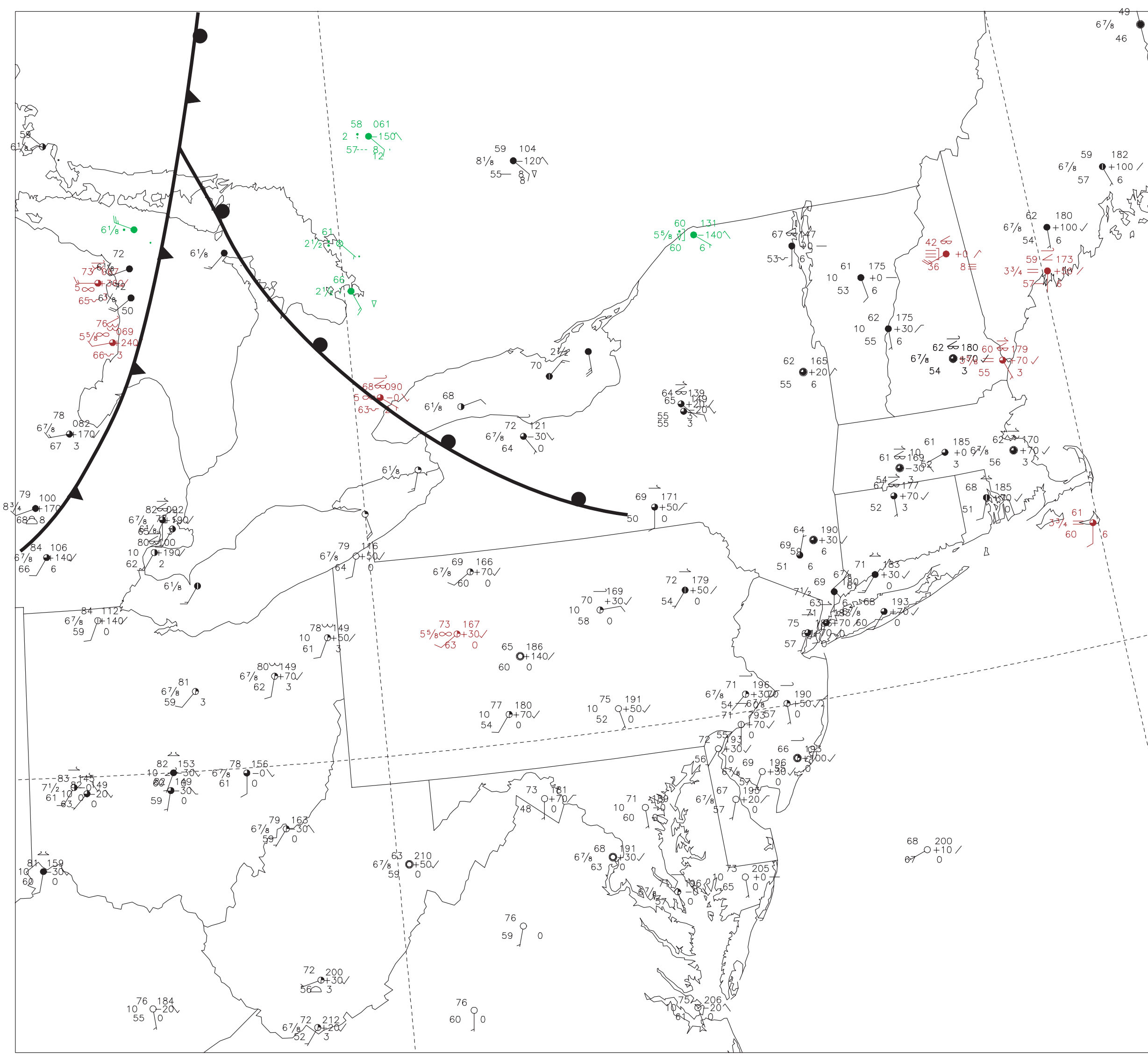

Figure 8. Standard surface weather reports at 0000 UTC 19 September 1983. A color coded station model is used for quick identification of current weather categories: Green symbols indicate reports of rain or showers, blue symbols represent frozen precipitation, red symbols denote thunderstorms, pink symbols indicate a thunderstorm nearby but not overhead, brown symbols represent obstructions to visibility (fog, haze) and black symbols indicate no significant weather.

Observed Data From 06UTC 19SEP1983

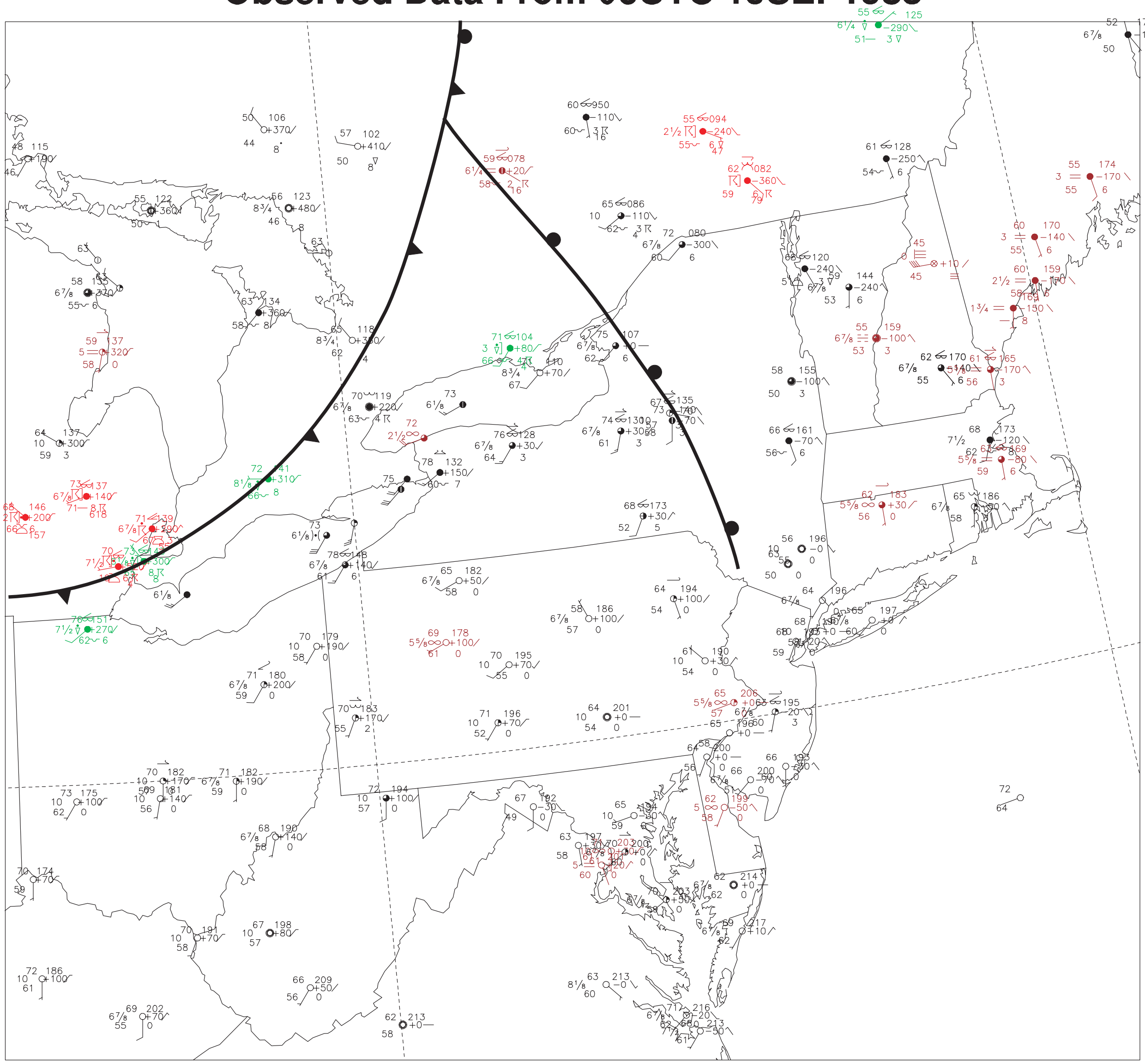

Figure 9. Standard surface weather reports at 0600 UTC 19 September 1983. A color coded station model is used for quick identification of current weather categories: Green symbols indicate reports of rain or showers, blue symbols represent frozen precipitation, red symbols denote thunderstorms, pink symbols indicate a thunderstorm nearby but not overhead, brown symbols represent obstructions to visibility (fog, haze) and black symbols indicate no significant weather.

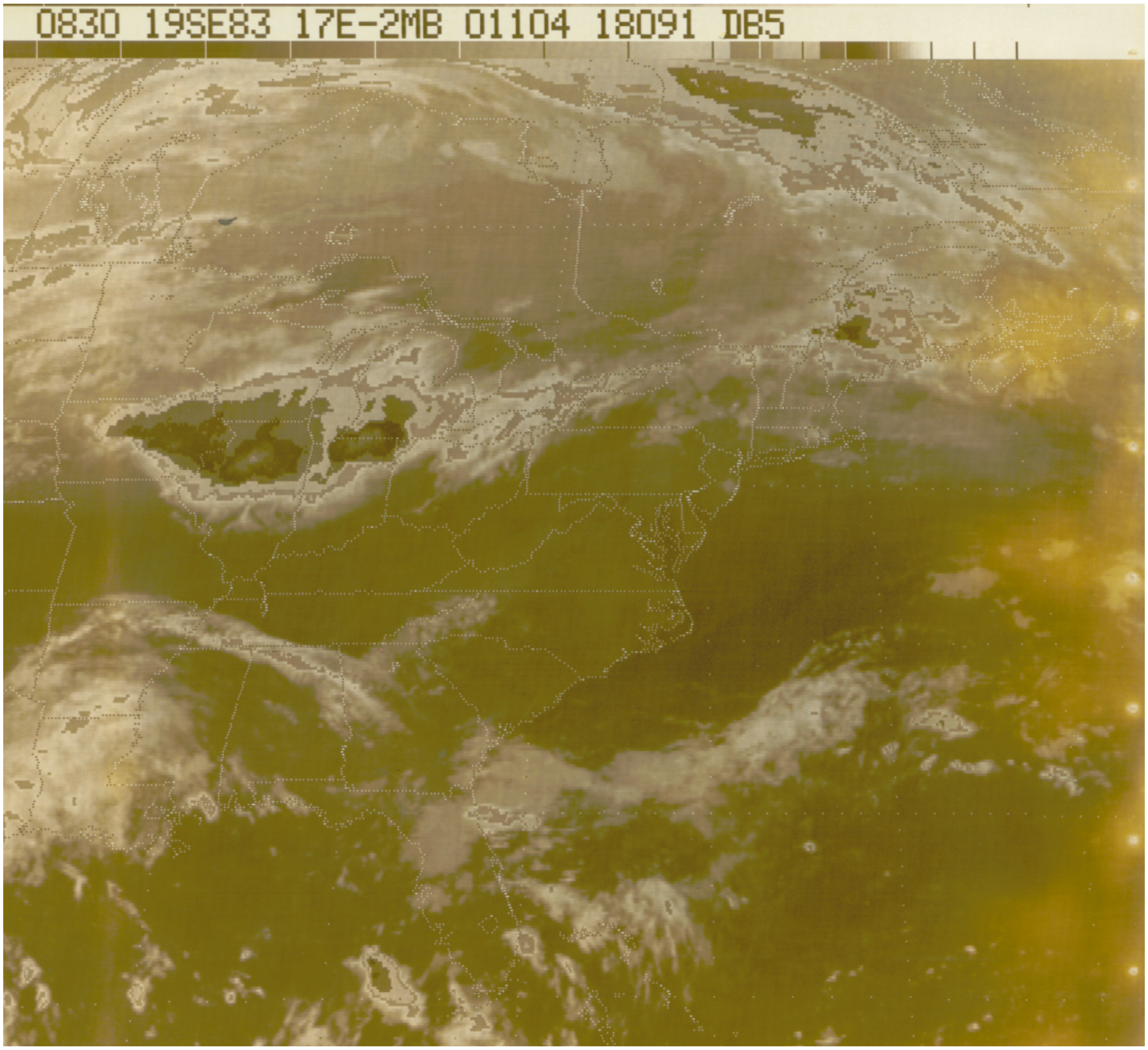

Figure 10. Satellite cloud imagery (IR) at 0830 UTC 19 September 2003, covering eastern U.S.

Observed Data From 12UTC 19SEP1983

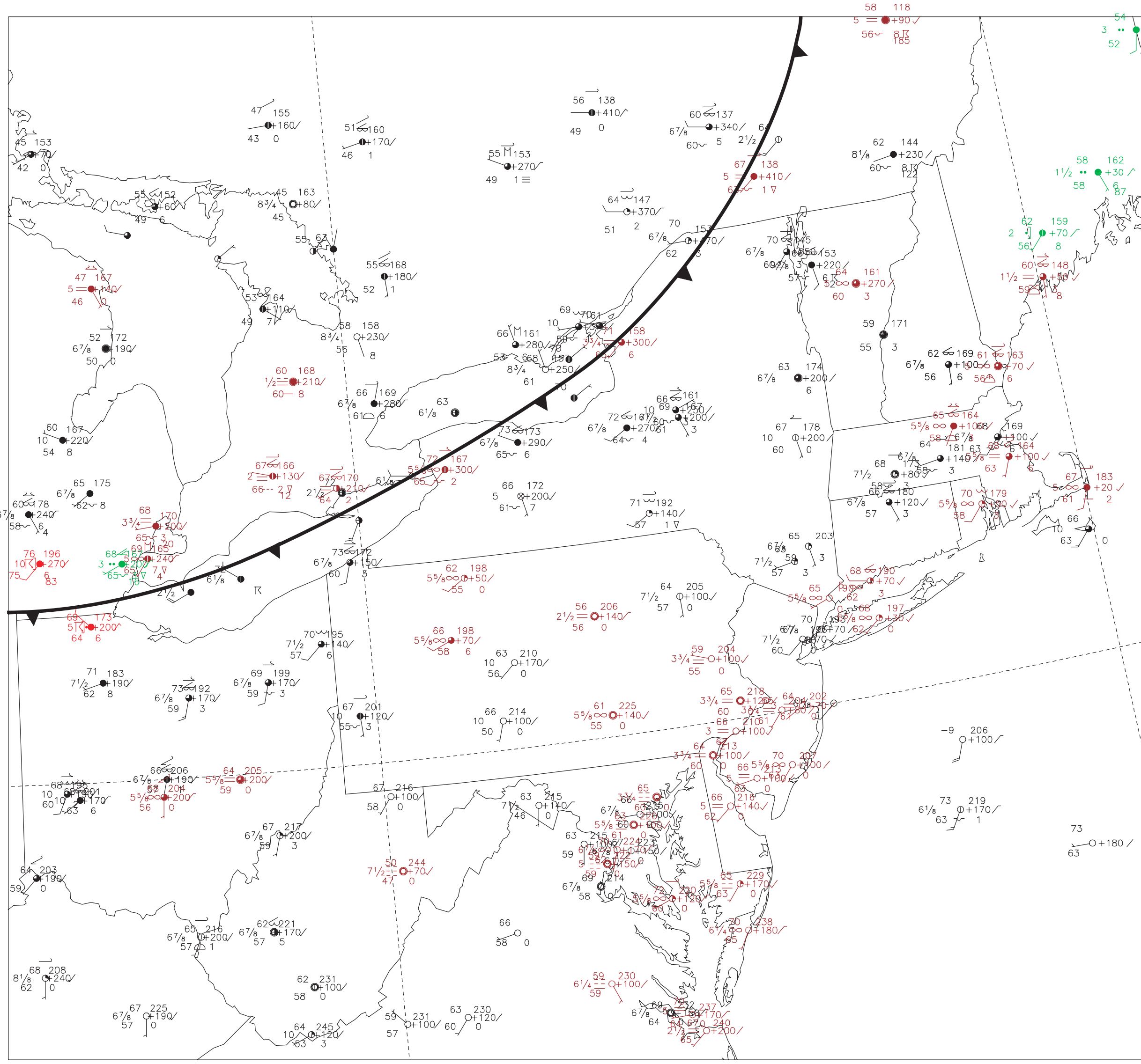

Figure 11. Standard surface weather reports at 1200 UTC 19 September 1983. A color coded station model is used for quick identification of current weather categories: Green symbols indicate reports of rain or showers, blue symbols represent frozen precipitation, red symbols denote thunderstorms, pink symbols indicate a thunderstorm nearby but not overhead, brown symbols represent obstructions to visibility (fog, haze) and black symbols indicate no significant weather.

Observed Data From 18UTC 19SEP1983

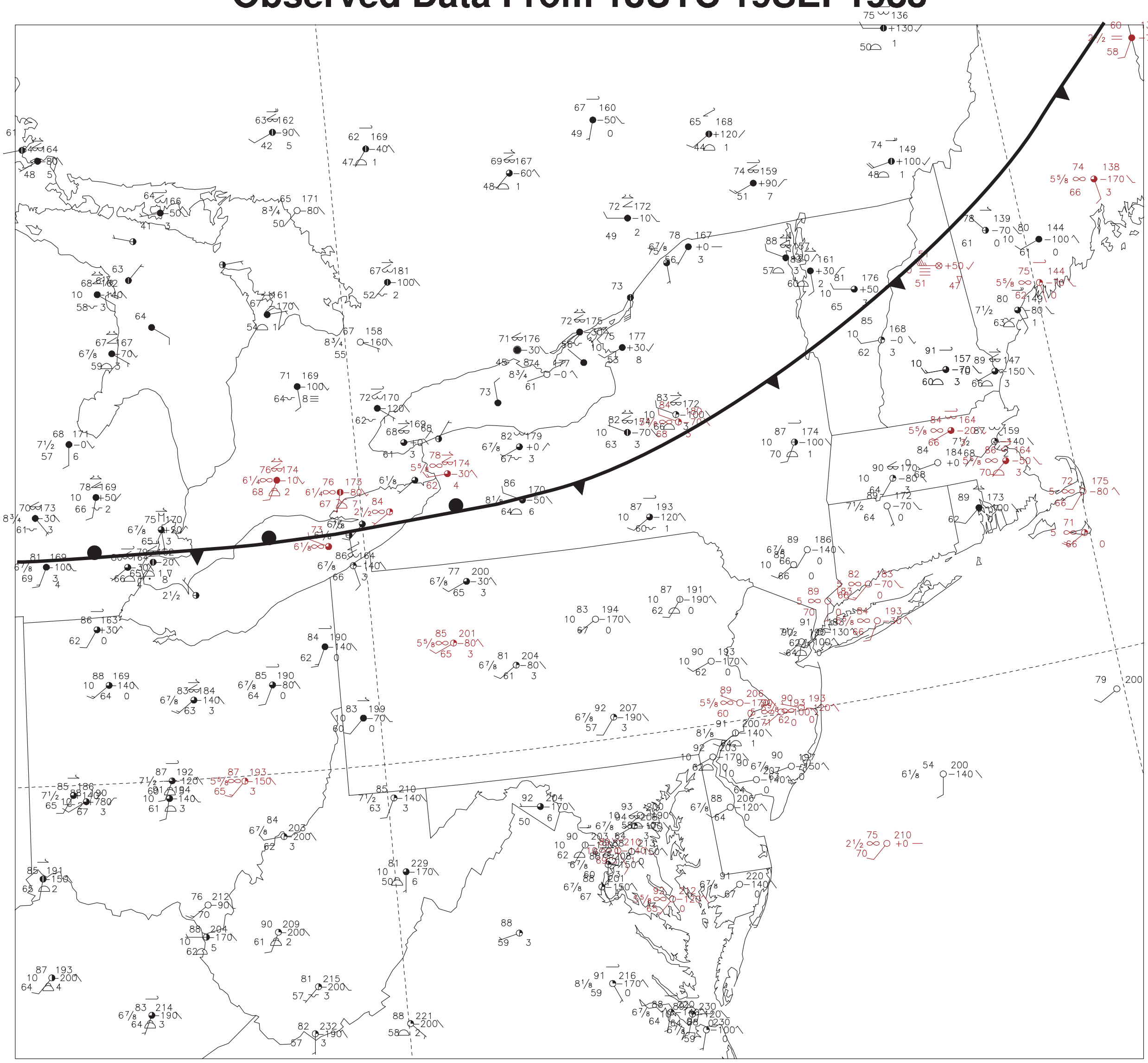

Figure 12. Standard surface weather reports at 1800 UTC 19 September 1983. A color coded station model is used for quick identification of current weather categories: Green symbols indicate reports of rain or showers, blue symbols represent frozen precipitation, red symbols denote thunderstorms, pink symbols indicate a thunderstorm nearby but not overhead, brown symbols represent obstructions to visibility (fog, haze) and black symbols indicate no significant weather.

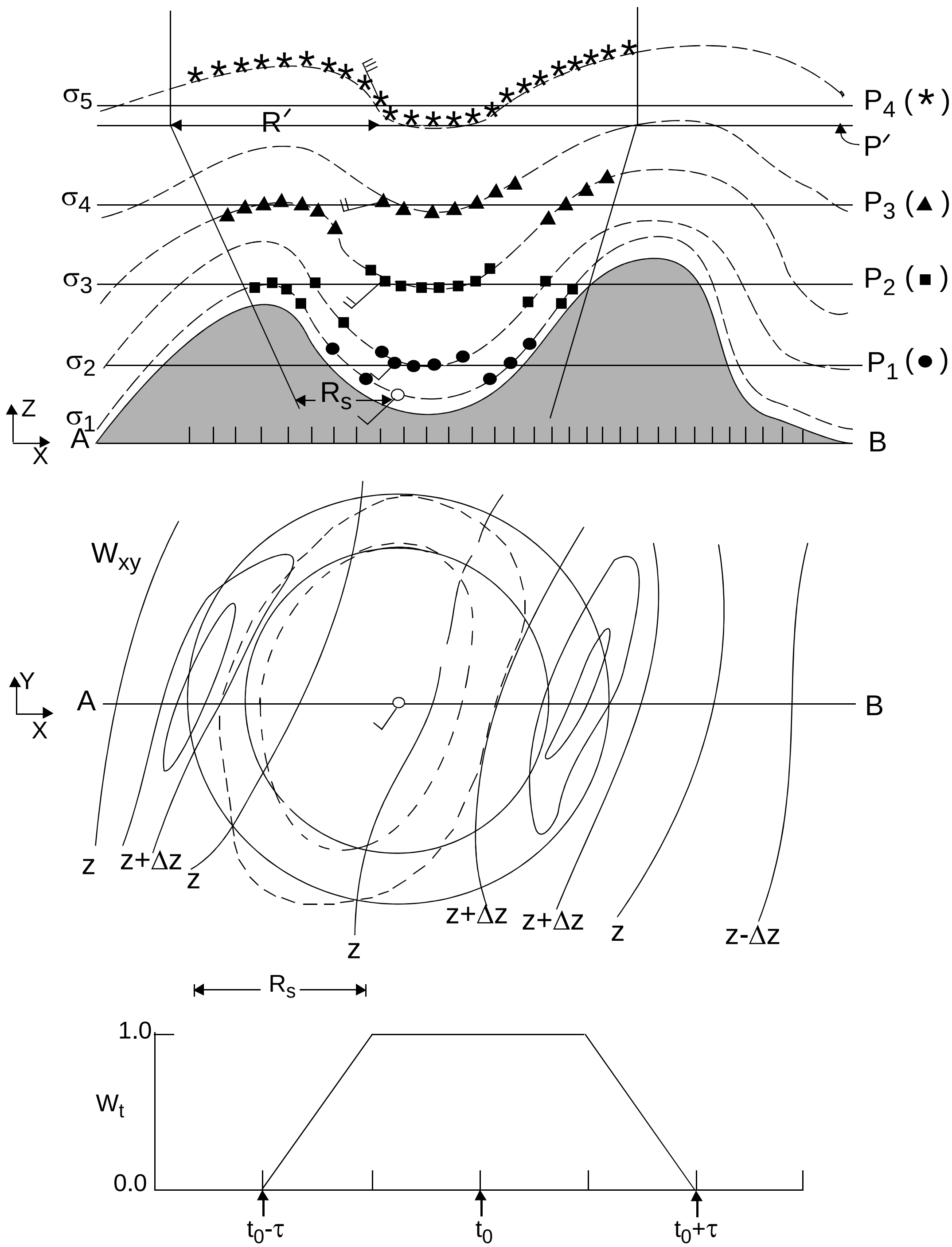

Figure 13 Schematic showing the horizontal weighting function, w_{xy}, and the temporal weighting function, w_t, used for obs nudging. From Stauffer and Seaman (1994).

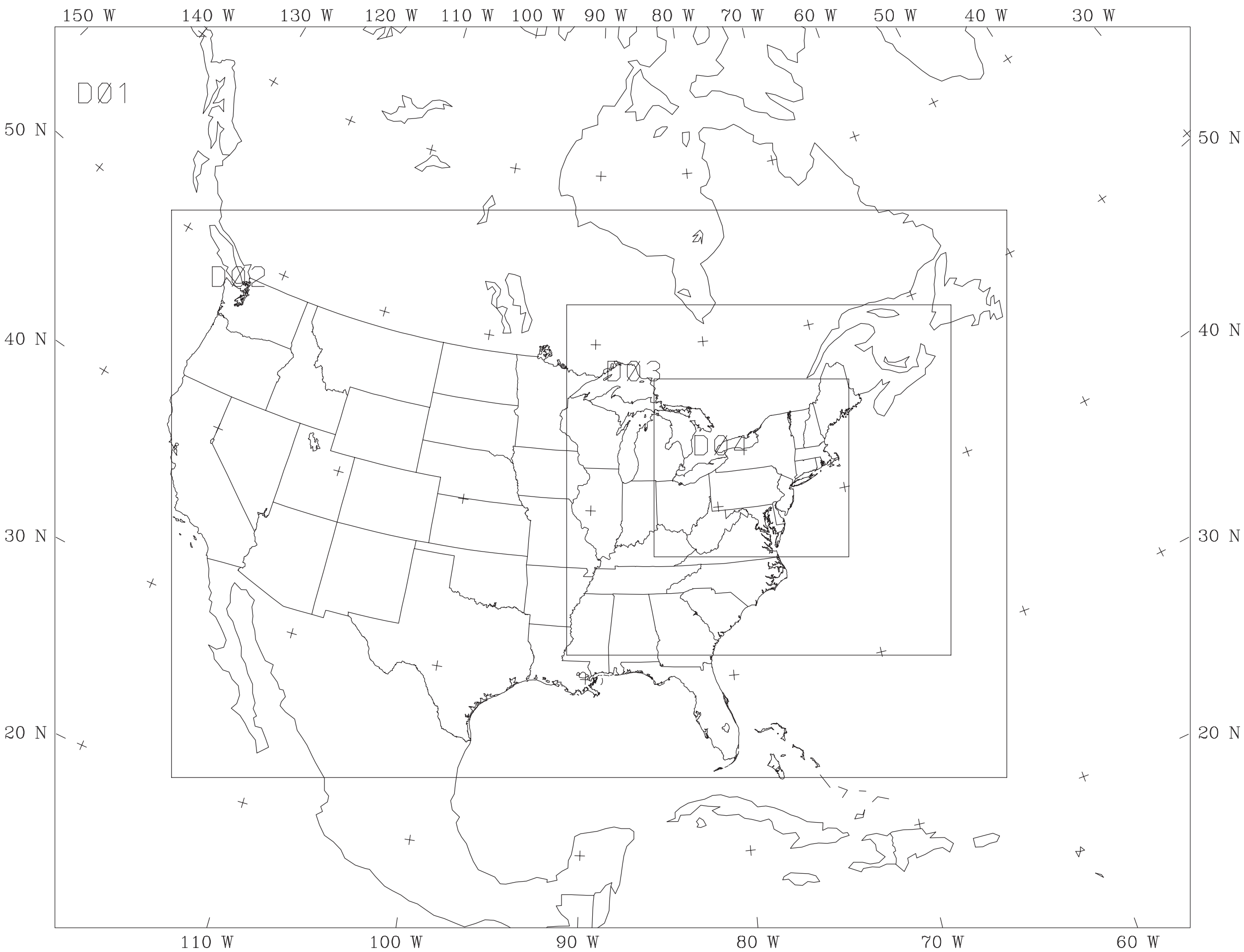

Figure 14. Location of 108-km, 36-km, 12-km and 4-km nested domains for MM5.

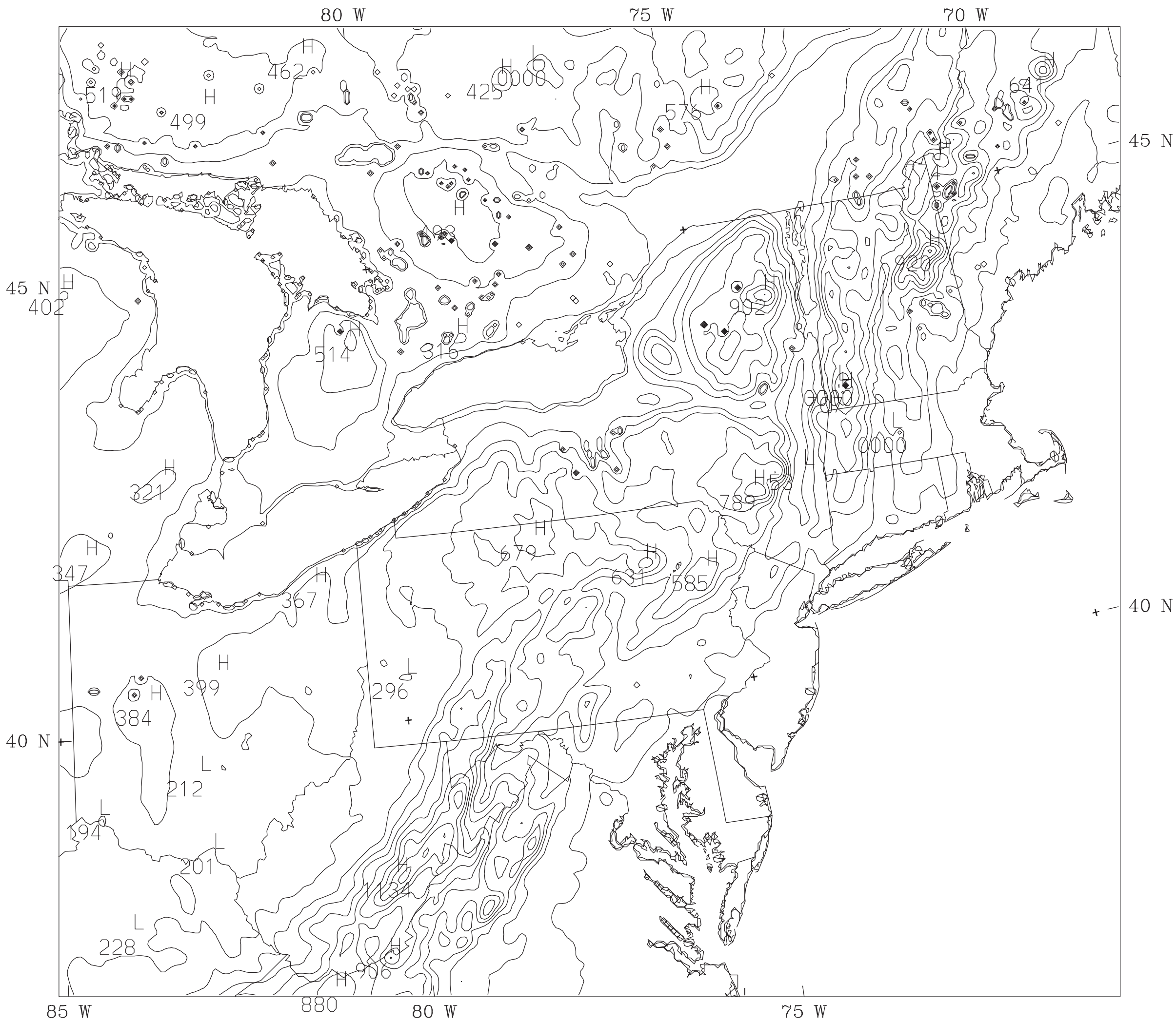

Figure 15. Terrain (m) for the MM5 4-km domain. Contour interval is 100 m.

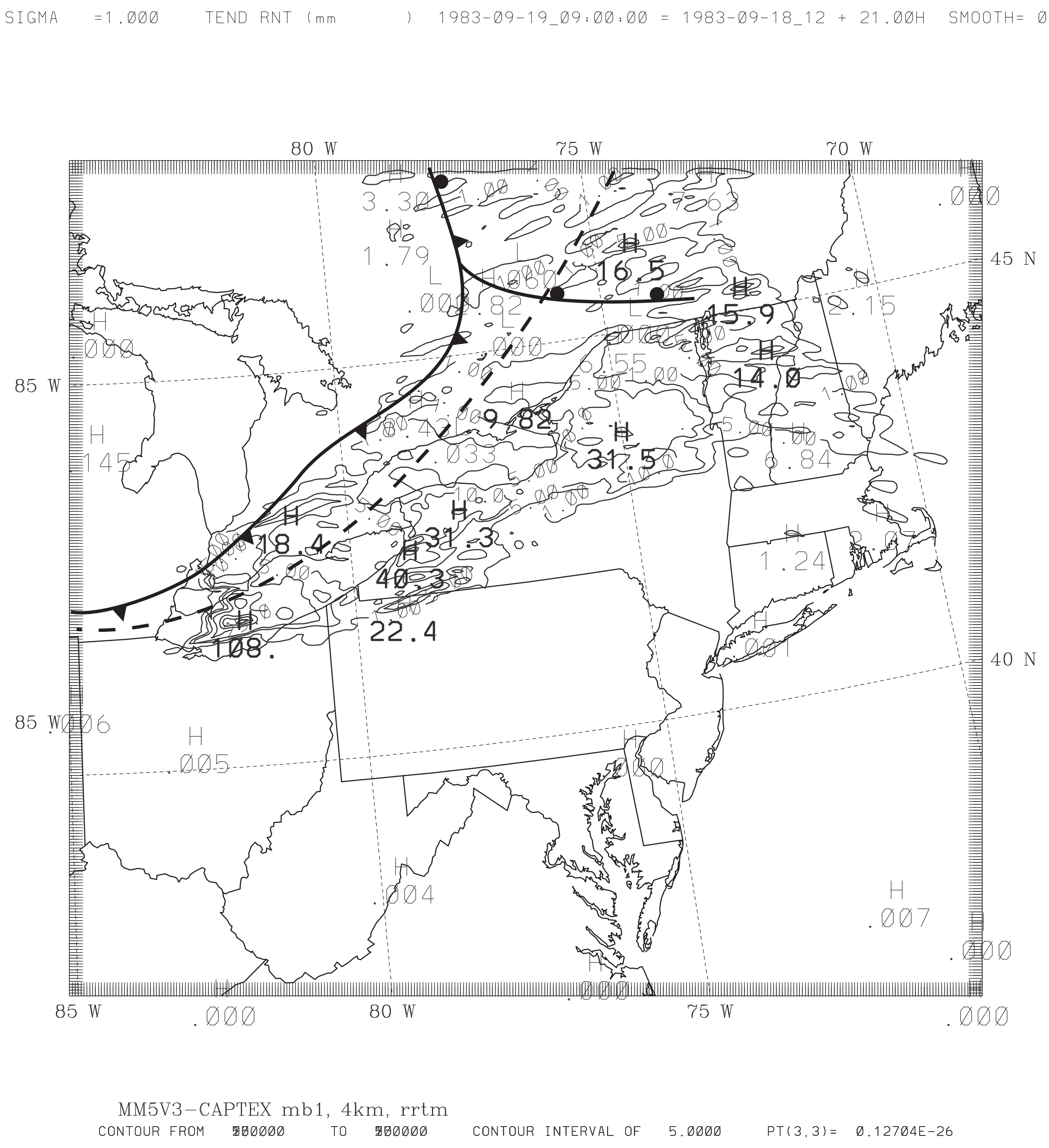

Figure 16 MM5 simulation of 3-h non-convective rainfall (mm) ending at 21 h (0900 UTC 19 September 1983) on the 4-km domain in Exp. MB1. Contours are 1, 5, 10, 20, 30 and 40 mm. Simulated front is shown on the figure for reference and the dashed line indicates the approximate location of the observed front at this time.

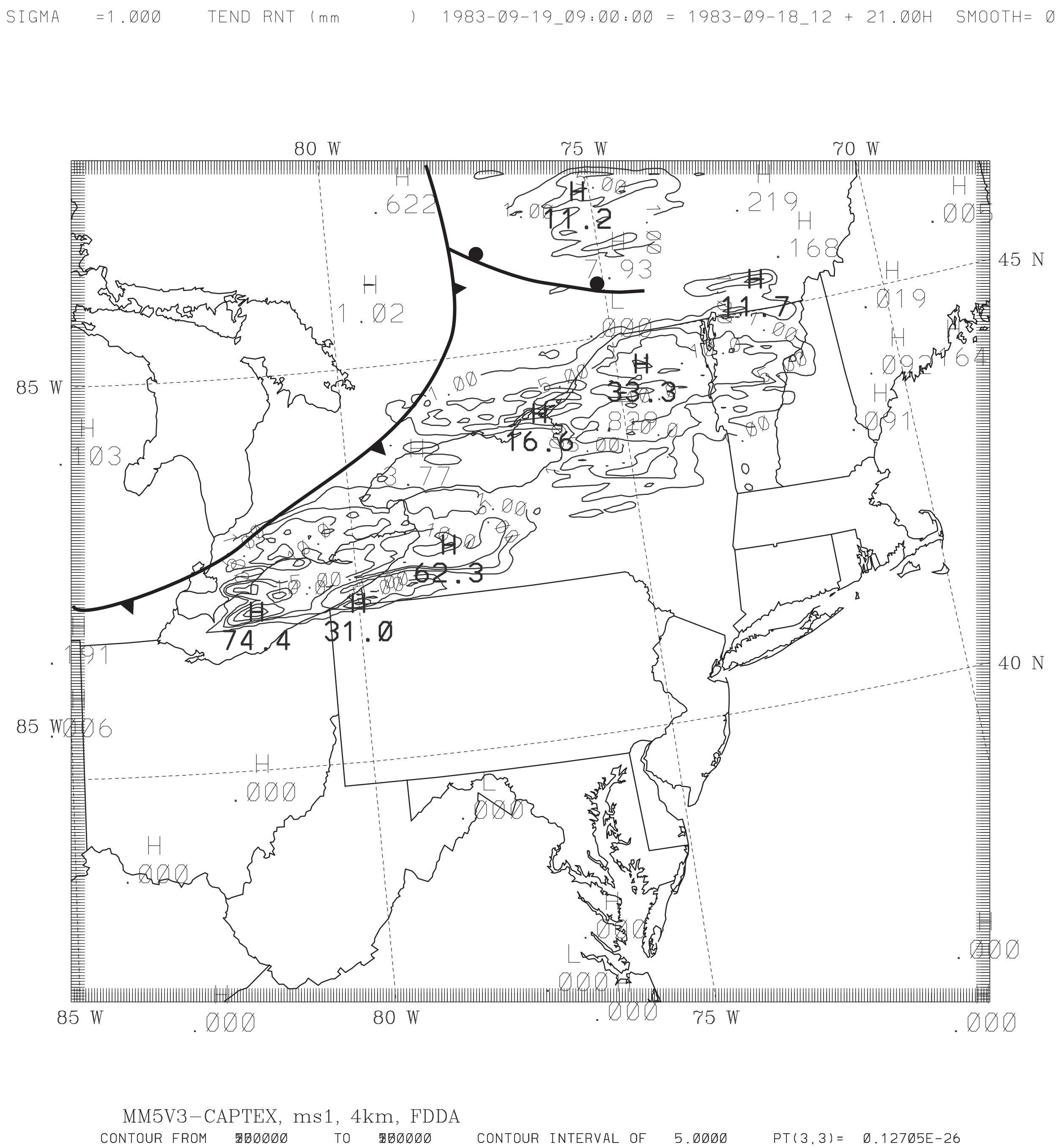

Figure 17 MM5 simulation of 3-h non-convective rainfall (mm) ending at 21 h (0900 UTC 19 September 1983) on the 4-km domain in Exp. MS1. Contours are 1, 5, 10, 20, 30 and 40 mm. Simulated front is shown on the figure for reference.

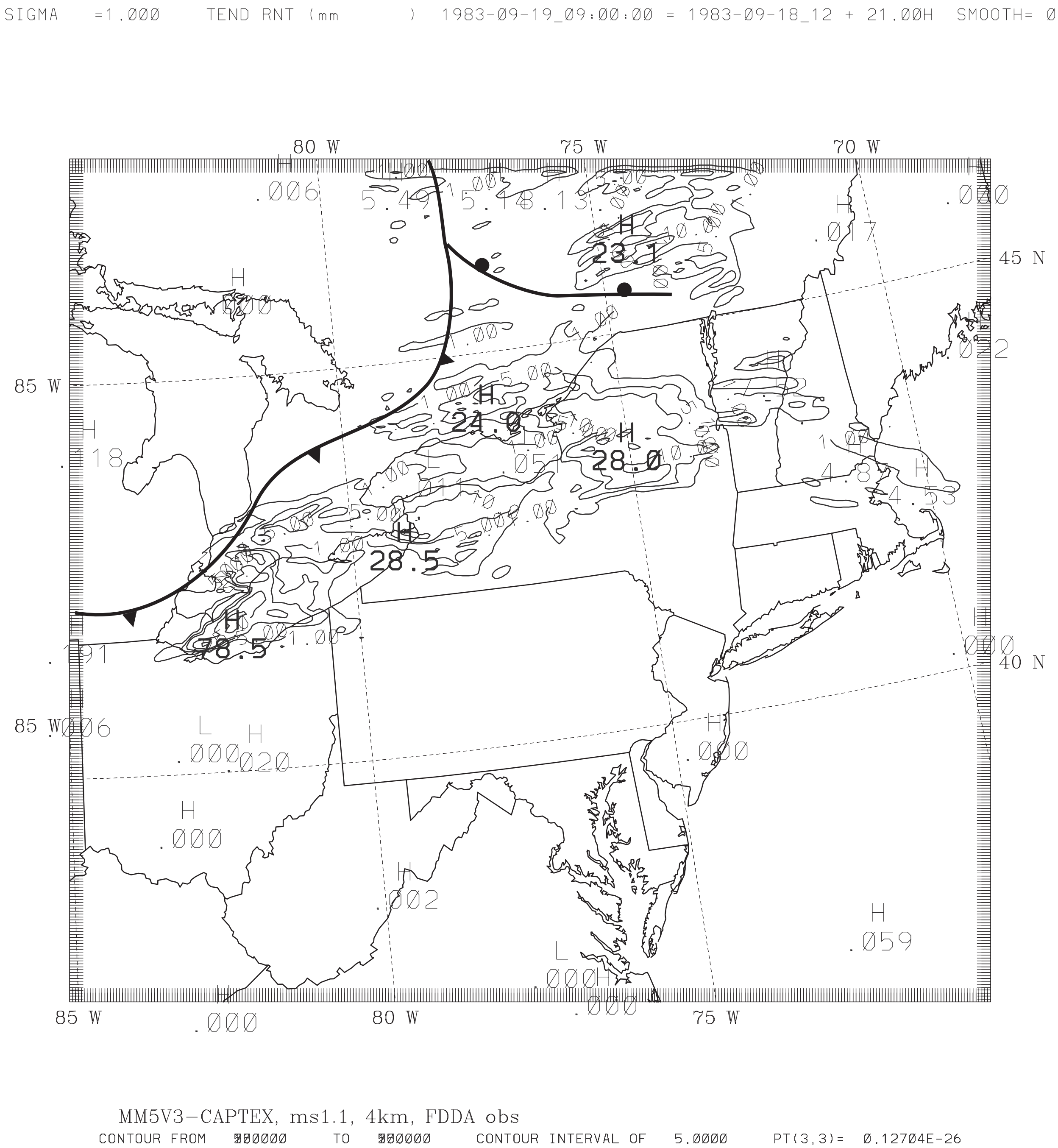

Figure 18 MM5 simulation of 3-h non-convective rainfall (mm) ending at 21 h (0900 UTC 19 September 1983) on the 4-km domain in Exp. MS1.1. Contours are 1, 5, 10, 20, 30 and 40 mm. Simulated front is shown on the figure for reference.

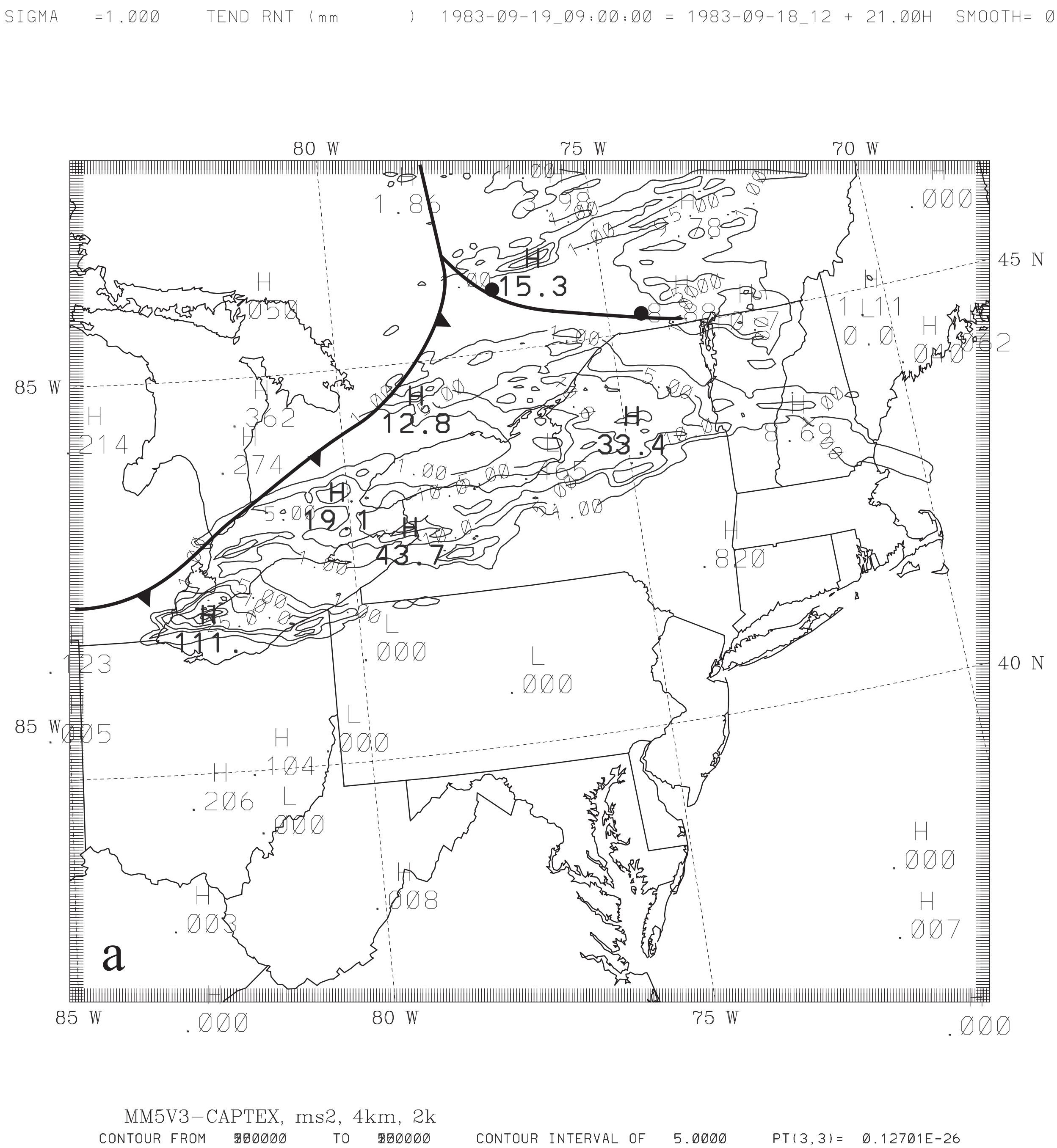

Figure 19 MM5-simulated field at 21 h (0900 UTC 19 September 1983) on the 4-km domain in Exp. MS2 for (a) 3-h non-convective rainfall (mm), with contours: 1, 5, 10, 20, 30 and 40 mm; and (b) surface-layer wind (29 m AGL) (speed contours are 5 ms^{-1} and one barb is 10 ms^{-1}). Simulated front is shown on the figure for reference.

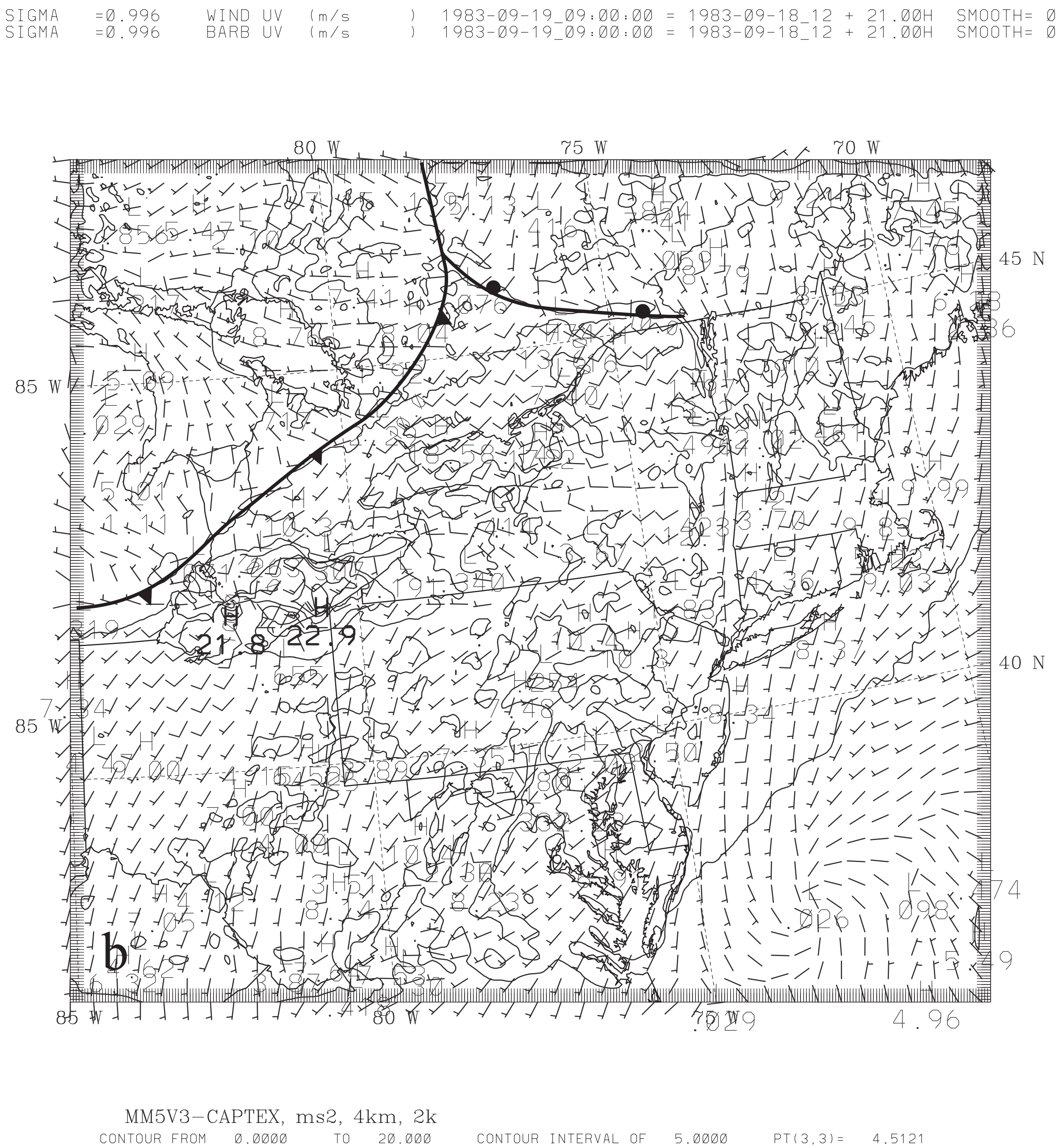

Figure 19 (Continued)

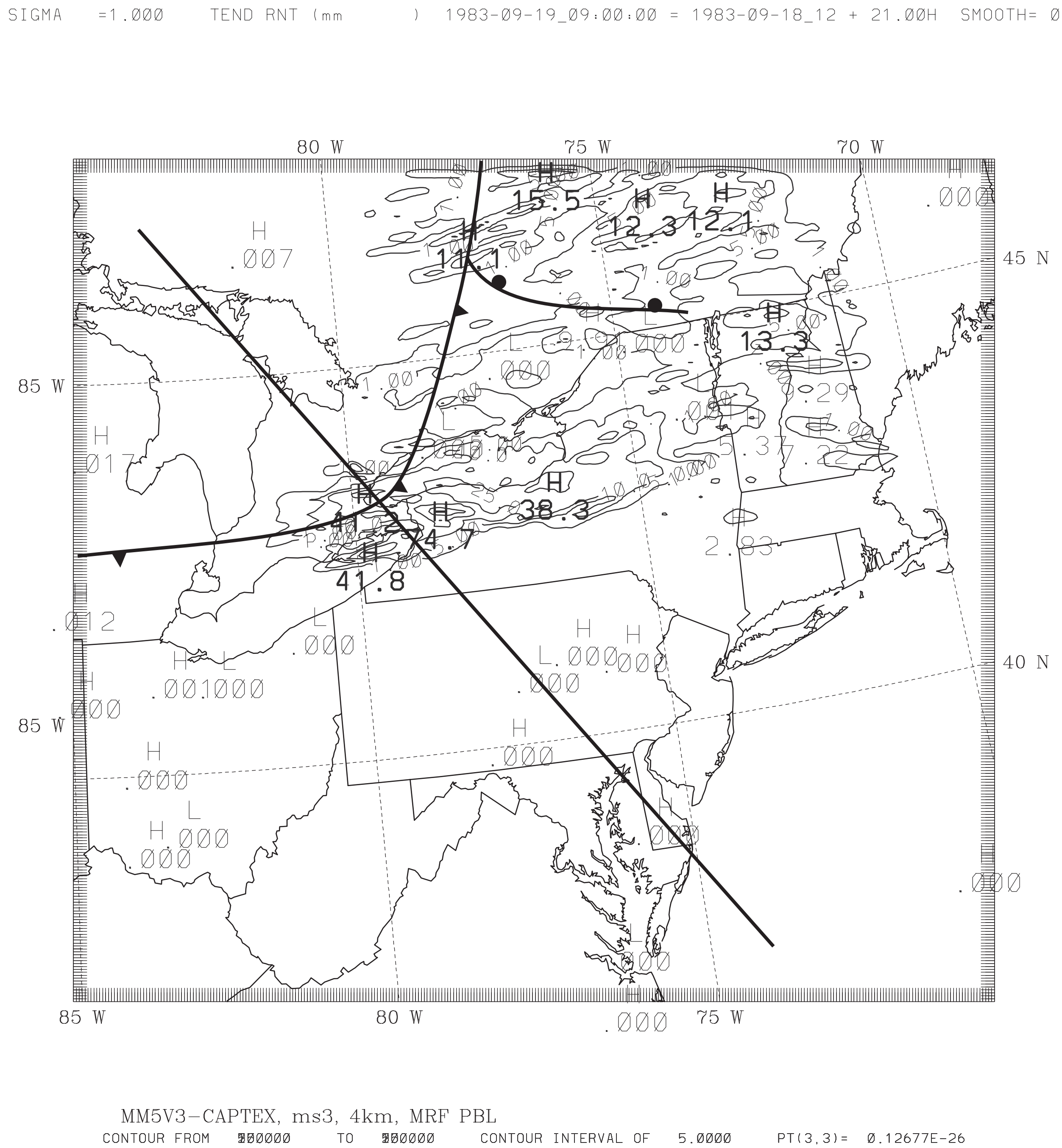

Figure 20 MM5 simulation of 3-h non-convective rainfall (mm) ending at 21 h (0900 UTC 19 September 1983) on the 4-km domain in Exp. MS3. Contours are 1, 5, 10, 20, 30 and 40 mm. Simulated front is shown on the figure for reference and the straight line indicates the location of the cross section used in Figures 21 and 32.

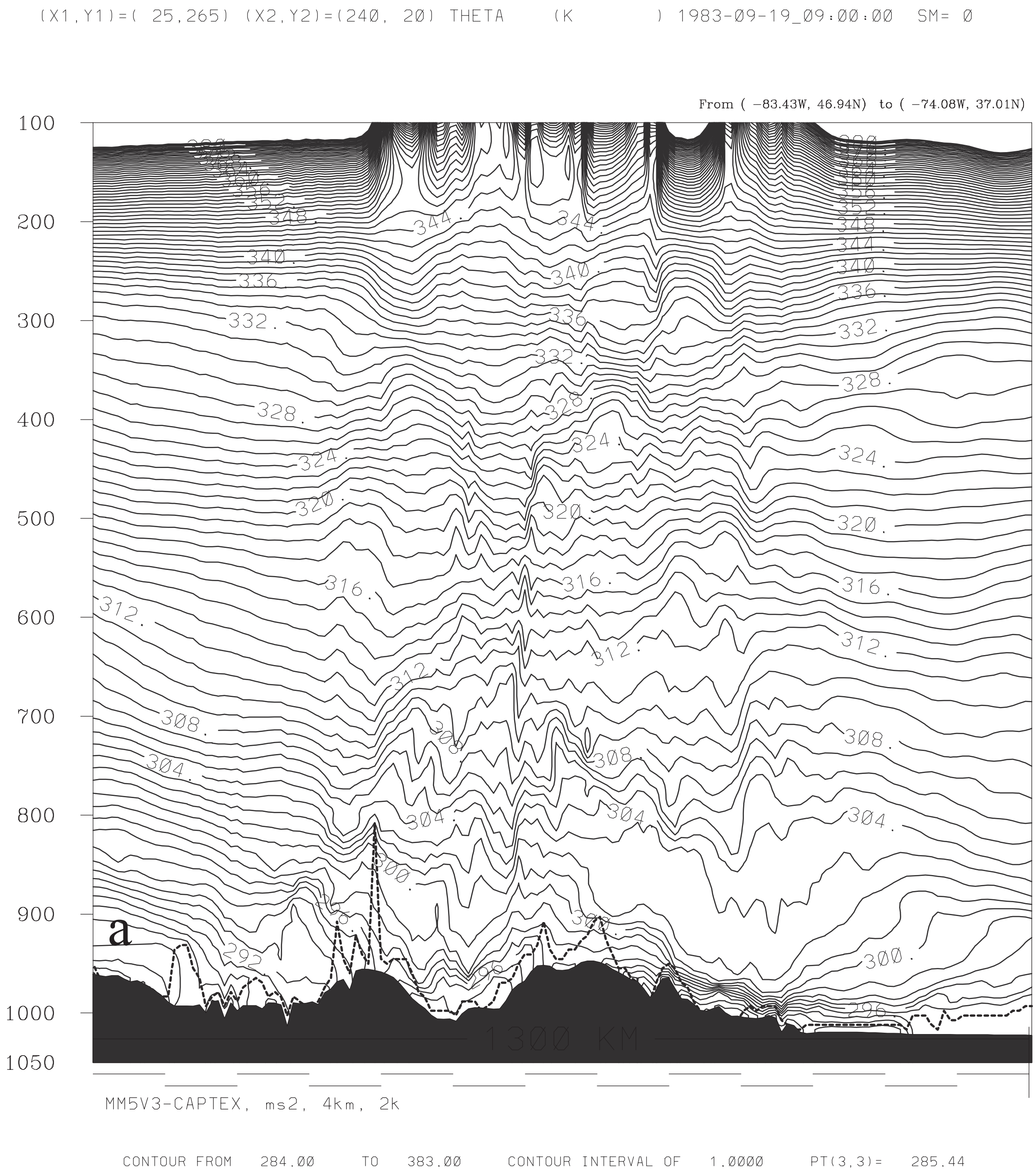

Figure 21 Cross-section of MM5-simulated fields on the 4-km domain at 21 h (0900 UTC, 19 September 1983). (a) potential temperature (K) for Exp. MS2 (MB2), (b) potential temperature (K) Exp. MS3 and (c) PBL depth for all experiments. Isentrope interval is 1 K. Dashed line indicates depth of the MM5 PBL. Location of the southwest-northeast cross section is shown in Figure 19. Line segments just below 1050 mb level each indicate 100 km distance from left.

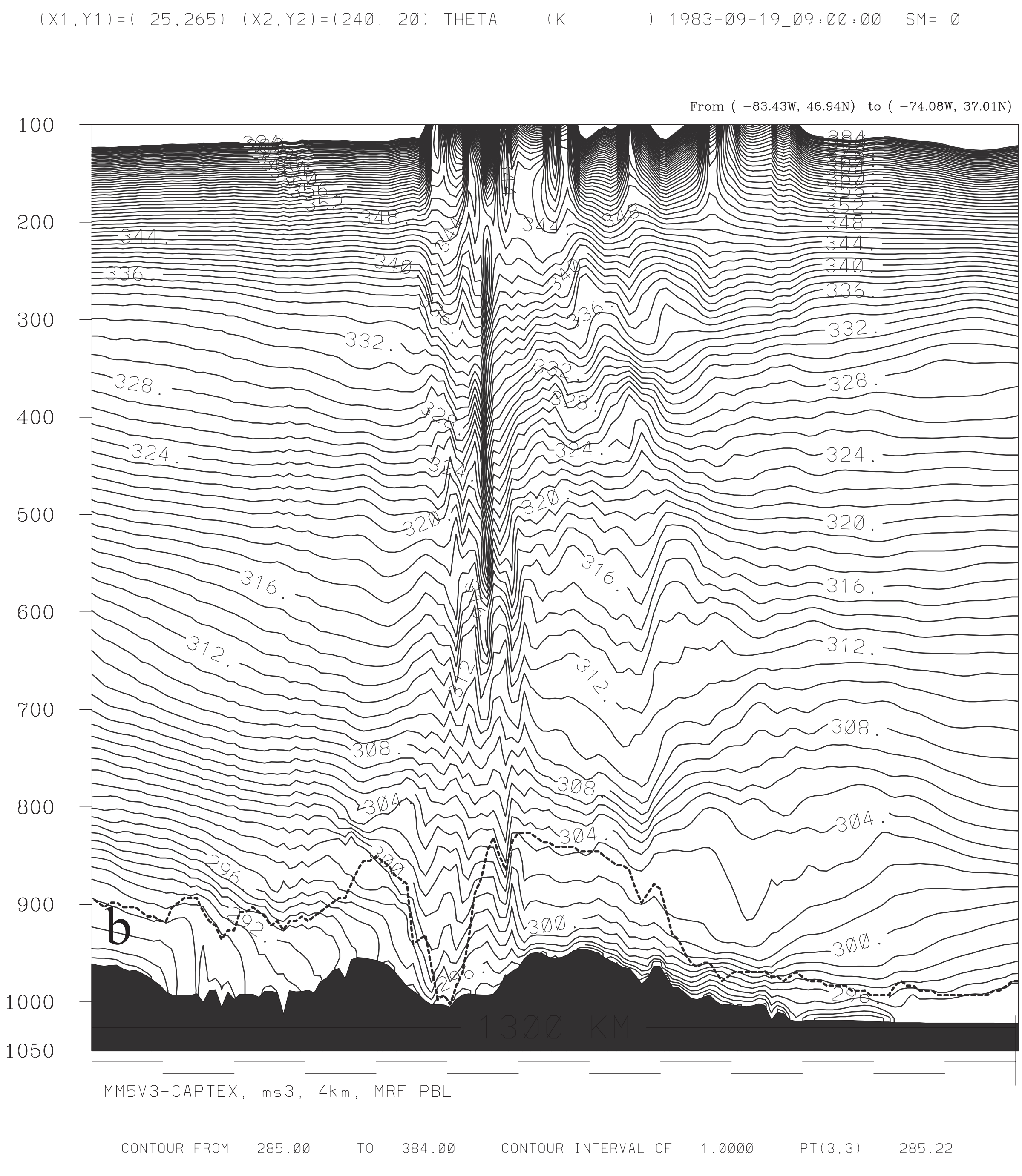

Figure 21 (Continued)

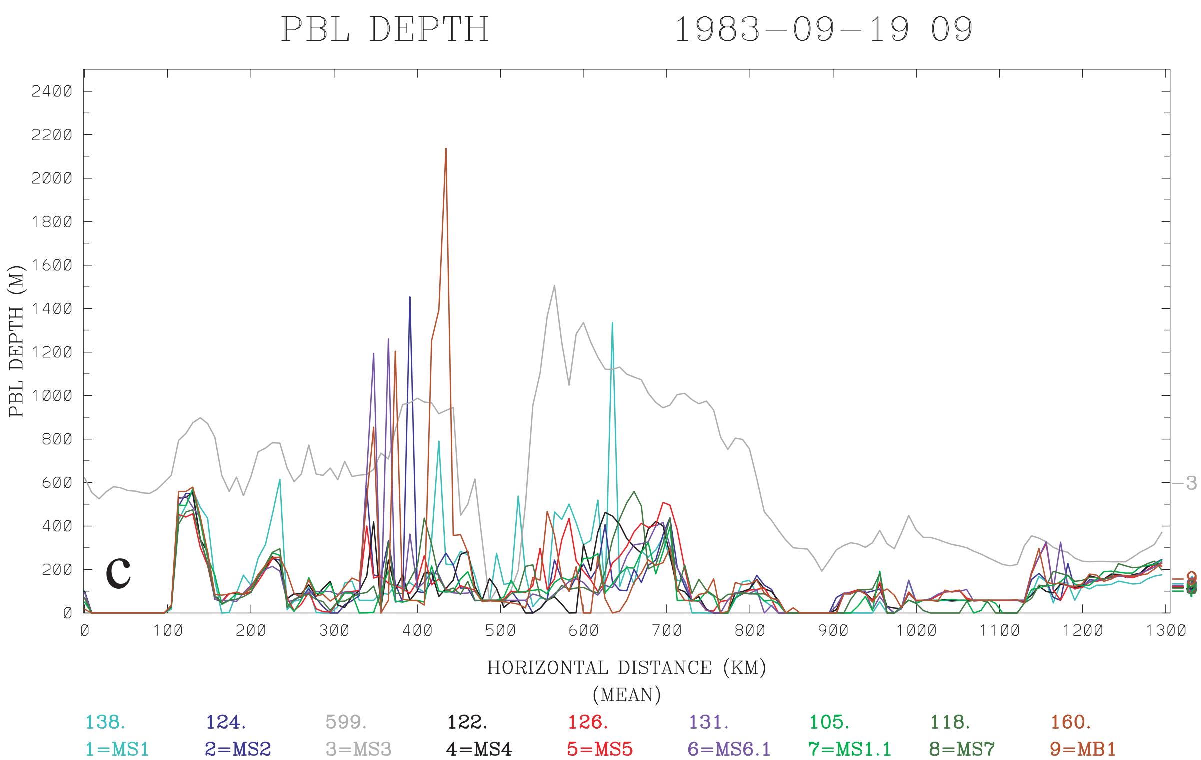

Figure 21 (Continued)

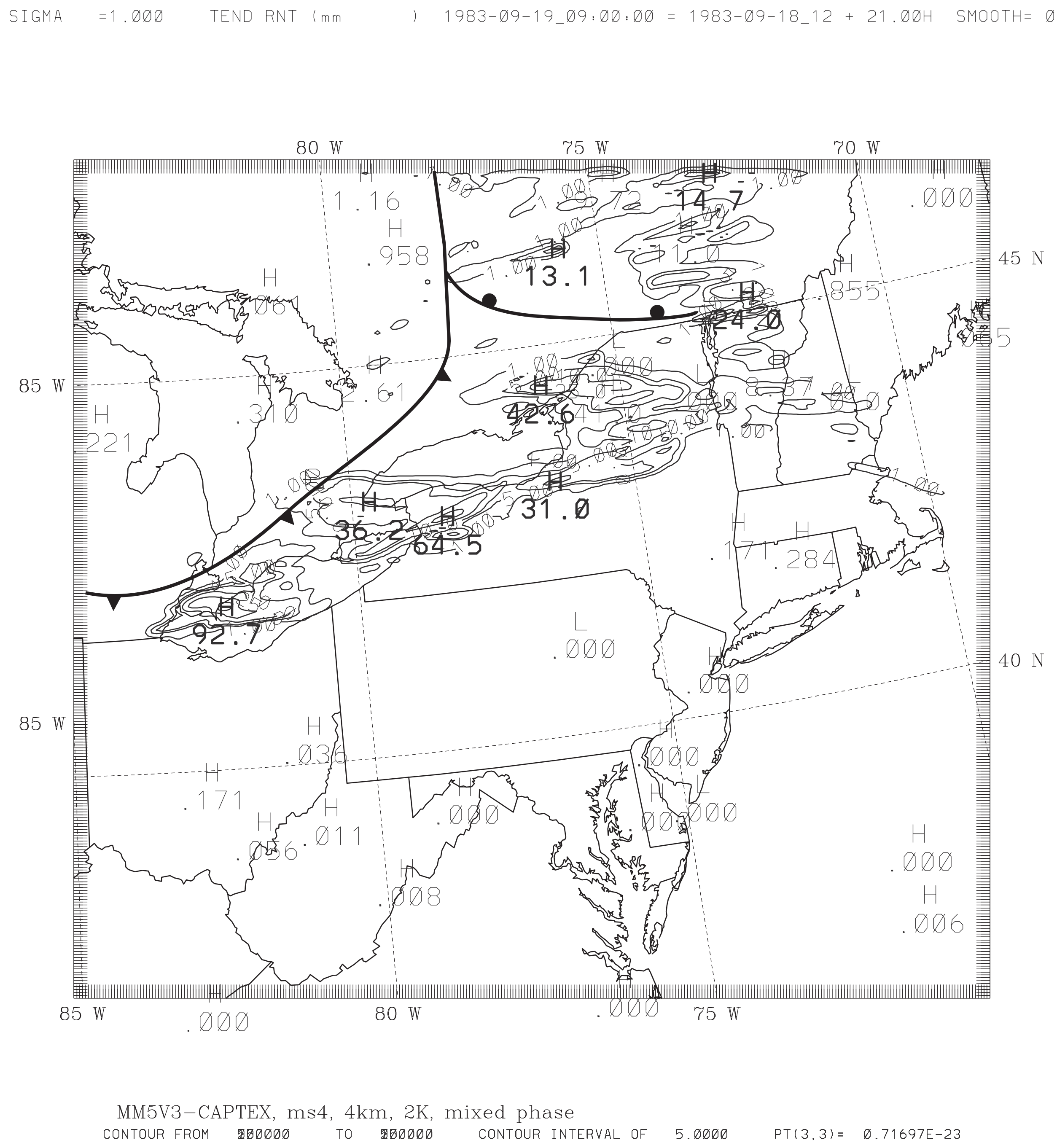

Figure 22 MM5 simulation of 3-h non-convective rainfall (mm) ending at 21 h (0900 UTC 19 September 1983) on the 4-km domain in Exp. MS4. Contours are 1, 5, 10, 20, 30 and 40 mm. Simulated front is shown on the figure for reference.

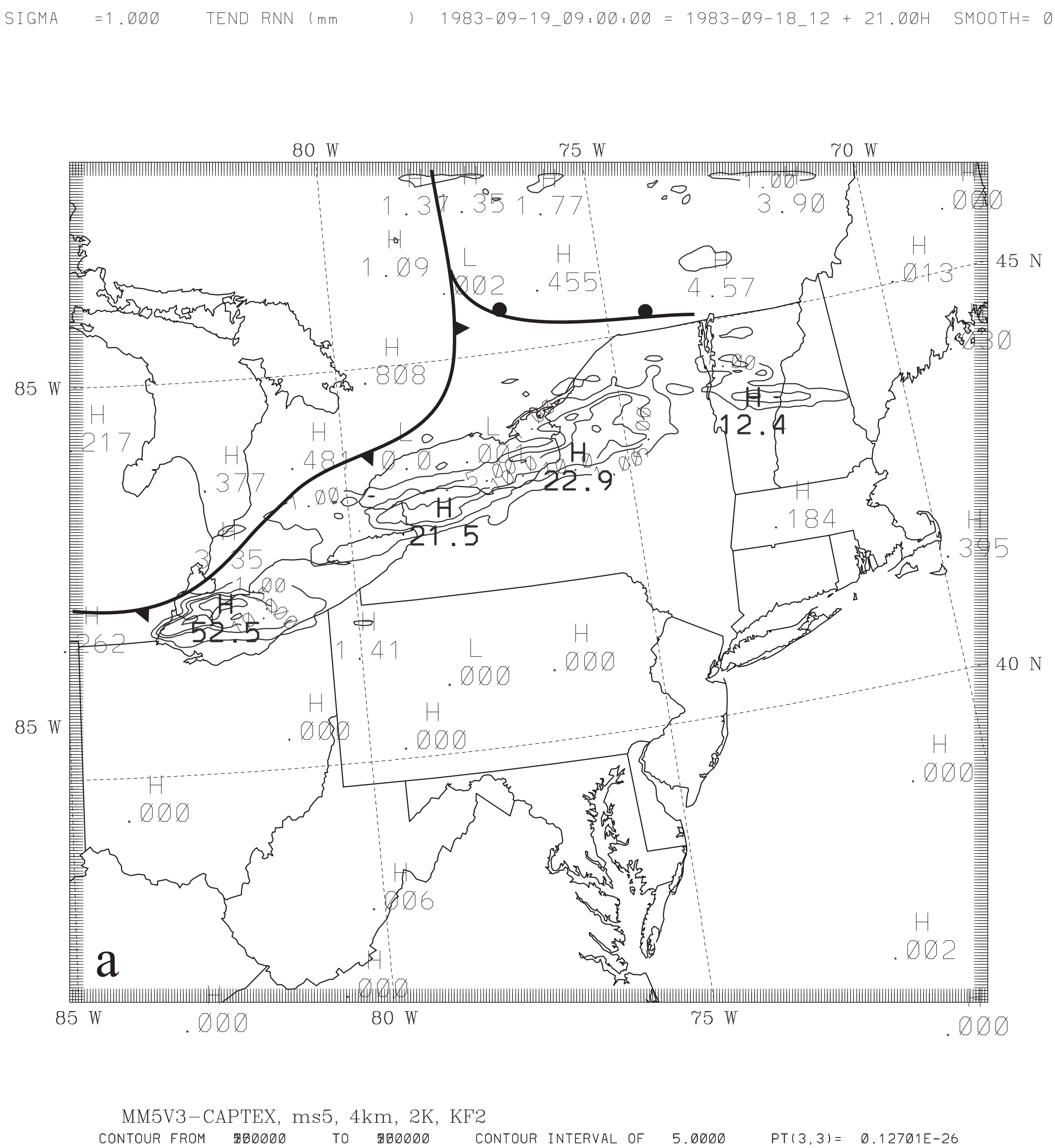

Figure 23 MM5 simulation of 3-h rainfall (mm) ending at 21 h (0900 UTC 19 September 1983) on the 4-km domain in Exp. MS5. Contours are 1, 5, 10, 20, 30 and 40 mm. (a) Non-convective (grid-resolved) rain, (b) Convective (parameterized) rain, (c) Total (non-convective plus convective) rain. Simulated front is shown on the figure for reference.

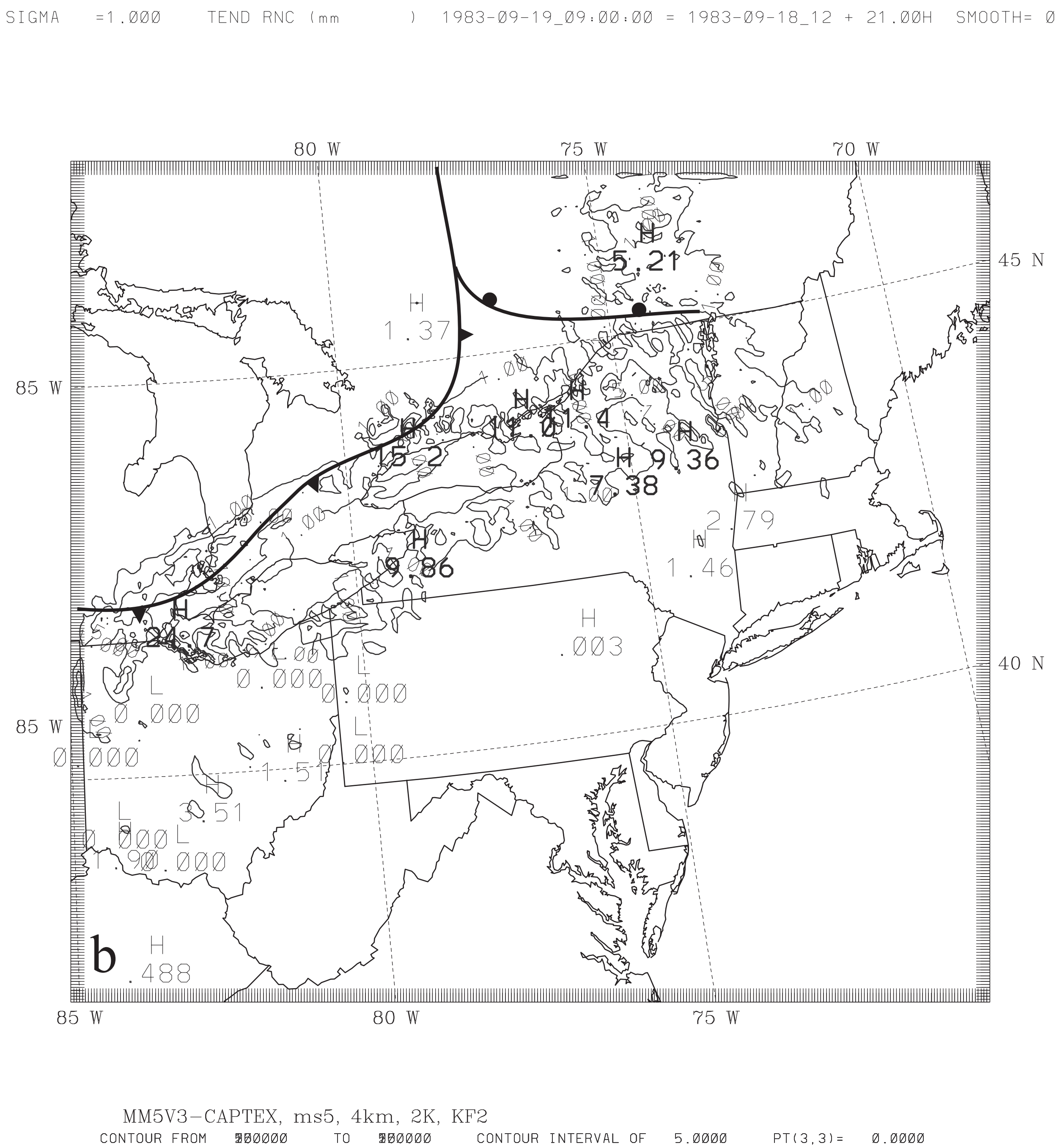

Figure 23 (Continued)

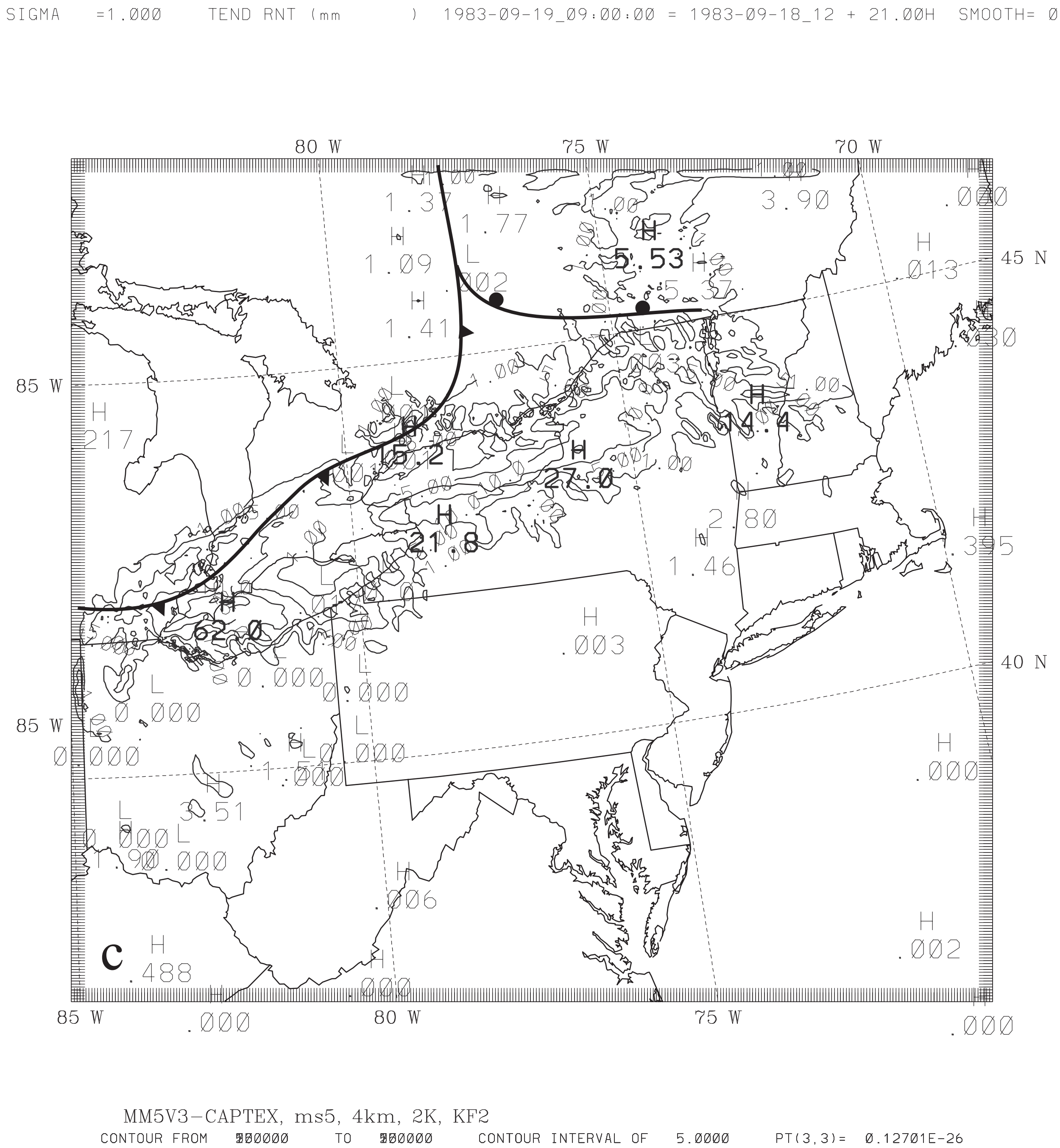

(c)

Figure 23 (Continued)

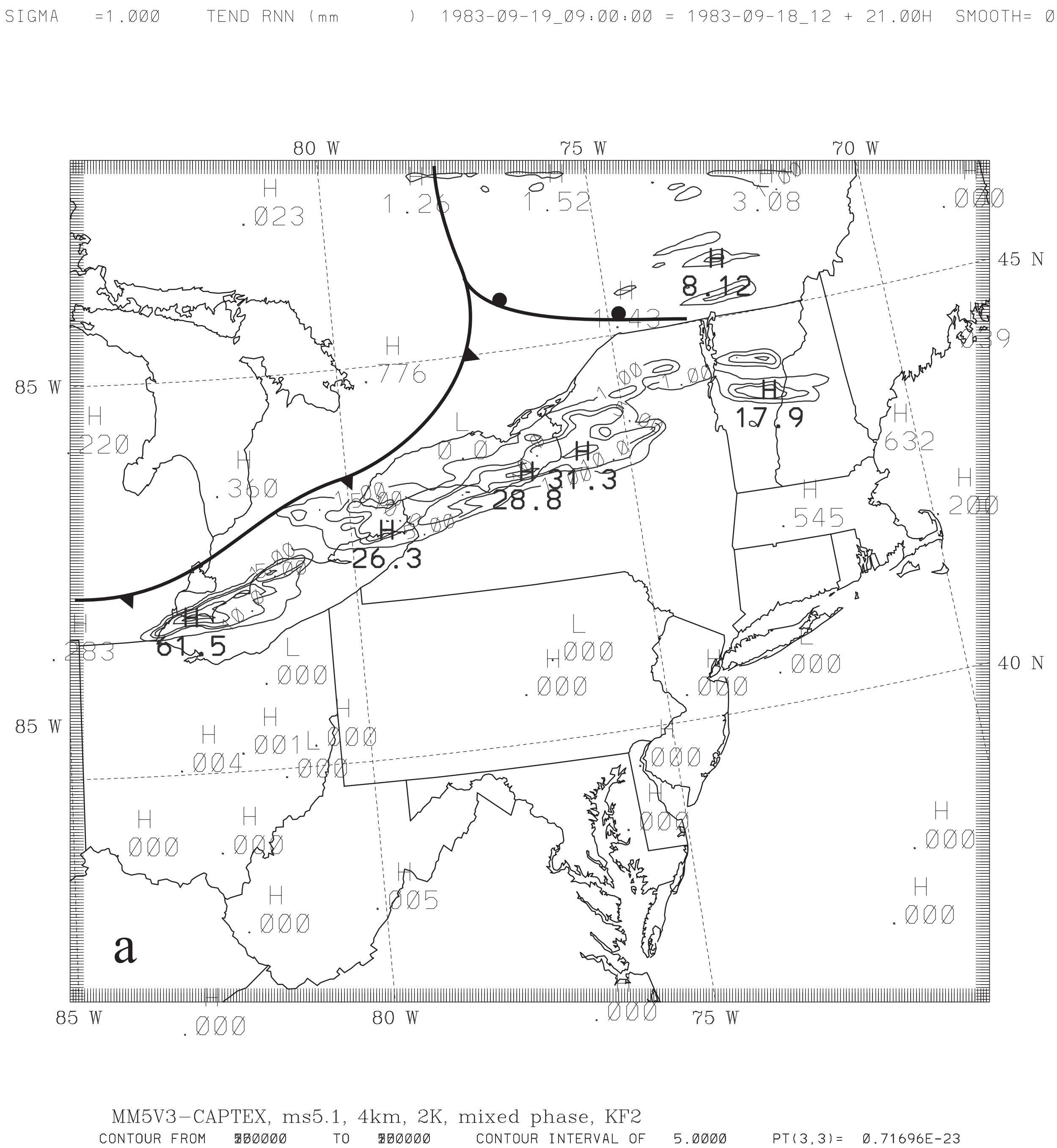

Figure 24 MM5 simulation of 3-h rainfall (mm) ending at 21 h (0900 UTC 19 September 1983) on the 4-km domain in Exp. MS5.1. Contours are 1, 5, 10, 20, 30 and 40 mm. (a) Non-convective (grid-resolved) rain, (b) Convective (parameterized) rain, (c) Total (non-convective plus convective) rain. Simulated front is shown on the figure for reference.

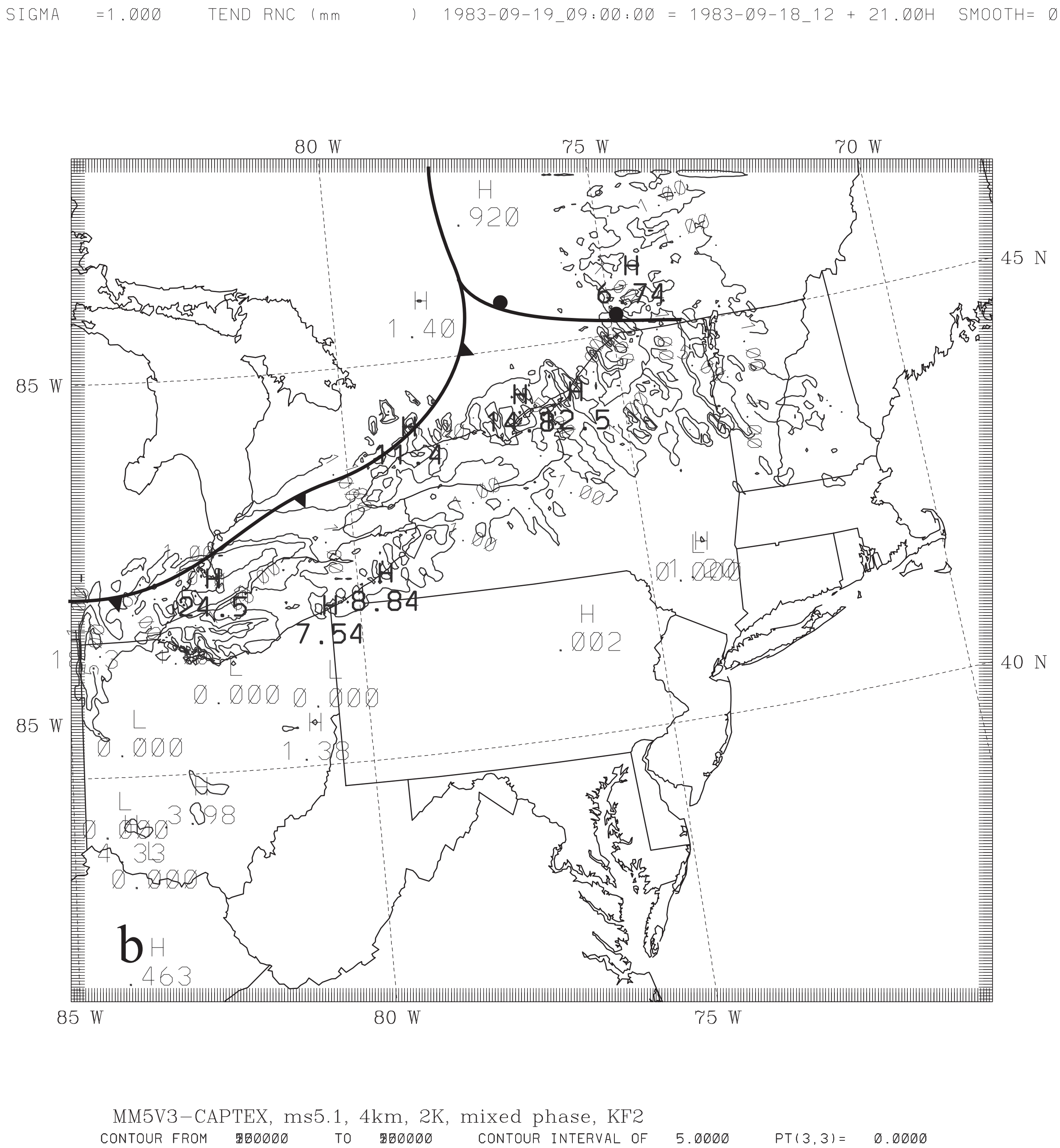

Figure 24 (Continued)

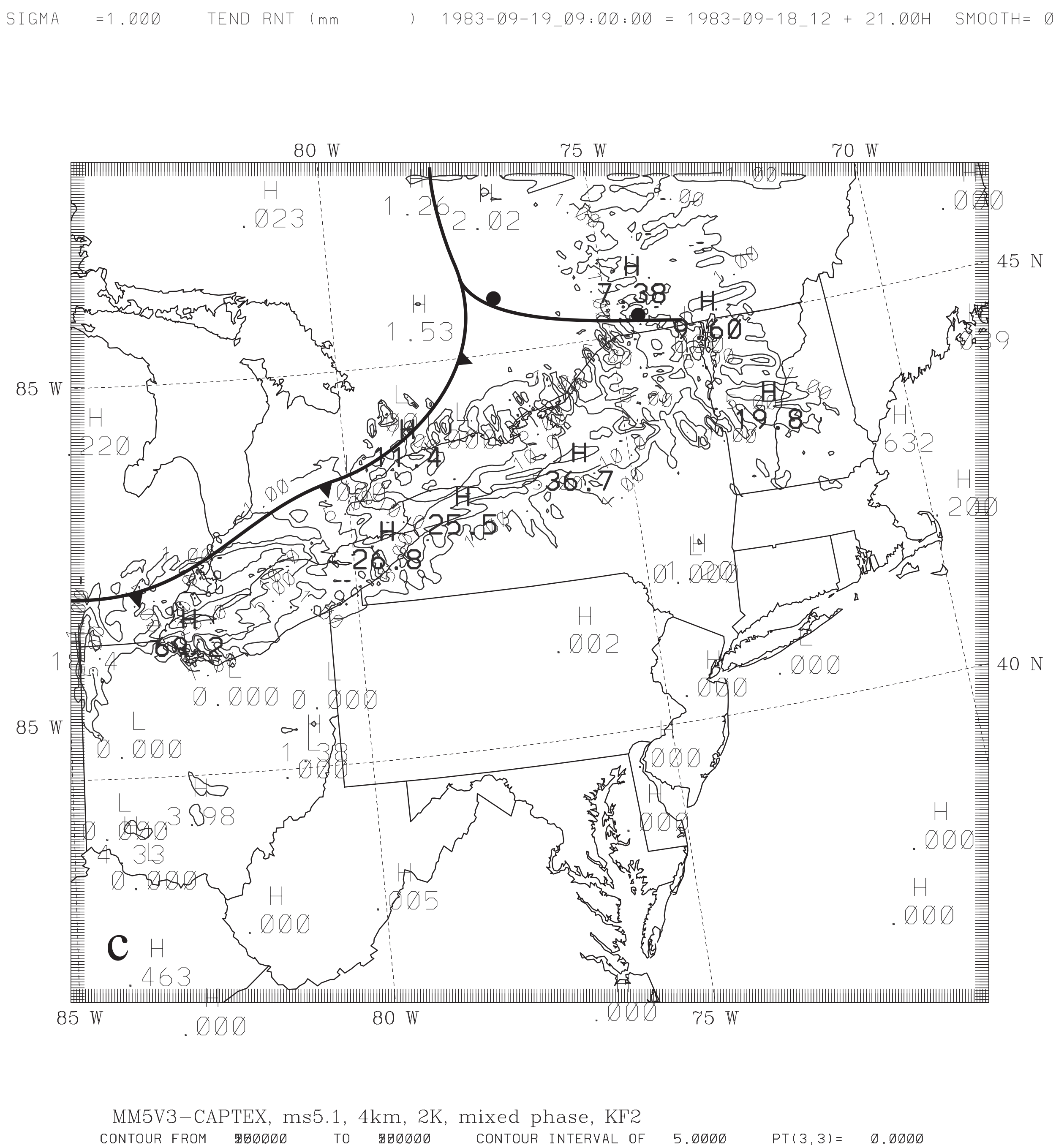

Figure 24 (Continued)

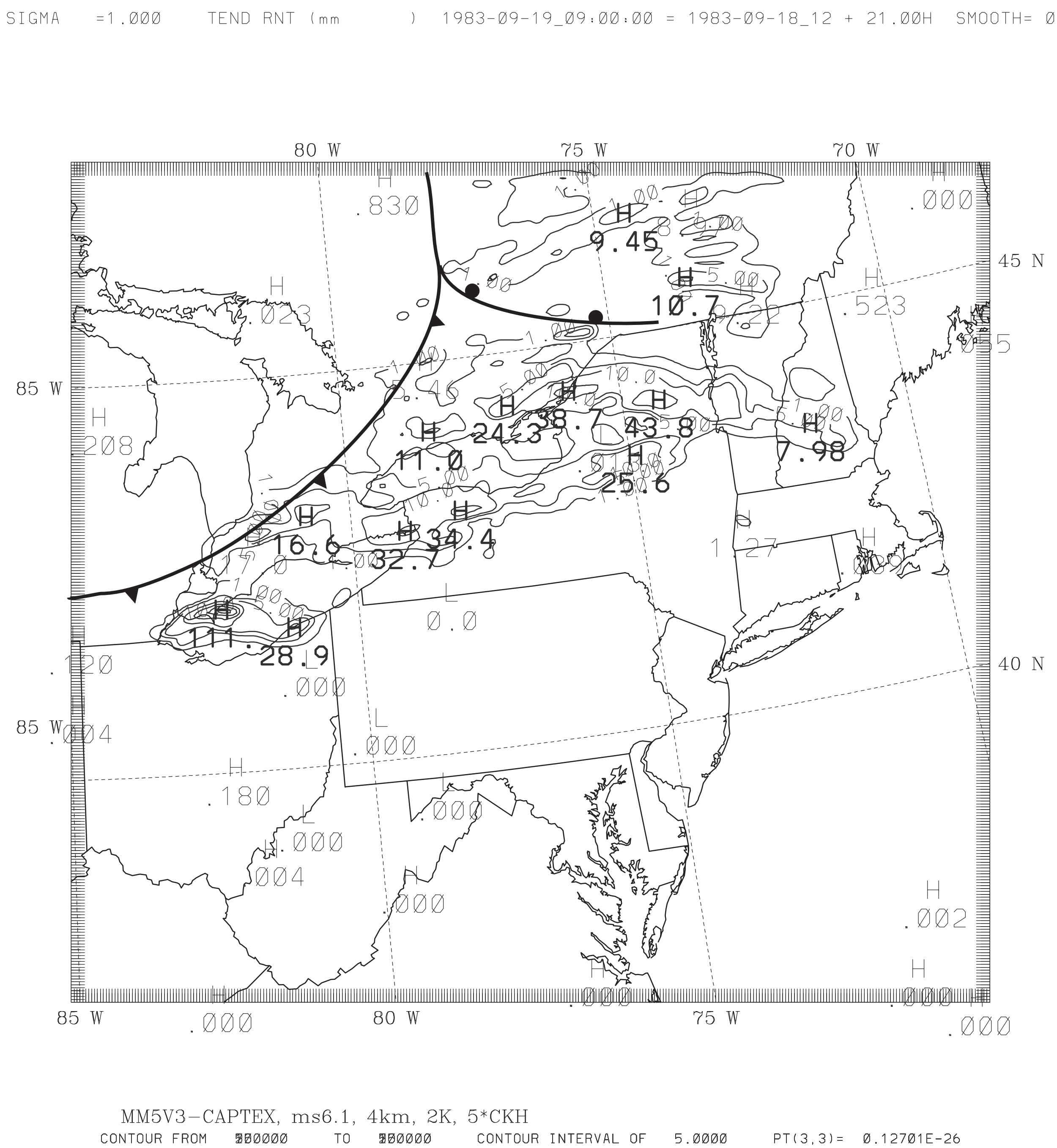

Figure 25 MM5 simulation of 3-h non-convective rainfall (mm) ending at 21 h (0900 UTC 19 September 1983) on the 4-km domain in Exp. MS6.1. Contours are 1, 5, 10, 20, 30 and 40 mm. Simulated front is shown on the figure for reference.

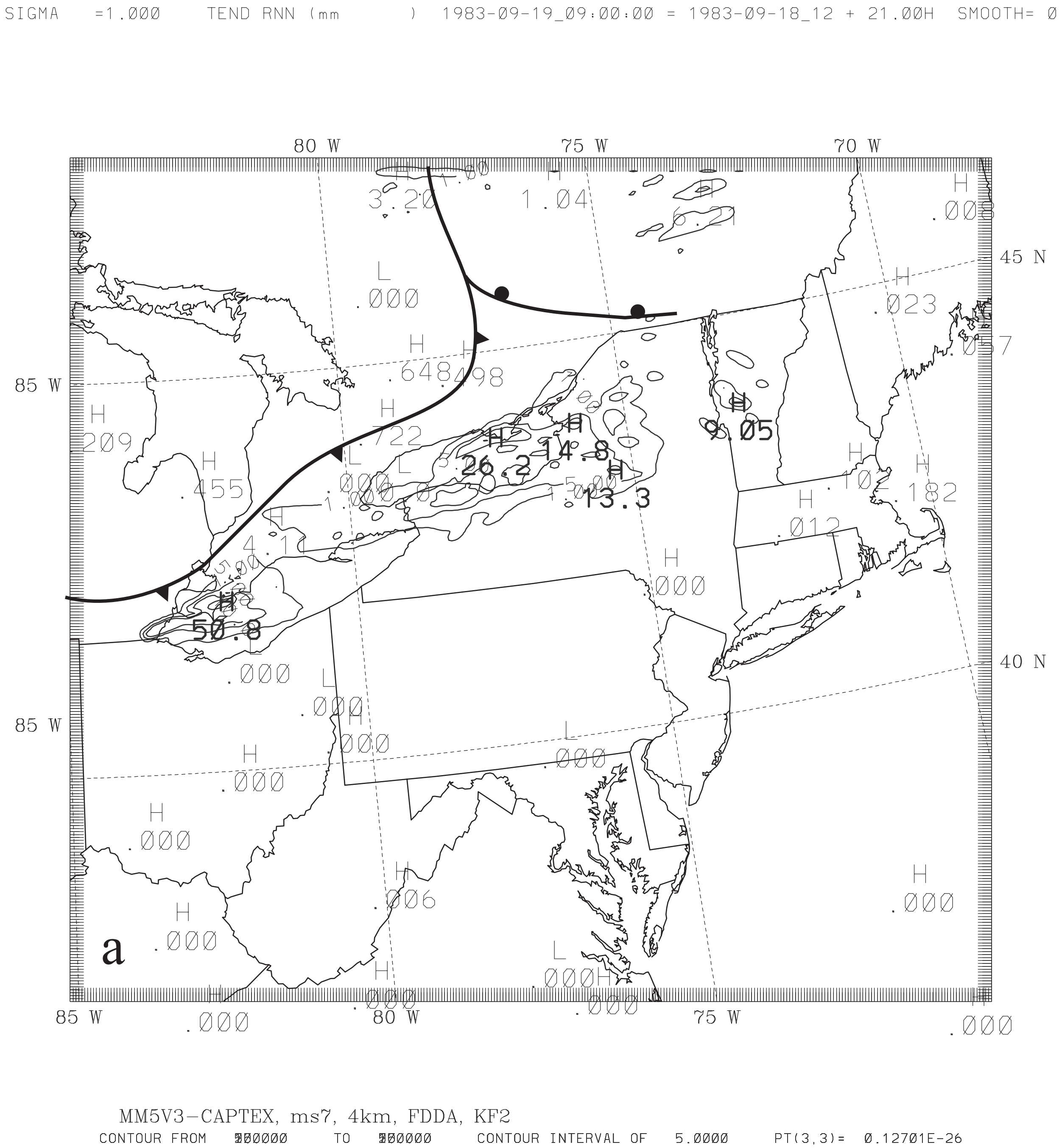

Figure 26 MM5-simulated fields at 21 h (0900 UTC 19 September 1983) on the 4-km domain in Exp. MS7. (a) Non-convective (grid-resolved) rain, (b) Convective (parameterized) rain, (c) Total (non-convective plus convective) rain, (d) Surface-layer wind (29 m AGL). Rain contours are 1, 5, 10, 20, 30 and 40 mm, and speed contours are 5 ms^{-1} and one barb is 10 ms^{-1}. Simulated front is shown on the figure for reference.

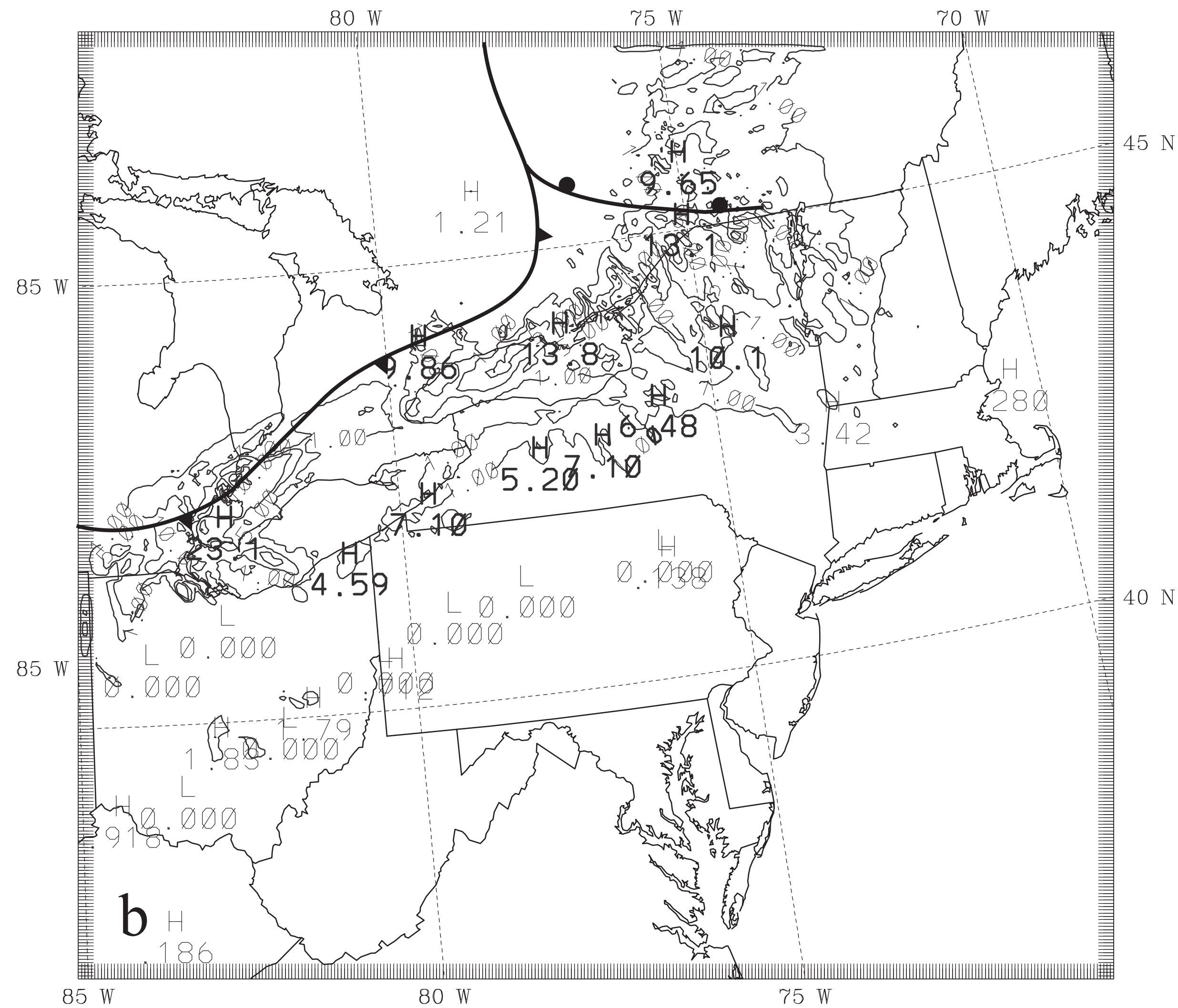

Figure 26 (Continued)

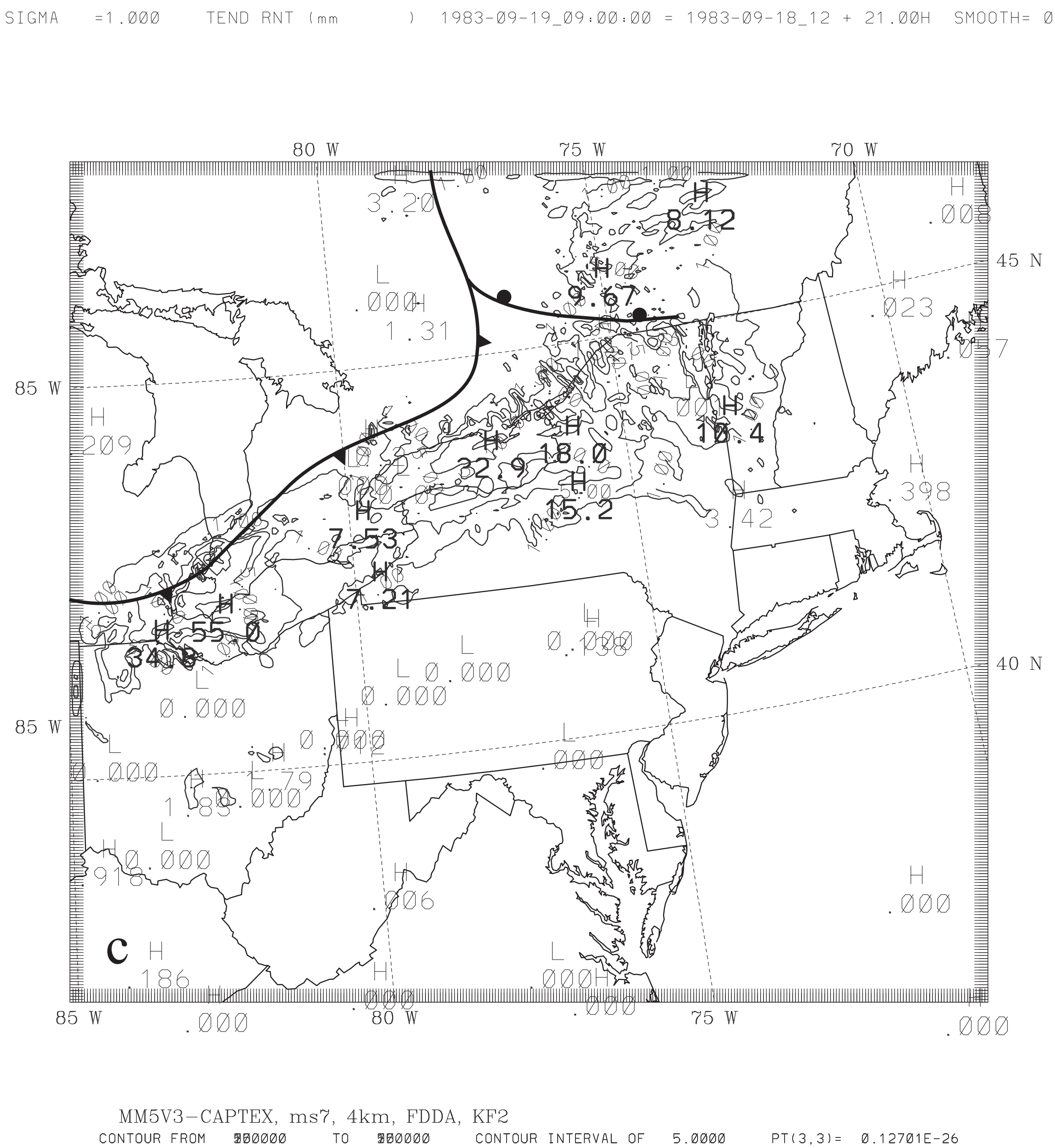

Figure 26 (Continued)

SIGMA =Ø.996 WIND UV (m/s) 1983-Ø9-19_Ø9:ØØ:ØØ = 1983-Ø9-18_12 + 21.ØØH SMOOTH= Ø
SIGMA =Ø.996 BARB UV (m/s) 1983-Ø9-19_Ø9:ØØ:ØØ = 1983-Ø9-18_12 + 21.ØØH SMOOTH= Ø

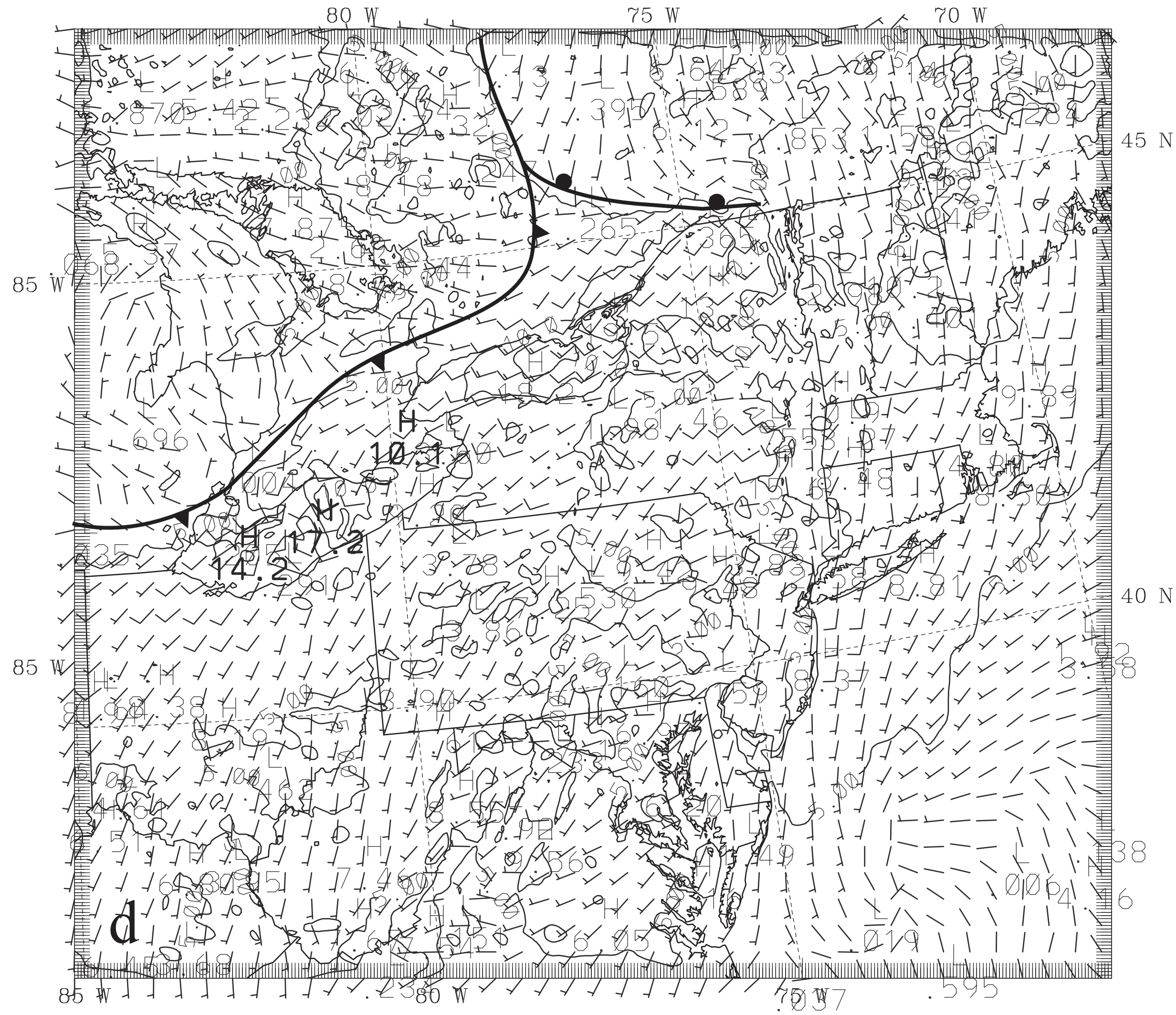

MM5V3-CAPTEX, ms7, 4km, FDDA, KF2
CONTOUR FROM Ø.ØØØØ TO 15.ØØØ CONTOUR INTERVAL OF 5.ØØØØ PT(3,3)= 4.47Ø5

Figure 26 (Continued)

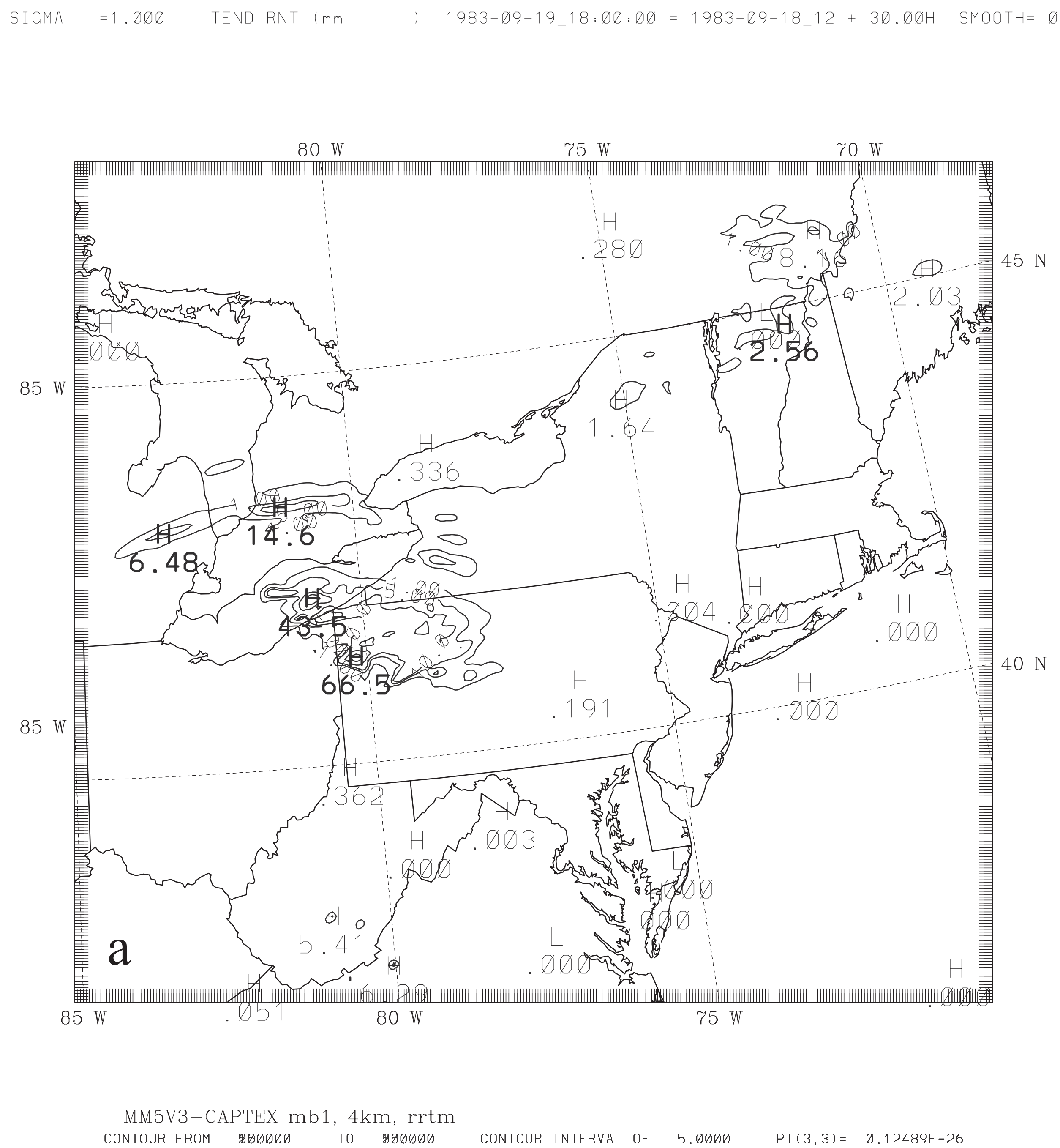

Figure 27 MM5-simulated fields at 30 h (1800 UTC 19 September 1983) on the 4-km domain in Exp. MB1. (a) Non-convective (grid-resolved) rain, (b) Surface-layer wind (29 m AGL), (c) Surface-layer temperature. Rain contours are 1, 5, 10, 20, 30 and 40 mm, speed contours are 5 ms^{-1} and one barb is 10 ms^{-1}, and temperature contours are 2 ºC. Dashed line in (b) indicates the outflow boundary.

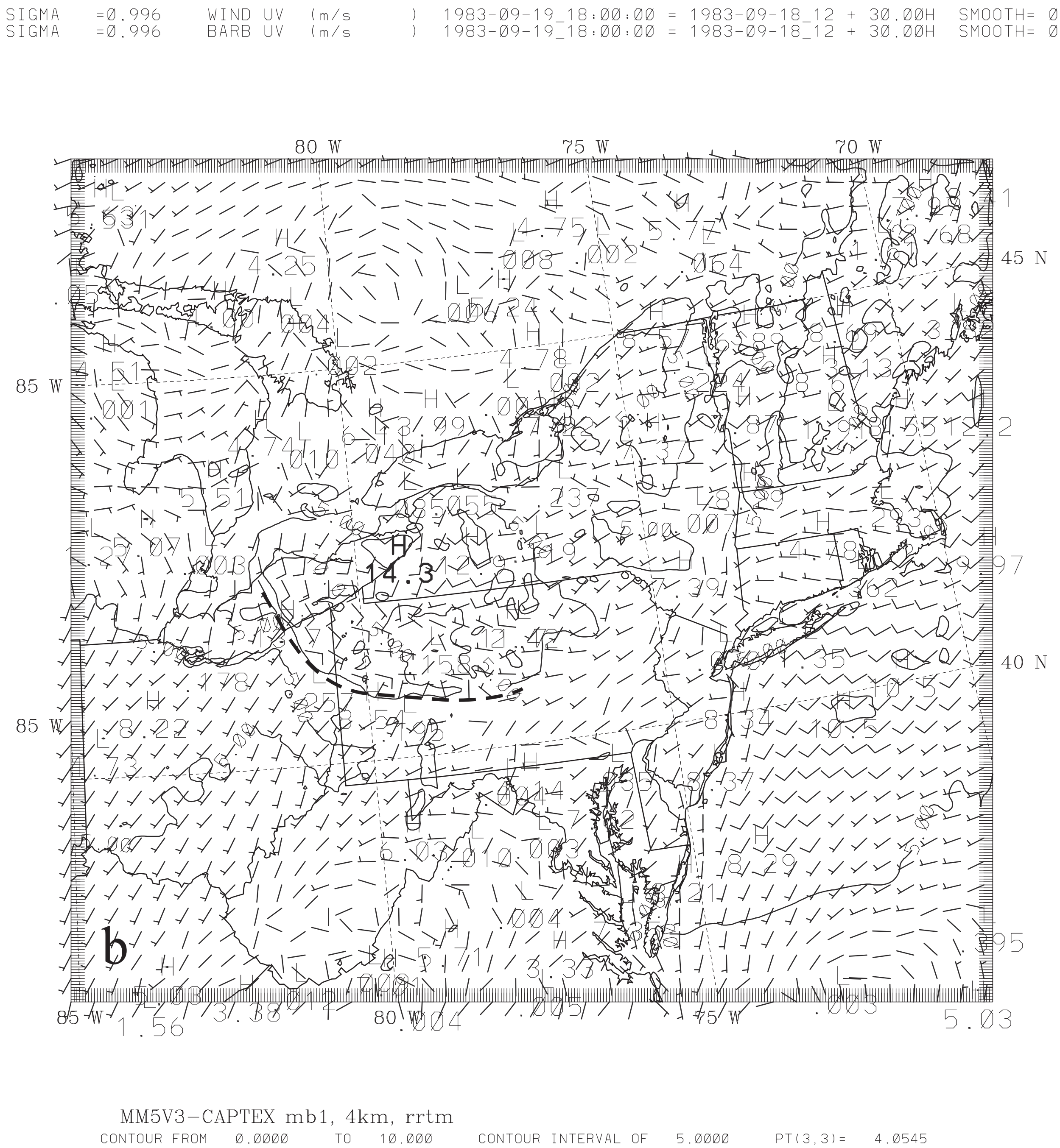

Figure 27 (Continued)

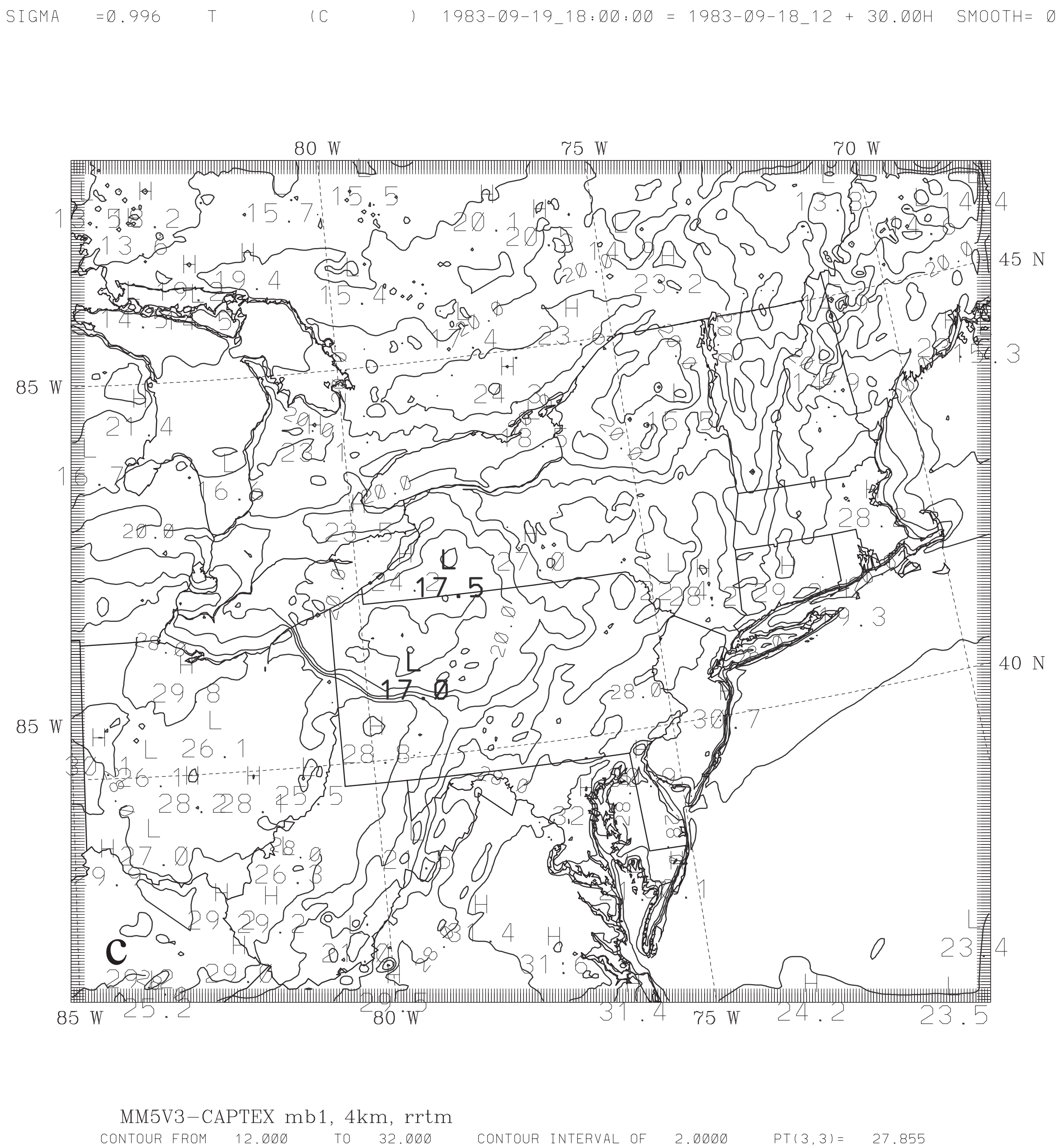

Figure 27 (Continued)

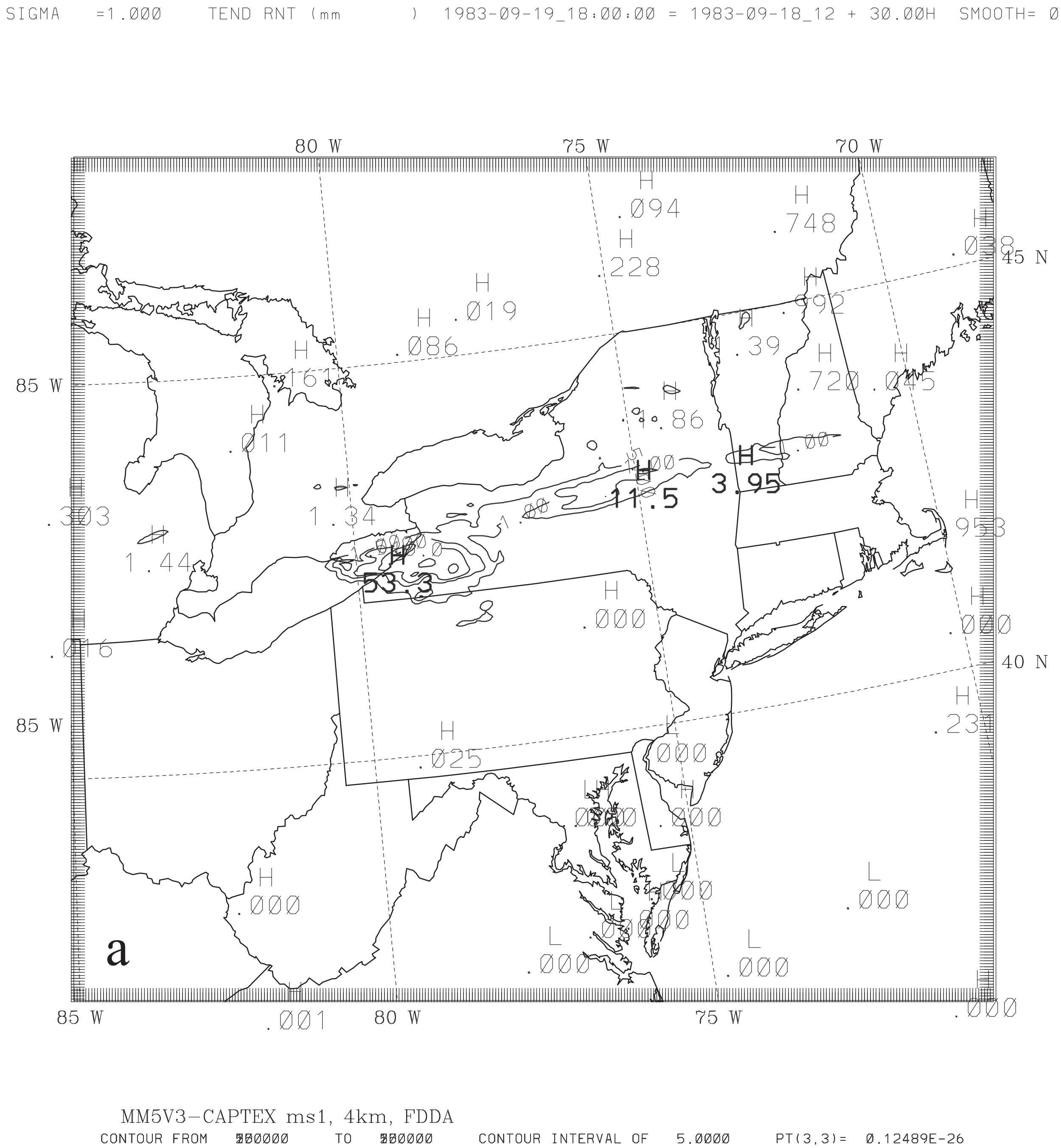

Figure 28 MM5-simulated fields at 30 h (1800 UTC 19 September 1983) on the 4-km domain in Exp. MS1. (a) Non-convective (grid-resolved) rain, (b) Surface-layer wind (29 m AGL), (c) Surface-layer temperature. Rain contours are 1, 5, 10, 20, 30 and 40 mm, speed contours are 5 ms^{-1} and one barb is 10 ms^{-1}, and temperature contours are 2 ºC. Dashed line in (b) indicates the outflow boundary.

SIGMA =0.996 WIND UV (m/s) 1983-09-19_18:00:00 = 1983-09-18_12 + 30.00H SMOOTH= 0
SIGMA =0.996 BARB UV (m/s) 1983-09-19_18:00:00 = 1983-09-18_12 + 30.00H SMOOTH= 0

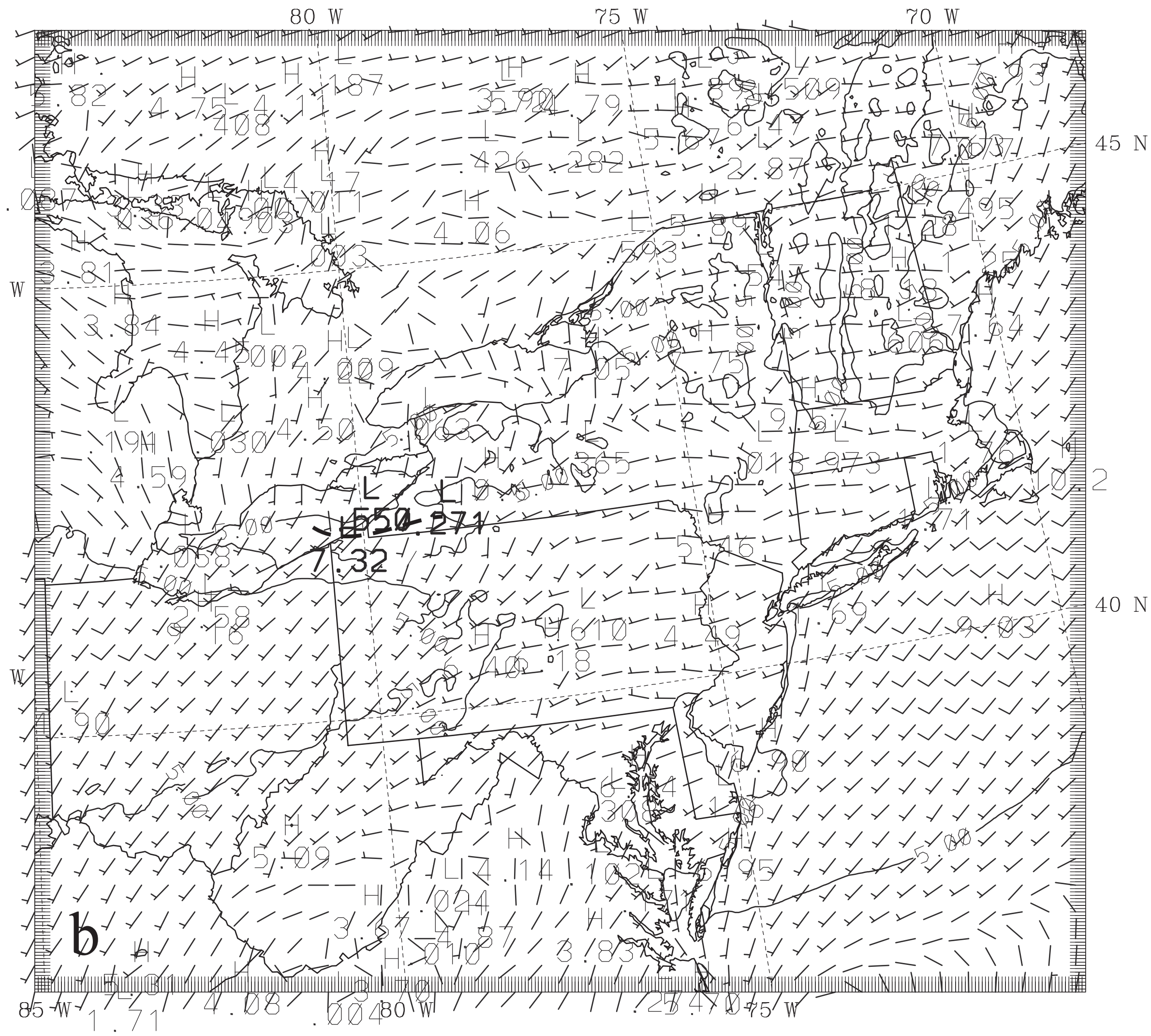

MM5V3-CAPTEX ms1, 4km, FDDA
CONTOUR FROM 0.0000 TO 10.000 CONTOUR INTERVAL OF 5.0000 PT(3,3)= 4.1559

Figure 28 (Continued)

SIGMA =0.996 T (C) 1983-09-19_18:00:00 = 1983-09-18_12 + 30.00H SMOOTH= 0

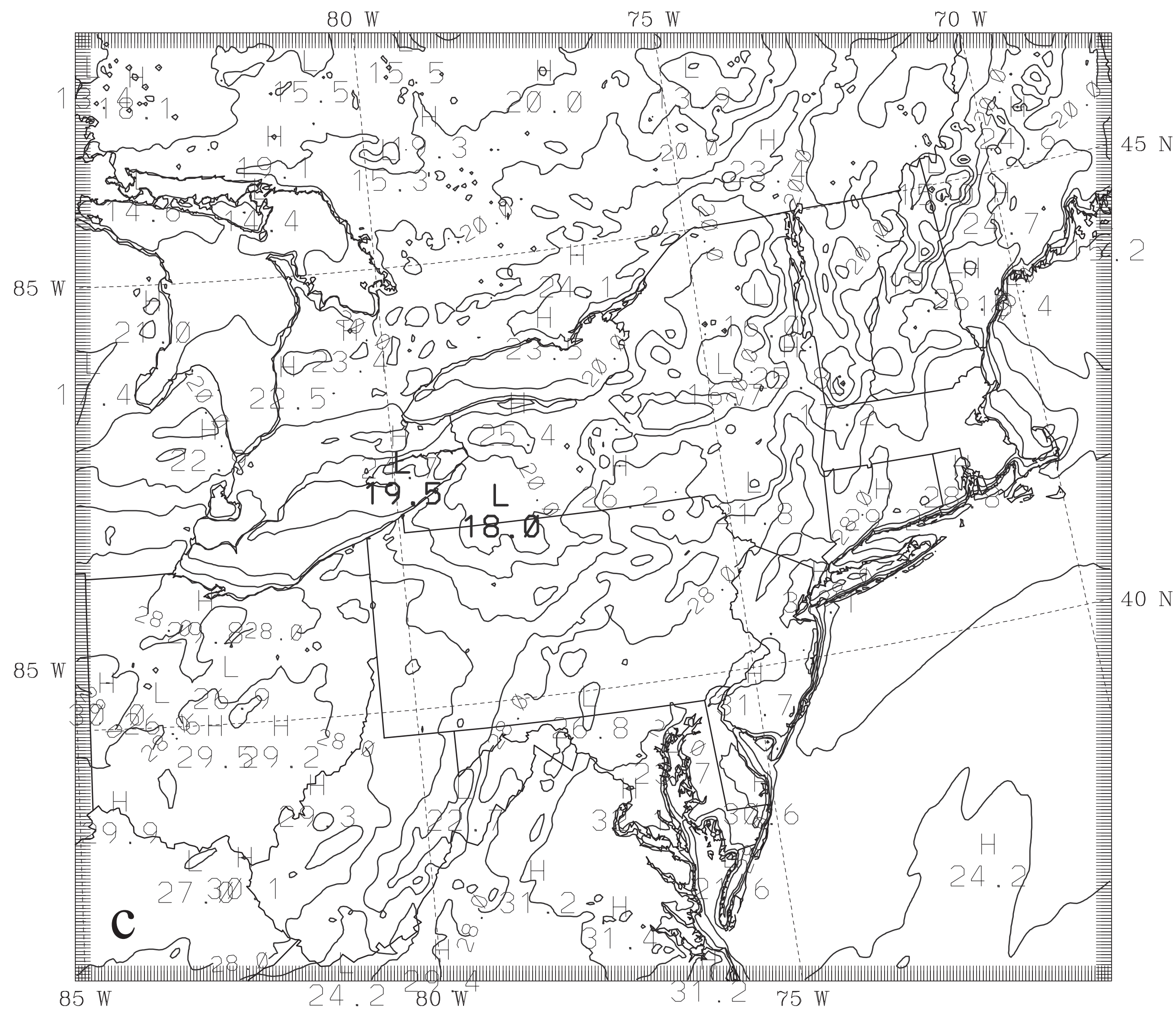

MM5V3-CAPTEX, ms1, 4km, FDDA
CONTOUR FROM 12.000 TO 32.000 CONTOUR INTERVAL OF 2.0000 PT(3,3)= 27.854

Figure 28 (Continued)

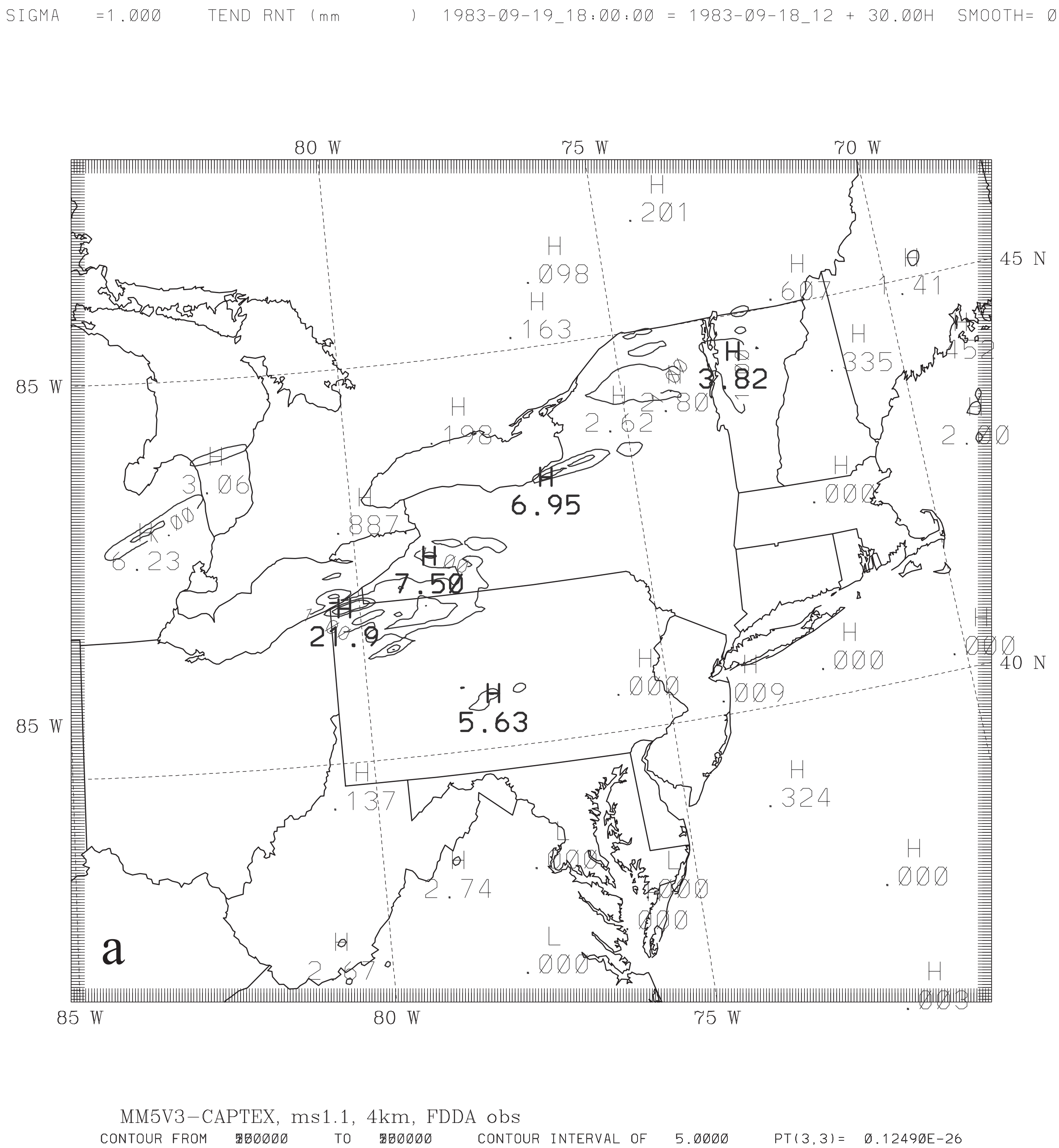

Figure 29 MM5-simulated fields at 30 h (1800 UTC 19 September 1983) on the 4-km domain in Exp. MS1.1. (a) Non-convective (grid-resolved) rain, (b) Surface-layer wind (29 m AGL), (c) Surface-layer temperature. Rain contours are 1, 5, 10, 20, 30 and 40 mm, speed contours are 5 ms^{-1} and one barb is 10 ms^{-1}, and temperature contours are 2 ºC. Dashed line in (b) indicates the out-flow boundary.

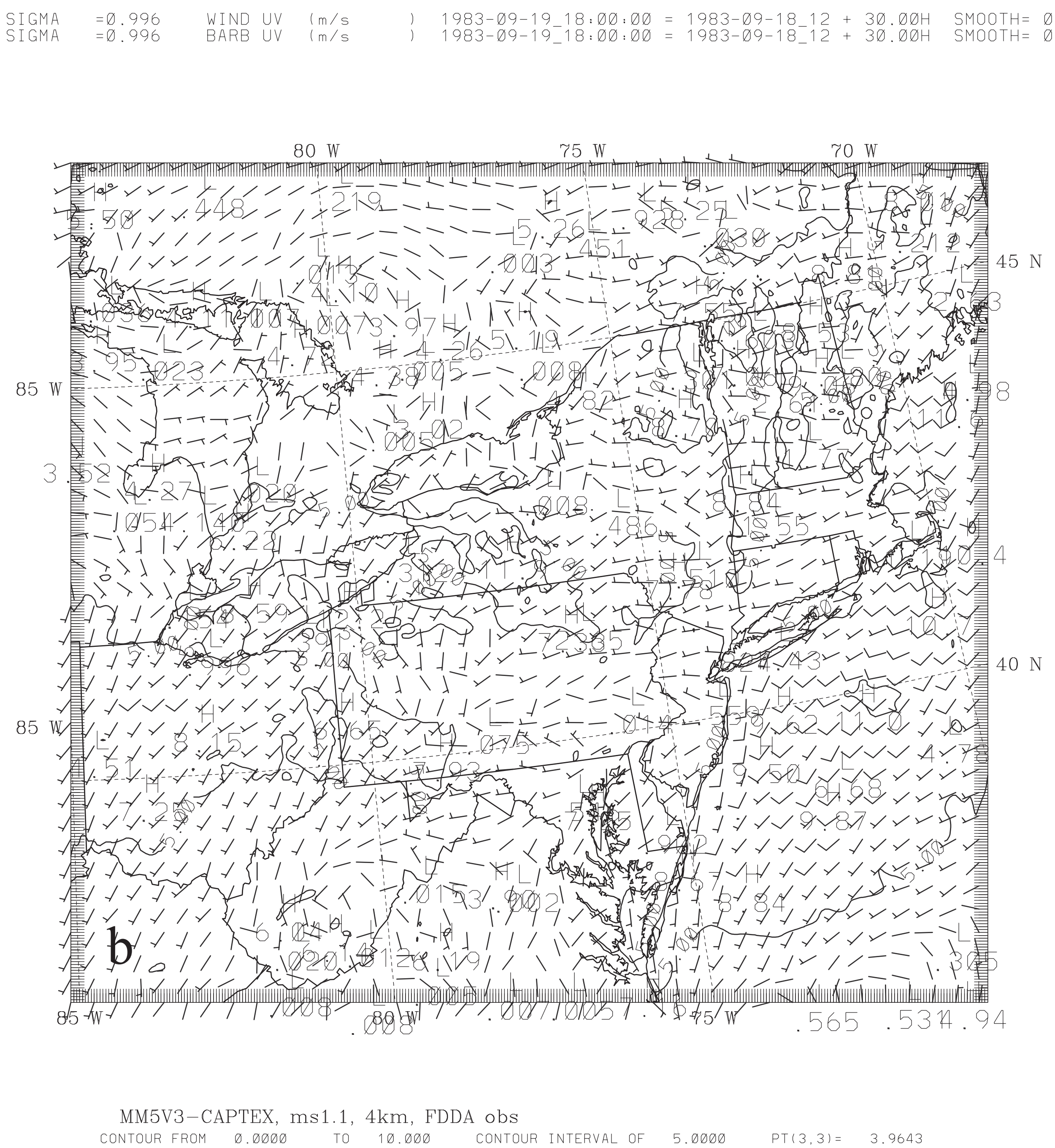

Figure 29 (Continued)

SIGMA =0.996 T (C) 1983-09-19_18:00:00 = 1983-09-18_12 + 30.00H SMOOTH= 0

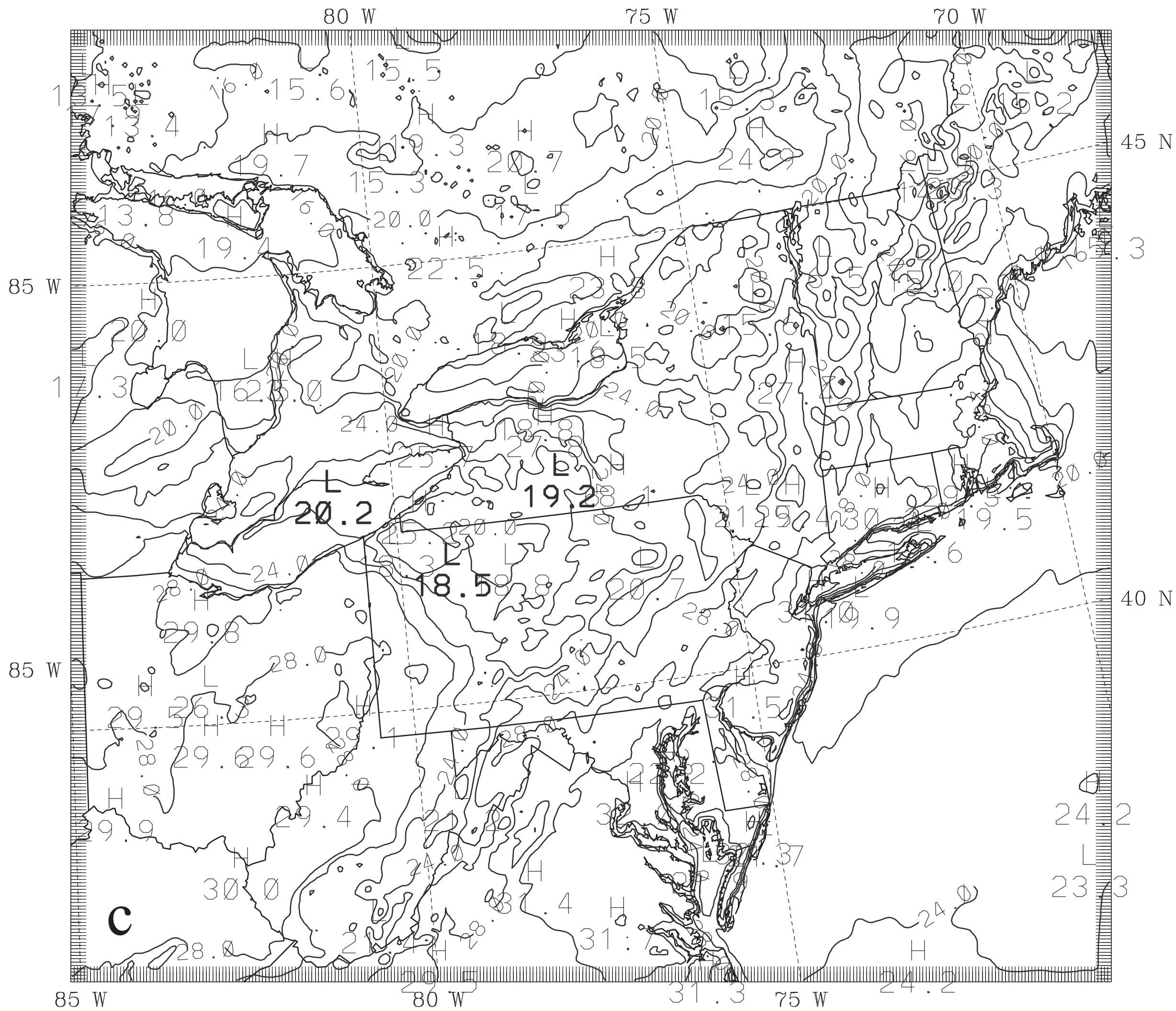

MM5V3–CAPTEX, ms1.1, 4km, FDDA obs
CONTOUR FROM 12.000 TO 30.000 CONTOUR INTERVAL OF 2.0000 PT(3,3)= 27.859

Figure 29 (Continued)

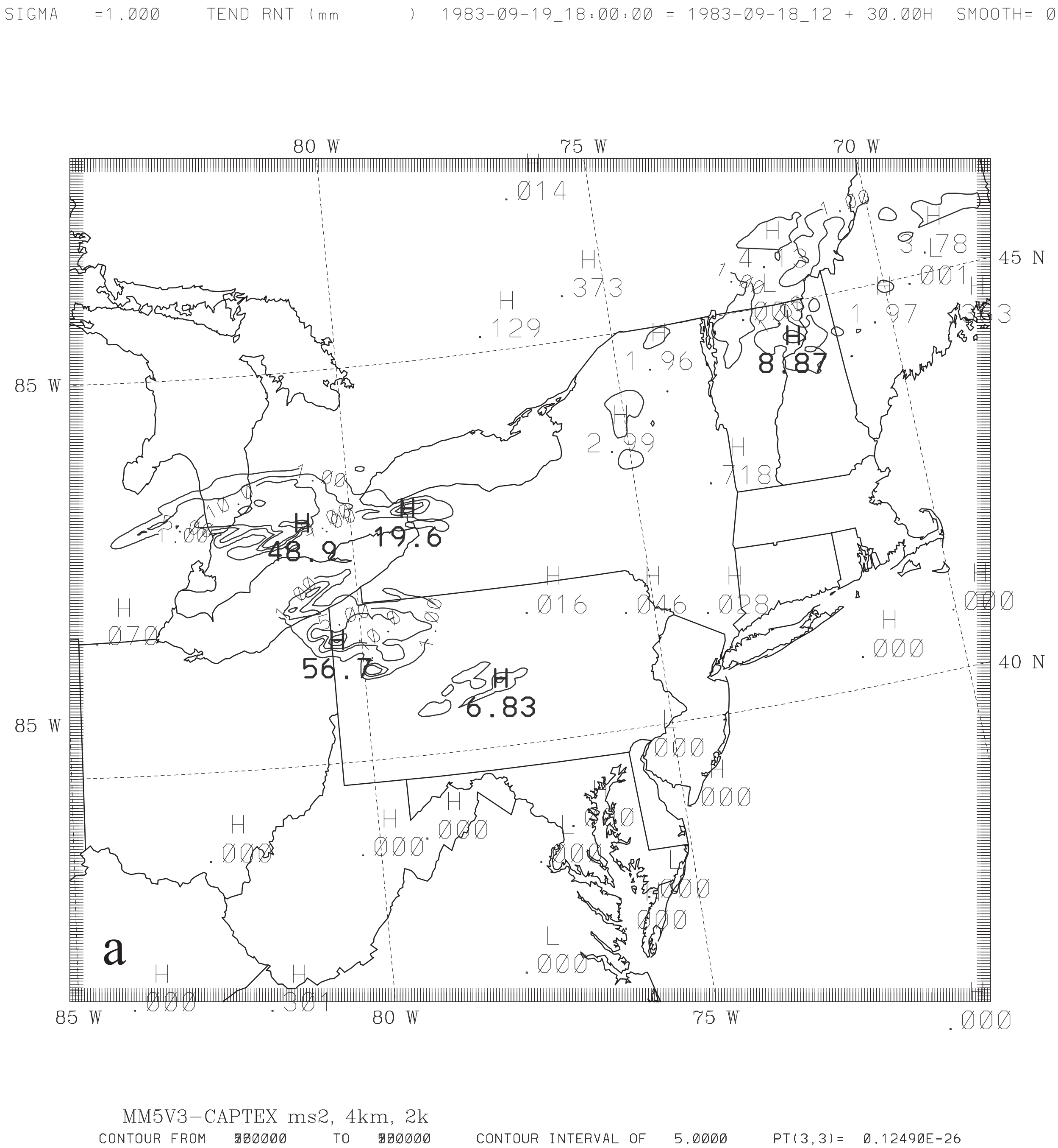

Figure 30 MM5-simulated fields at 30 h (1800 UTC 19 September 1983) on the 4-km domain in Exp. MS2 (MB2). (a) Non-convective (grid-resolved) rain, (b) Surface-layer wind (29 m AGL), (c) Surface-layer temperature. Rain contours are 1, 5, 10, 20, 30 and 40 mm, speed contours are 5 ms^{-1} and one barb is 10 ms^{-1}, and temperature contours are 2 ºC. Dashed line in (b) indicates the outflow boundary.

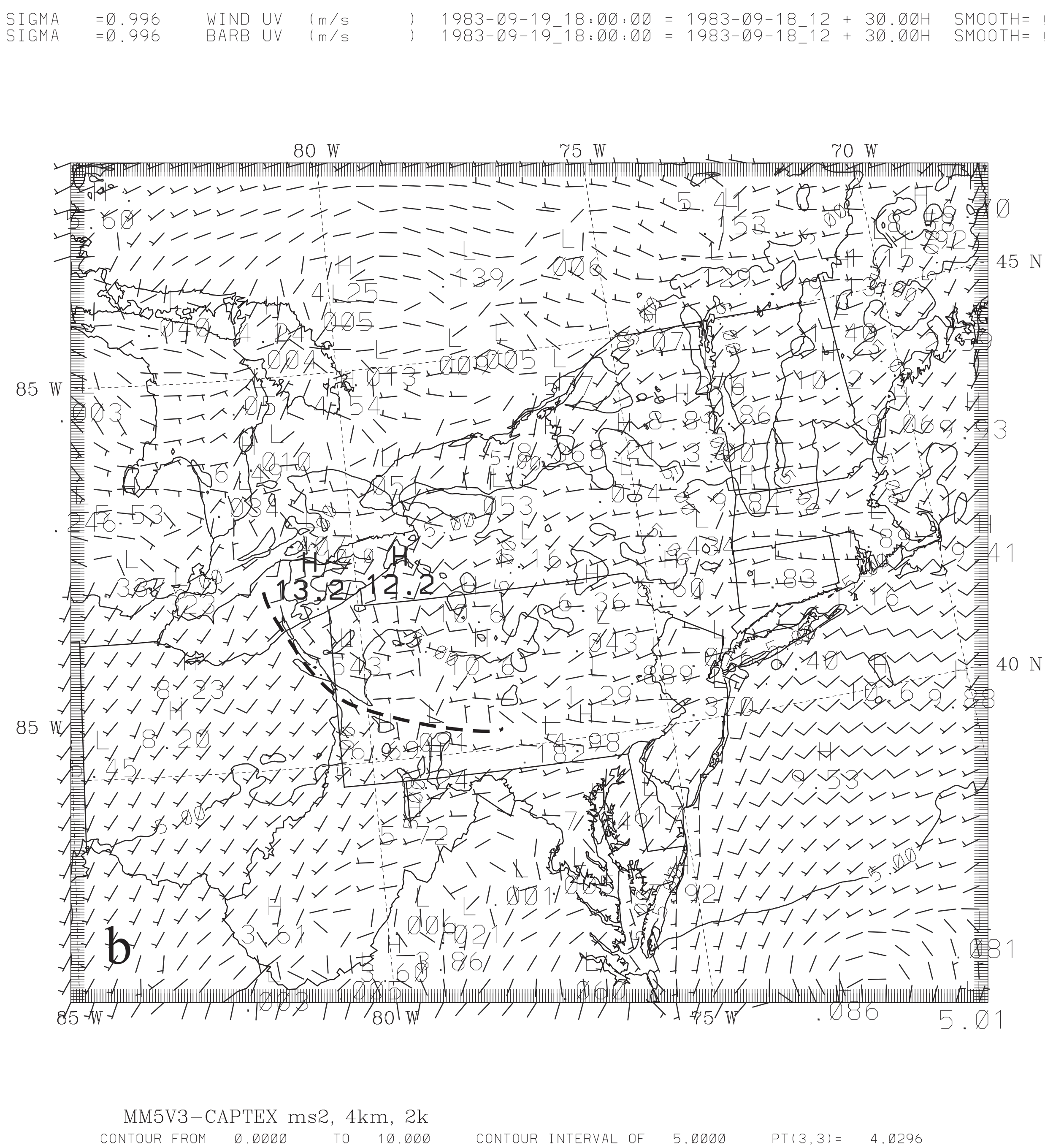

Figure 30 (Continued)

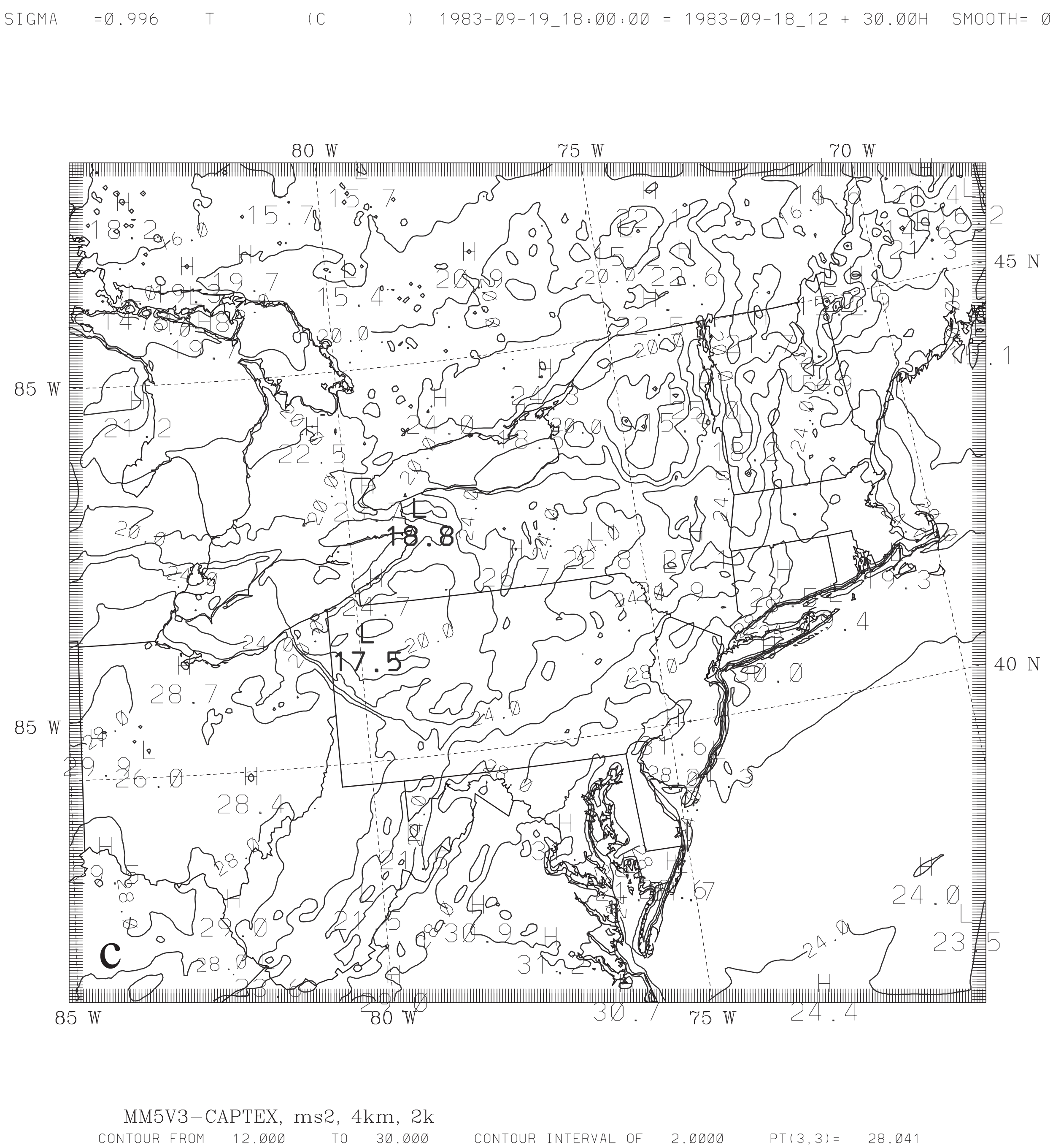

Figure 30 (Continued)

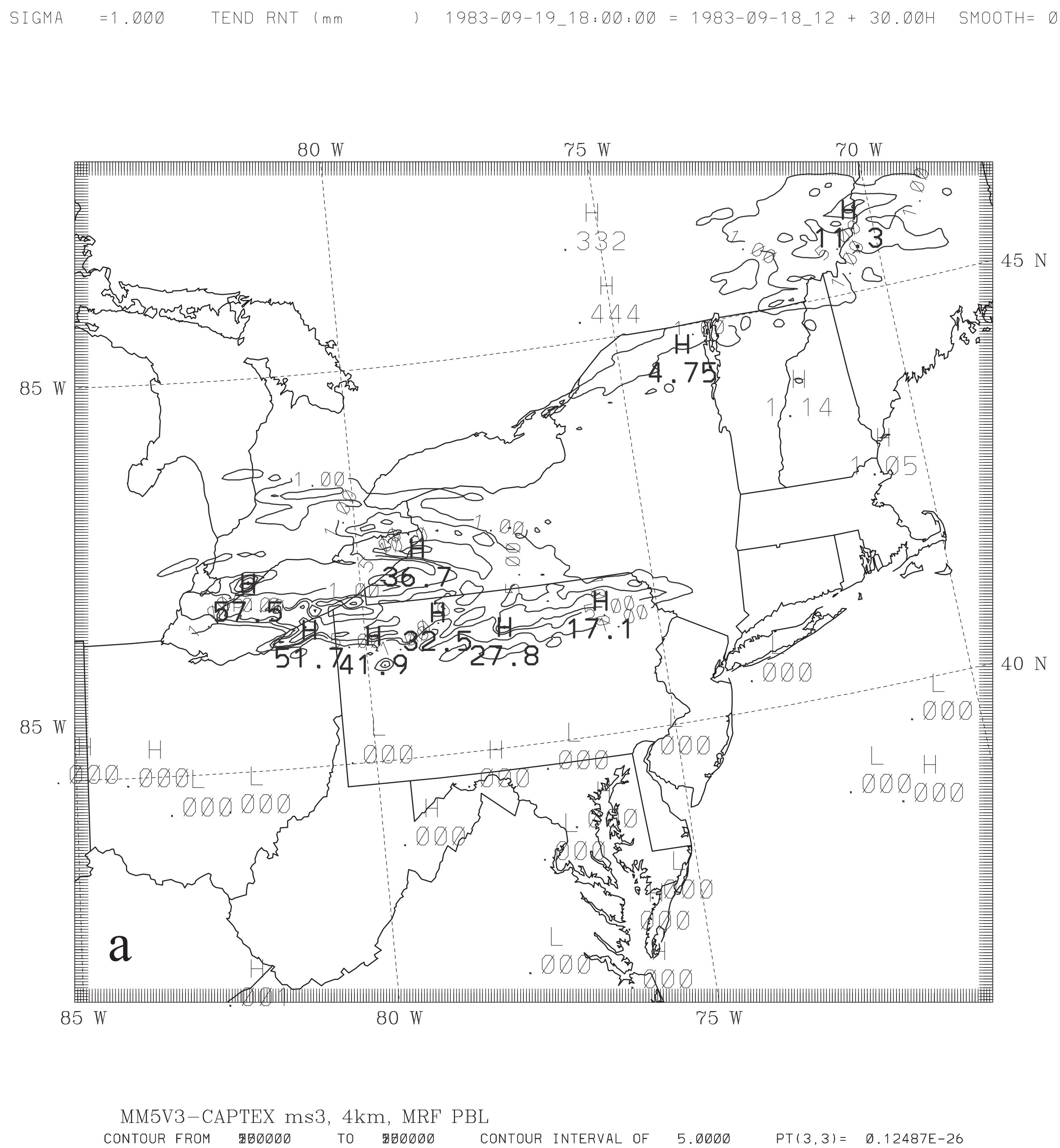

Figure 31 MM5-simulated fields at 30 h (1800 UTC 19 September 1983) on the 4-km domain in Exp. MS3. (a) Non-convective (grid-resolved) rain, (b) Surface-layer wind (29 m AGL), (c) Surface-layer temperature. Rain contours are 1, 5, 10, 20, 30 and 40 mm, speed contours are 5 ms^{-1} and one barb is 10 ms^{-1}, and temperature contours are 2 ºC. Dashed line in (b) indicates the outflow boundary.

SIGMA =0.996 WIND UV (m/s) 1983-09-19_18:00:00 = 1983-09-18_12 + 30.00H SMOOTH= 0
SIGMA =0.996 BARB UV (m/s) 1983-09-19_18:00:00 = 1983-09-18_12 + 30.00H SMOOTH= 0

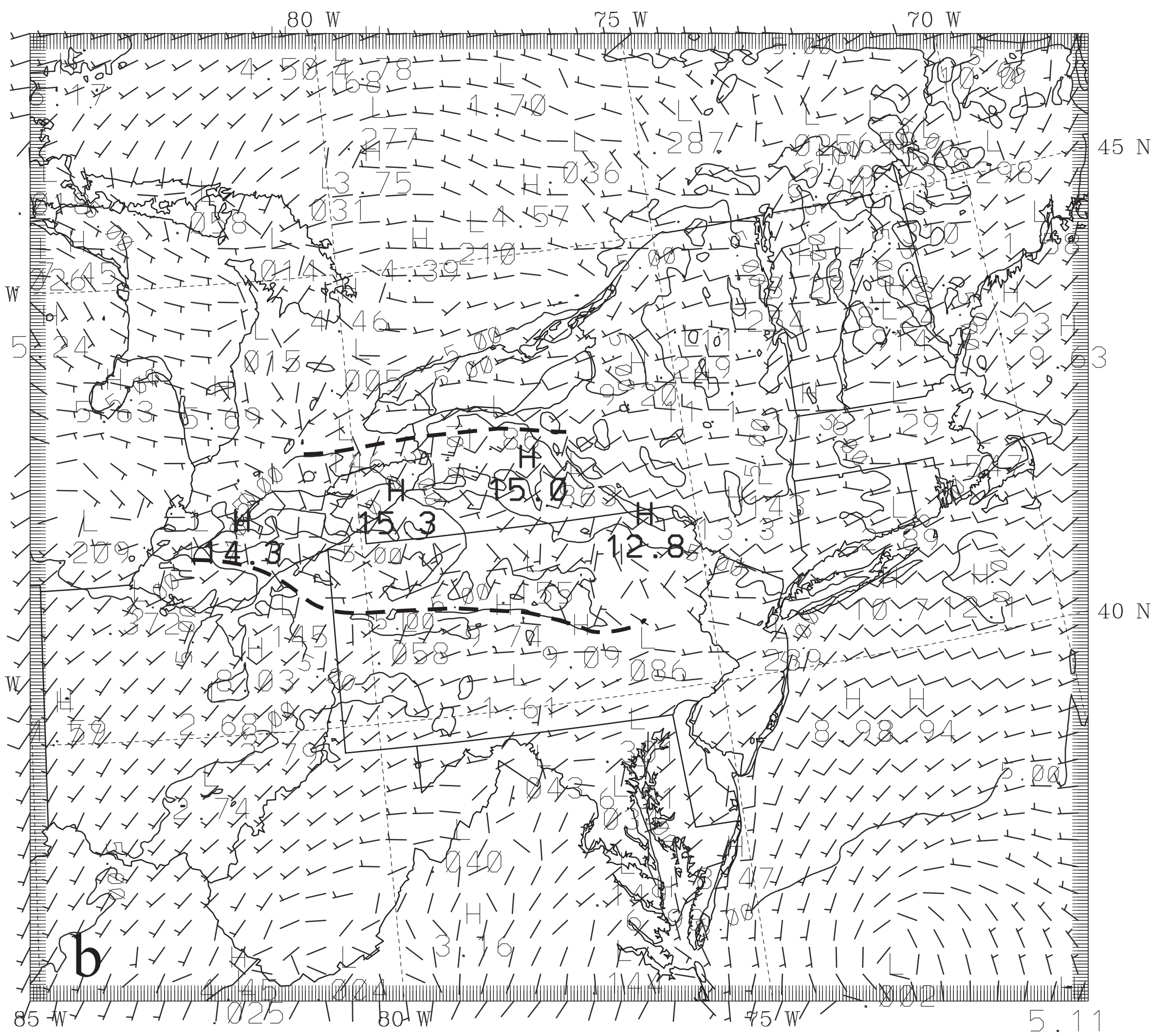

MM5V3-CAPTEX ms3, 4km, MRF PBL
CONTOUR FROM 0.0000 TO 15.000 CONTOUR INTERVAL OF 5.0000 PT(3,3)= 4.6816

Figure 31 (Continued)

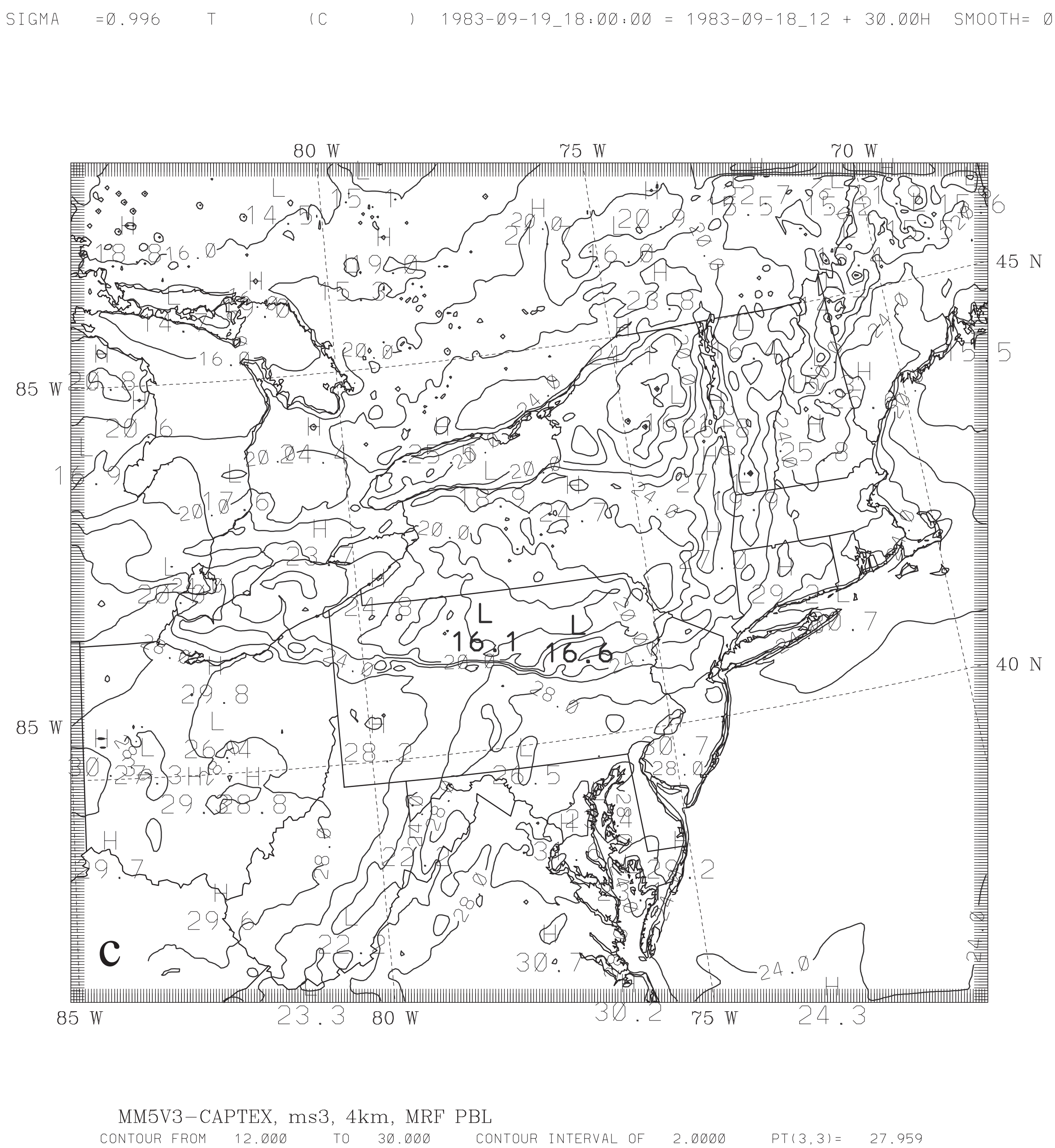

Figure 31 (Continued)

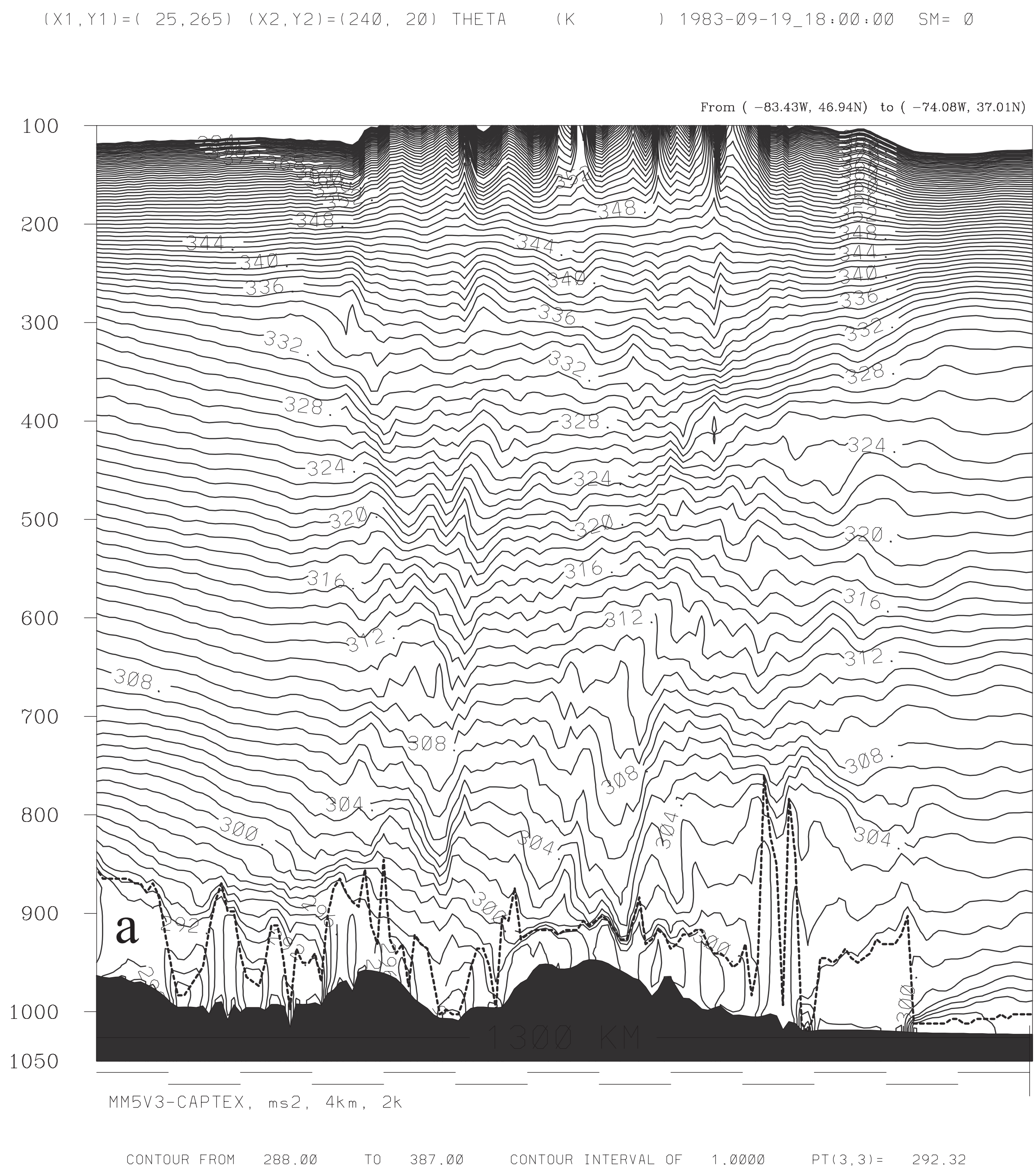

Figure 32 Cross-section of MM5-simulated fields on the 4-km domain at 30 h (1800 UTC, 19 September 1983). (a) potential temperature (K) for Exp. MS2 (MB2), (b) potential temperature (K) Exp. MS3 and (c) PBL depth for all experiments. Isentrope interval is 1 K. Dashed line indicates depth of the MM5 PBL. Location of the southwest-northeast cross section is shown in Figure 19. Line segments just below 1050 mb level each indicate 100 km distance from left

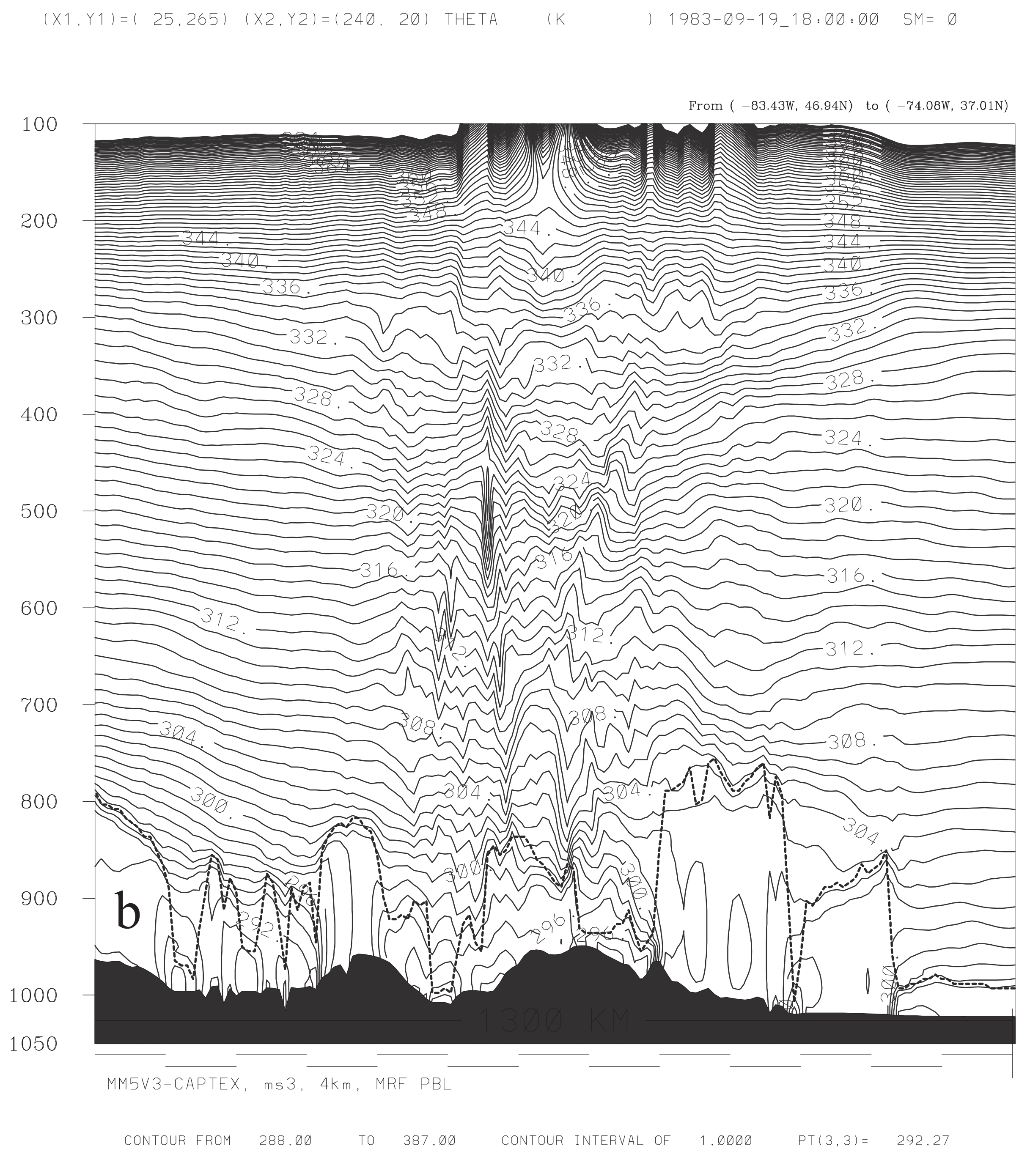

Figure 32 (Continued)

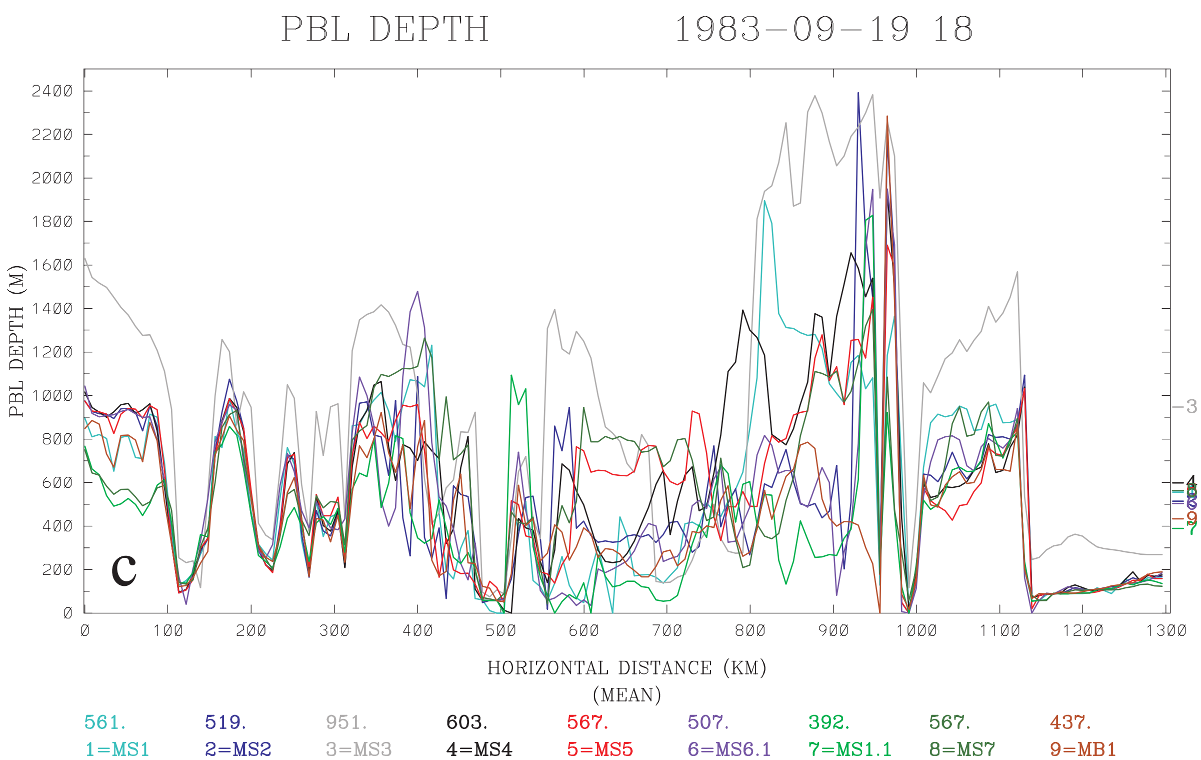

Figure 32 (Continued)

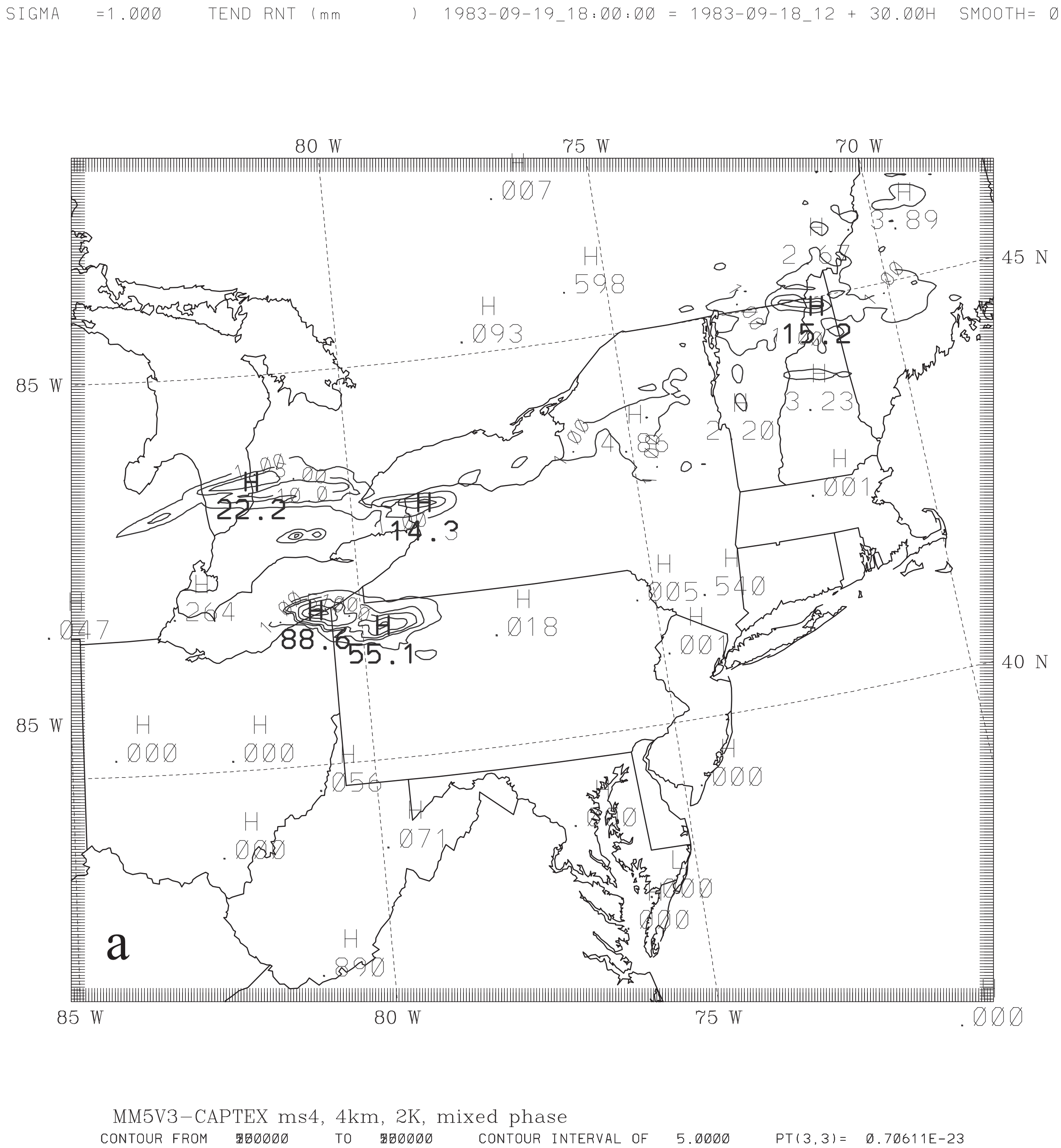

Figure 33 MM5-simulated fields at 30 h (1800 UTC 19 September 1983) on the 4-km domain in Exp. MS4. (a) Non-convective (grid-resolved) rain, (b) Surface-layer wind (29 m AGL) and (c) Surface-layer temperature. Rain contours are 1, 5, 10, 20, 30 and 40 mm, speed contours are 5 ms^{-1} and one barb is 10 ms^{-1}, and temperature contours are 2 ºC. Dashed line in (b) indicates the outflow boundary.

SIGMA =0.996 WIND UV (m/s) 1983-09-19_18:00:00 = 1983-09-18_12 + 30.00H SMOOTH= 0
SIGMA =0.996 BARB UV (m/s) 1983-09-19_18:00:00 = 1983-09-18_12 + 30.00H SMOOTH= 0

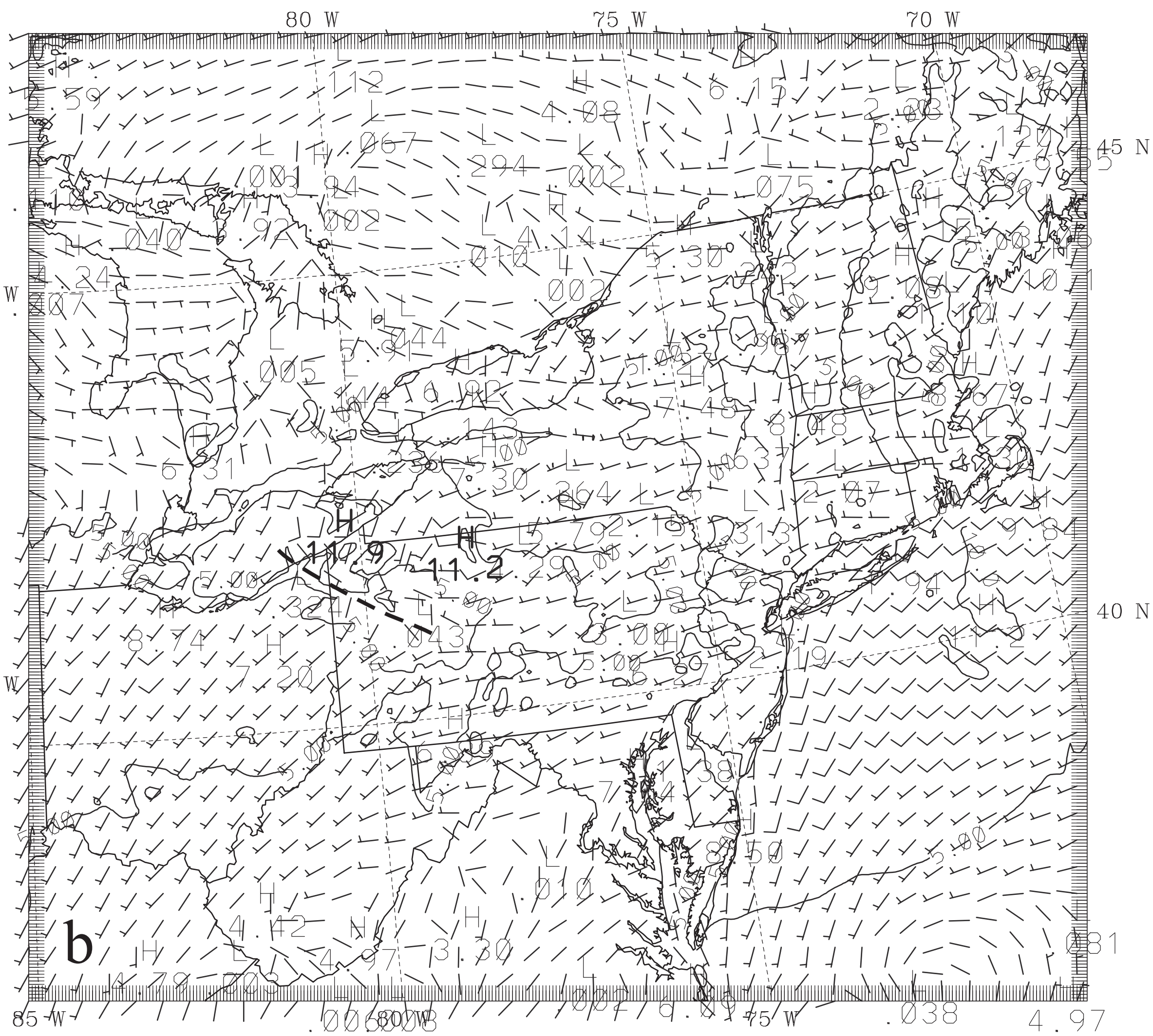

MM5V3–CAPTEX ms4, 4km, 2K, mixed phase
CONTOUR FROM 0.0000 TO 10.000 CONTOUR INTERVAL OF 5.0000 PT(3,3)= 4.0453

Figure 33 (Continued)

SIGMA =0.996 T (C) 1983-09-19_18:00:00 = 1983-09-18_12 + 30.00H SMOOTH= 0

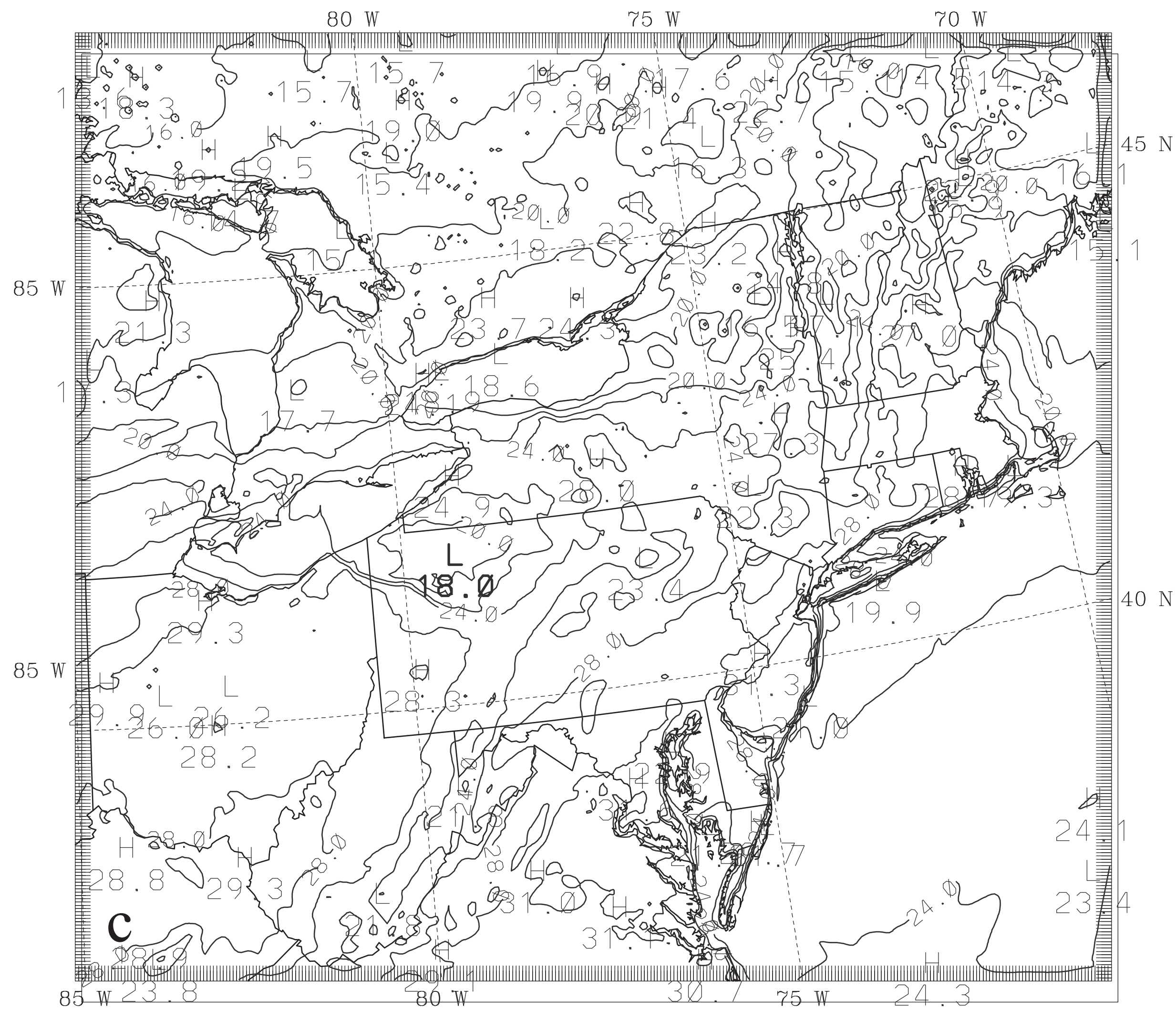

MM5V3–CAPTEX, ms4, 4km, 2K, mixed phase
CONTOUR FROM 12.000 TO 30.000 CONTOUR INTERVAL OF 2.0000 PT(3,3)= 28.025

Figure 33 (Continued)

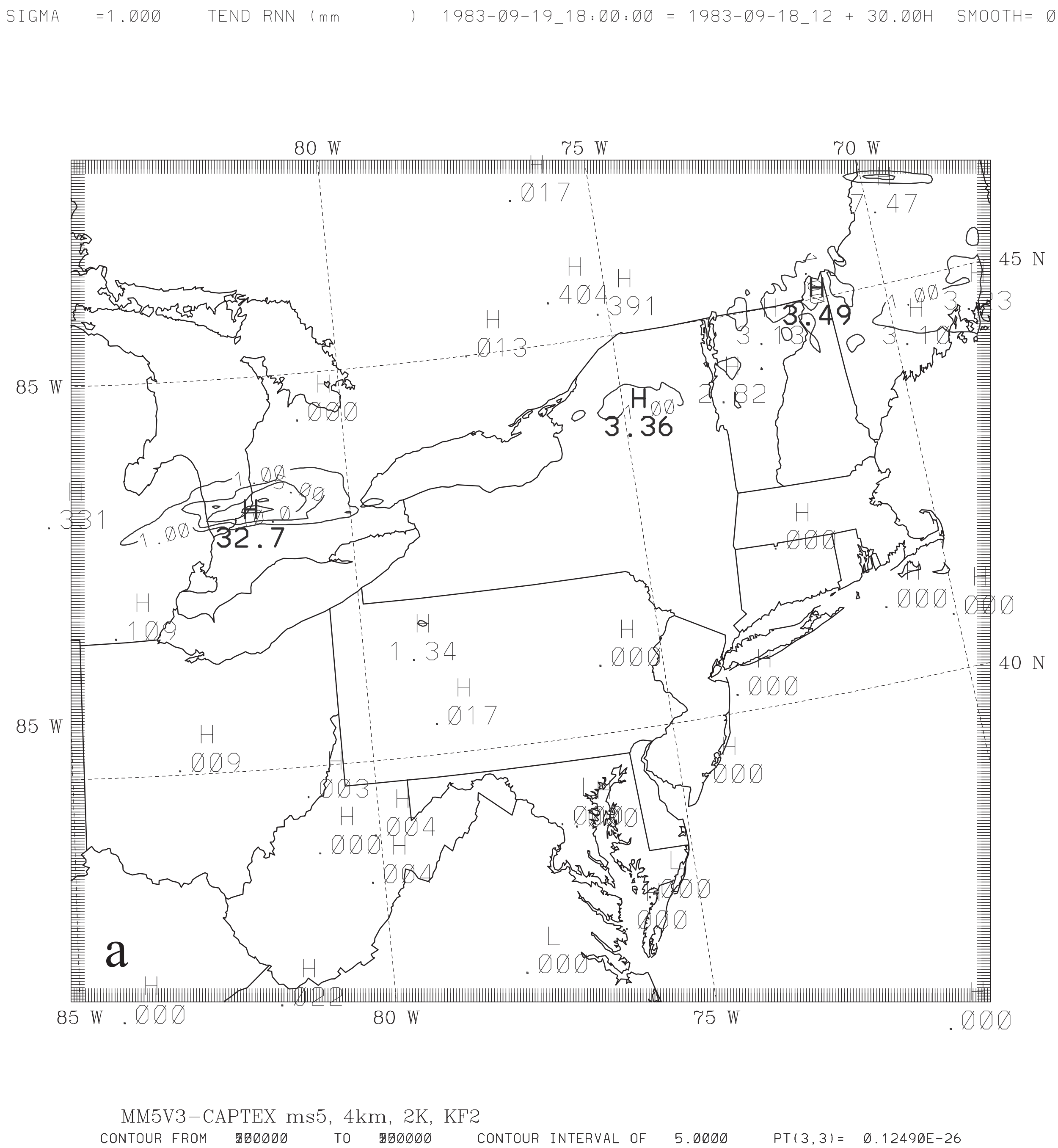

Figure 34 MM5-simulated fields at 30 h (1800 UTC 19 September 1983) on the 4-km domain in Exp. MS5. (a) Non-convective (grid-resolved) rain, (b) Convective (parameterized) rain, (c) Total (non-convective plus convective) rain, (d) Surface-layer wind (29 m AGL), (e) Surface-layer temperature. Rain contours are 1, 5, 10, 20, 30 and 40 mm, speed contours are 5 ms^{-1} and one barb is 10 ms^{-1}, and temperature contours are 2 ºC.

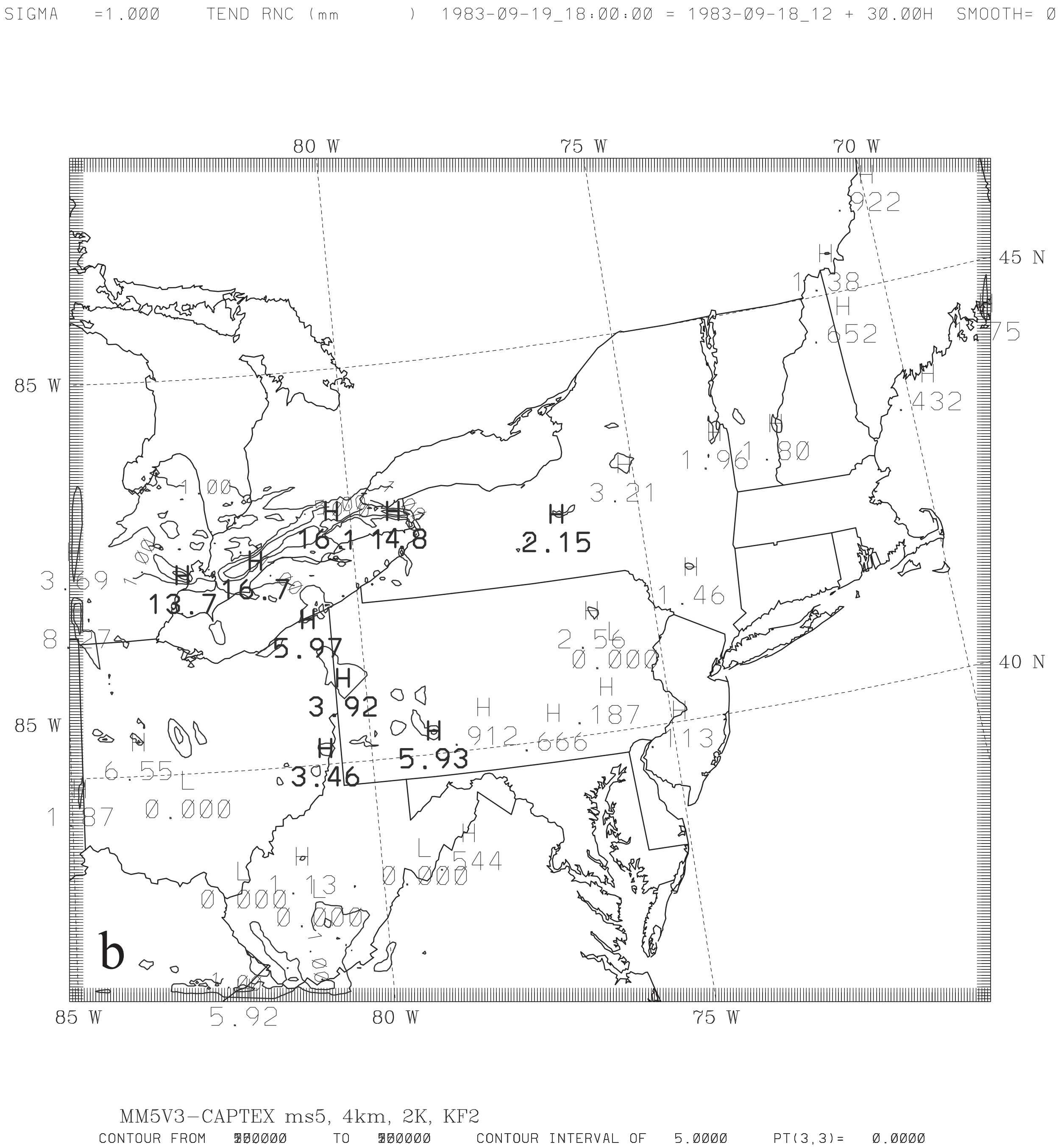

Figure 34 (Continued)

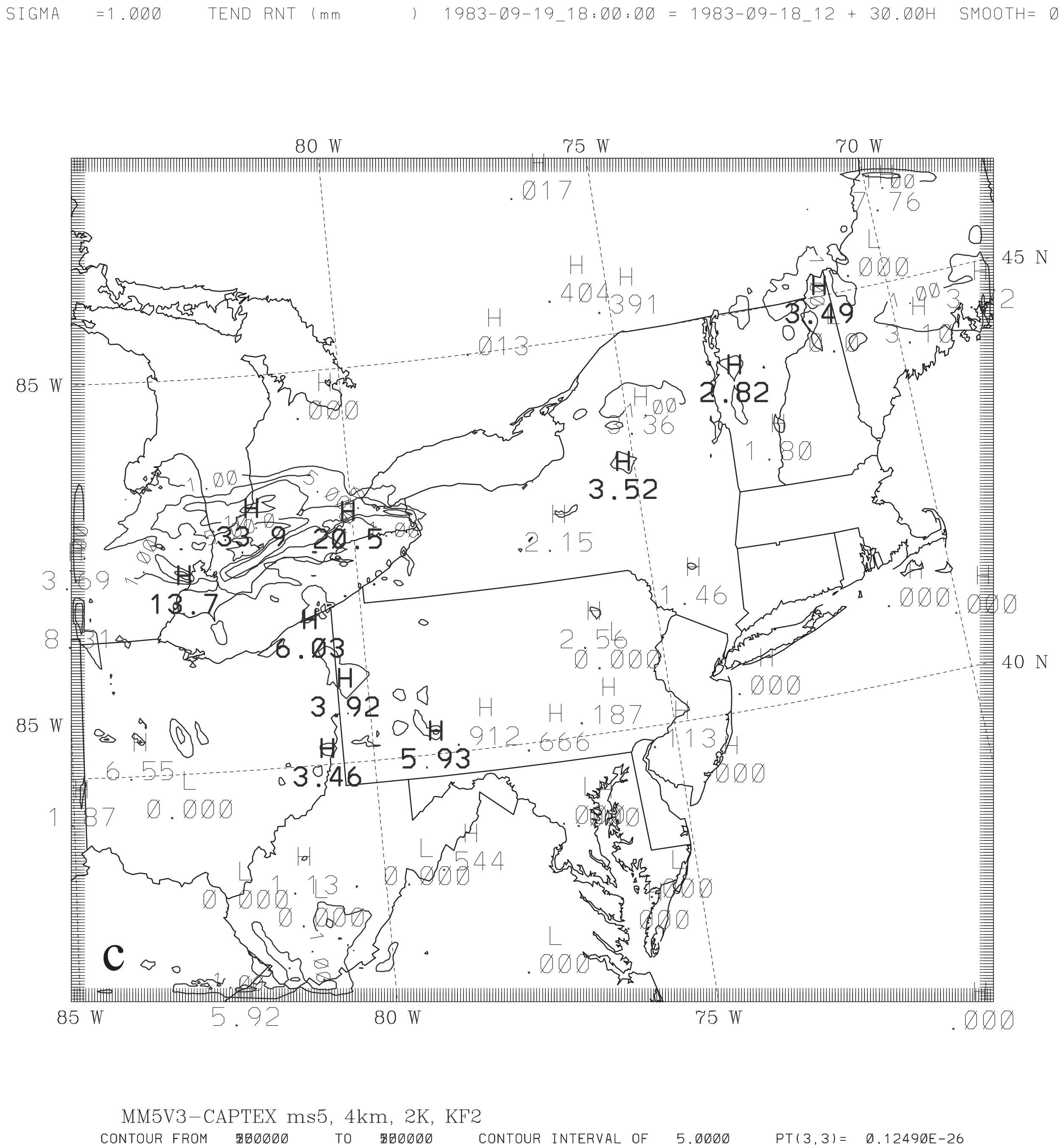

Figure 34 (Continued)

SIGMA =0.996 WIND UV (m/s) 1983-09-19_18:00:00 = 1983-09-18_12 + 30.00H SMOOTH= 0
SIGMA =0.996 BARB UV (m/s) 1983-09-19_18:00:00 = 1983-09-18_12 + 30.00H SMOOTH= 0

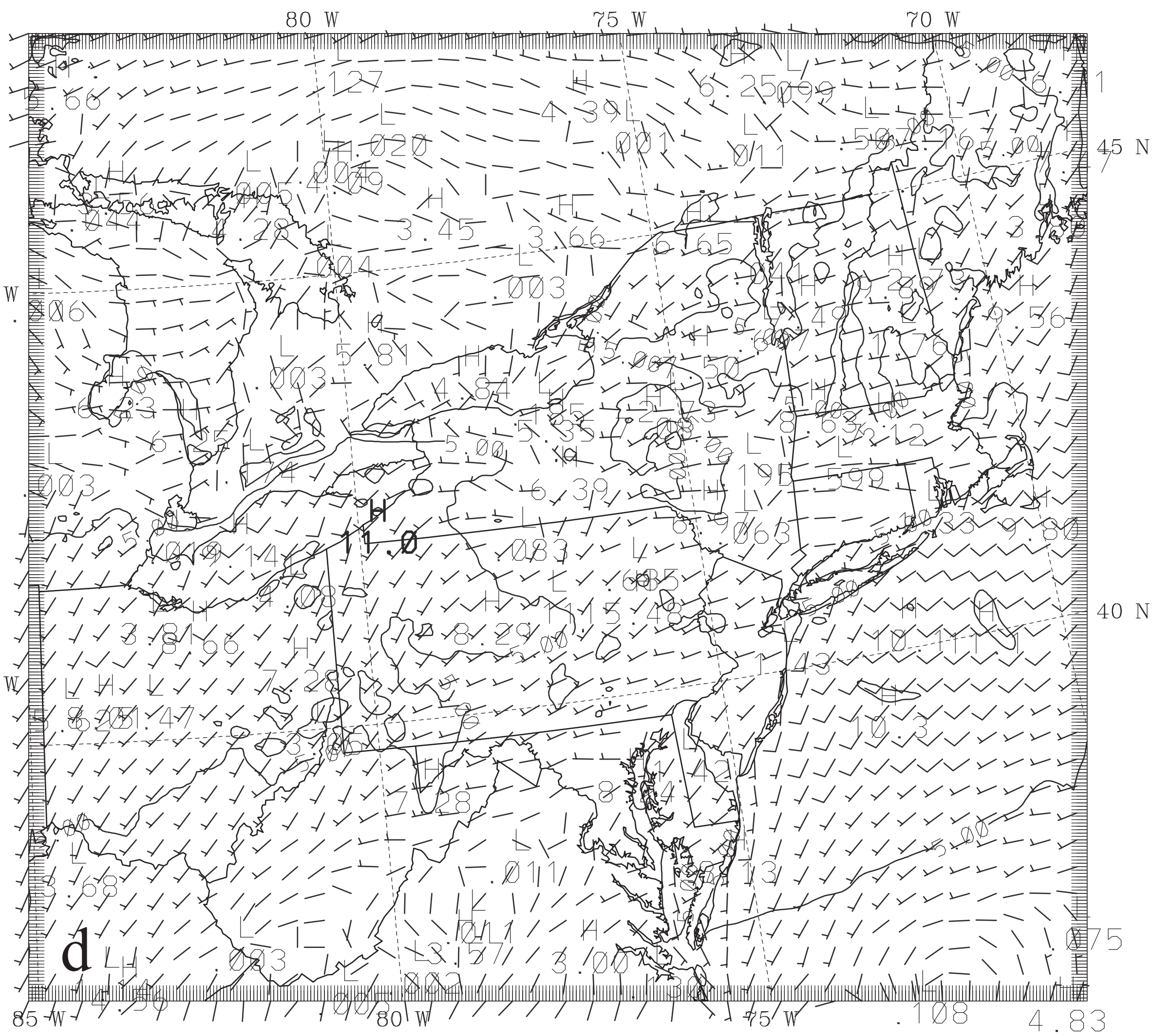

MM5V3-CAPTEX ms5, 4km, 2K, KF2
CONTOUR FROM 0.0000 TO 10.000 CONTOUR INTERVAL OF 5.0000 PT(3,3)= 4.0570

Figure 34 (Continued)

SIGMA =0.996 T (C) 1983-09-19_18:00:00 = 1983-09-18_12 + 30.00H SMOOTH= 0

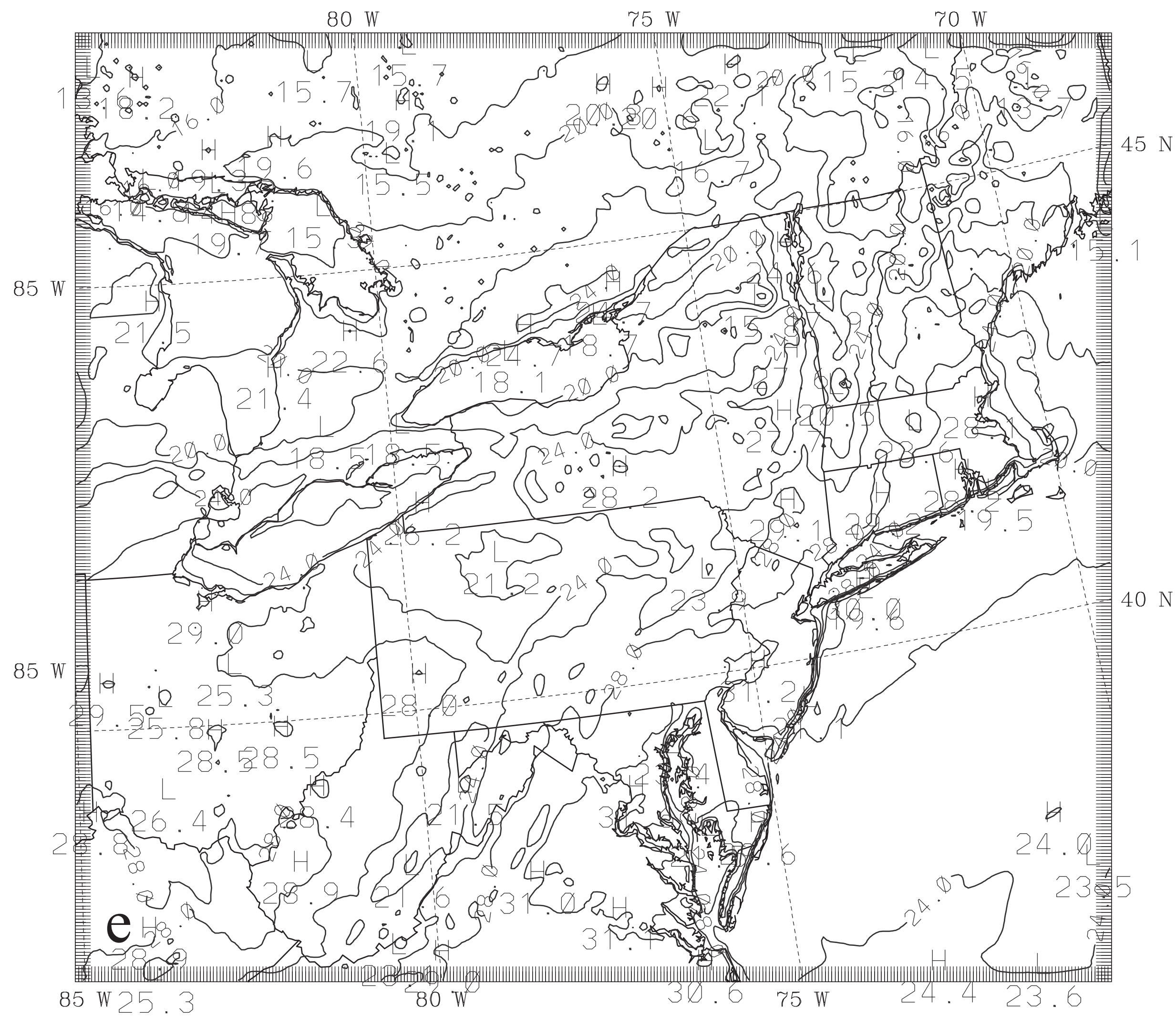

MM5V3-CAPTEX, ms5, 4km, 2K, KF2

CONTOUR FROM 12.000 TO 30.000 CONTOUR INTERVAL OF 2.0000 PT(3,3)= 28.040

Figure 34 (Continued)

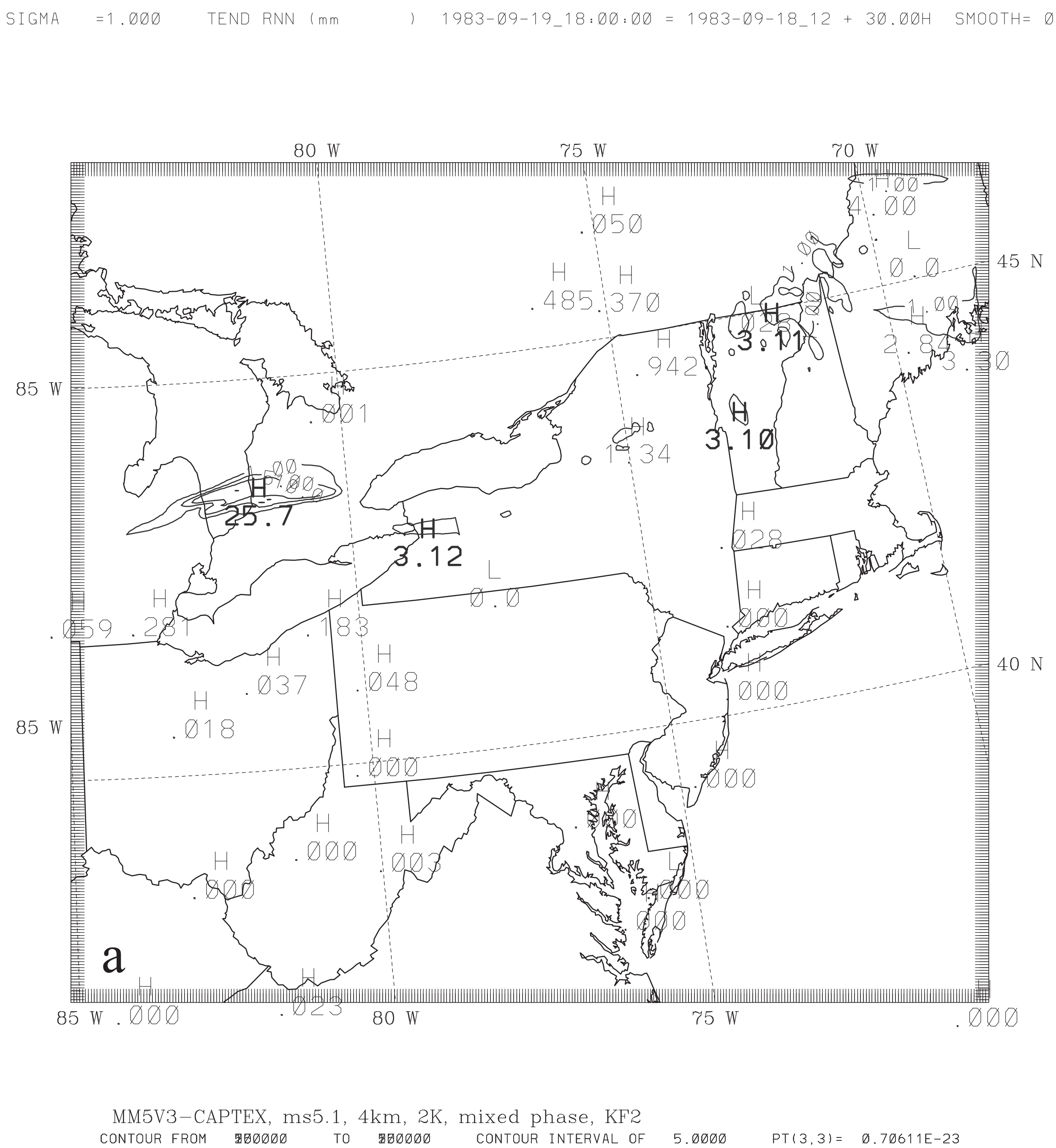

Figure 35 MM5-simulated fields at 30 h (1800 UTC 19 September 1983) on the 4-km domain in Exp. MS5.1. (a) Non-convective (grid-resolved) rain, (b) Convective (parameterized) rain, (c) Total (non-convective plus convective) rain, (d) Surface-layer wind (29 m AGL), (e) Surface-layer temperature. Rain contours are 1, 5, 10, 20, 30 and 40 mm, speed contours are 5 ms^{-1} and one barb is 10 ms^{-1}, and temperature contours are 2 ºC.

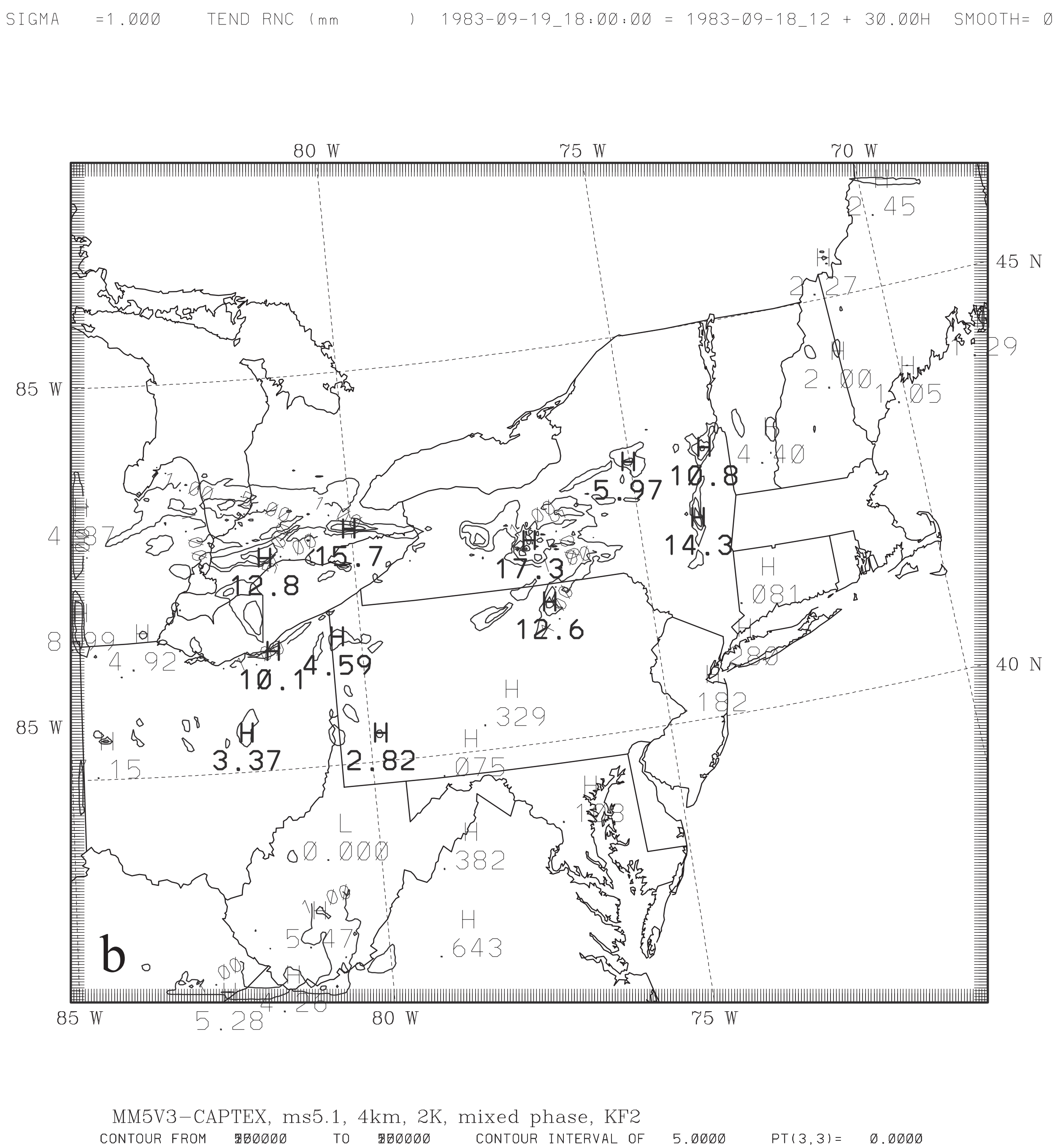

Figure 35 (Continued)

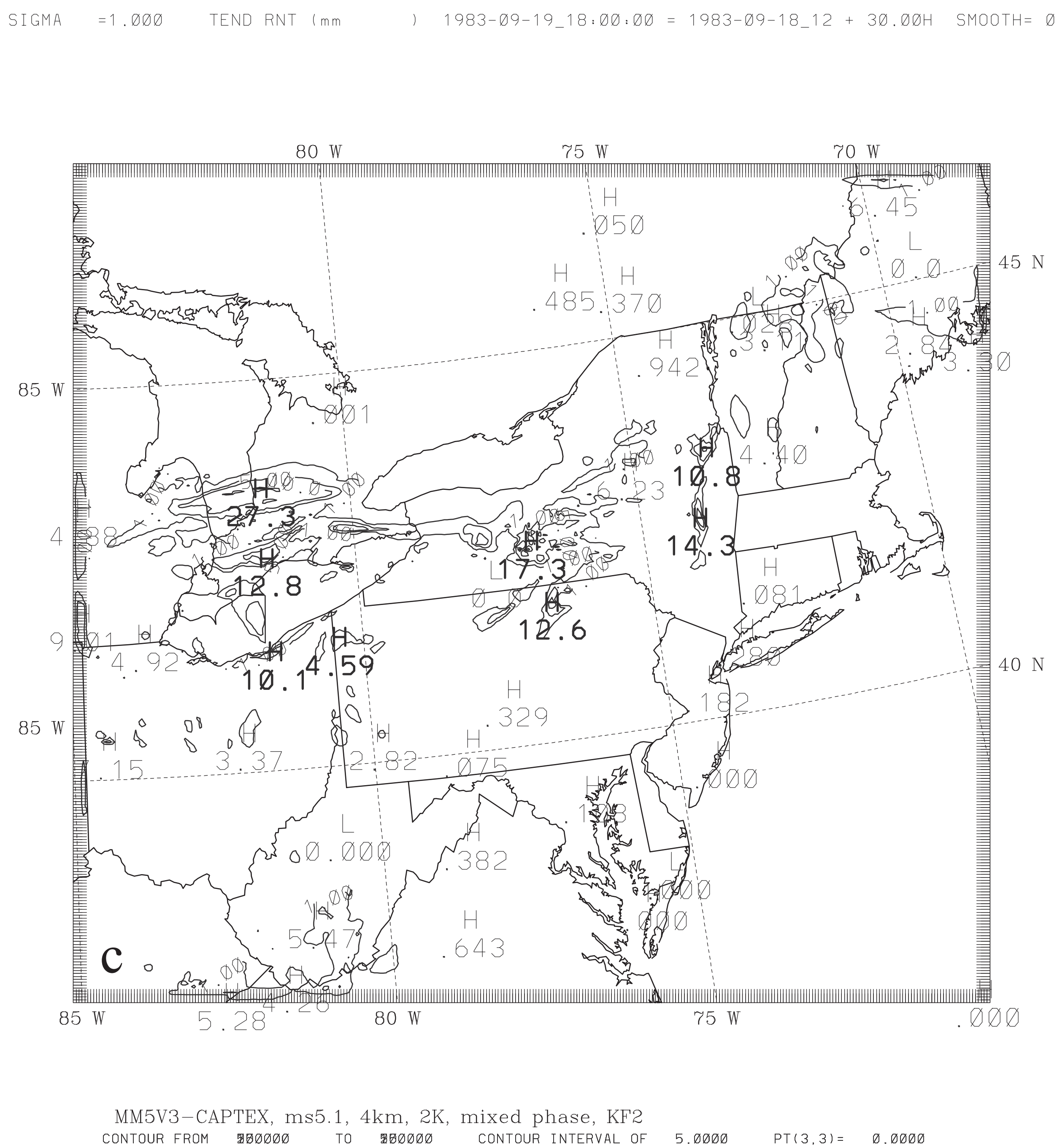

Figure 35 (Continued)

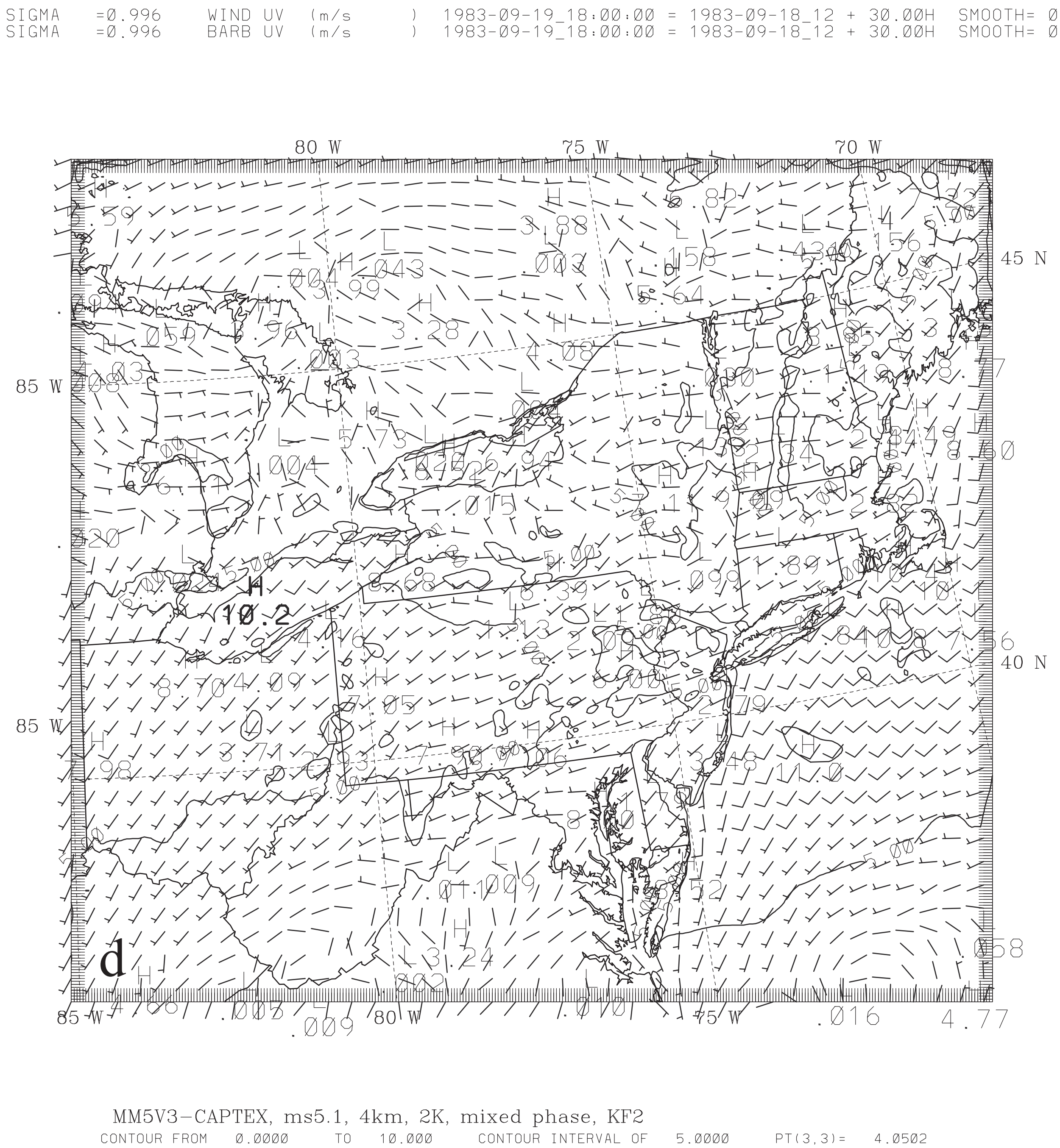

Figure 35 (Continued)

SIGMA =0.996 T (C) 1983-09-19_18:00:00 = 1983-09-18_12 + 30.00H SMOOTH= 0

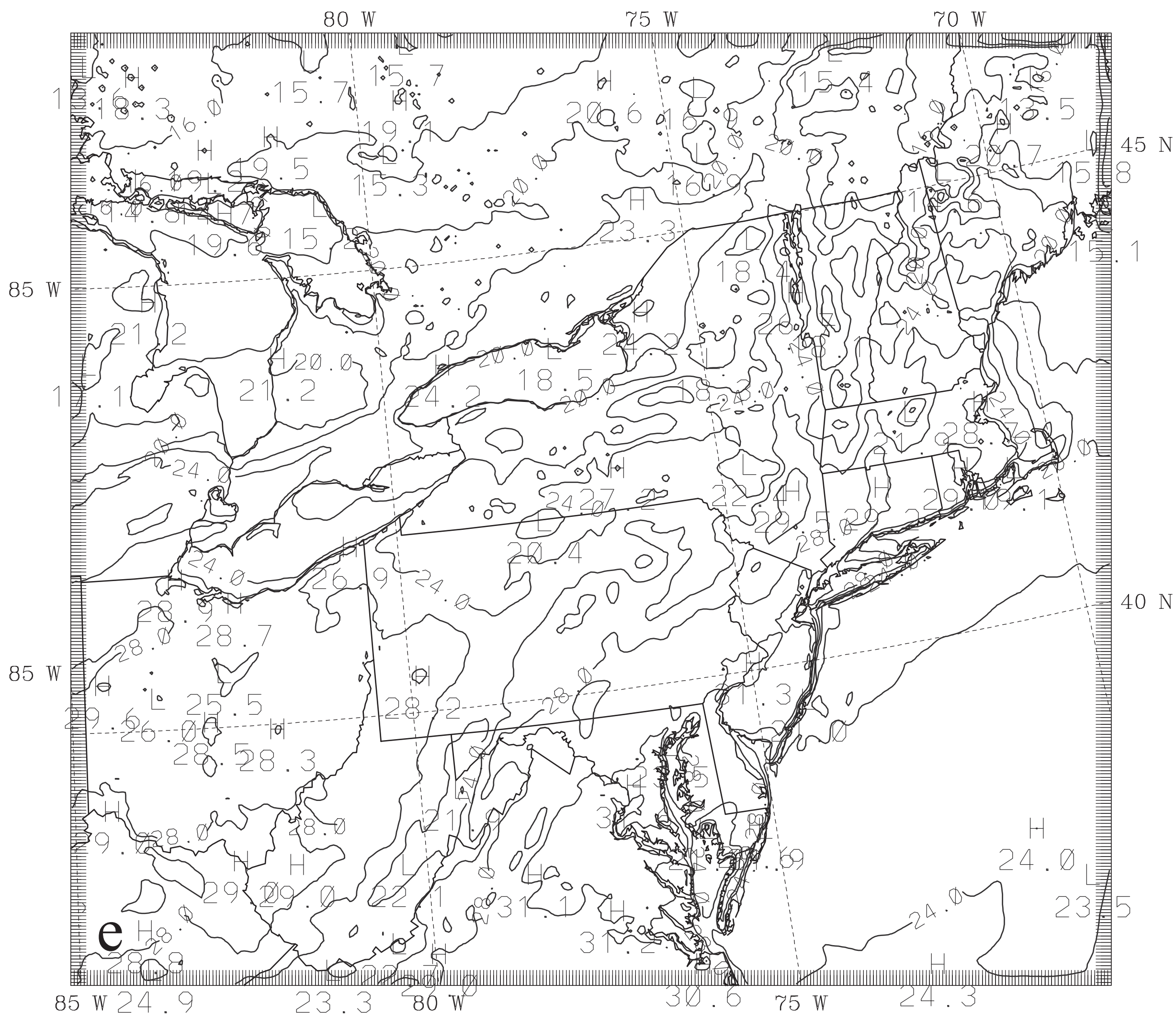

MM5V3-CAPTEX, ms5.1, 4km, 2K, mixed phase, KF2
CONTOUR FROM 12.000 TO 30.000 CONTOUR INTERVAL OF 2.0000 PT(3,3)= 28.025

Figure 35 (Continued)

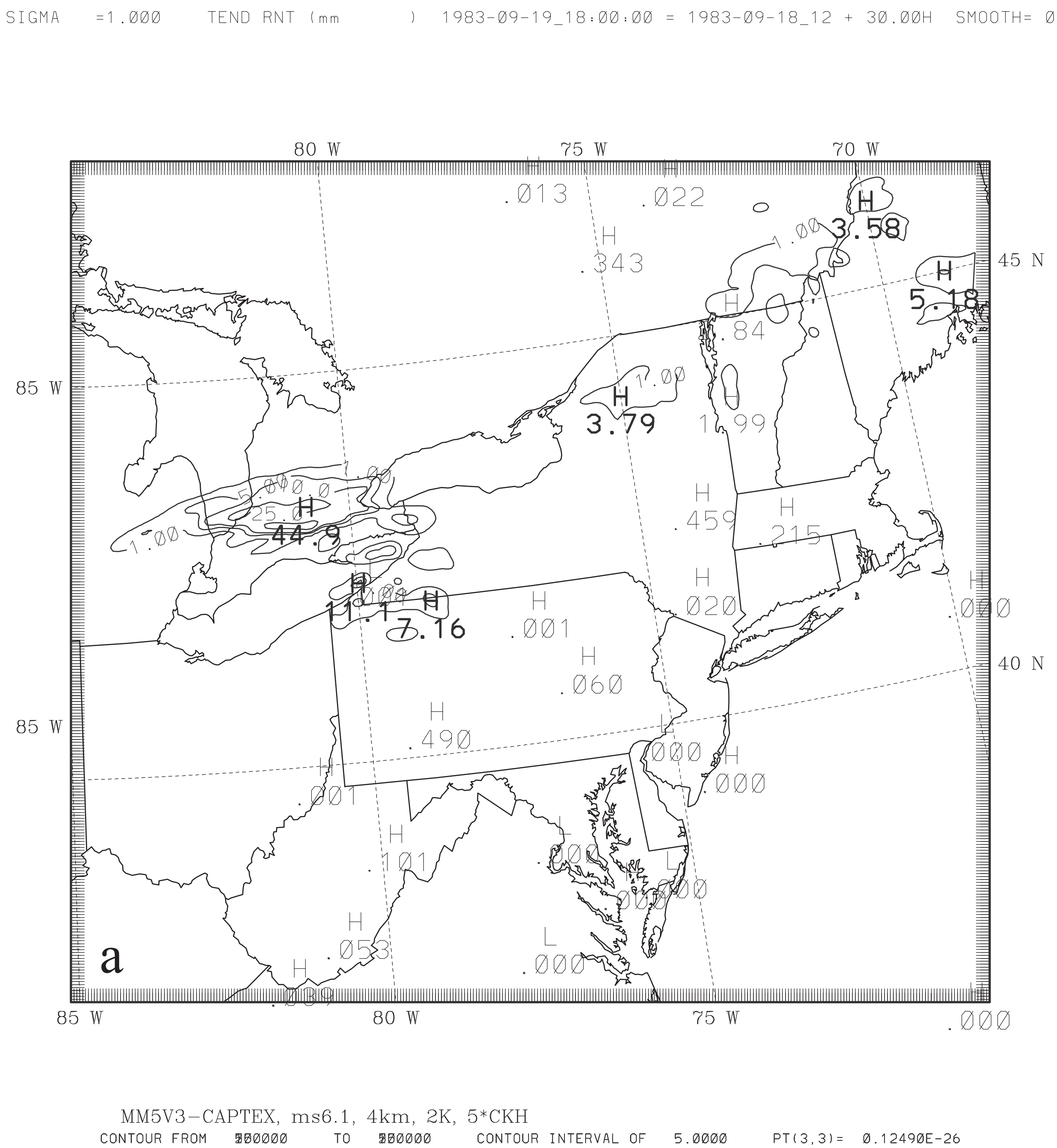

Figure 36 MM5-simulated fields at 30 h (1800 UTC 19 September 1983) on the 4-km domain in Exp. MS6.1. (a) Non-convective (grid-resolved) rain, (b) Surface-layer wind (29 m AGL) and (c) Surface-layer temperature. Rain contours are 1, 5, 10, 20, 30 and 40 mm, speed contours are 5 ms^{-1} and one barb is 10 ms^{-1}, and temperature contours are 2 ºC.

SIGMA =0.996 WIND UV (m/s) 1983-09-19_18:00:00 = 1983-09-18_12 + 30.00H SMOOTH= 0
SIGMA =0.996 BARB UV (m/s) 1983-09-19_18:00:00 = 1983-09-18_12 + 30.00H SMOOTH= 0

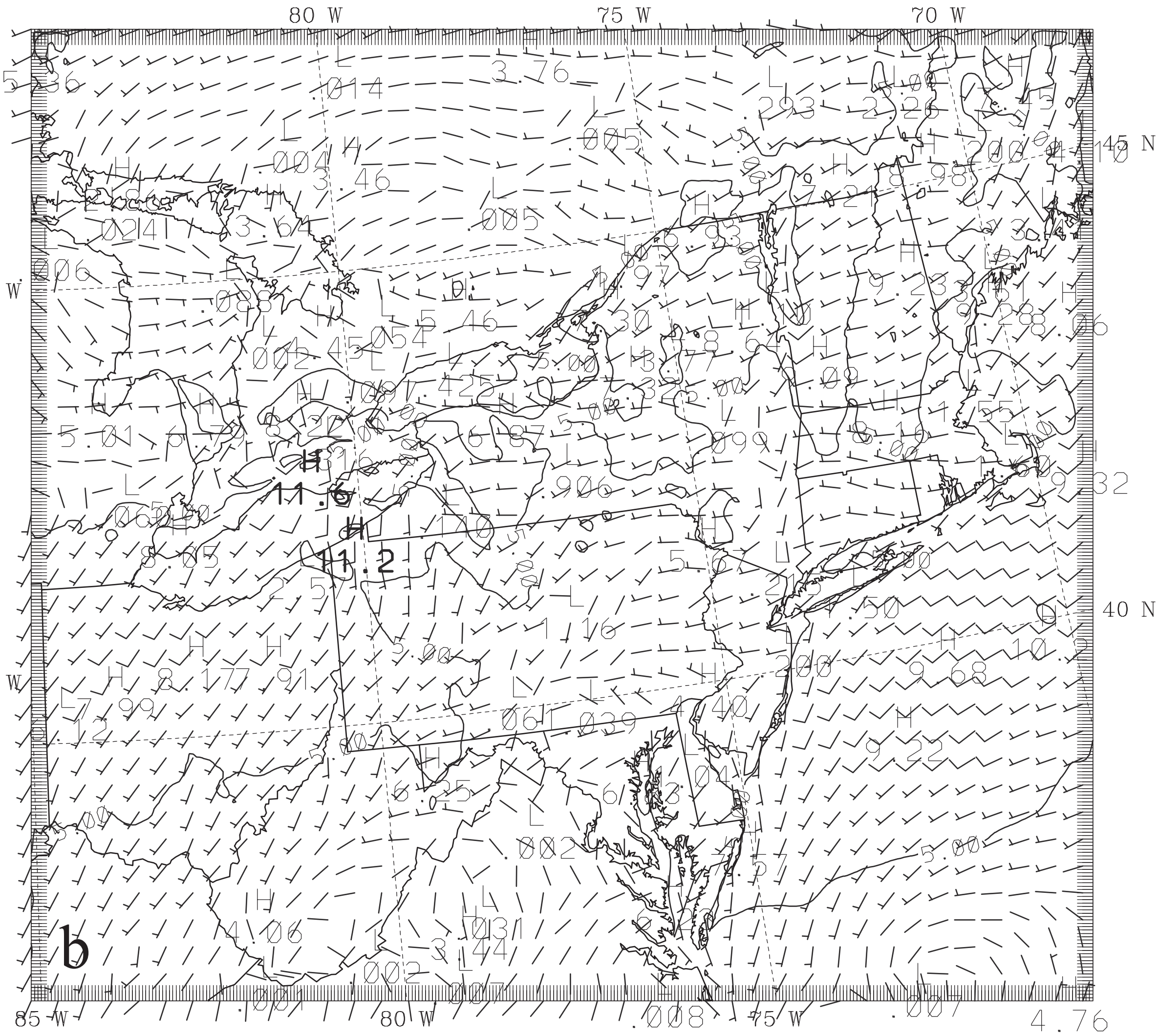

MM5V3-CAPTEX, ms6.1, 4km, 2K, 5*CKH
CONTOUR FROM 0.0000 TO 10.000 CONTOUR INTERVAL OF 5.0000 PT(3,3)= 3.9468

Figure 36 (Continued)

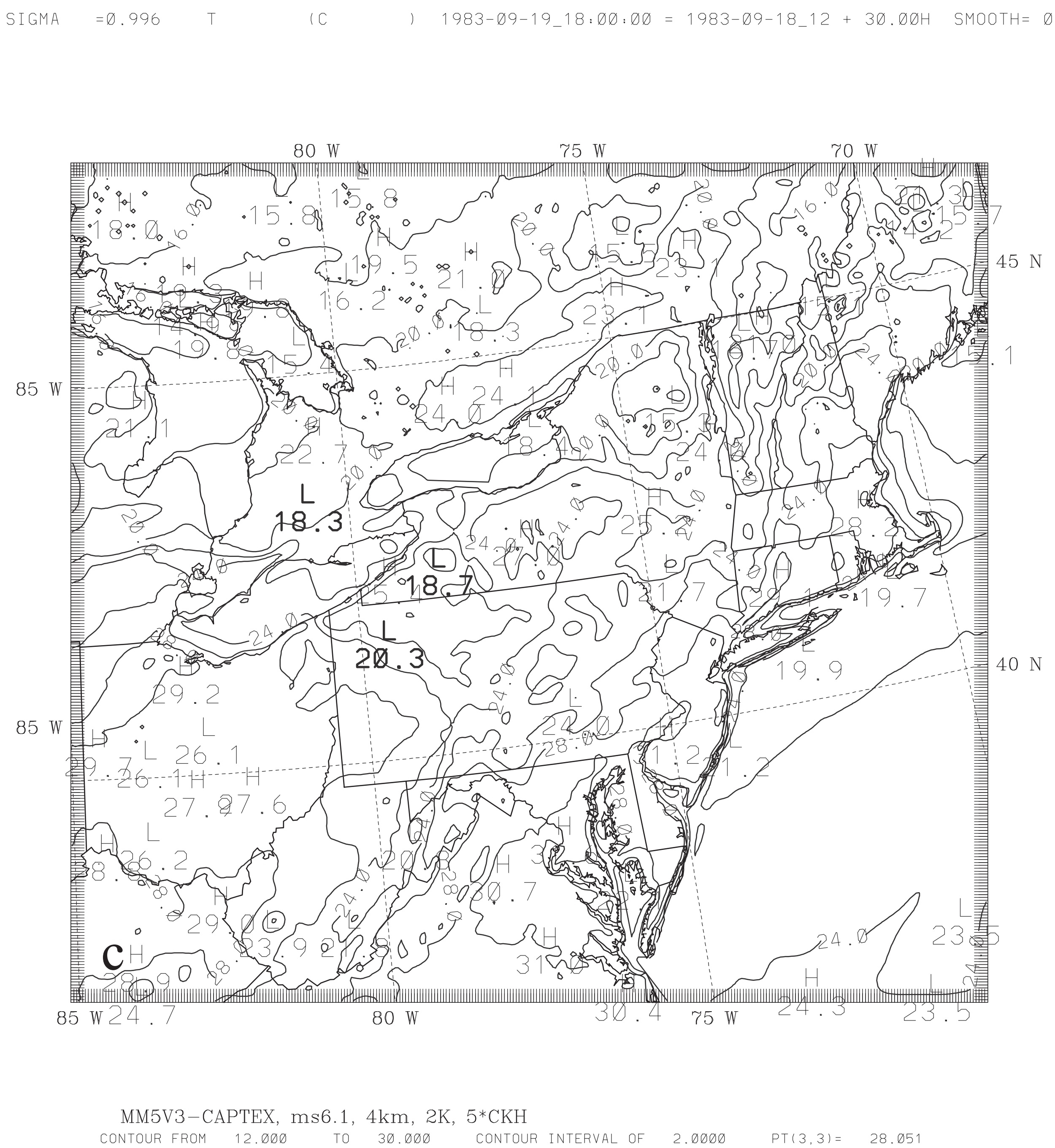

Figure 36 (Continued)

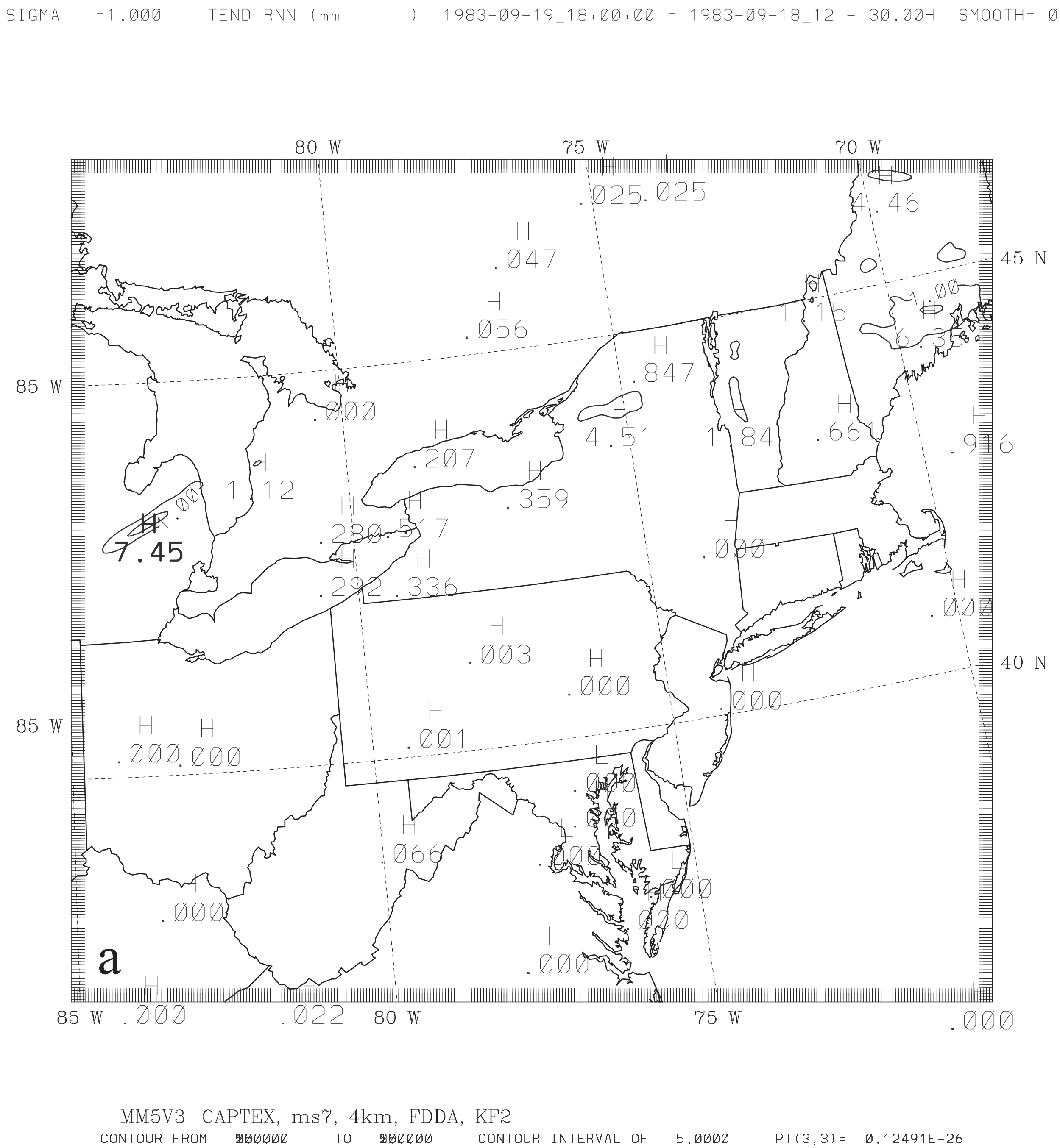

Figure 37 MM5-simulated fields at 30 h (1800 UTC 19 September 1983) on the 4-km domain in Exp. MS7. (a) Non-convective (grid-resolved) rain, (b) Convective (parameterized) rain, (c) Total (non-convective plus convective) rain, (d) Surface-layer wind (29 m AGL), (e) Surface-layer temperature. Rain contours are 1, 5, 10, 20, 30 and 40 mm, speed contours are 5 ms^{-1} and one barb is 10 ms^{-1}, and temperature contours are 2 ºC.

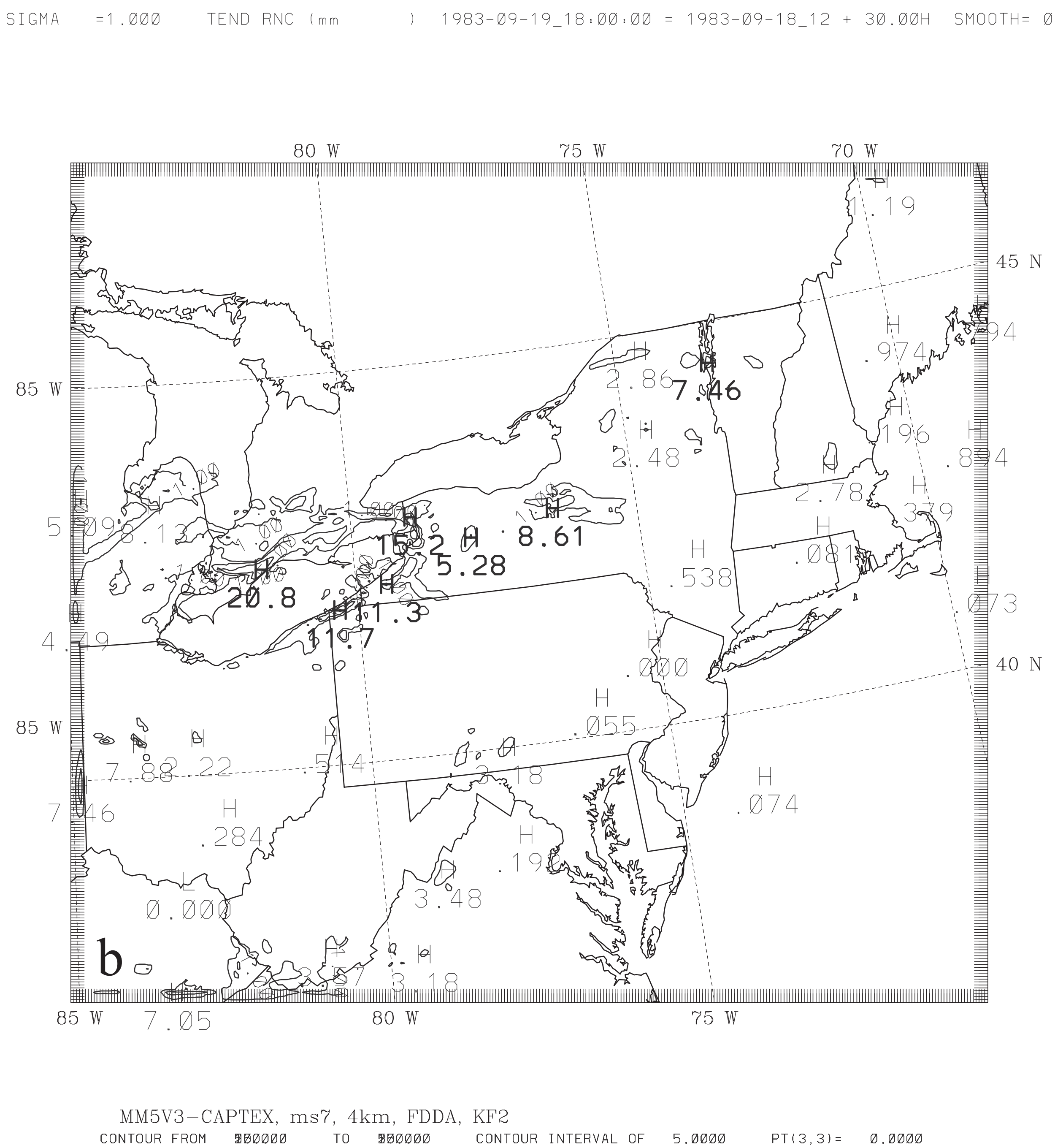

Figure 37 (Continued)

SIGMA =1.000 TEND RNT (mm) 1983-09-19_18:00:00 = 1983-09-18_12 + 30.00H SMOOTH= 0

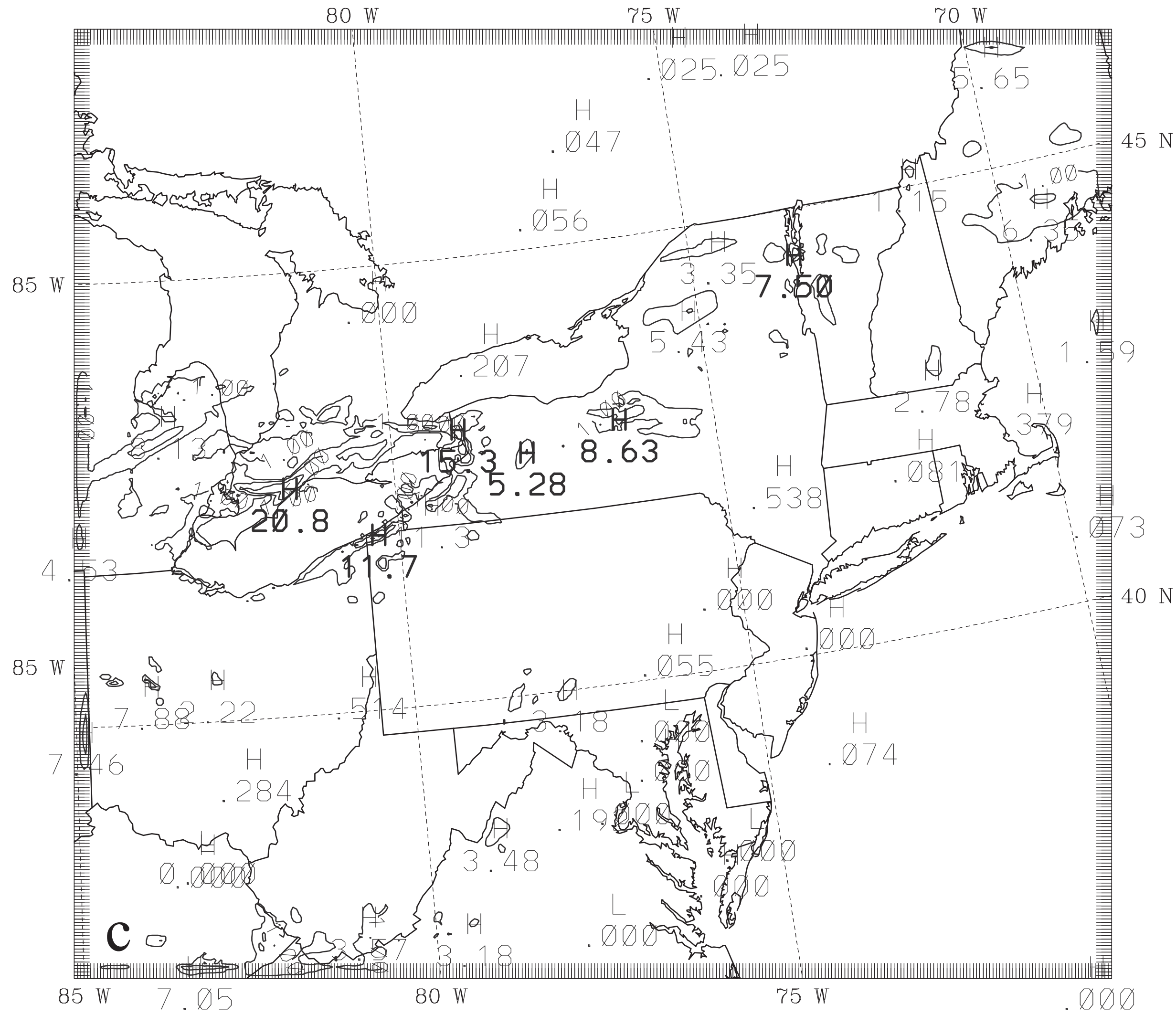

MM5V3-CAPTEX, ms7, 4km, FDDA, KF2

CONTOUR FROM 5.0000 TO 20.000 CONTOUR INTERVAL OF 5.0000 PT(3,3)= 0.12491E-26

Figure 37 (Continued)

SIGMA =0.996 WIND UV (m/s) 1983-09-19_18:00:00 = 1983-09-18_12 + 30.00H SMOOTH= 0
SIGMA =0.996 BARB UV (m/s) 1983-09-19_18:00:00 = 1983-09-18_12 + 30.00H SMOOTH= 0

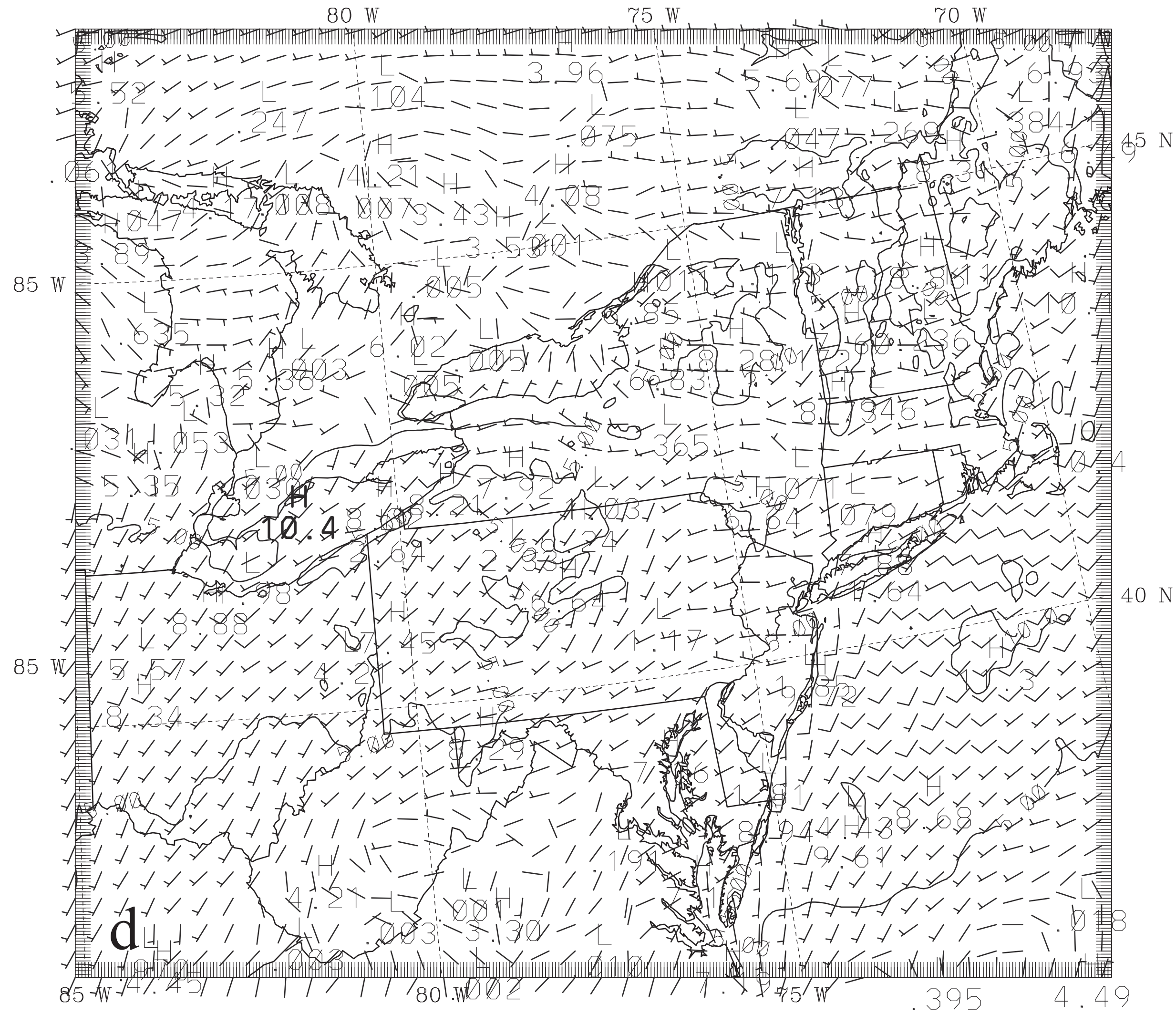

MM5V3-CAPTEX, ms7, 4km, FDDA, KF2
CONTOUR FROM 0.0000 TO 10.000 CONTOUR INTERVAL OF 5.0000 PT(3,3)= 3.9857

Figure 37 (Continued)

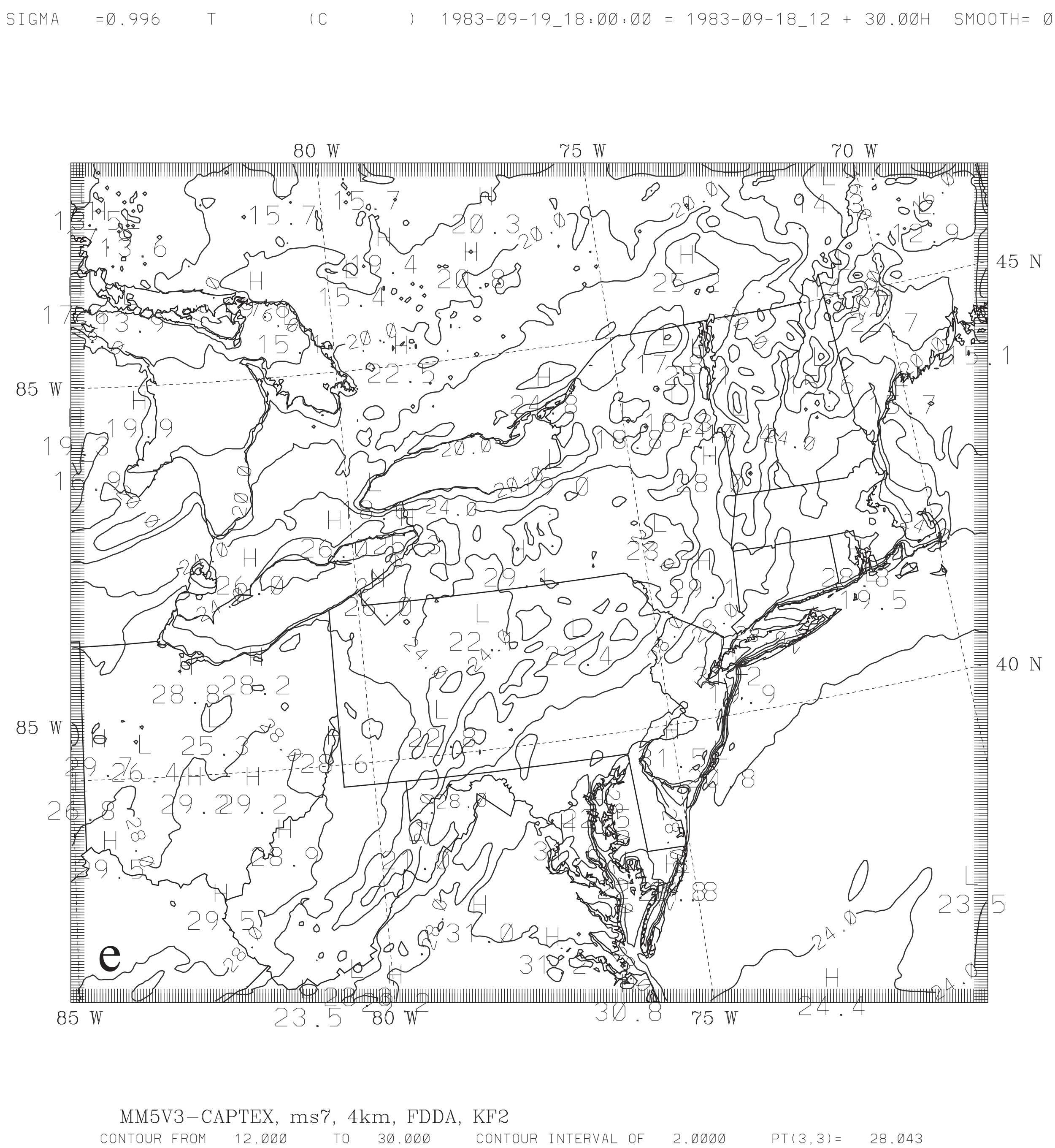

Figure 37 (Continued)

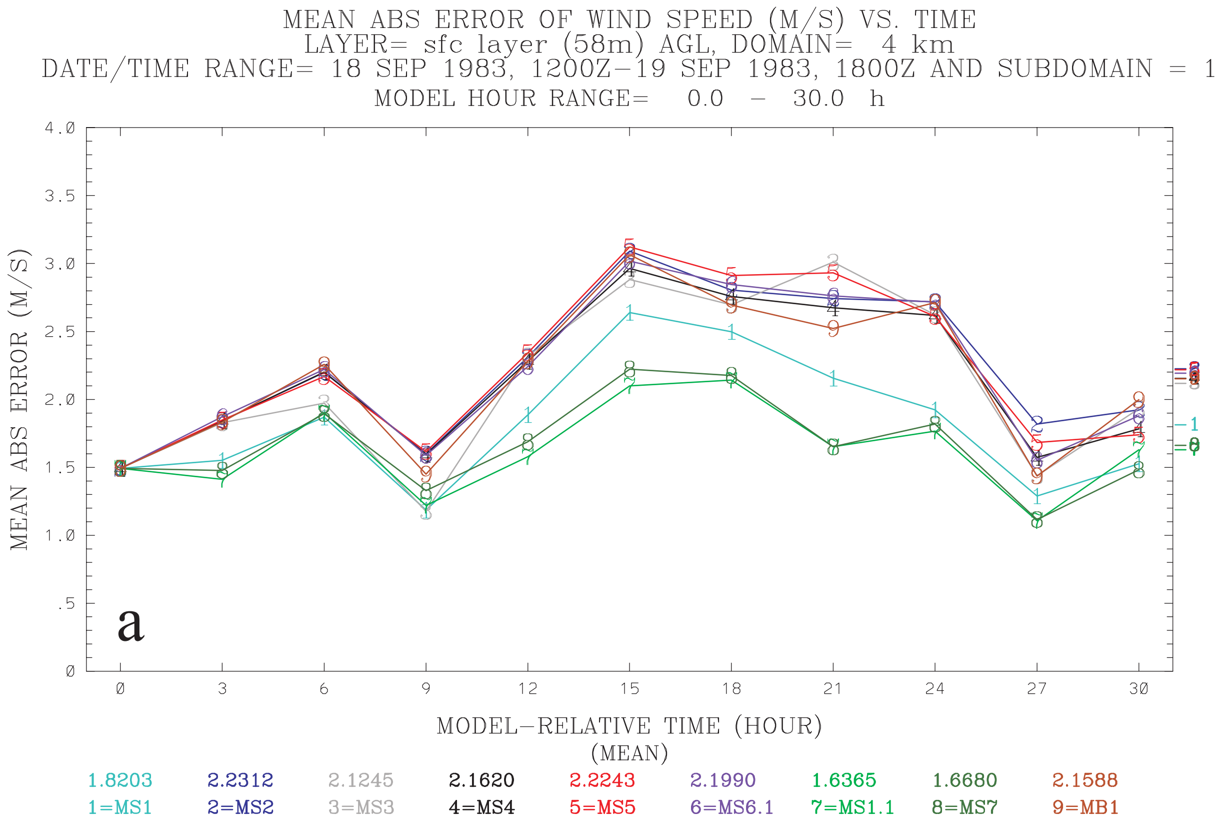

Figure 38 Mean absolute error (*MAE*) of MM5-simulated wind speed field in CAPTEX-83 Episode 1 (1200 UTC, 18 September - 1800 UTC, 19 September 1983) on the 4-km verification domain. (a) *MAE* versus time for the surface-layer (29 m AGL) wind speed, (b) All-layer averaged *MAE* versus time, (c) Vertical profiles of the 30-h averaged *MAE* at all model layers. The 30-h mean statistics are plotted on the right end of each time series chart or top of each vertical profile chart with the digital values also included above the experiment key at the bottom of the figure.

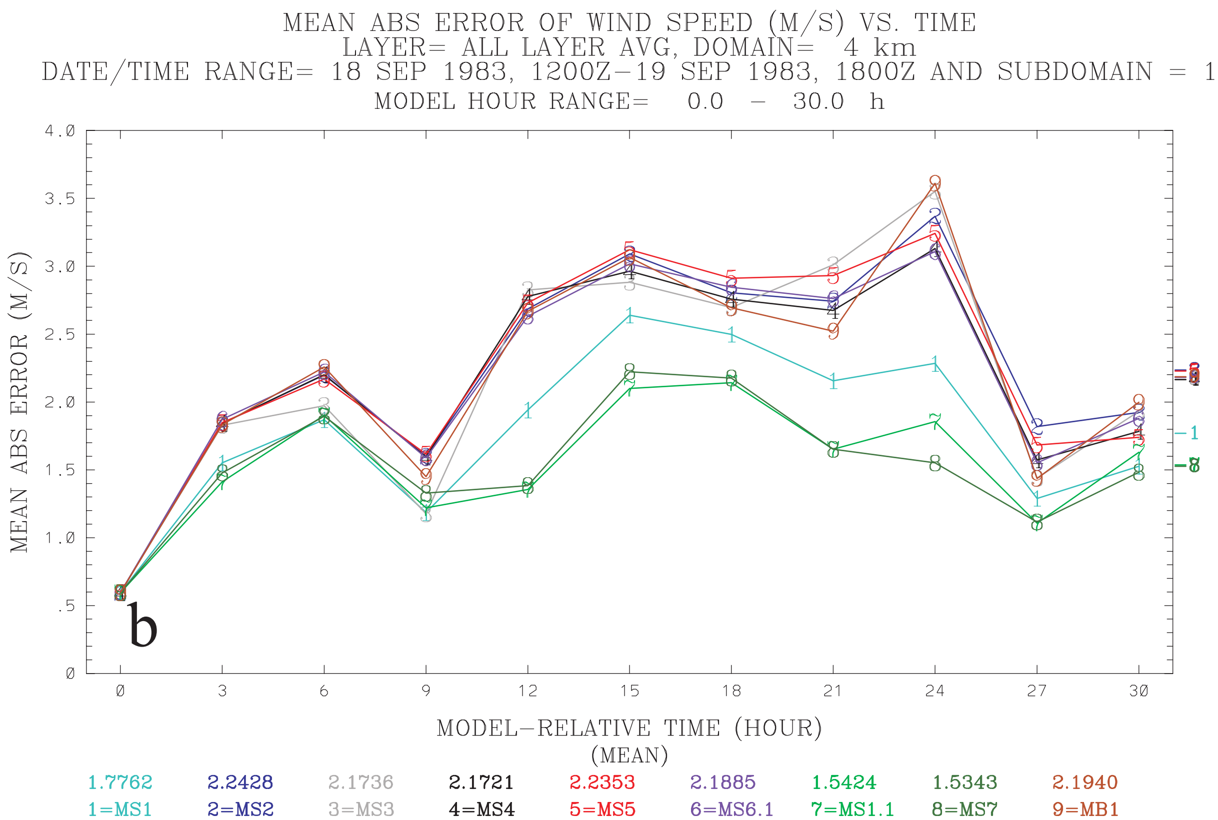

Figure 38 (Continued)

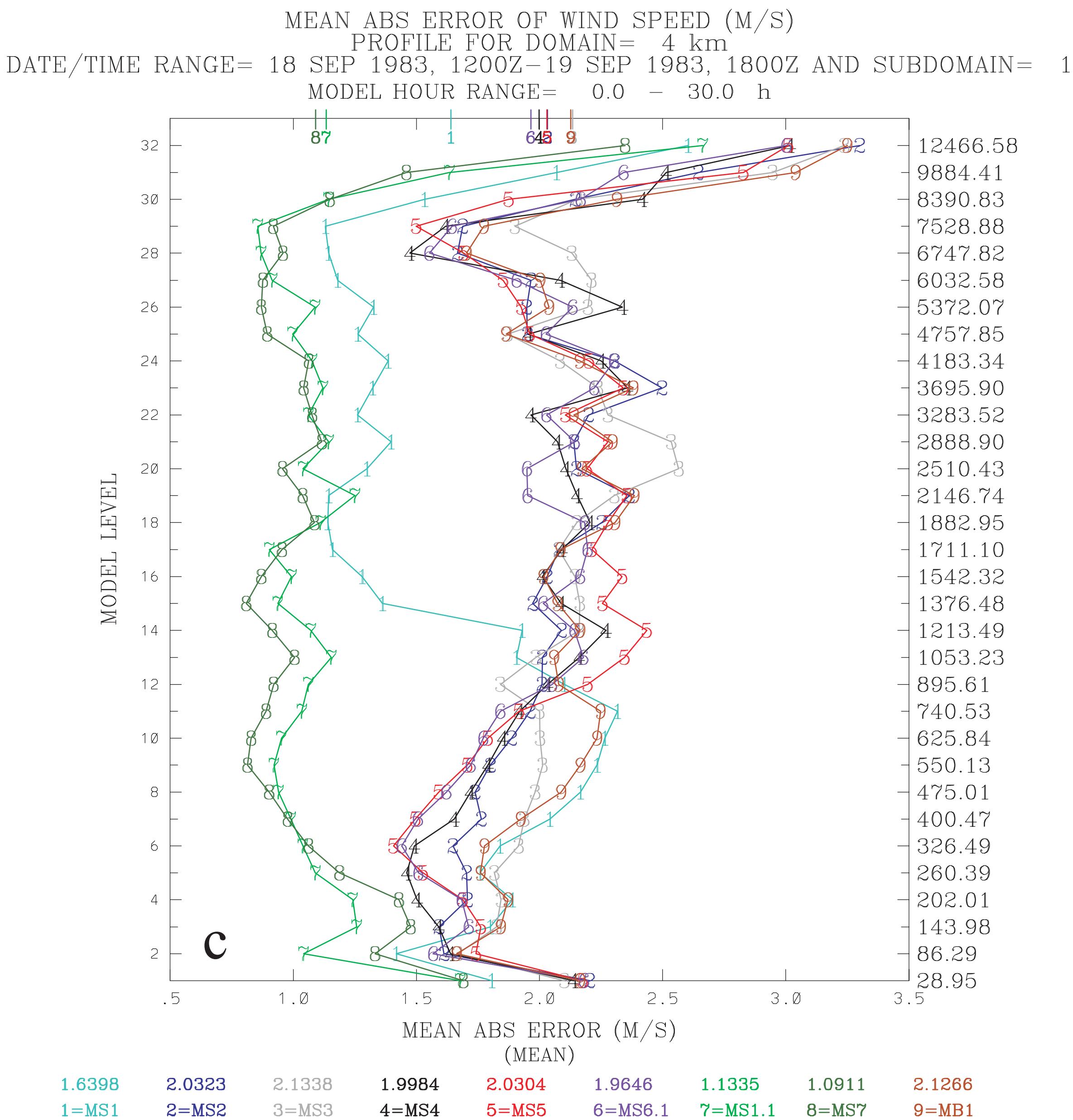

Figure 38 (Continued)

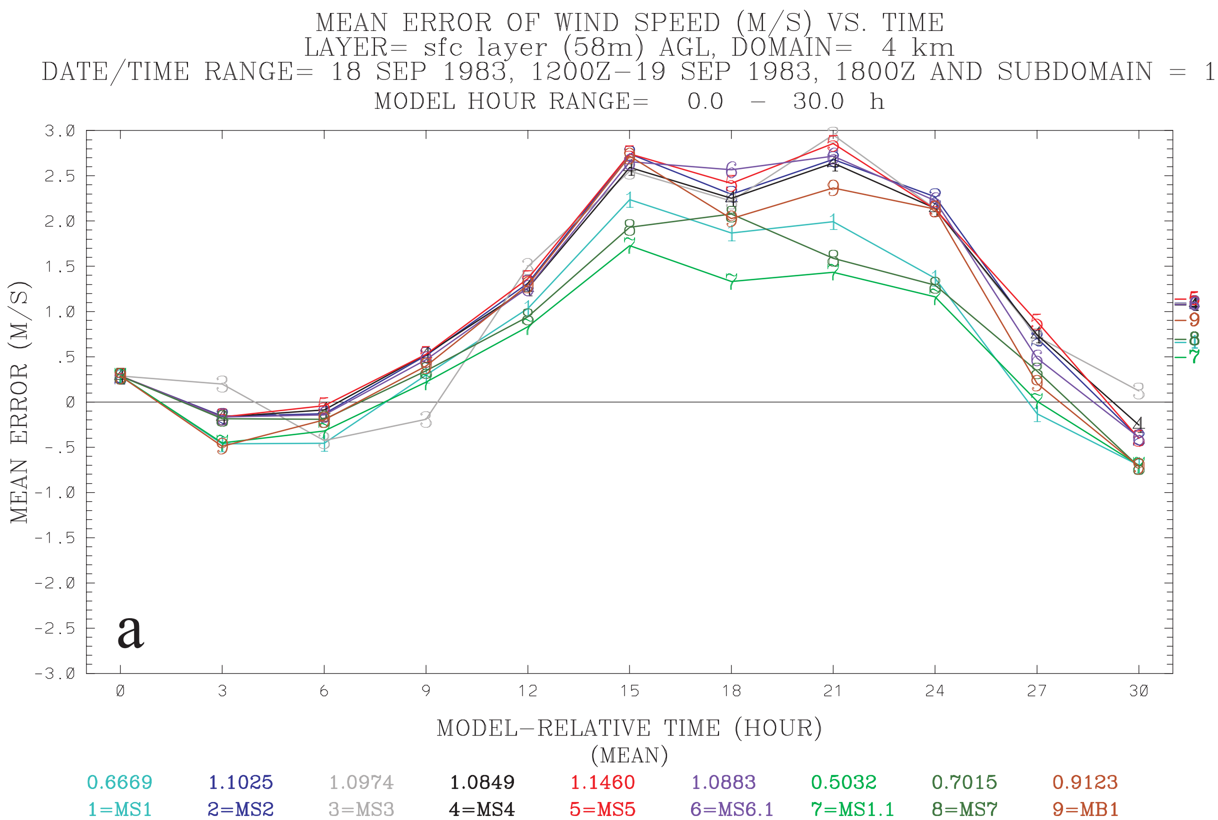

Figure 39 Mean error (*ME*) of MM5-simulated wind speed field in CAPTEX-83 Episode 1 (1200 UTC, 18 September - 1800 UTC, 19 September 1983) on the 4-km verification domain. (a) *ME* versus time for the surface-layer (29 m AGL) wind speed, (b) Vertical profiles of the 30-h averaged *ME* at all model layers. The 30-h mean statistics are plotted on the right end of each time series chart or top of each vertical profile chart with the digital values also included above the experiment key at the bottom of the figure.

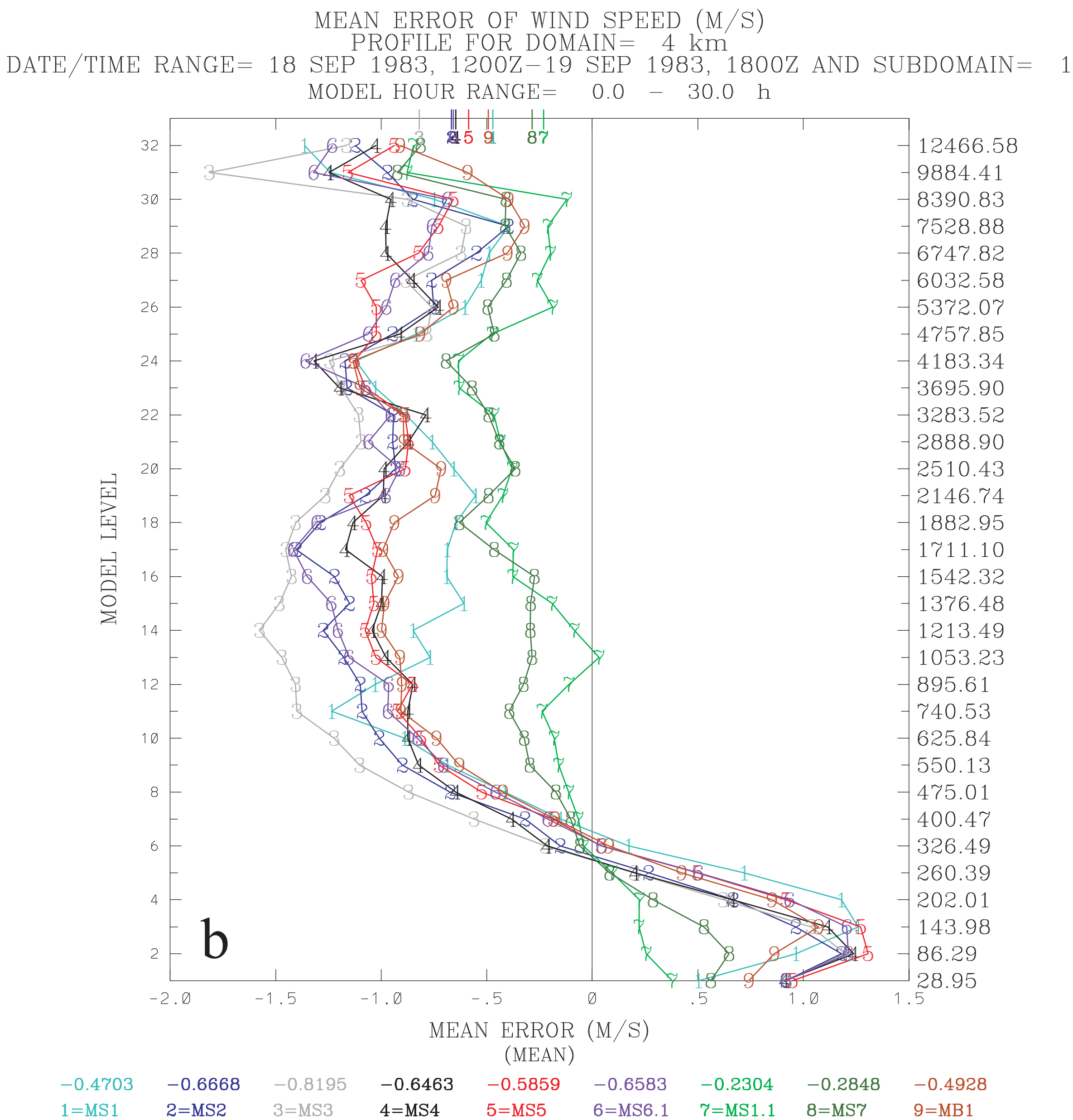

Figure 39 (Continued)

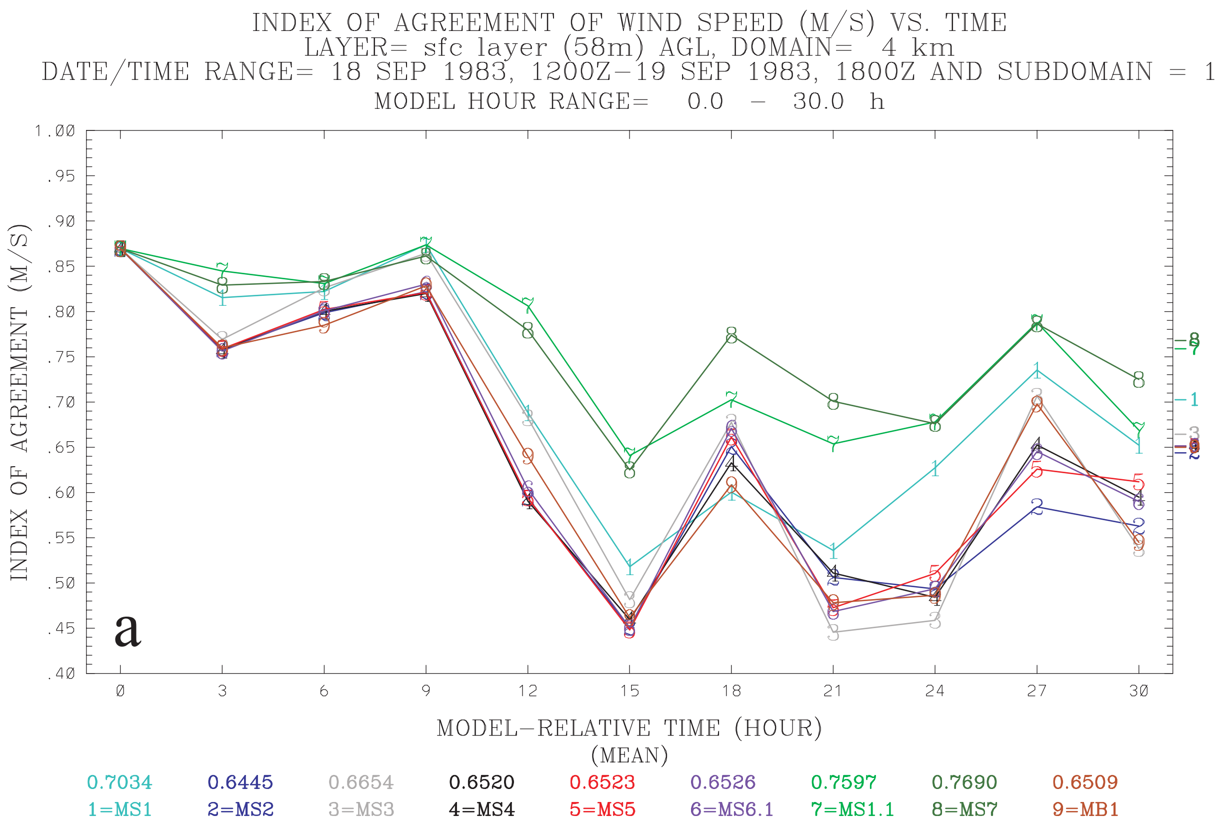

Figure 40 Index of agreement (I) of MM5-simulated wind speed field in CAPTEX-83 Episode 1 (1200 UTC, 18 September - 1800 UTC, 19 September 1983) on the 4-km verification domain. (a) I versus time for the surface-layer (29 m AGL) wind speed, (b) All-layer averaged I versus time, (c) Vertical profiles of the 30-h averaged I at all model layers. The 30-h mean statistics are plotted on the right end of each time series chart or top of each vertical profile chart with the digital values also included above the experiment key at the bottom of the figure.

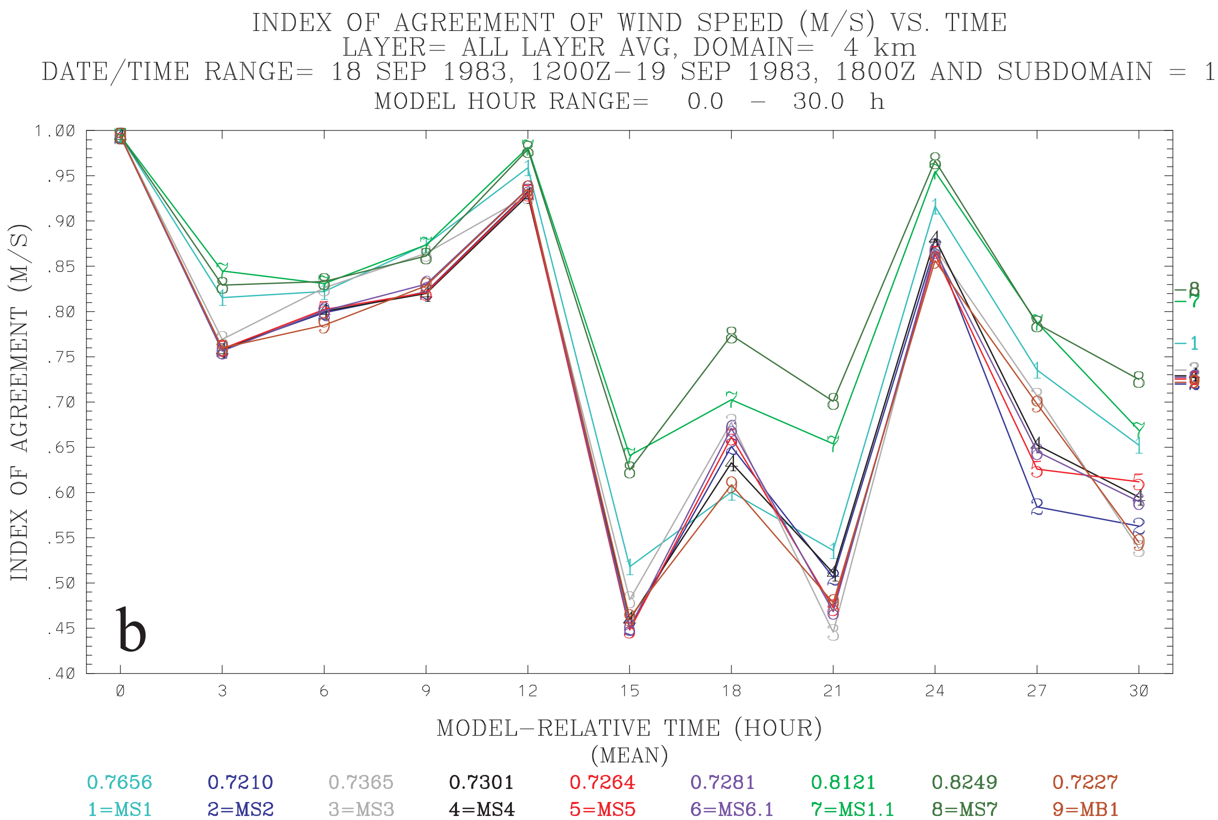

Figure 40 (Continued)

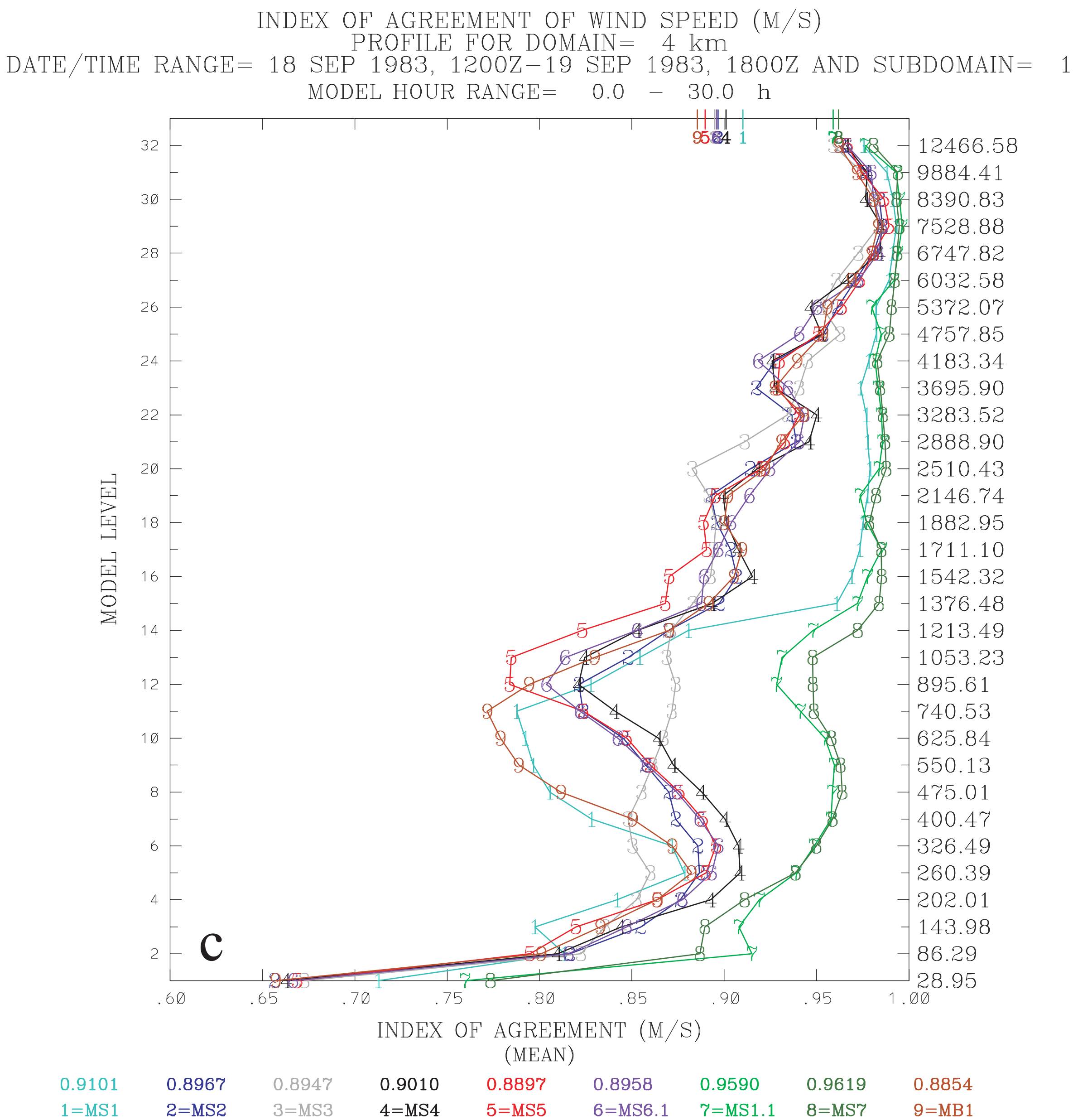

Figure 40 (Continued)

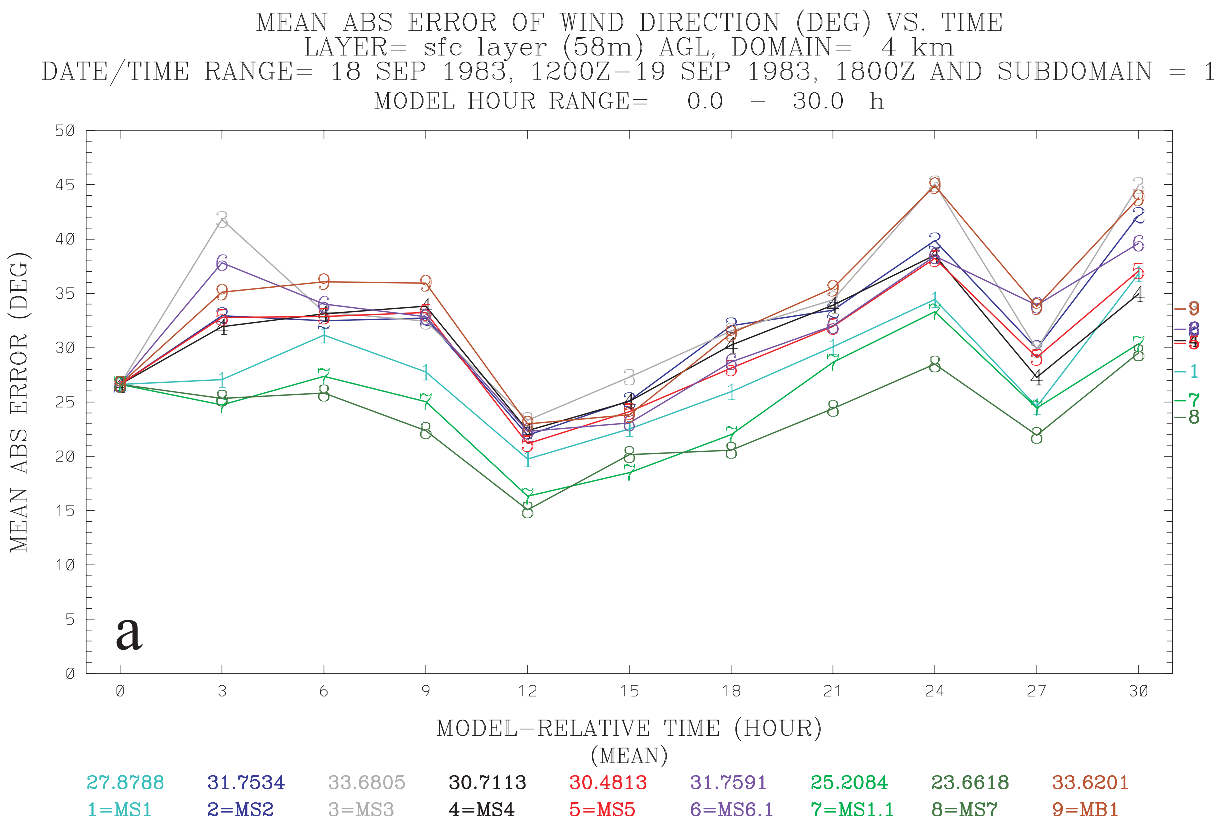

Figure 41 Mean absolute error (*MAE*) of MM5-simulated wind direction field in CAPTEX-83 Episode 1 (1200 UTC, 18 September - 1800 UTC, 19 September 1983) on the 4-km verification domain. (a) *MAE* versus time for the surface-layer (29 m AGL) wind direction, (b) All-layer averaged *MAE* versus time, (c) Vertical profiles of the 30-h averaged *MAE* at all model layers. The 30-h mean statistics are plotted on the right end of each time series chart or top of each vertical profile chart with the digital values also included above the experiment key at the bottom of the figure.

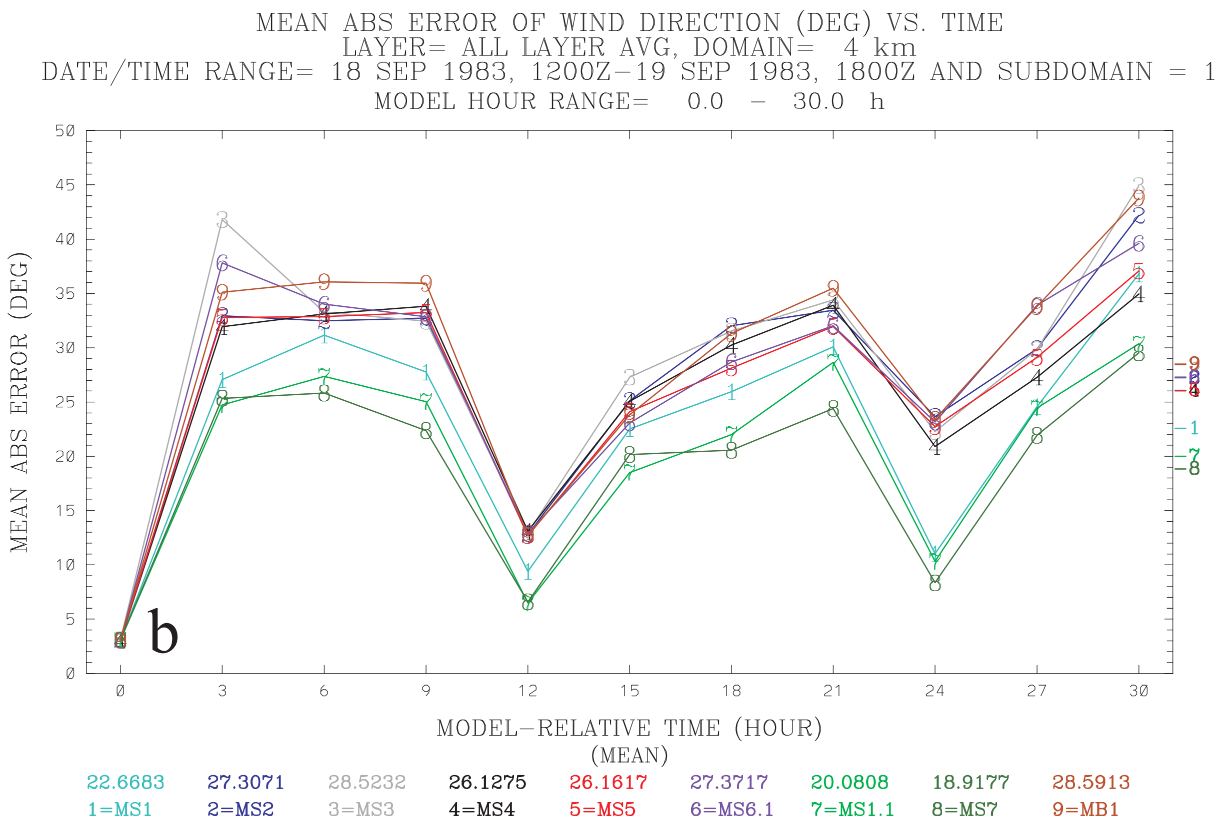

Figure 41 (Continued)

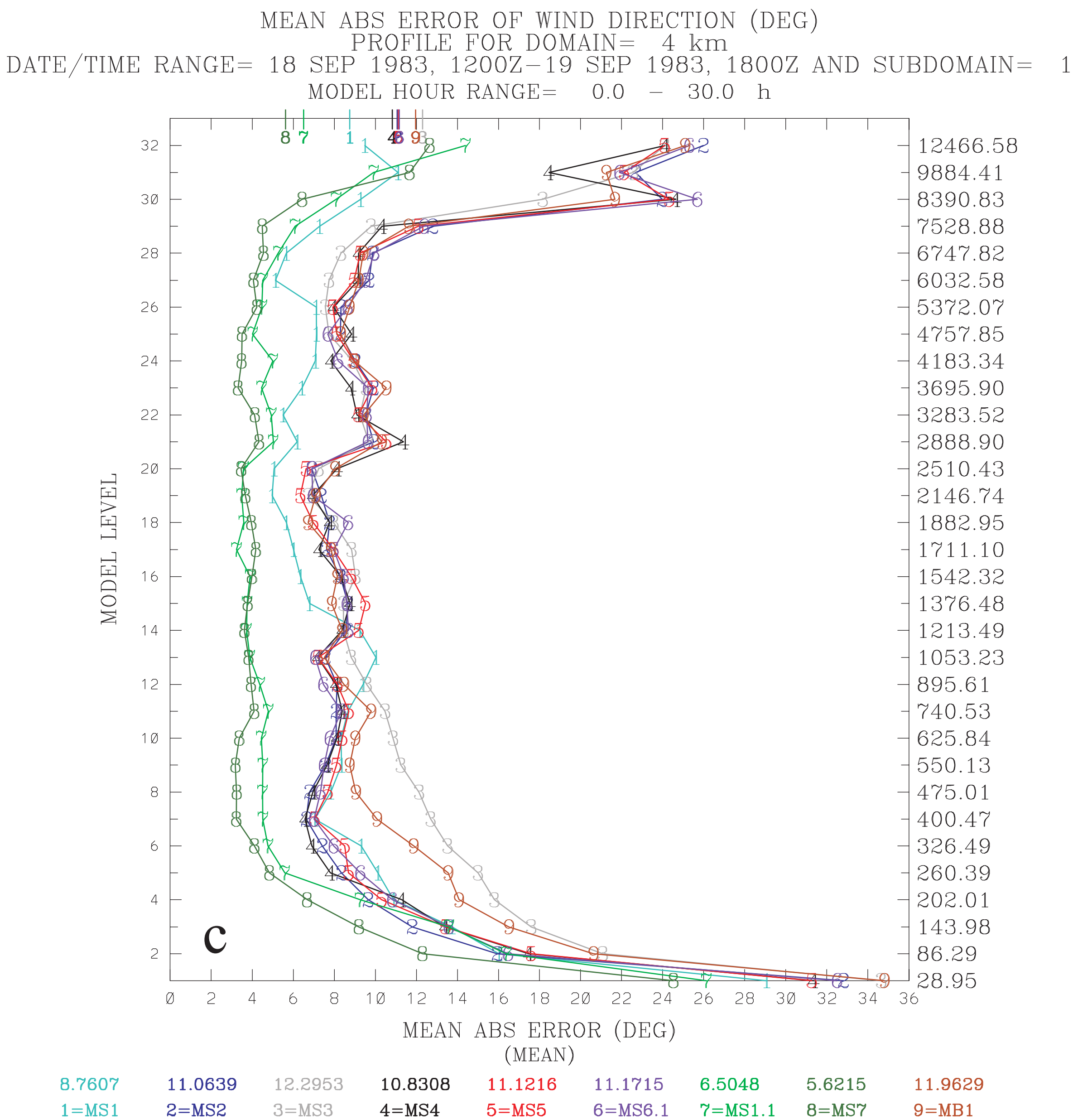

Figure 41 (Continued)

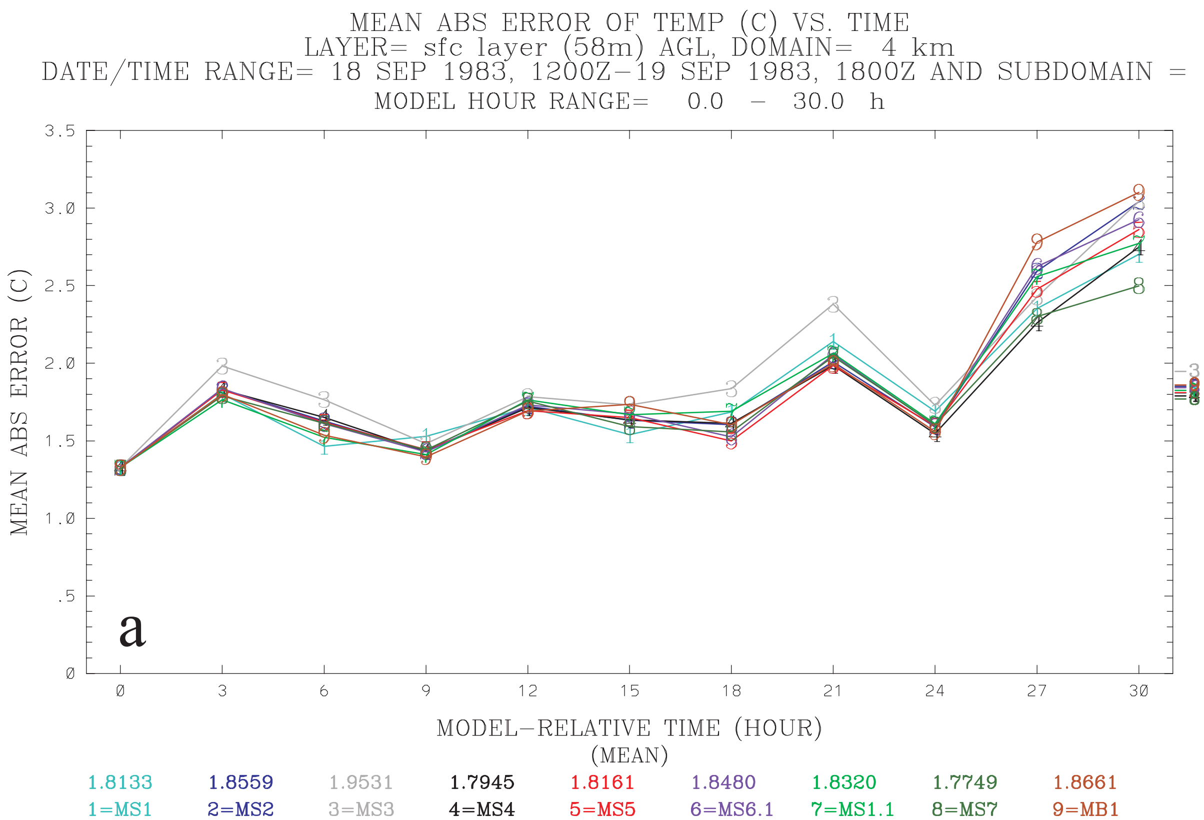

Figure 42 Mean absolute error (*MAE*) of MM5-simulated temperature field in CAPTEX-83 Episode 1 (1200 UTC, 18 September - 1800 UTC, 19 September 1983) on the 4-km verification domain. (a) *MAE* versus time for the surface-layer (29 m AGL) temperature, (b) All-layer averaged *MAE* versus time, (c) Vertical profiles of the 30-h averaged *MAE* at all model layers. The 30-h mean statistics are plotted on the right end of each time series chart or top of each vertical profile chart with the digital values also included above the experiment key at the bottom of the figure.

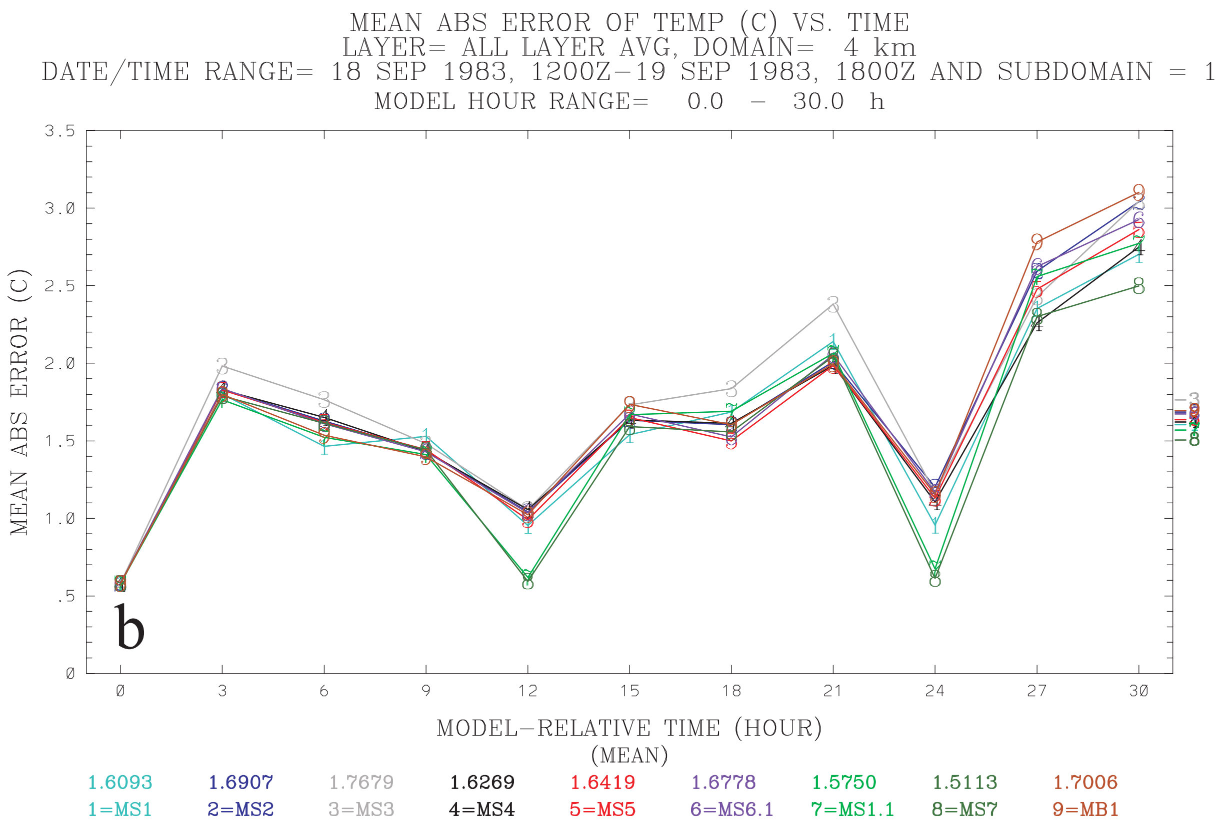

Figure 42 (Continued)

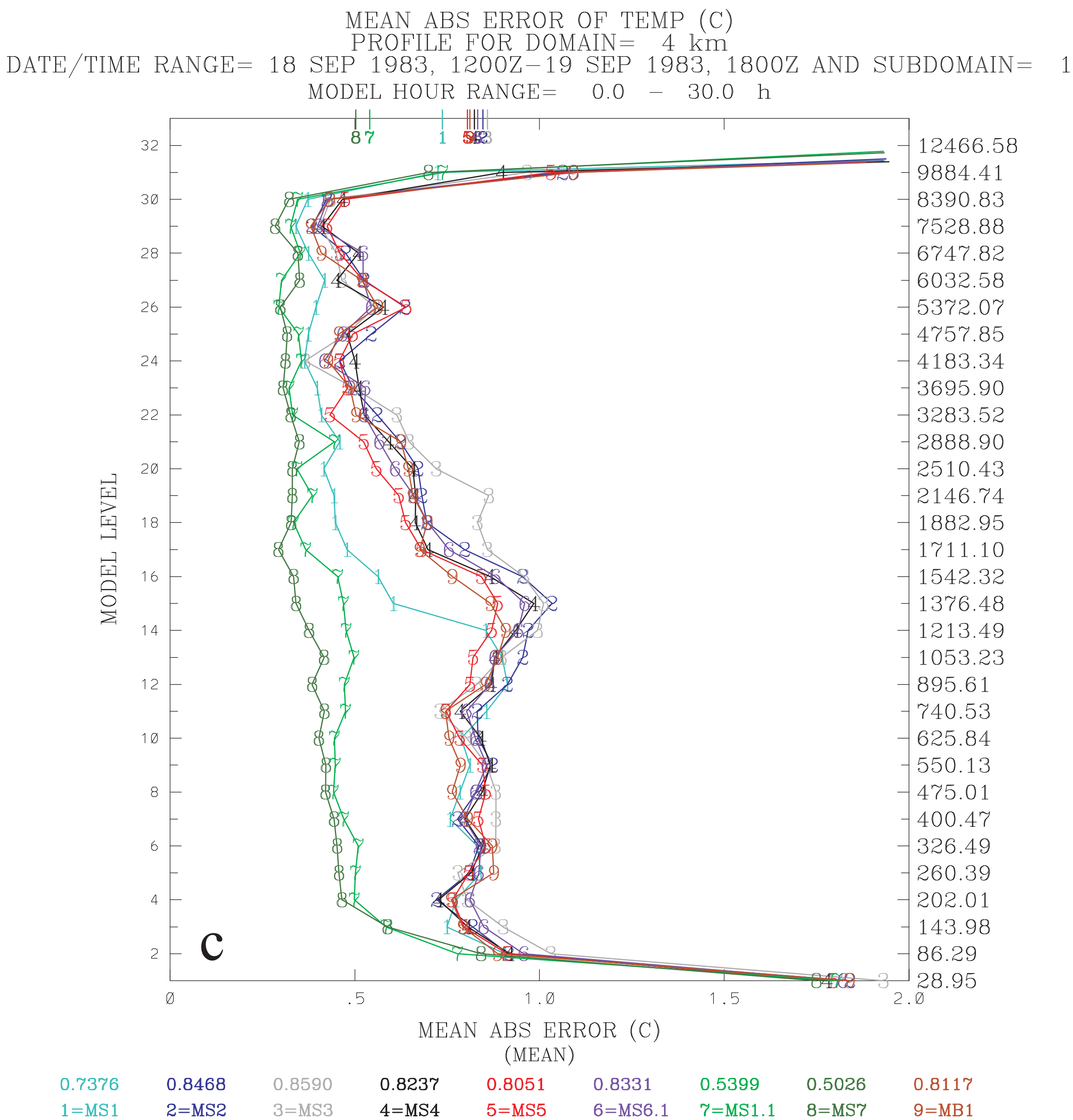

Figure 42 (Continued)

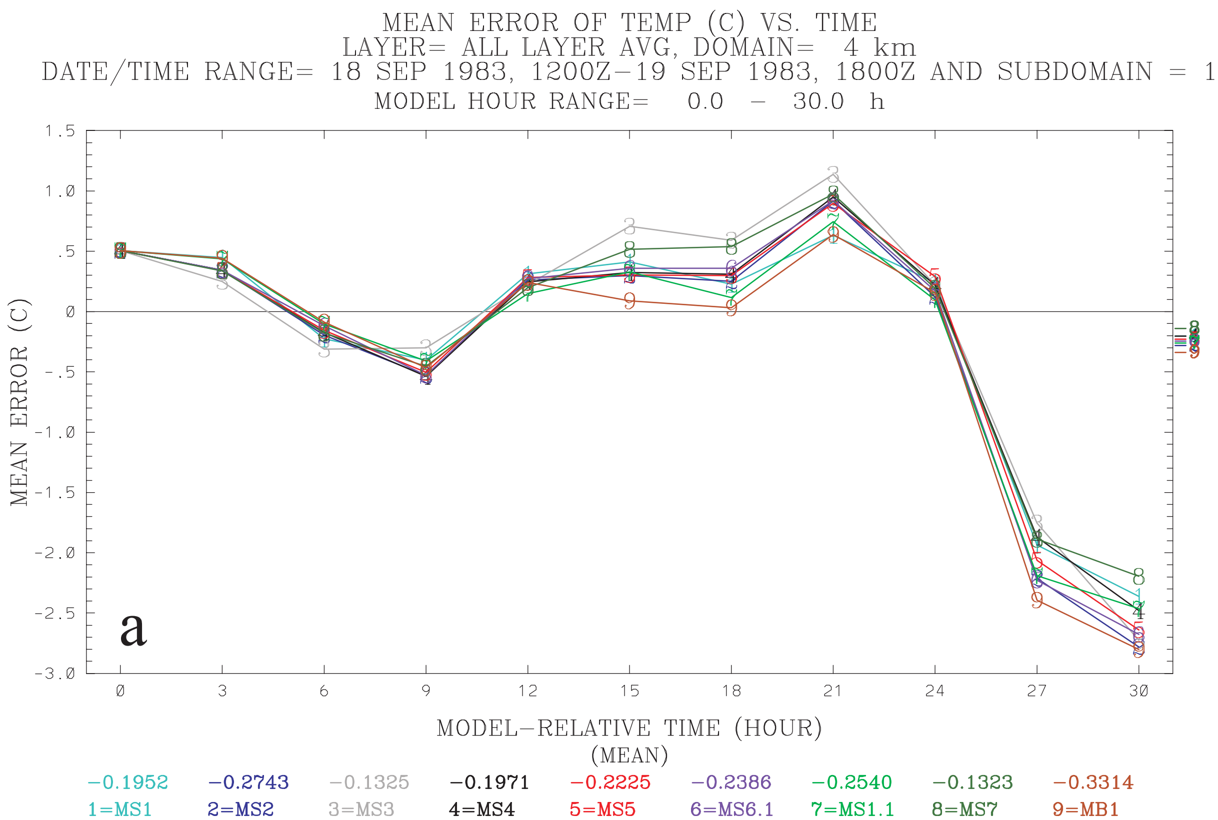

Figure 43 Mean error (*ME*) of MM5-simulated temperature field in CAPTEX-83 Episode 1 (1200 UTC, 18 September - 1800 UTC, 19 September 1983) on the 4-km verification domain. (a) *ME* versus time for the surface-layer (29 m AGL) temperature, (b) Vertical profiles of the 30-h averaged *ME* at all model layers. The 30-h mean statistics are plotted on the right end of each time series chart or top of each vertical profile chart with the digital values also included above the experiment key at the bottom of the figure.

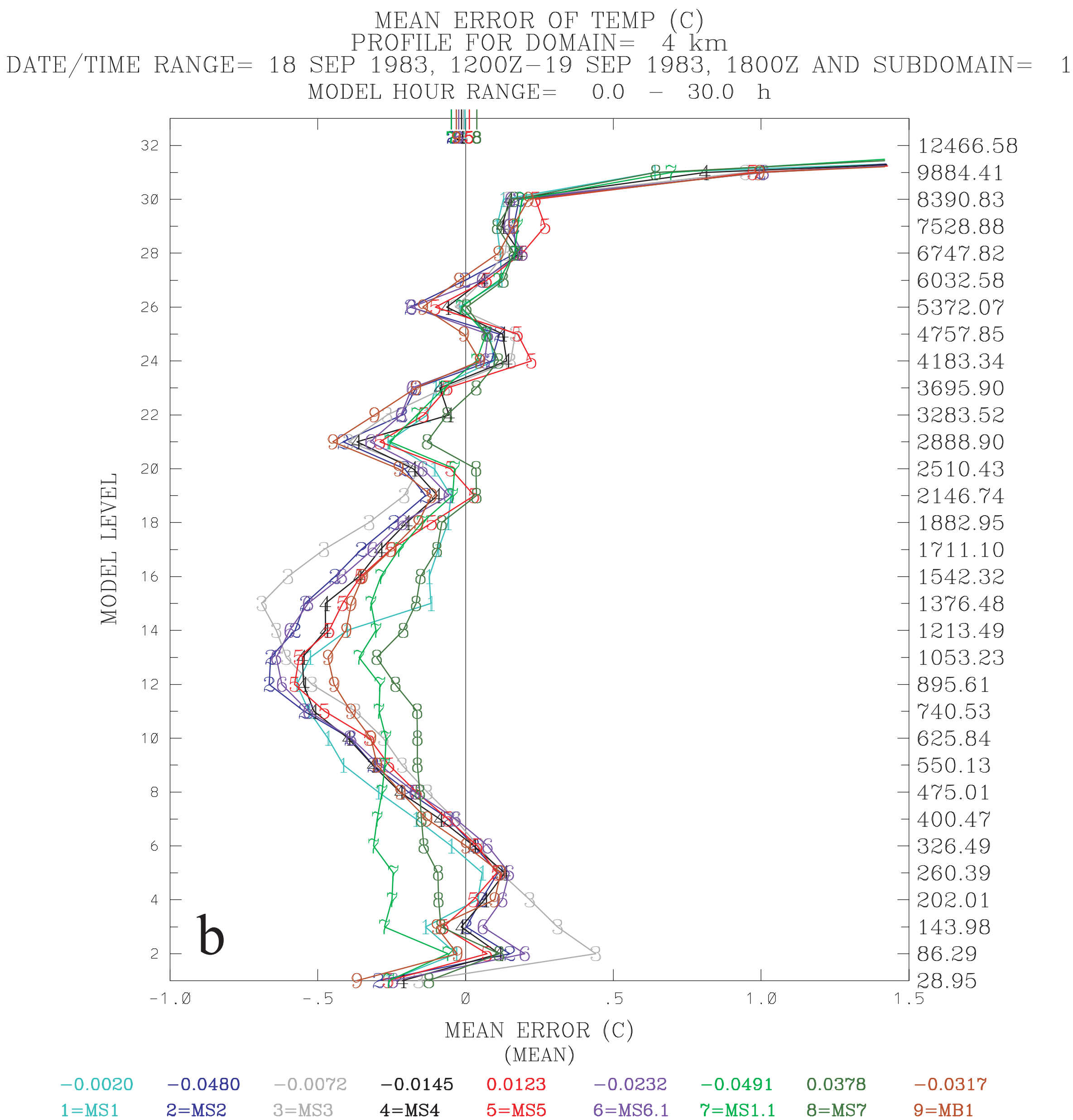

Figure 43 (Continued)

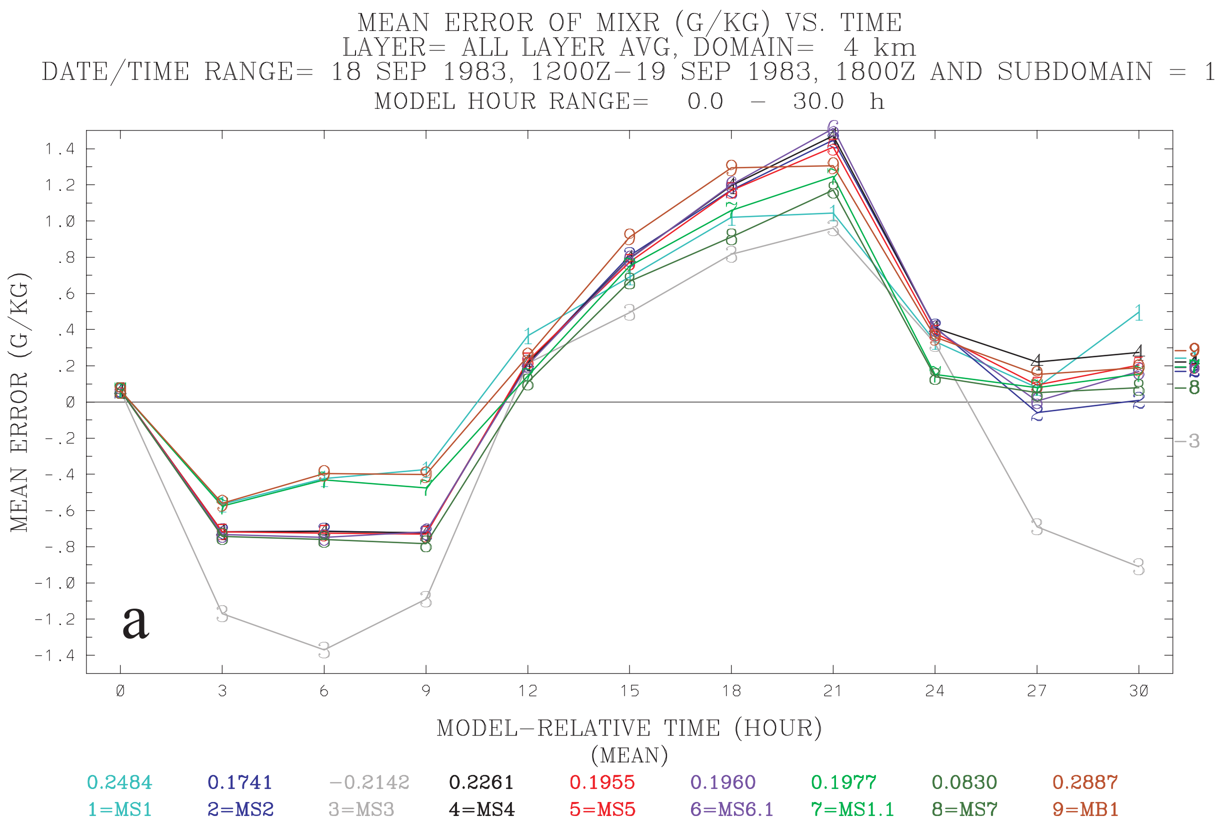

Figure 44 Mean error (*ME*) and mean absolute error (*MAE*) of MM5-simulated water vapor mixing ratio field in CAPTEX-83 Episode 1 (1200 UTC, 18 September - 1800 UTC, 19 September 1983) on the 4-km verification domain. (a) All-layer averaged *ME* versus time, (b) *MAE* versus time for the surface-layer (29 m AGL) water vapor mixing ratio (29 m AGL), (c) All-layer averaged *MAE* versus time, (d) Vertical profiles of the 30-h averaged *MAE* at all model layers. The 30-h mean statistics are plotted on the right end of each time series chart or top of each vertical profile chart with the digital values also included above the experiment key at the bottom of the figure.

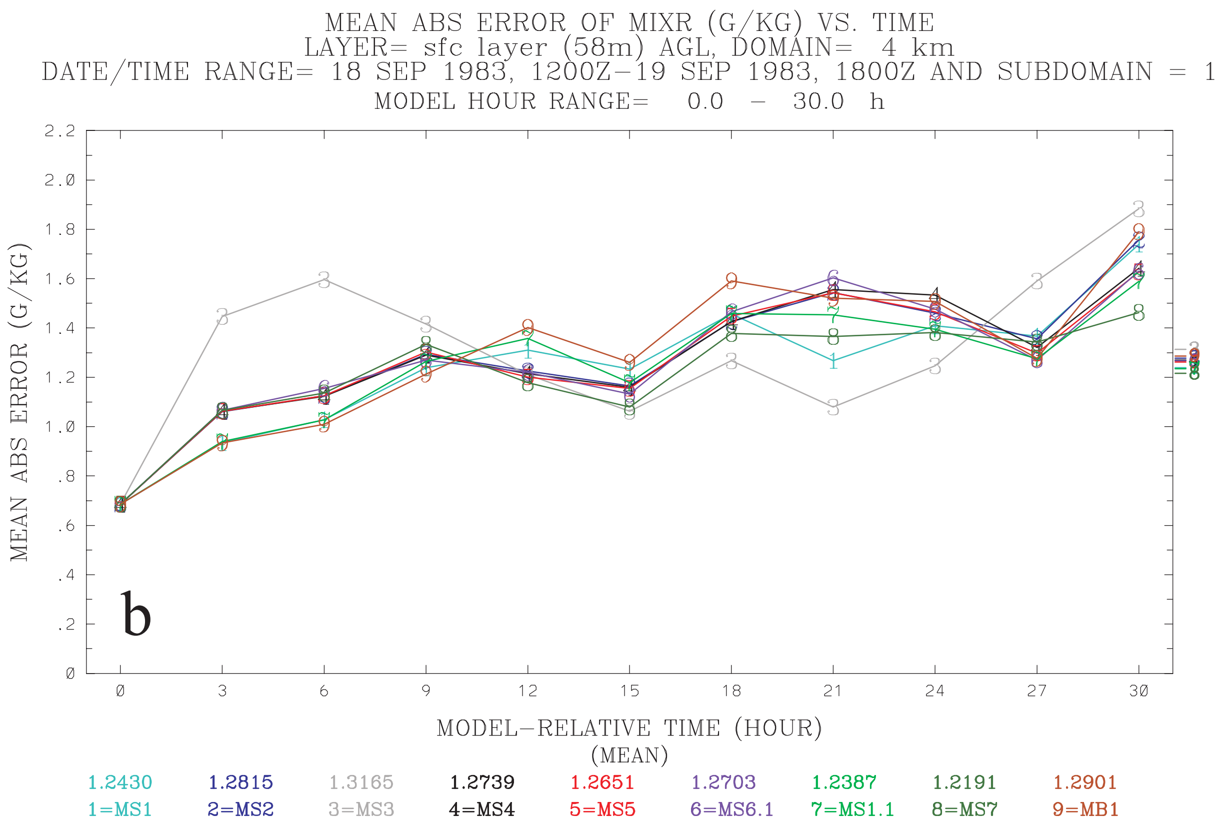

Figure 44 (Continued)

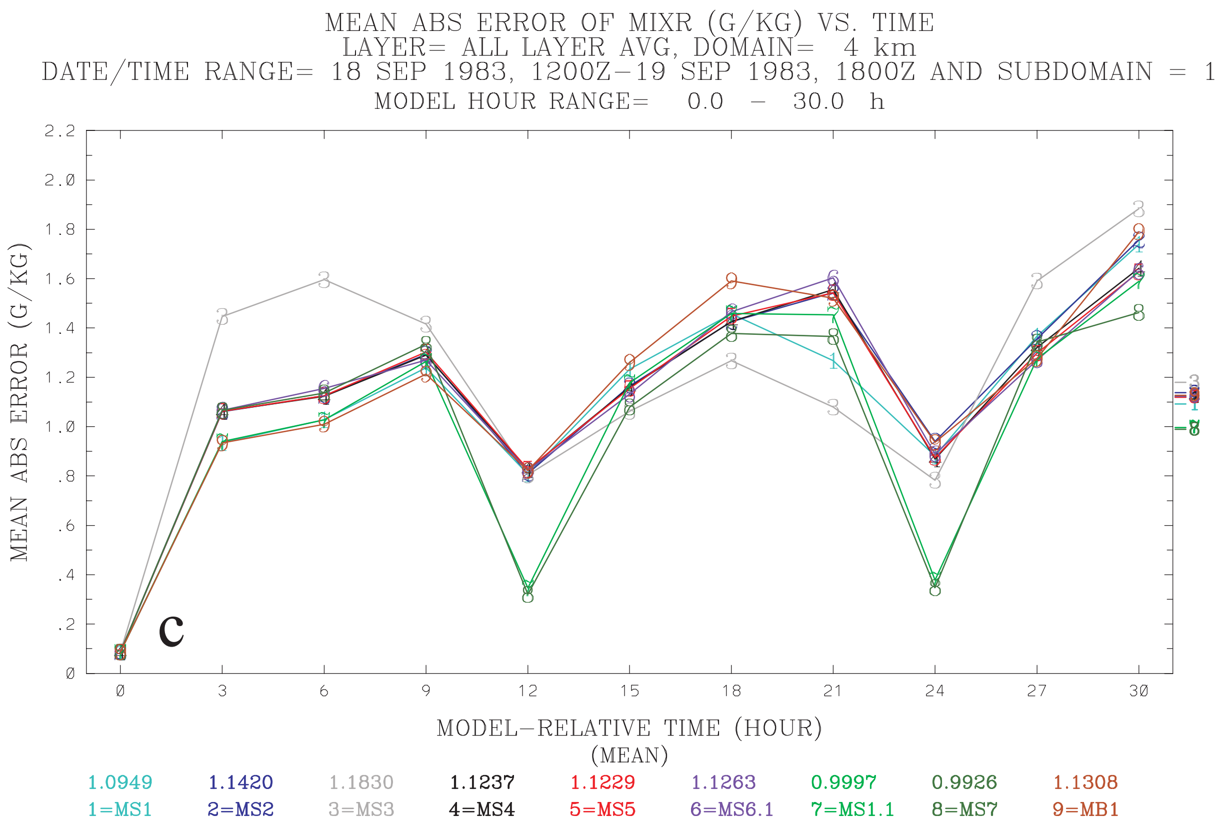

Figure 44 (Continued)

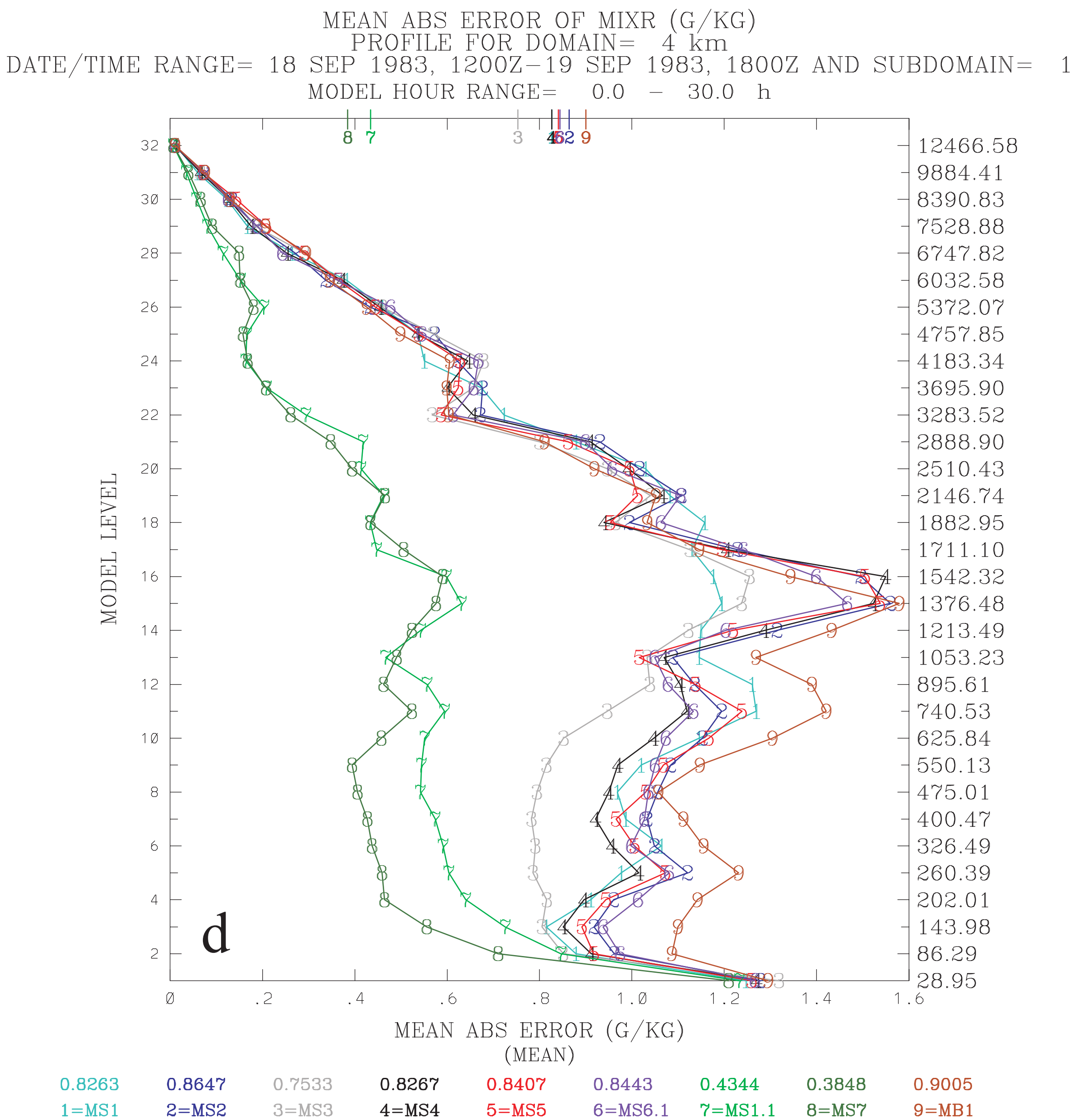

Figure 44 (Continued)

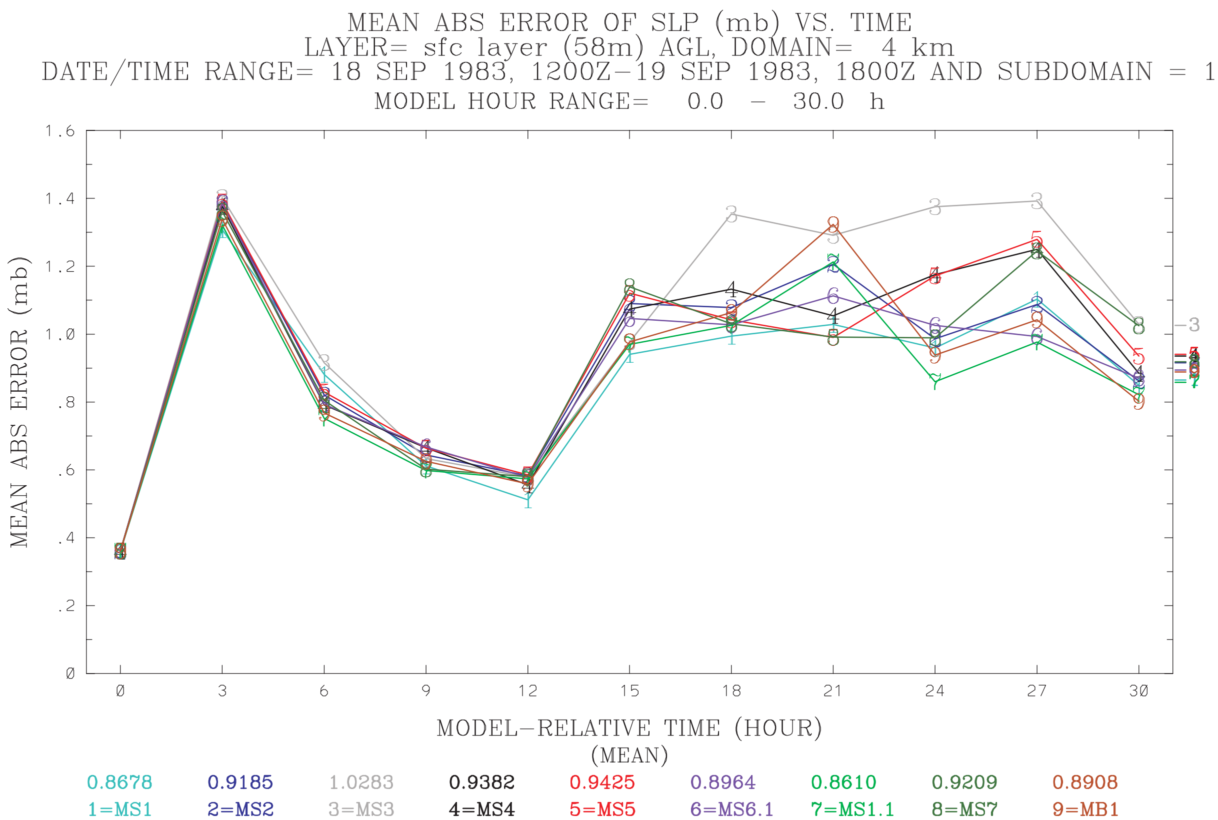

Figure 45 Mean absolute error (*MAE*) of MM5-simulated sea-level pressure field in CAPTEX-83 Episode 1 (1200 UTC, 18 September - 1800 UTC, 19 September 1983) on the 4-km verification domain. The 30-h mean statistics are plotted on the right end of each time series chart with the digital values also included above the experiment key at the bottom of the figure.